Dottorato di Ricerca in Ingegneria Civile
Graduate School in Civil Engineering
Sede: Facoltà di Ingegneria - Università di Pavia - via Ferrata 1 – 27100 Pavia – Italy

Dottorato di Ricerca in Ingegneria Civile XX Ciclo

Passive Control of Industrial Structures for Natural Hazard Mitigation: Analytical Studies and Applications

Ph.D. Dissertation
Gian Paolo Cimellaro

Relatore:
Prof. Elio Calligarich
Prof. Andrei M. Reinhorn

Controrelatore:
Prof. Lucia Faravelli

October 2007

Description of the Ph.D. course

Settore: **Field:**	Ingegneria Engineering
Sede Amministrativa non consortile: **Administrative location:**	Università degli Studi di Pavia University of Pavia
Durata del dottorato: **Duration**	3 anni 3 years
Periodo formativo estero: **Period in external organization:**	come previsto dal regolamento del Dottorato di Ricerca as required by the school by law
Numero minimo di corsi: **Minimum number of courses:**	6 6

Il dottorato di ricerca in Ingegneria Civile dell`Universita` degli Studi di Pavia è stato istituito nell'anno accademico 1994/95 (X ciclo).

Il corso consente al dottorando di scegliere tra quattro curricula: idraulico, Sanitario, Sismico e Strutturale. Egli svolge la propria attività di ricerca rispettivamente presso il Dipartimento di Ingegneria Idraulica e Ambientale per i primi due curricula, quello di Meccanica Strutturale per i rimanenti. Durante i primi due anni sono previsti almeno sei corsi. Il Collegio dei Docenti, composto da professori dei due Dipartimenti, organizza i corsi con lo scopo di fornire allo studente di dottorato opportunità di approfondimento su alcune delle discipline di base. Corsi e seminari vengono tenuti da docenti di Università nazionali ed estere. Il Collegio dei Docenti, cui spetta la pianificazione della didattica, si è orientato ad attivare ad anni alterni corsi sui seguenti temi:

- Meccanica dei solidi e dei fluidi
- Metodi numerici per la meccanica dei solidi e dei fluidi
- Rischio strutturale e ambientale
- Metodi sperimentali per la meccanica dei solidi e dei fluidi
- Intelligenza artificiale

più corsi specifici di indirizzo. Al termine dei corsi del primo anno il Collegio dei Docenti assegna al dottorando un tema di ricerca da sviluppare sotto forma di tesina entro la fine del secondo anno; il tema, non necessariamente legato all'argomento della tesi finale, è di norma coerente con il curriculum, scelto dal dottorando. All'inizio del secondo anno il dottorando discute con il Coordinatore l'argomento della tesi di dottorato, la cui assegnazione definitiva viene deliberata dal Collegio dei Docenti. Alla fine di ogni anno i dottorandi devono presentare una relazione particolareggiata sull'attività svolta. Sulla base di tale relazione il Collegio dei Docenti, "previa valutazione della assiduità e dell'operosità dimostrata dall'iscritto", ne propone al Rettore l'esclusione dal corso o il passaggio all'anno successivo. Il dottorando può svolgere attività di ricerca sia di tipo teorico che sperimentale, grazie ai laboratori di cui entrambi i Dipartimenti dispongono, nonché al Laboratorio Numerico di Ingegneria delle

Infrastrutture. Il “Laboratorio didattico sperimentale” del Dipartimento di Meccanica Strutturale offre:

- una tavola vibrante che consente di effettuare prove dinamiche su prototipi strutturali;
- opportuni sensori e un sistema di acquisizione dati per la misura della risposta strutturale;
- strumentazione per la progettazione di sistemi di controllo attivo e loro verifica sperimentale;
- strumentazione per la caratterizzazione dei materiali, attraverso prove statiche e dinamiche.

Il laboratorio del Dipartimento di Ingegneria Idraulica e Ambientale dispone di:

- un circuito in pressione che consente di effettuare simulazioni di moto vario;
- un tunnel idrodinamico per lo studio di problemi di cavitazione;
- canalette per lo studio delle correnti a pelo libero.

The Graduate School of Civil engineering at the University of Pavia was established in the Academic Year of 1994/95 (X cycle). The School allows the student to select one of the four offered curricula: Hydraulics, Environment, Seismic Engineering and Structyural mechanics. Each student develops his research activity either at the Department of Hydraulics and Environmental Engineering or at the Department of Structural Mechanics. During the first two years, a minimum of six courses must be selected and their examinations successfully passed. The faculty, made by professor of the two Departments of by internationally recognized scientists, organizes courses and provides the student with opportunities to enlarge his basic knowledge. Courses and seminars are held by University Professors from all over the country and abroad. The Faculty starts up in alternate years common courses, on the following subjects:

- solid nad fluid mechanics;
- Numerical methods for solid and fluid mechanics;
- Structyural and environmental risks;
- Experimental methods for solid and fluid mechanics;
- Artificial intelligence

More specific courses are devoted to students of the single curricula.
At the end of each course, for the first year the Faculty assigns the student a research argument to develop, in the form of report, by the end of the second year; the topic not necessarily part of the final doctorate thesis, should be consistent with the curriculum selected by the student. At the beginning of the second year the student discusses with his Coordinator the subject of the thesis and, eventually the Faculty assigns it to the student. At the end of every year, the student has to present a complete report on his research activity, on the basis of which the Faculty proposes to the Rector his admission to the next academic year or the final examination. The student is suspposed to develop either theoretical or experimental research activities, and therefore has access to the Department Experimental Laboratories, even to the Numerical Laboratory of

Infrastructure Engineering. The experimental Teaching Laboratory of the Department of Structural Mechanics offers:

- A shaking table which poermits one to conduct dynamic tests on structural properties;
- Sensors and acquisition data system for the structural response measurements;
- Instrumentation for the desing of the active control system and their experimental checks;
- An universal testing machine for material characterization through static and dynamic tests;

The Department of Hydraulics and Environmental Engineering offers:

- A pressure circuit simulating various movements;
- A hydrodynamic tunnel studying cavitation problems;
- micro-channels studying free currents;

Recapiti - Addresses

Dipartimento di Meccanica Strutturale
via Ferrata 1 - 27100 Pavia - Italy
Tel. 0382 / 505450 Fax 0382 / 528422

Dipartimento di Ingegneria Idraulica e Ambientale
via Ferrata 1 - 27100 Pavia - Italy
Tel. 0382 / 505300 Fax 0382 / 505589

Coordinatore - Coordinator

CASCIATI Fabio - Professore Ordinario (ICAR08)
Dipartimento di Meccanica Strutturale
via Ferrata 1 - 27100 Pavia – Italy
Tel. 0382 / 505458 - Fax 0382 / 528422
e-mail: fabio@dipmec.unipv.it

Collegio dei Docenti – Teaching Staff

CAPODOGLIO Andrea Giuseppe		Professore Associato – ICAR/03
CASCIATI Fabio		Professore Ordinario – ICAR/08 – (Coordinatore)
CAUVIN Aldo	-	Professore Ordinario ICAR/09[†]
CIAPONI Carlo	-	Professore Straordinario - ICAR/01
FARAVELLI Lucia	-	Professore Ordinario – ICAR08
FUGAZZA Mario	-	Professore Associato – ICAR/02
GOBETTI Armando	-	Professore Associato – ICAR08
MOISELLO Ugo	-	Professore Ordinario – ICAR/02
PAPIRI Sergio	-	Professore Associato – ING-IND/08
SALA Roberto	-	Professore Associato – ING-IND/08
MARCELLINI Alberto		Dirigente di Ricerca CNR- Milano

[†] Decedeuto il 30 Gennaio 2007

Previous Ph.D. Theses

Battaini Marco (X Ciclo)	Sistemi strutturali controllati: progettazione e affidabilità
Claudia Mariani (X Ciclo)	Problemi di ottimizzazione per strutture bidimensionali anisotrope
Antonella Negri (X Ciclo)	Stima delle perdite idrologiche nei bacini di drenaggio urbani" (Febbraio 1999).
Pisano Aurora Angela (XI Ciclo)	Structural System Identification :Advanced Approaches and Applications
Saltalippi Carla (XI Ciclo)	Preannuncio delle piene in tempo reale nei corsi d'acqua naturali
Barbieri Eugenio (XI Ciclo)	Thermofluid Dynamics and Topology Optimization of an Active Thermal Insulation Structure
Barbolini Massimiliano (XII Ciclo)	Dense snow Avalanches: Computational Models, Hazard Mapping and Related Uncertainties
Espa Paolo (XII Ciclo)	Moti atmosferici generate da forze di galleggiamento: simulazioni numeriche e studio su modello fisico
Petrini Lorenza (XII Ciclo)	Shape Memory Alloys: Modelling the Martensitic Phase Behavior for Structural Engineering Exploitation
Podestá Stefano (XIII Ciclo)	Risposta sismica di antichi edifice religiosi: una nuova proposta per un modello di vulnearabilitá"

Sturla Daniele (XIII Ciclo) Simulazioni lagrangiane di flussi rapidamente variati nell`approssimazione di acquae poco profonde"

Marazzi Francesco (XV Ciclo) Semi-active control of civil structures: implementation aspects

Nascimbene Roberto (XV Ciclo) Sail modelling for Maximum speed optimum design

Giudici Massimo (XVI Ciclo) Progettazione in regime nonlineare di Strutture in CAP a cavi aderenti e non aderenti

Mutti Matteo (XVI Ciclo) Stability analysis of stratified three-phase flows in pipes

Petaccia Gabriella (XVI Ciclo) Propagazione di onde a fronte ripido per rottura di sbarramenti in alvei naturali

Casciati Sara (XVII Ciclo) Damage detection and localization in the Space of the Observed Variables

D`Amico Tiziana (XVI Ciclo) Ricerca e sviluppo di metodologie diagnostiche per il recupero di edifice monumentali; Prove vibroacustiche sul tufo

Barco Olga Janet (XVII Ciclo) Modeling the quantity and quality of storm water runoff using SWMM

Bornatici Laura (XVIII Ciclo) L'impiego degli algoritmi generici per la risoluzione dei problemi di progetto di reti di distribuzione idrica

Boguniewicz Joanna (XVIII Ciclo) Integration of monitoring and modelling in the surface water state evaluation process of a sub-Alpine lake watershed

Collivignarelli Maria Cristina (XVIII Ciclo) Trattamento di rifiuti liquidi mediante processi biologici aerobici

termofili e mesofili e processi avanzati di ossidazione chimica in diversa sequenza

Domaneschi Marco (XVIII Ciclo) Structural Control of Cable-stayed and Suspended Bridges

Raduly Botond (XVIII Ciclo) Artificial neural network applications in urban water quality modeling"

Antoci Carla (XVIII Ciclo) Simulazione numerica dell'interazione fluido-struttura con la tecnica SPH"

Cappabianca Federica (XVIII Ciclo) La valutazione del rischio valanghivo attraverso la modellazione dinamica

Callegari Arianna (XVIII Ciclo) Applicazione di tecnologie di monitoraggio on-line per la gestione dei processi di trattamento reflui

Gazzola Elisa (XVIII Ciclo) Applicazione di processi biologici anaerobici al trattamento di acque reflue e fanghi di depurazione: aspetti tecnici ed energetici

Maranca Federica (XVIII Ciclo) Valutazione del ciclo di vita (LCA): confronto tra sistemi di trasporto gas via gasdotto

Giuliano Fabio (XIX Ciclo) Performance based design and structural control for cable suspension bridges

Falappi Stefano (XIX Ciclo) Simulazioni numeriche di flussi di fluidi viscosi e materiali granulari con la tecnica SPH

Zanaboni Sabrina (XIX Ciclo) Pre-trattamento di rifiuti liquidi industriali mediante ossidazione ad umido

Acknowledgments

This work was supported by INFN. The author is grateful to professor Alberto Rotondi, the new director of INFN-section Pavia and to professor Claudio Conta, the past director of INFN-section Pavia for his patience during the development of this work.

The author would like to thank Fabio Casciati for taking time to review this work and provide helpful feedback and Dr. Praveen Malhotra for his assistance in the analysis of the sloshing.

Thanks to all the students, staff and Faculty of University at Buffalo and University of Pavia. The atmosphere of academic excellence and collegiality fostered there played a big role in my productivity and my enjoinment of my Ph.D. experience.

Most importantly the author thanks his advisors and mentors in this work: Professor Calligarich and Professor Andrei M. Reinhorn, whose insight and enthusiasm has made this research experience incredibly rewarding.

Finally I'm most grateful to my parents and sisters for their support and encouragement that have enabled me to complete this dissertation.

Abstract

This Ph.D. dissertation investigates two different systems:

The first is the characterization of earthquake forces, including sloshing phenomena in the rectangular and horizontal cylindrical tanks of the T600 module of ICARUS project.

The second of the complementary research efforts in this dissertation is the mitigation of earthquakes forces due to coupling of adjacent buildings with passive devices that has been modeled as velocity dependent links both linear and nonlinear.

TABLE OF CONTENTS

LIST OF ILLUSTRATIONS

FIGURE
PAGE

LIST OF TABLES

TABLE
PAGE

Chapter 1

1 ICARUS: Image Cosmic And Rare Underground Signals

1.1 Introduction

"The ICARUS project represents a new generation of very large sensitive mass detectors ideal to fulfill one of the most challenging goals in the present Particle Physics, that is, the search for rare underground events such as proton decay, solar neutrino observations, neutrino oscillations and relic supernovae neutrinos. This ambitious programme involves the construction of a multi-kiloton (3000t) liquid Argon TPC at the Gran Sasso Laboratory by means of a modular-wise strategy; the construction of a number of identical T600 detectors installed next to one another allows to reach the final liquid argon sensitive mass.

One of the main issues of such kind of devices lies in the fact that the detector is continuously sensitive, self-triggering and able to provide unbiased three-dimensional views of the ionizing events. In addition, the actual availability of ultrapure liquid Argon with high electronion pair yield compared with the event energy deposited in the fluid makes possible ionization electron drifts over distance of several meters.

The present work is set against the background of those engineering research activities oriented towards the definition of the optimal T600 working lay-out."

Geneve, 1999 Carlo Rubbia

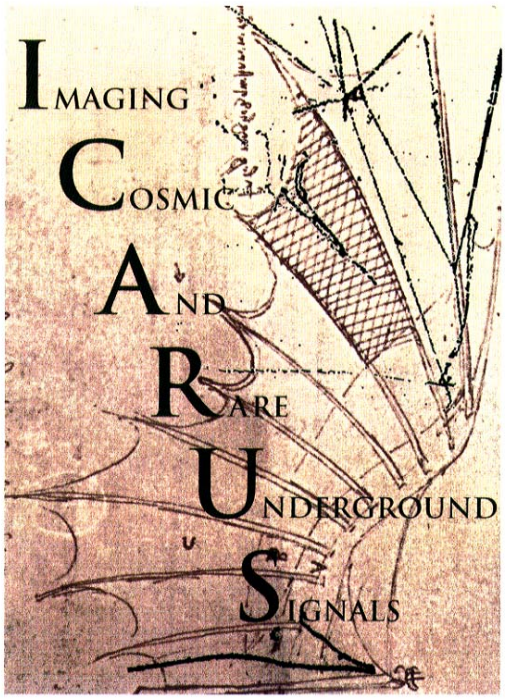

Figure 1.1 Logo

1.2 Research Motivations

The ICARUS T600 is an experimental programme, with significant physics potentialities, combined with challenging aspects of technological development, in view of the operability of a large mass liquid Argon "bubble chamber" inside the Gran Sasso underground Laboratory located in Assergi, near l`Aquila (Figure 1.2). LNGS (National Laboratory Gran Sasso) is the largest underground laboratory in the world for experiments in particle physics.

In the recent past **ANPA** (Agenzia Nazionale per la Protezione dell'Ambiente) have recognized the proximity of the Gran Sasso Laboratory to two important direct faults oriented WNW-ESE called M. S. Franco – Assergi – Valle Fredda Tre selle – Fontari – Campo Imperatore. Therefore, the area is considered seismic zone. Faults are active and they belong to seismic tectonic zone of Center Appennini mountains. These type of fault (normal fault) are responsible of the mayor earthquakes in Italy (e.g. Colfiorito1997, Irpinia 1980, Fucino 1915) that generated vertical displacements up to 150cm for an extension up to 40 km. The seismicity of the area and the underground location of the cryostat requires a detailed seismic analysis of the entire system.

Figure 1.2 Areal View of the LNGS

1.3 Goal of the ICARUS Experiment

The ICARUS detector is a Time Projection Chamber (TPC) filled with liquid Argon. It represents a new generation of bubble chambers, with the advantage of being operated over a very large sensitive volume, continuously sensitive, self-triggering, able to provide three-dimensional views of ionising events with particle identification from dE/dx and range measurements.

The experiment aims at the demonstration and at a comprehensive study of neutrino oscillations through the detection and detailed analysis of neutrino events coming both from natural (*solar* and *atmospheric neutrinos*) and *artificial* (CERN to Gran Sasso Long Baseline Neutrino Beam) sources. The other major issue of the ICARUS scientific program is the search for nucleon decay especially in SUSY favored (N --> ν K) or exotic channels.

1.4 History of ICARUS

A proposal for the first T600 module has been submitted for funding to INFN in 1995 and fully approved in 1996 and the construction started immediately after.

The final project and designing of all the detector components, including cryogenics, read-out chambers and electronics, have been completed by mid 1998. The construction of the detector has been completed by the end of 2000 in Pavia, near Milan (Italy). The major industrial counterparts collaborating to the ralization of the ICARUS 600 t detector were AIR LIQUIDE, for the cryogenic system, and CAEN, for the electronics and recently also the STIRLING.

A full test of the experimental set-up was foreseen, prior to its final installation at GranSasso in Pavia, near Milan (Italy). The start-up operations begun on April 23rd, 2001 and, after smooth vacuum pumping and cool-down procedures, one of the two half-modules (300t of LAr) of the T600 has been

filled with ultra-purified liquid Argon. The wire chambers were instrumented with the read-out electronics and the HV rised-up to nominal voltage. Immediately, first long muon tracks have been detected (June, 2nd 2001).

The two semi module of T600 were transported to LNGS December, 2004 due to delays and the installation started right after. In march 2005 was completed the tank of the external insulation system. March 2006 was completed the installation of the base isolation system. April 2007 was mounted the thermical screen. At the beginning of Jenuary 2008 the experiment will be ready to start.

1.5 Organization

This dissertation investigates two different systems:

The first is the characterization of earthquake forces, including sloshing phenomena in the rectangular and horizontal cylindrical tanks of the T600 module of ICARUS project.

The second of the complementary research efforts in this dissertation is the mitigation of earthquakes forces due to coupling of adjacent buildings with passive devices.

Chapter 2 describes the ICARUS T600 module and its geometric properties. A finite element model in SAP2000 of the entire system has been built and displacement and acceleration response of the main structural parts have been determined under different loading conditions.

Chapter 3 describes the basic form of the governing partial differential equations that LS-DYNA`s flow solver treats and provides a general description of the explicit time integration method that is used in their solution. A description of the contact algorithm that is based on the penalty method is also provided.

Chapter 4 describes the finite element model in LS-DYNA and ANSYS of the T300 semi-module. Both models have been built to analyze the nonlinear phenomena of sloshing.

Chapter 5 characterizes the ground motion input at the site. A clear description of the methods available to simulate earthquake ground motions is given. They consists in the selection of real earthquake that consider in different scaling procedures and stochastic methods that are based on synthetic earthquakes.

Chapter 6 describes the earthquake loads due to sloshing in two horizontal cylindrical tanks filled with liquid Nitrogen (LN2) and liquid Argon (LAr). Overturning moments and lateral forces have been evaluated in the transversal and longitudinal direction for four different liquid heights using the approach described in the paper of Karamanos et al. (2006).

Chapter 7 describes the seismic forces due to sloshing and impulsive motion of the semi-module T600. Overturning moments, lateral forces and pressures distributions on the walls have been evaluated both in the longitudinal and transversal direction. Hydrodynamic pressures on the lateral walls has been evaluated more accurately using the finite element model developed in LS-DYNA. Hydrodynamic pressures generated on the roof of the tank due to sloshing have been evaluated following the procedure described in the paper of Malhotra (2005) that has been opportunely modified to be adapted to rectangular tank.

Chapter 8 describes different seismic qualification requirements of the piping system. The final pipe support arrangement to retrofit the piping system of the entire project is described.

Chapter 9 evaluates comprehensively the seismic response of a set of pairs of adjacent linear building structures linked to one another at different floor levels by linear and nonlinear passive devices.

Chapter 2

2 The ICARUS T600 module

The ICARUS detector is a Time Projection Chamber (TPC) filled with liquid Argon. The operating principle is rather simple: any ionizing event (from particle interaction or decay) taking place in a volume of liquid Argon, where a uniform electric field is applied, produces ion-electron pairs. A fraction of them, depending on the field intensity and on the density of ion pairs, will not recombine and will immediately start to drift parallel to the field in opposite directions. Only the motion of the much faster electrons induces a current on a number of parallel wire planes (the read-out chambers) located at the end of the sensitive volume. The choice of the liquid was driven by the following considerations:

- it must be an excellent insulator and available at an extremely high purity level, so that free electrons produced by ionization can drift in the liquid over long distances;
- it must have a high electron-ion pair yield with respect to the energy deposited in the liquid;
- it must be easily available in large quantities, which is the case for Argon, a natural component of the Earth's atmosphere (1%).

The main cryogenic container for the ICARUS 600-ton consists of two semi-independent and symmetric parallelepids of approximately 3.6 by 3.9 by 19.9 cubic meters (Figure 2.3, Figure 2.8 and Figure 2.9). Its walls are made of aluminium honeycomb panels. The thermal insulation uses an innovative method requiring no vacuum and based on honeycomb insulating material with cold gas flowing through the cells. Details about the insulation system can be found in the Ph.D. thesis of Barbieri (Barbieri, 1999).

2.1 Building details of the ICARUS T600 module

Figure 2.1 shows the plan view of the Hall B of the laboratory with the effective location of the T600 module. Figure 2.2 and Figure 2.3 are some pictures of the Hall before and during the installation of the sub-module, while in Figure 2.5 is shown a tranversal view of the Hall with the effective location of the service structure and the cylindrical tanks on top of it. A plan view of the steel frame structure surrounding the Cryostat is shown in Figure 2.6, together with a 3D view of the steel service structure (Figure 2.7).

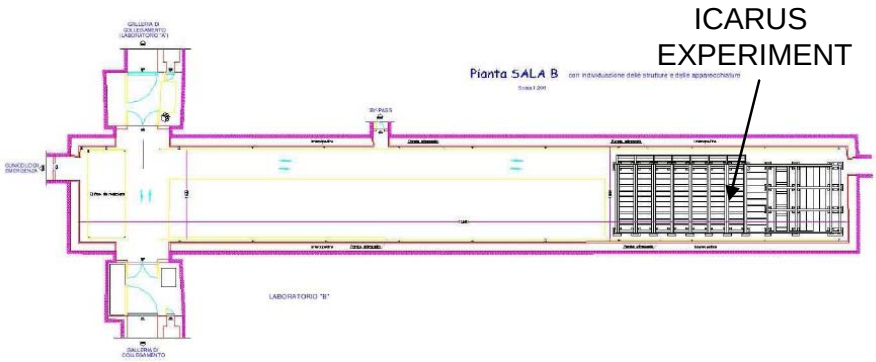

Figure 2.1 Plan view of hall B

The T600 Detector is composed of two submodules (Figure 2.8, Figure 2.9). Geometric properties of the submodules are reported in section 2.2. Figure 2.4 shows the current status of the experiment.

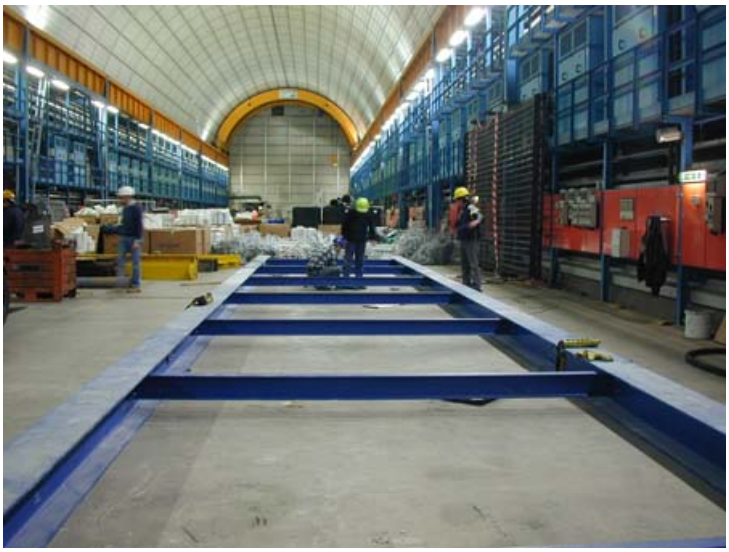

Figure 2.2 Picture of Hall B of LNGS before installation of T600 module

Figure 2.3 The first T300 module during its positioning in the Hall B of the Gran Sasso Laboratories

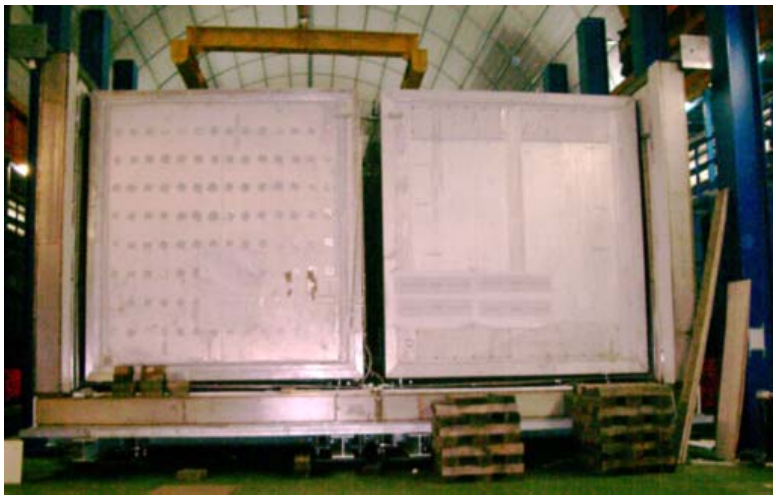

Figure 2.4 Current Status with two sub-modules located in their final position

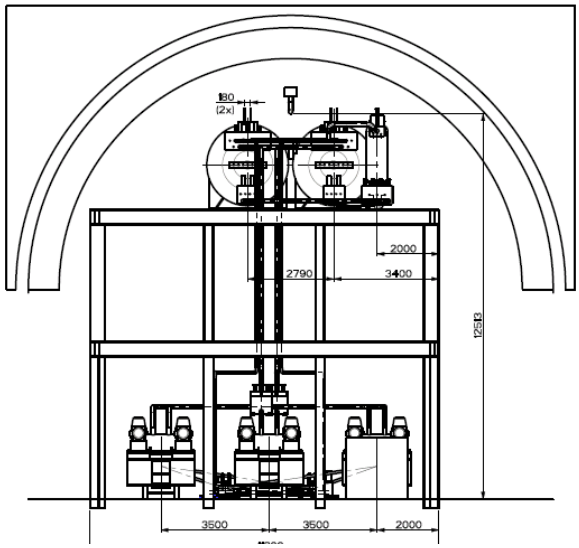

Figure 2.5 Transversal view of Hall B at the Gran Sasso Laboratory

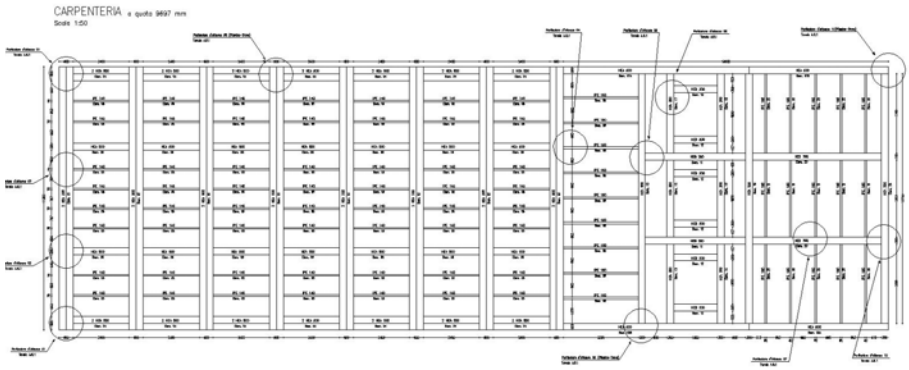

Figure 2.6 Plan view of the steel frame service structure inside the hall B

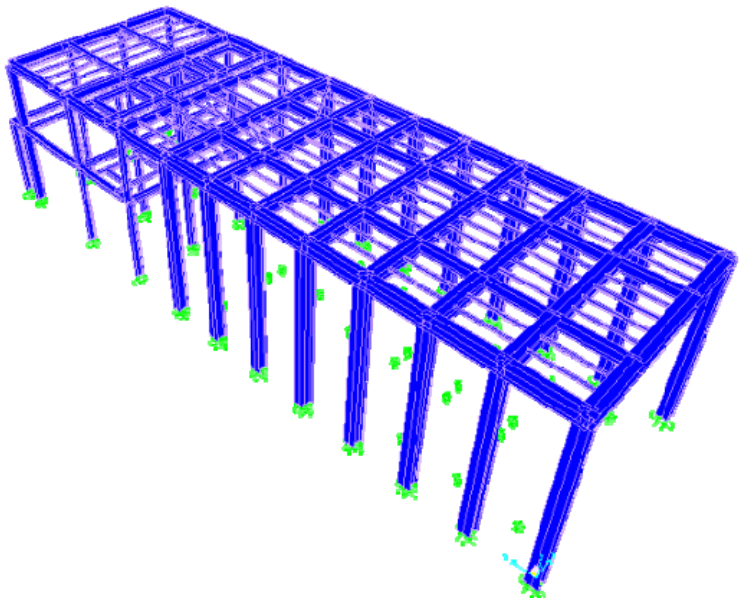

Figure 2.7 3D view of the Steel Service Structure

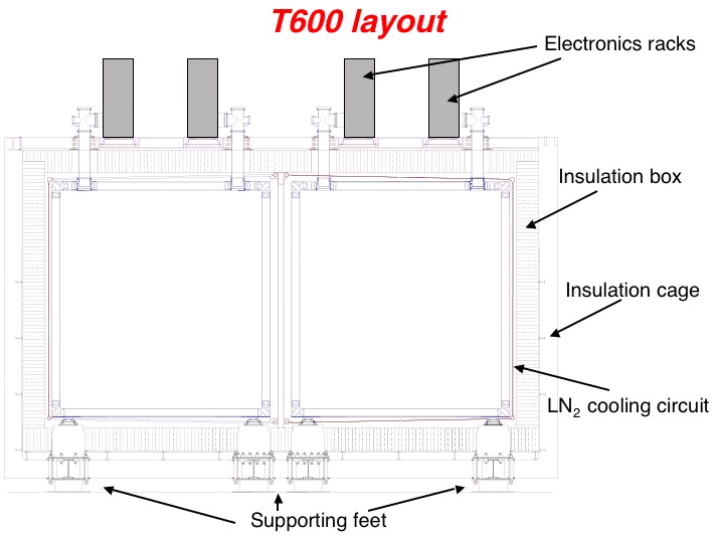

Figure 2.8 Front view of T600 module

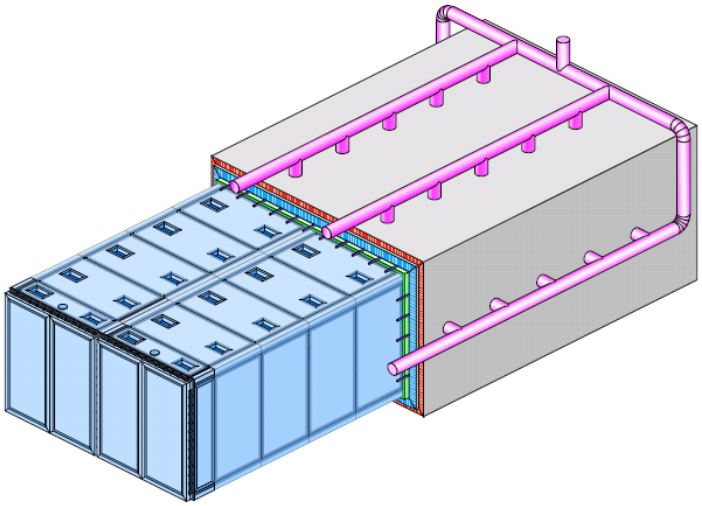

Figure 2.9 Schematic view of ICARUS T600 cryostat

2.2 Geometric properties of the rectangular tank of T600 module

The T600 cryostat is composed by two adjacent identical Aluminum parallelepiped sub-modules (called "T300") whose internal dimensions are 3.6 m (width) × 3.9 m (height) × 19.6 m (length), which means a volume of 275 m^3. At regime each T300 is full with liquid Argon up to 0.1 m from the top, kept in stable conditions at a typical working pressure of about 1.25 bar abs. Main geometric characteresitics of the sub module of T600 are listed in Table 2-1.

Table 2-1 Main Characteristics of sub module of T600

Single sub-module internal dimensions	
length L	19.6 m
width L	3.6 m
height H	3.9 m
Sub-module material	Aluminum
Sub-module walls thickness	0.15 m
Single sub-module own weight	28.0 ton
Thermal insulation thickness	0.4 m
Thermal insulation material	Evacuated Nomex panels
Number of TPCs per sub-modules	2
Number of wires per TPC	13440
Total number of wires	53760
Detector material	Stainless steel
Detector weight per sub-module	20 ton
Total (cold) internal volume	534 m3
Total LAr mass	735 ton

2.2.1 Laminated-Rubber bearings

Laminated-rubber bearings (elastomeric bearings) can withstand large gravity loads, while providing only a small lateral stiffness compared to the lateral stiffness of the superstructure they support. As shown in Figure 2.10.

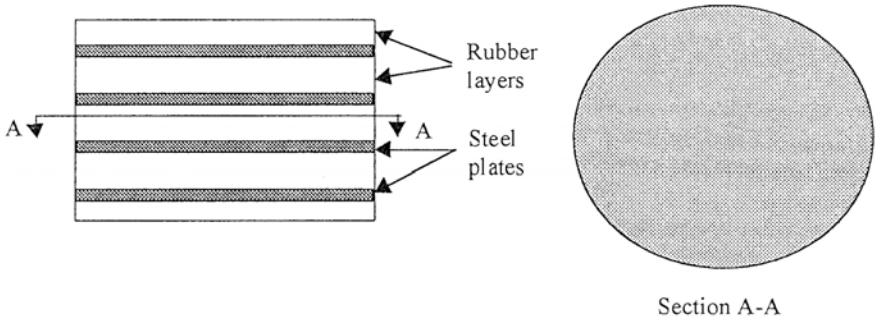

Figure 2.10 Scheme of Laminated Rubber Bearing

By alternating steel and rubber layers, the gravity load resisting capacity of laminated-rubber bearing is increased by reducing the thickness of individual rubber layers. Also, the lateral and rocking stiffness of a laminated-rubber bearing are proportional to the height of the unit. The layers of steel plates improve the stability of tall bearings under lateral loads.

The key parameters in the design of laminated-rubber bearings are the gravity load carrying capacity, the lateral stiffness and the maximum acceptable relative displacement between the top and the base of the bearing. The lateral stiffness will determine the natural period of the assumed-fixed superstructure, while the maximum acceptable relative displacement is limited by the allowable strain in the rubber or the overall stability of the bearing.

One of the disadvantage of this type of bearing is the relatively low damping provided by the rubber.

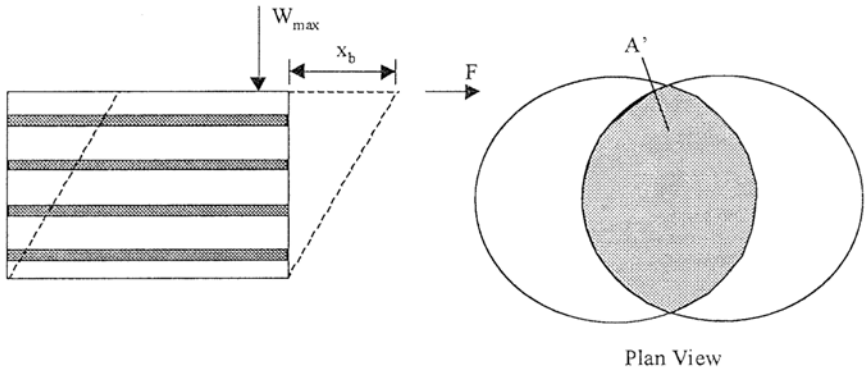

Figure 2.11 Circular Laminated rubber Bearing under gravity and lateral loads

The maximum allowable vertical load that can be carried by a bearing, W_{MAX} , can be approximated by the following semi-empirical equation:

$$W_{MAX} = A' GS\gamma_w \tag{2.1}$$

where A' is the overlap area between the displacement top and bottom of bearing (Figure 2.11); G is the shear modulus of rubber (1.4 MPa); S is the shape factor of each rubber layer equal to the loaded area of the bearing divided by the force-free aea of the bearing; γ_w is the allowable shear strain due to gravity load.

The shape factor for a cylindrical bearing of diameter D and made of rubber layers of thickness t is given by:

$$S = \frac{loaded\_area}{force\_free\_area} \frac{\frac{\pi D^2}{4}}{\pi Dt} = \frac{D}{4t} \tag{2.2}$$

The steel plates vulcanized to the rubber layers limit severely the flexural deformations of a laminated-rubber bearing. Therefore, it can be assumed that

pure shear deformations occur in the rubber only. The lateral stiffness of a laminated-rubber bearing, k_b can be approximated as:

$$k_b = \frac{GA}{h} \tag{2.3}$$

where A is the rubber layer area and h is the total rubber height. Note that equation (2.3) neglects the reduction in lateral stiffness at large displacements. For shape factor S, in the order of 10 to 20, this reduction is not serious.

Both semi-modules are mounted on top of 28 rubber bearings provided by ALGA (Figure 2.13, Figure 2.14) . The dynamic characteristic obtained from experimental tests of the two types of bearings are reported in Table 2-2 and Table 2-3.

Table 2-2 HDH.E 500 (Hard Rubber): 12 bearings

Max vertical load:	1500 kN
Max horizontal deformation:	±140 mm
Horizontal stiffness:	3000 N/mm ±10%
Vertical stiffness:	1100 kN/mm±20%
Shear elastic modulus G (N/mm^2)	1.4
N° rubber layers	8
Thickness of rubber layers	11.5mm
N° steel layers	7
Thickness of steel layers	4 mm
Thickness external steel plates	25 mm
Dimension external plates	750×750×25
Equivalent damping ratio ζ	16%
Total thickness of bearing	195 mm

Table 2-3 HDS.E 500 (Soft Rubber): 16 bearings

Max vertical load:	1500 kN
Max horizontal deformation:	±140 mm
Horizontal stiffness:	875 N/mm ±10%
Vertical stiffness:	1100 kN/mm±20%
Shear elastic modulus G (N/mm^2)	0.4
N° rubber layers	15
Thickness of rubber layers	6 mm
N° steel layers	14
Thickness of steel layers	2 mm
Thickness external steel plates	27 mm
Dimension external plates	750×750×25
Equivalent damping ratio ζ	16%
Total thickness of bearing	195 mm

In a more accurate way the values of horizontal stiffness k_{eff} have been evaluated on experimental tests at the 5th cycle using the secant values and adopting the following formula:

$$G_{dyn} = 2W_e t_e / \left(A' d^2 \right) \tag{2.4}$$

Detailed vales of horizontal stiffness as function of horizontal deformation can be found in the report of ALGA (ALGA, 2001). The equivalent damping ratio obtained with this type of rubber bearing obtained by comparison of dissipated energy with equivalent viscous damper is ζ=16%. The damped elastic response spectra for two hazard levels considered for design (T_r=475 years and 10000 years) are shown in Figure 2.12.

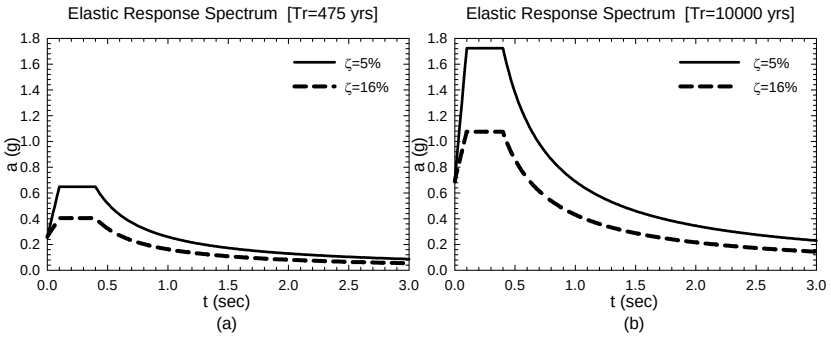

Figure 2.12 Elastic damped response spectrum for return period of 475 years (a) and for return period of 10000 years

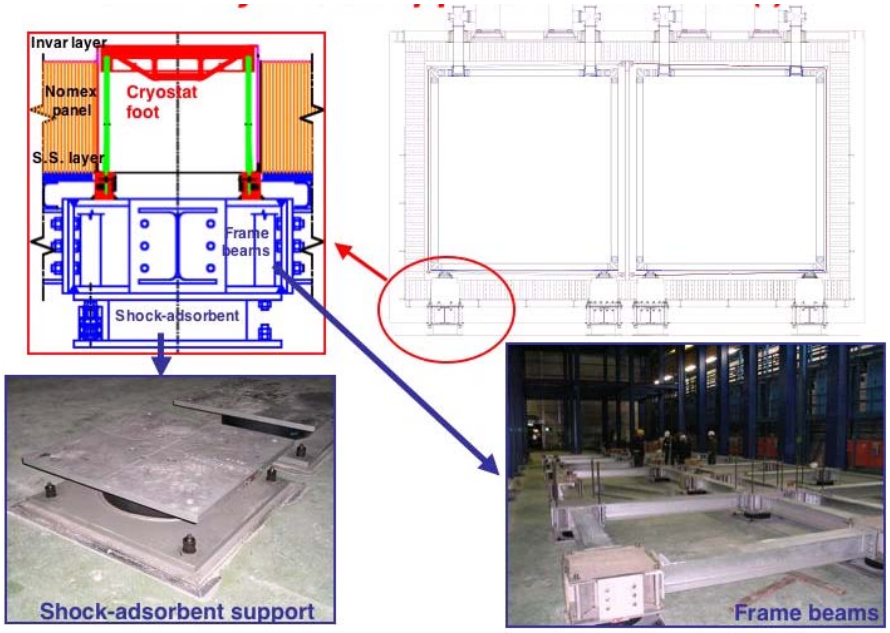

Figure 2.13 Base isolation system

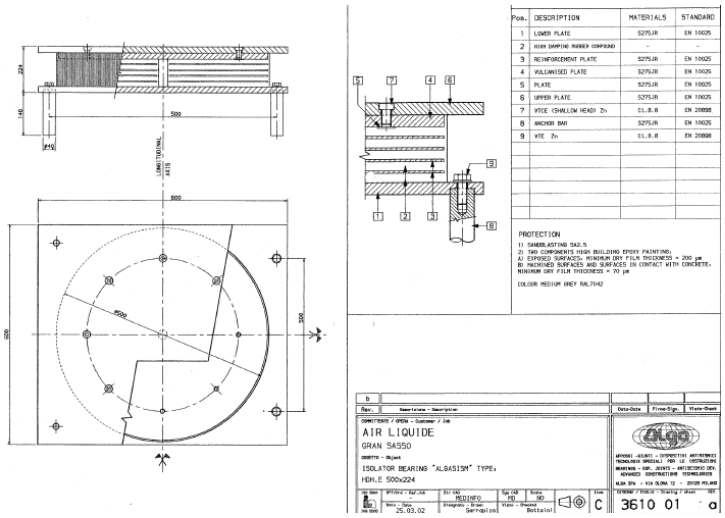

Figure 2.14 ALGA Laminated Rubber Bearing

2.3 Seismic analysis of Service`s structure and Cryostat

2.3.1 Description of the numerical model

A finite element model of the Steel Service structure around the detector (in blu in Figure 2.15) and the T600 Cryostat (in red in Figure 2.15) has been developed in SAP 2000 (Computer and Structures, 2005). The material selected for the frame is steel Fe 430 (CNR-UNI 10011). The properties of the material are reported in the following table:

Table 2-4 Properties of the material used in the numerical model

Elastic modulus , E	200000MPa
Poissson coefficient ν	0.3
Yielding Tension, R_s (CNR-UNI 10011, plate t≤ 16 mm)	275 MPa
Admissible Tension σ_{adm} (CNR-UNI 10011)	190 MPa
Mass Densisty	7800 Kg/m^3

The main structure, the Cryostat is base isolated. Inside the structure there are two semi-modules filled with liquid Argon, with a unit weight of 420 ton. Around the two semi-modules there is a cold vessel structure, made of aluminium, that is realized by assembling, in a suitable way, several sandwich panels connected together by means of aluminium profiles obtained by estrusion. The sandwich solution for the dewar panels has been chosen in order to achieve two of the most important requirements:

1. maximum lightness
2. high stiffness

The choice of using aluminium for building the inner vessel arises from the need to endow the cold part of the T600 module with high thermal conductivity so as to ensure an uniform thermalization of the whole structure in direct contact with liquid Argon. Inside the aluminium honeycomb panels there is the liquid Nitrogen cooling circuit with the function to keep the temperature of Argon constant and close to 89 K, with a difference equal to 1/10 or 2/10 degrees at most, since this represents the liquid Argon working temperature.

These protective panels have also a bunding function in the case during a seismic event one of the two modules breaks with spill out of liquid Argon.

Furthermore, Hall B is dotated of a ventilation system that can be activated in the extreme event that also the aluminium honeycomb panels break.

Every semimodule stands on 10 supports, and the entire Detector is located on 28 seismic base isolated rubber bearings.

The skeleton of the main structure (Cryostat) is constituted of H-shape beams (HEA 280, HEB 100, 300x300x12, HEB 240, HEB 200 equivalents) and has been designed to work to -188°C with an insulation system of foils in Perifer 36 (inner) and AISI 304 (external) that enclose a honeycomb of Nomex.

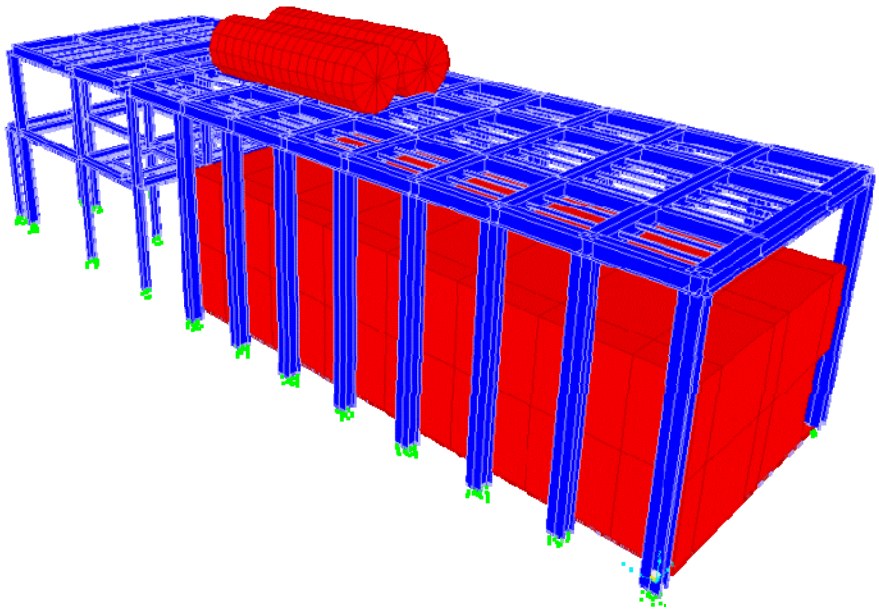

Figure 2.15 Finite element model in SAP 2000

These members have not been modeled, however their masses have been distributed as lumped masses around the cryostat represented in red in Figure 2.15. The entire detector has been modeled as a rigid body with distributed masses around the walls, the roof and the base.

The total mass of Argon is 735 ton. This mass has been distributed in lumped masses in the center of the rigid block element in 28 nodes along the longitudinal (7 nodes) and transversal (4 nodes) direction. So the translational mass on each node is M_N=26214.28kg, as shown in Figure 2.16.

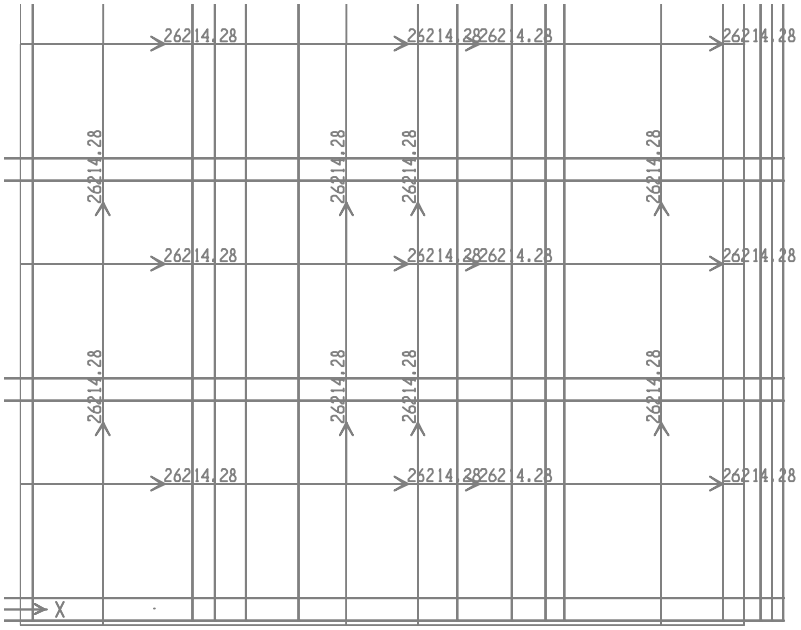

Figure 2.16 Nodal mass equivalent to the liquid argon

The mass of the walls of the insulation system is 9733kg for the longitudinal walls and it is distributed in 9 nodes with a lumped mass of 1081.4 kg.
The total mass of each transversal wall is 4297 kg distributed in 6 nodes with lumped mass of 716.6 kg. The mass on the roof of the main structure is 15983 kg, simulating 72 electric closet and 4 purification systems distributed in 54 nodal lumped masses of 295.98 kg. The mass of the base plus the slab is 43997.9kg and it is distributed in 54 nodal lumped masses of 814.77 kg.

So finally the total mass distribution of the T600 module is shown in Figure 2.17.

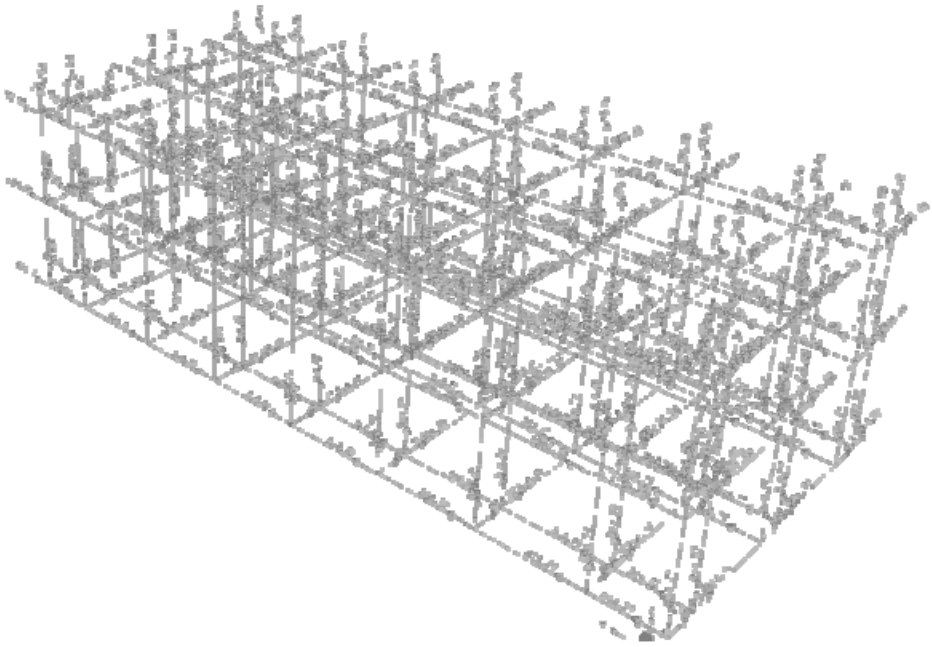

Figure 2.17 Total mass distribution of the module T600

For the mass distribution of the service structure has been used the same distribution provided by AIR LIQUIDE as shown in Figure 2.18.

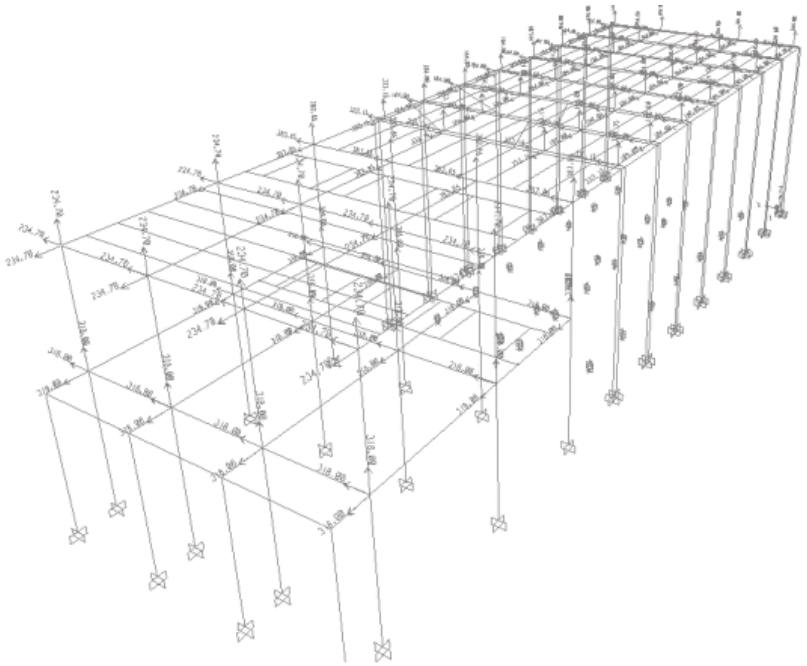

Figure 2.18 Mass distribution of the service structure

For the two cylindrical tanks on top of the steel frame, the external radius is 1325mm and the longitudinal length is 8500mm. The shell thickness of the tank due to the insulation system is 400mm, so the final internal radius is 925mm. The density of Argon is $\delta = 1.395 kg/lt$ while the density of Nitrogen (LN2) is $\delta = 0.808 kg/lt$. The total mass of liquid Argon (LAr) and Nitrogen (LN2) are respectively 31.85 ton and 18.45 ton. The mass has been distribute along the longitudinal axis of the cylindrical tank in 4 nodes of respectively 8 ton and 4.6 ton. The total mass of each tank empty is assumed 10 ton, so each nodal mas has an additional 2.5 ton of mass.

The first natural period of the Cryostat is 2.83 sec (Figure 2.19), while the first mode of the steel service structure is 2.37 sec in the longitudinal direction when one tank is filled with liquid Argon (LAr), while the other tank is filled

with liquid Nitrogen (LN2). Details about the other modes are reported in the following figures:

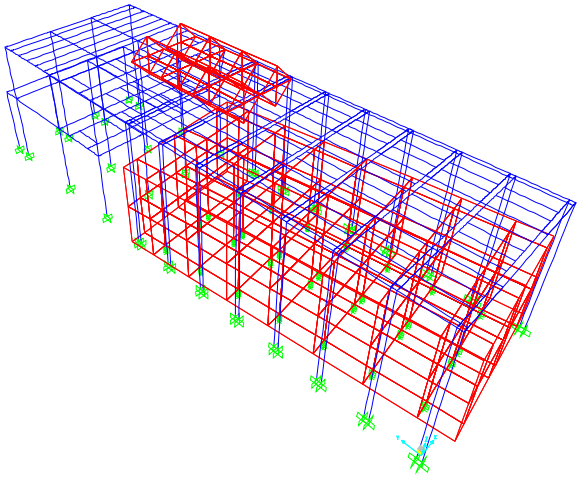

Figure 2.19 First torsional mode of the Cryostat T=2.83 sec – Modal Partecipating mass ratios = 0%

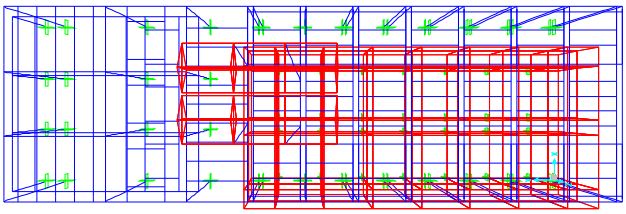

Figure 2.20 Second transversal translational mode of the Cryostat T=2.5253 sec – Mass participating mass ratio =89.4% in X direction

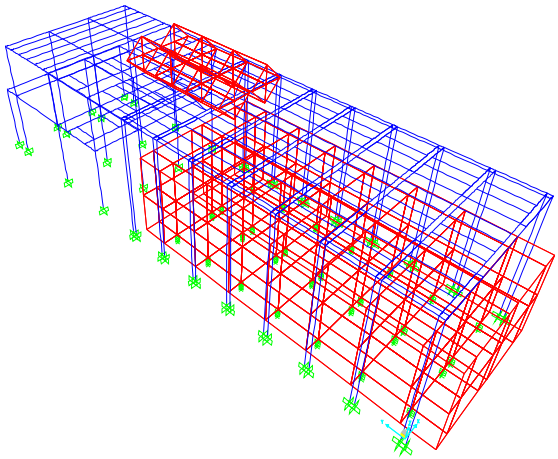

Figure 2.21 Third longitudinal translational mode of the Cryostat T=2.5234 sec – Mass participating mass ratio =94.6% in Y direction

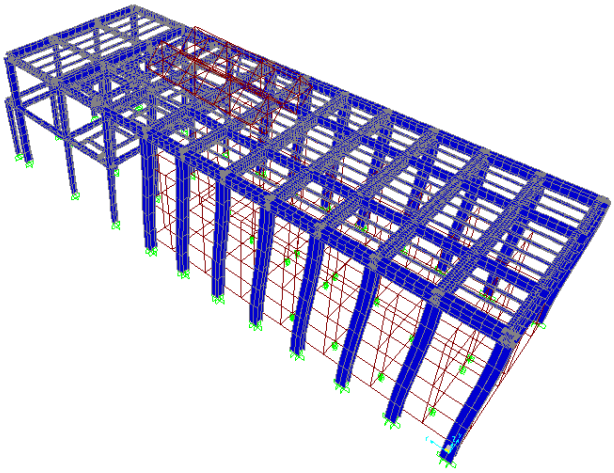

Figure 2.22 First longitudinal mode of the Structural Steel frame T=2.37 sec – Mass participating mass ratio =3.5% in Y direction

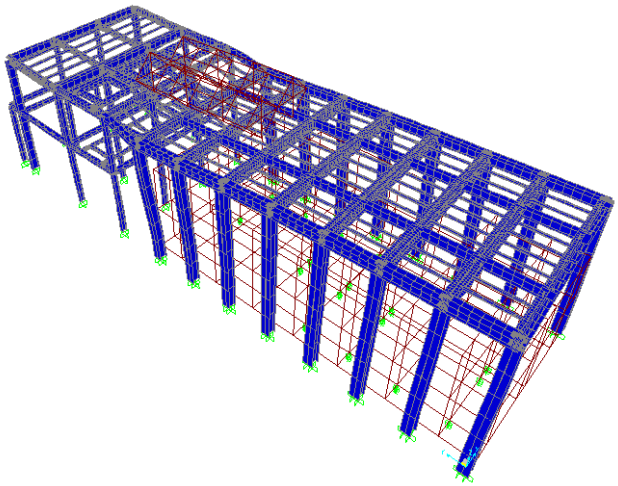

Figure 2.23 Torsional mode shape of the Structural Steel frame T=0.97 sec - Mass participating mass ratio =8.7 % in X direction

The damping ratio to be used in the seismic analysis of entire system is assumed 5% on all modes.

2.4 Displacements response of seismic analysis

The model has been subjected to a synthetic simulated earthquake generated according to the procedure described in section 5.1.2, while resultant accelrogrmas are shown in section 5.5 and are generated sing the program SIMQKE (Gasparini, 1976). An earthquake with a duration of 20 sec and a sampling frequency of 100 Hz is adopted, while the model records the response for a total length of 50 sec, because in some cases the maximum response appears at the end of the earthquake history.

2.4.1 Full tanks with liquid Nitrogen and liquid Argon

This section describes the time history response during a transitent condition when one tank is full with liquid Argon (LAr), while the other one is full with liquid Nitrogen (LN2).

Figure 2.24 shows the displacement time history in the X direction of the base isolated Cryostat with an earthquake oriented in the X direction too. Analogous plot, but in the Y direction is shown in Figure 2.27. For the horizontal cylindrical tanks analogous plots are obtained showing the displacement time history in the X, Y and Z direction in Figure 2.26 and Figure 2.29 respectively for earthquake in the X and Y direction.

The maximum displacements in the X and Y direction for all cases are shown in Table 2-5.

Table 2-5 Maximum displacement response with an earthquake with return period of 10000 yrs

Earthquake Direction	Cryostat	Hor. Cyl. Tank - X dir	Hor. Cyl. Tank - Y dir	Hor. Cyl. Tank - Z dir
	(mm)	(mm)	(mm)	(mm)
X	219.4	268.2	19.2	4.7
Y	263.9	15.7	120.6	60.2

The relative displacement time history between the Cryostat and the upper Cylindrical tanks for earthquake respectively in the X and Y direction are shown in Figure 2.25 and Figure 2.28, and the maximum displacement in the X direction is 398.5 mm and in the Y direction is 296.1mm.

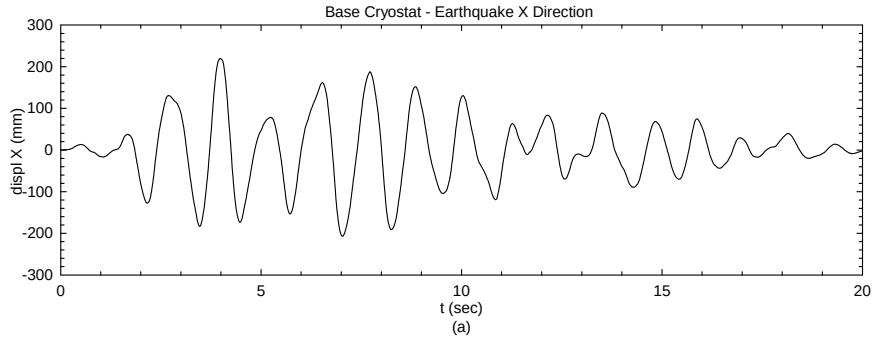

Figure 2.24 Displacement history of the Cryostat in the X direction with an Earthquake in the X direction with return period of 10000 yrs.

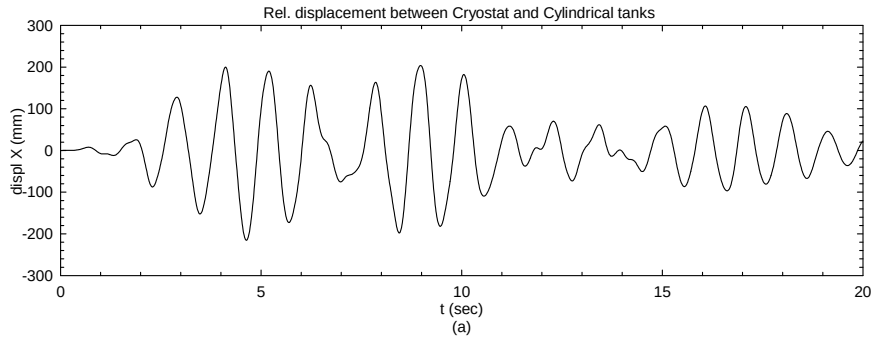

Figure 2.25 Relative displacement history between the Cryostat and the Cylindrical tanks in the X direction with an Earthquake in the X direction with return period of 10000 yrs.

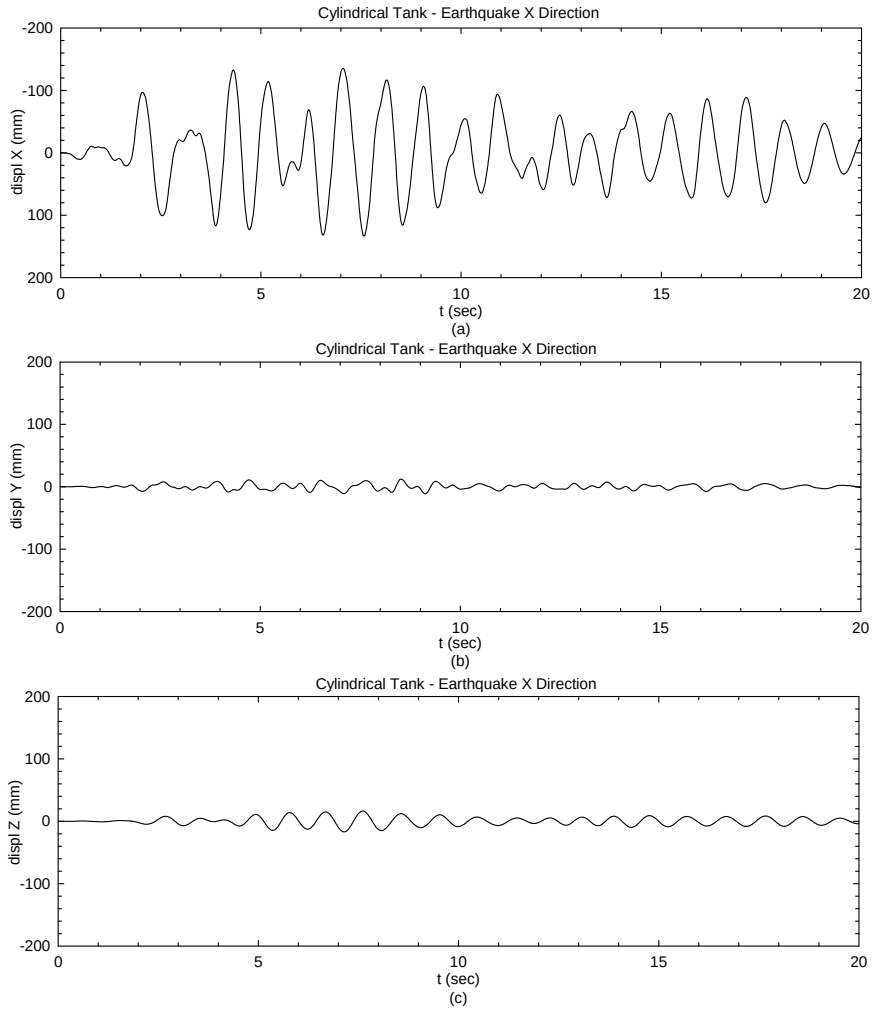

Figure 2.26 Displacement history of the Cylindrical tank in the X, Y and Z direction with an Earthquake in the X direction with return period of 10000 yrs.

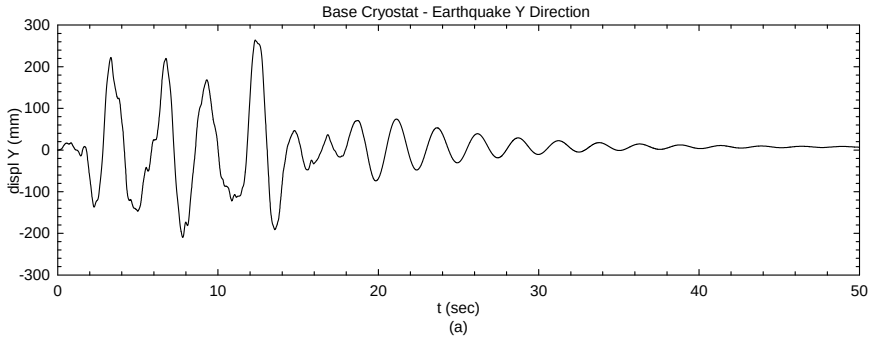

Figure 2.27 Displacement history of the Cryostat in the Y direction with an Earthquake in the Y direction with return period of 10000 yrs.

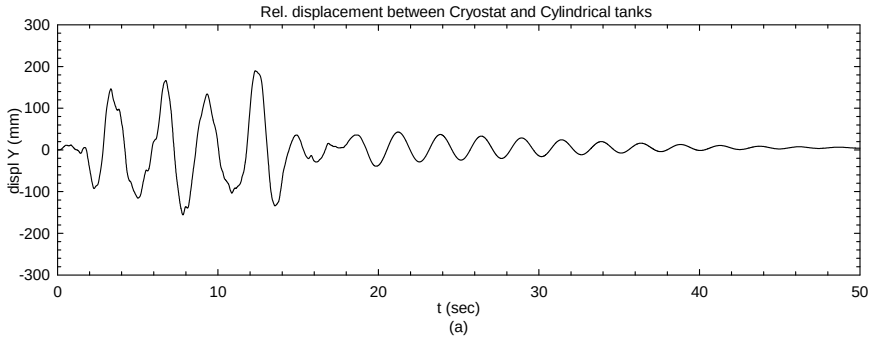

Figure 2.28 Relative displacement history between the Cryostat and the Cylindrical tanks in the X direction with an Earthquake in the Y direction with return period of 10000 yrs.

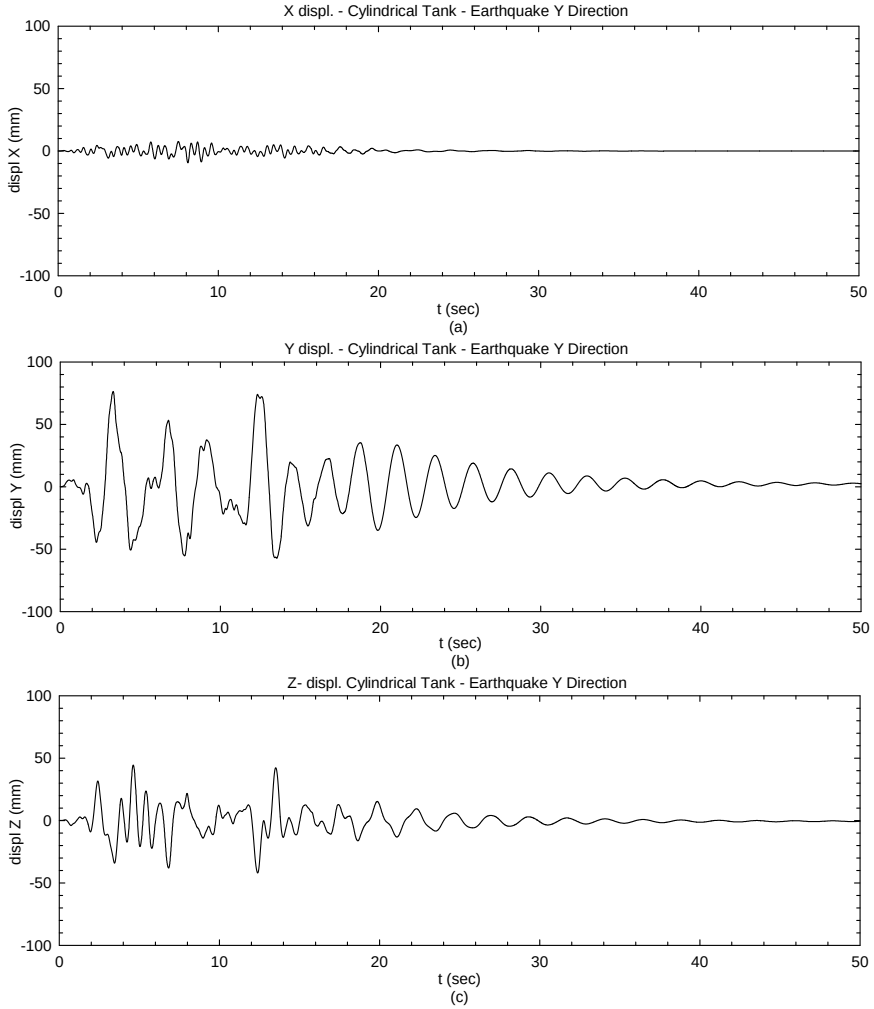

Figure 2.29 Displacement history of the Cylindrical tank in the X, Y and Z direction with an Earthquake in the Y direction with return period of 10000 yrs.

As observed in Figure 2.29 when the structure is excited with an earthquake in the Y direction the cylindrical tank has displacements mainly in the same

direction Y combined with uplift displacements in the Z direction, while displacments in the perpendicular direction is almost zero (Figure 2.29a).

2.4.1.1 Acceleration response of seismic analysis

The seismic acceleration in the upper part of the steel service structure is lower than at the ground as verified by using a specific dynamic evaluation. The peak ground acceleration is 0.67g, while peak acceleration measured at the top of the service structure is 0.48g. The seismic reduction factor is 0.71, so peak ground acceleration at the top of the service structure reduces of about 29 %.

Figure 2.30a-b shows the comparison between the time histories of the ground acceleration and the acceleration at the top of the service structure when the earthquake shakes in the X direction.

On the contrary when the earthquake shakes in the Y direction there is an amplification of the ground acceleration, that is 0.40g at the top of the service structure. Therefore the acceleration increases of 40% (Figure 2.30c).

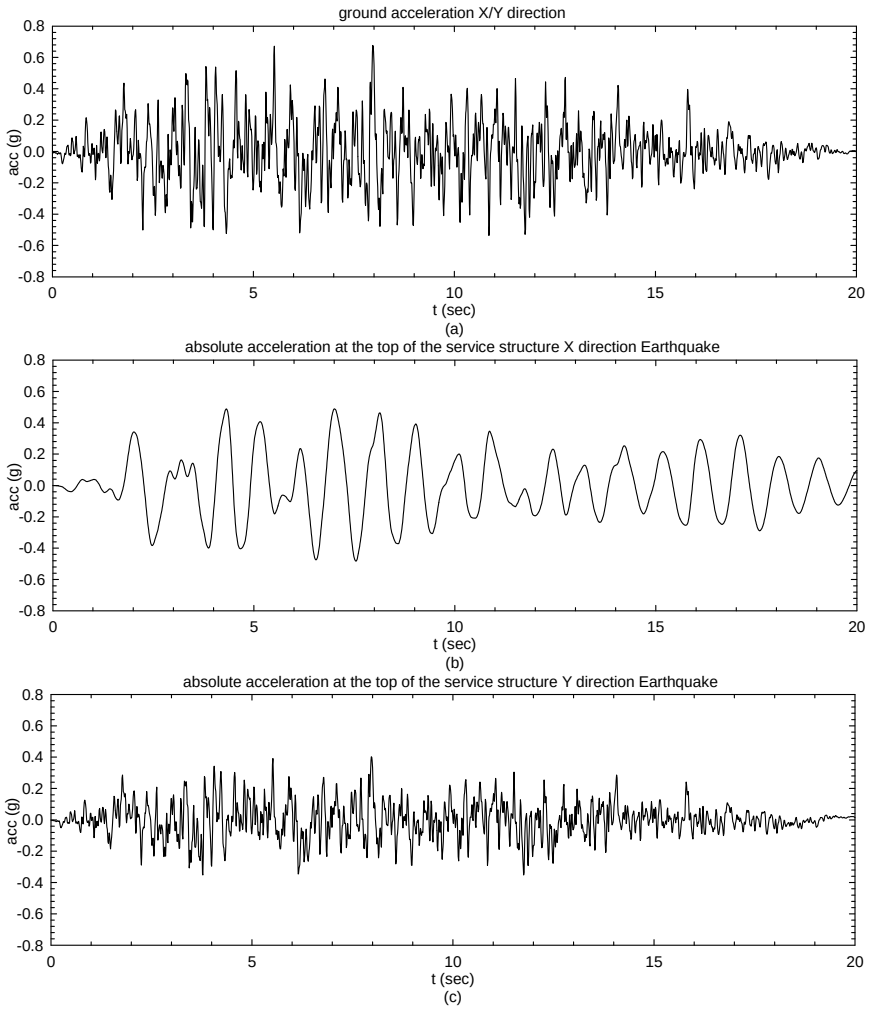

Figure 2.30 Time history comparison between accelerations at the ground and at the top of the service structure

2.4.2 Both tanks filled with liquid Nitrogen at 100% and 80%

This section describes the time history response during a normal operating condition when both tanks are filled with liquid Nitrogen respectively at 100% and 80% of their volume. The maximum displacements in the X and Y direction for all cases are shown in Table 2-6.

Table 2-6 Maximum displacement response with an earthquake with return period of 10000 yrs

Earthquake Direction	Cryostat	Hor. Cyl. Tank - X dir	Hor. Cyl. Tank - Y dir	Hor. Cyl. Tank - Z dir
	(mm)	(mm)	(mm)	(mm)
X	219.4	143.6	16.0	3.3
Y	263.9	4.9	127.2	81.1

The relative displacement time history between the Cryostat and the upper Cylindrical tanks for earthquake respectively in the X and Y direction are shown in next figures like in the previous section, and the maximum displacement in the X direction is 245 mm and in the Y direction is 291mm. The following figures are analogous to the ones shown in section 2.4.1.

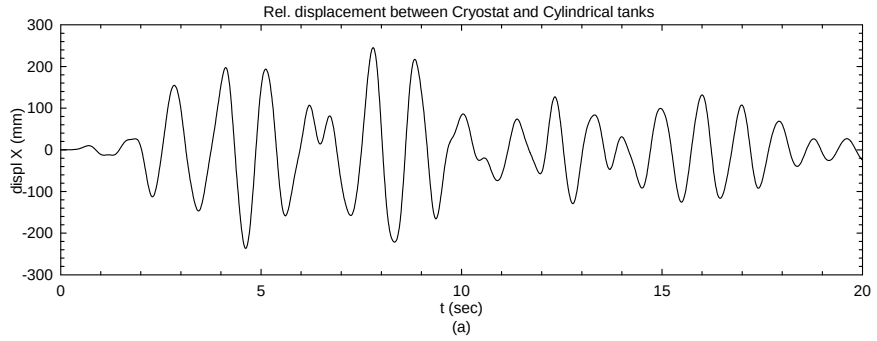

Figure 2.31 Relative displacement history between the Cryostat and the Cylindrical tanks in the X direction with an Earthquake in the X direction with return period of 10000 yrs.

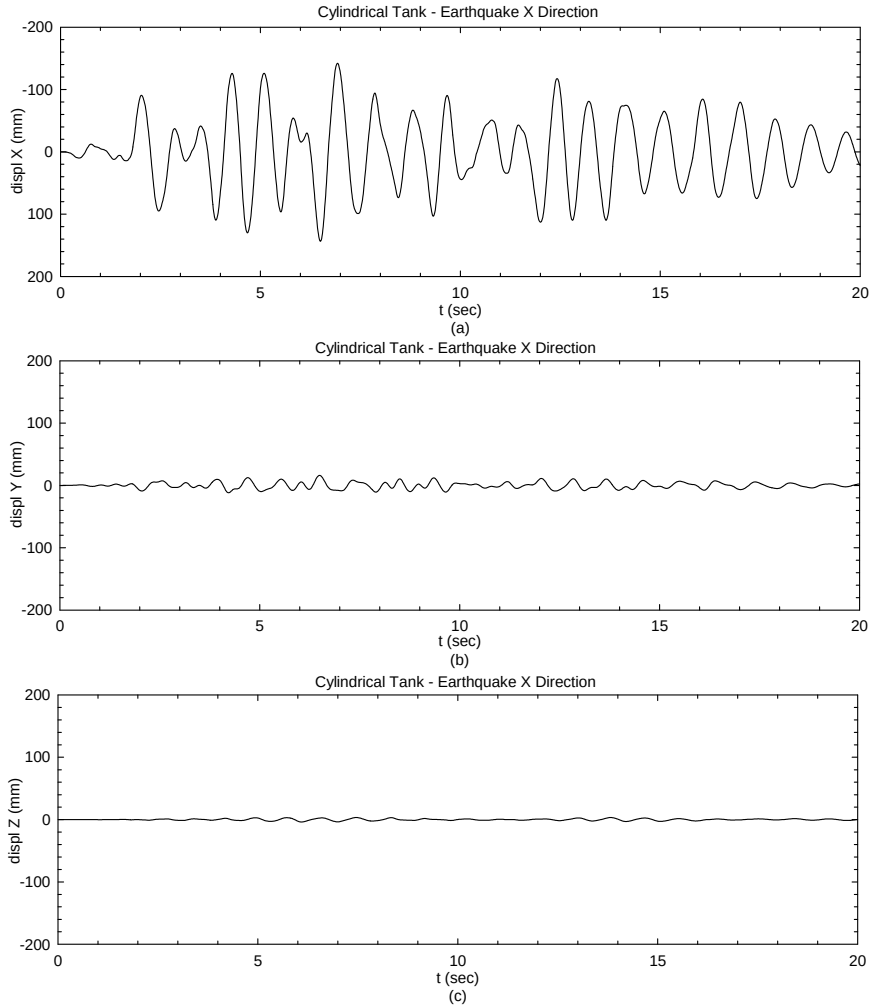

Figure 2.32 Displacement history of the Cylindrical tank in the X, Y and Z direction with an Earthquake in the X direction with return period of 10000 yrs.

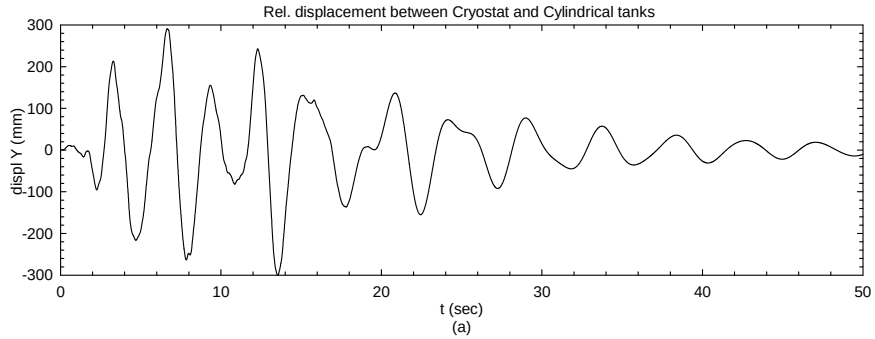

Figure 2.33 Relative displacement history between the Cryostat and the Cylindrical tanks in the X direction with an Earthquake in the Y direction with return period of 10000 yrs.

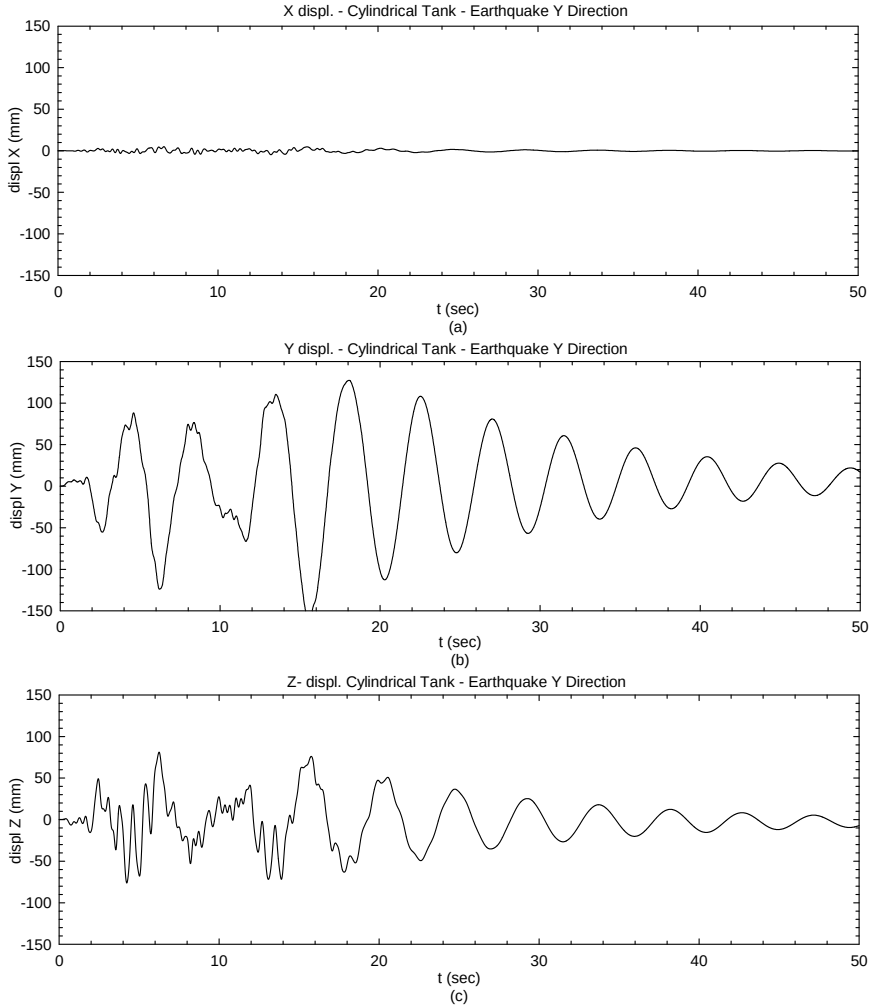

Figure 2.34 Displacement history of the Cylindrical tank in the X, Y and Z direction with an Earthquake in the Y direction with return period of 10000 yrs.

Chapter 3

3 Nonlinear equations governing finite element model of sloshing in tanks

3.1 Abstract

This chapter presents the basic forms of the partial differential equations that LS-DYNA`s flow solver treats and provides a general description of the methodologies employed in their solution.

3.2 Introduction

LS-DYNA`s incompressible flow solver is based, in part, upon the work of Gresho et al. (1984) and makes uses of advanced solution algorithms for both implicit and explicit time integration. The explicit solution algorithm (Gresho *et al.*, 1984a-b) sacrifices some phase accuracy, but decouples the momentum equations and minimizes the memory requirements. While both the diffusive and Courant-Freidrichs-Levy (CFL) stability limits must be respected in the explicit algorithm, balancing tensor diffusivity meliorates the restrictive diffusive stability limit and raises the order of accuracy of the time integration

scheme. The explicit algorithm, in combination with single point integration and hourglass stabilization, has proven to be both simple and efficient in a computational sense.

3.3 Governing equations

The *conservation equation of linear momentum* in vectorial form is:

$$\rho\left\{\frac{\partial \mathbf{u}}{\partial t}+\mathbf{u}\nabla\mathbf{u}\right\}=\nabla\sigma+\rho\mathbf{f} \tag{3.1}$$

Where **u**=(*u,v,w*) is the velocity vector, σ is the stress tensor, ρ the mass density, and f the body force. The body force contribution ρf typically accounts for buoyancy forces with f representing the acceleration due to gravity. The stress may be written in terms of the fluid pressure and the deviatoric stress tensor as:

$$\sigma=-p\mathbf{I}+\tau \tag{3.2}$$

Where p is the pressure, I is the identity tensor, and τ is the deviatoric stress tensor. A constitutive equation relates the deviatoric stress and the strain rate, e.g.,

$$\tau=2\mu\mathbf{S} \tag{3.3}$$

Where the dynamic viscosiy μ is a second rank tensor that is provided isotropically.

The strain-rate tensor is written in terms of the velocity gradients as:

$$\mathbf{S}=\frac{1}{2}\left\{\nabla\mathbf{u}+\left(\nabla\mathbf{u}\right)^{T}\right\} \tag{3.4}$$

The *mass conservation principle* in divergence form is:

$$\frac{\partial \rho}{\partial t} + \left(\rho \nabla \mathbf{u}\right) = 0 \tag{3.5}$$

In the incompressible limit, the velocity field is solenoidal,

$$\nabla \mathbf{u} = 0 \tag{3.6}$$

which implies a mass density transport equation,

$$\frac{\partial \rho}{\partial t} + \mathbf{u} \nabla \rho = 0 \tag{3.7}$$

For constant density equation (3.7) is neglected with equation (3.6) remaining as a constraint in the velocity field.

The *conservation of enery* is expressed in terms of temperature T, as:

$$\rho C_p \left\{ \frac{\partial T}{\partial t} + \mathbf{u} \nabla T \right\} = -\nabla \mathbf{q} + Q \tag{3.8}$$

Where C_p is the specific heat at constant pressure, q is the diffusional heat flux rate, and Q represents volumetric heat sources and sinks, e.g. due to exothermic/endothermic chemical reactions.

Fourier`s law relates the heat flux rate to the temperature gradient and thermal conductivity,

$$\mathbf{q} = -\mathbf{k} \nabla T \tag{3.9}$$

Where **k** is the thermal conductivity tensor. In many cases, the fluid properties are only available as scalar quantities, i.e. the thermal to be isotropic.

3.3.1 Boundary and initial conditions

The prescription of boundary conditions is based on a flow domain with boundaries that are either physical or implied for the purpose of performing a simulation.

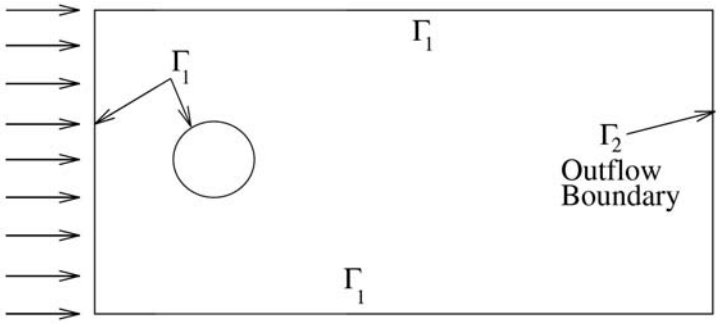

Figure 3.1 Flow domain for conservation equations

A simple flow domain is shown in where the boundary of the domain is $\Gamma = \Gamma_1 \cup \Gamma_2$. The moment equation (3.1) are subjected to boundary conditions that consist of specific velocity on Γ_1 as in equation , or traction boundary coditions on Γ_2 as in equation

$$\mathbf{u}(\mathbf{x},t) = \left|\hat{\mathbf{u}}(\mathbf{x},t)\right| \; on \; \Gamma_1 \tag{3.10}$$

In the case of a no-slip and no-penetration boundary, **u**=0 is the prescribed velocity boundary condition. The prescribed traction boundary conditions are:

$$\sigma \cdot \mathbf{n} = \hat{\mathbf{f}}(\mathbf{x},t) \; on \; \Gamma_2 \tag{3.11}$$

Where n is the outward normal for the domain boundary, and $\hat{\mathbf{f}}$ are the components of the prescribed traction.

3.4 Explicit time integration

This section presents the spatial discretization and explicit time-integration method for the incompressible Navier-Stokes equations. The spatially discrete form of equation (3.1) and equation (3.6) are:

$$M \cdot \dot{\mathbf{u}} + A(\mathbf{u})\mathbf{u} + K\mathbf{u} + Cp = \mathbf{F} \tag{3.12}$$

$$C^T \mathbf{u} = g \tag{3.13}$$

Where M is the mass matrix, A(**u**) and K are the advection and te viscous diffusion operators respectively, **F** is the body force, and g accounts for the presence of prescribed velocity boundary conditions. C is the gradient operator, and C^T is the divergence operator. Here, u and p are understood to be discrete approximations to the continous velocity and pressure fields. Equations (3.12) and (3.13) constitute a differential-algebraic system of equations that precludes the direct application of time-marching algorithms to the presence of the discrete incompressibility constraint.

Following Gresho *et al*. (1984), a consistent, discrete pressure Poisson equation (PPE) is constructued using a row-sum lumped mass matrix, M_L

$$\left[C^T M_L^{-1} C\right] p = C^T M_L^{-1} \left[\mathbf{F} - K\mathbf{u} - A(\mathbf{u})\mathbf{u}\right] - \dot{g} \tag{3.14}$$

Here, $\dot{g}$ accounts for time-dependent velocity boundary conditions. The PPE constitutes an algebraic system of equations that is solved for the element-centered pressure during the time-marching procedure. Figure 3.2 shows the dual, staggered grid associated with the pressure varibles.

Equations (3.12) and (3.13) form the basis for a description of the explicit time integration algorithm. It is assumed that the explicit algorithm begins with a given divergence-free velocity field, u^0, that satisfies the essential velocity boundary conditions, and an initial pressure , p^0. To simplify the description of the explicit algorithm, velocity boundary coditions that are constant in time are assumed making $\dot{g} = 0$. Therefore, the explicit algorithm proceed as follows:

1. *Calculate the partial acceleration, i.e., acceleration neglecting the pressure gradient, at time level n.*

$$\tilde{\mathbf{a}}^n = M_L^{-1}\tilde{\mathbf{F}}^n \qquad (3.15)$$

where

$$\tilde{\mathbf{F}}^n = \mathbf{F}^n - K\mathbf{u}^n - A(\mathbf{u})\mathbf{u}^n \qquad (3.16)$$

2. *Solve the global PPE for the current pressure field.*

$$\left[C^T M_L^{-1} C\right] p^n = C^T \tilde{\mathbf{a}}^n \qquad (3.17)$$

3. *Update the nodal velocities.*

$$\mathbf{u}^{n+1} = \mathbf{u}^n + \Delta t\left[\tilde{\mathbf{a}}^n + M_L^{-1} C p^n\right] \qquad (3.18)$$

4. *repeat steps 1-3 until a maximum siulation time limit or a maximum number of time stes is reached.*

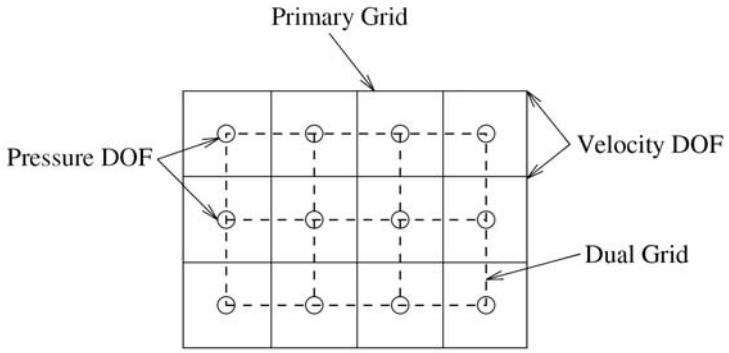

Figure 3.2 Velocity mesh with two degree of freedom per node, and the PPE dual grid with one DOF per element

3.5 Contact algorithm

The "*CONSTRAINED_LAGRANGE_IN_SOLID*" command in LS-DYNA provides the mechanism for coupling interaction between a (slave) Lagrangian geometric entity (e.g. Lagrangian mesh of shell in the case study) to a (master) Eulerian geometric entity (i..e. an ALE or Eulerian mesh). Since the slave entity is rigid, a *penalty coupling method* without erosion (CTYPE=4) between shell and solid elements is used.

The *penalty method* consists of placing normal interface springs between all penetrating nodes and the contact surface. The penalty method respect to the other two methods available in LS-DYNA called *kinematics constraint method* and *distributed parameter method* is found to excite little if any mesh hourglassing. This lack of noise is attributable to the impact and release conditions. Furthermore, no special treatment of intersecting interfaces is required, greatly simplifying the implementation.

Currently three implementations of the penalty algorithm are available:

1. Standard Penalty Formulation
2. Soft Constraint Penalty Formulation, Which has been implemented to treat contact between bodies with dissimilar material properties. Stiffness calculation and its update during the simulation differs from the Standard Penalty Formulation.
3. Segment-based Penalty Formulation. It is a powerful contact algorithm whose logic is a slave segment-master segment approach instead of a traditional slave node-master segment approach.

In the standard penalty formulation, the interface stiffness is chosen to be approximately the same order of magnitude as the stiffness of the interface element normal to the interface. Consequently the computed time step size is unaffected by the existence of the interfaces. However, if interface pressures become large, unacceptable penetration may occur. By scaling up the stiffness and scaling down the time step size, we may still solve such problems using the penalty approach.

In the penalty approach method, each slave node is checked for penetration through the master surface. If the slave node does not penetrate, nothing is done. If it does penetrate, an interface force is applied between the slave node and its contact point. The magnitude of this force is proportional to the amount of penetration. This may be though of as the addition of an interface spring.

Penetration of the slave node n_s (Figure 3.3) through the master segment which contains its contact point is indicated if

$$l = n_i \times \left[t - r\left(\xi_c, \eta_c\right) \right] < 0 \tag{3.19}$$

where

$$n_i = n_i\left(\xi_c, \eta_c\right) \tag{3.20}$$

is normal to the master segment at the contact point. If the slave node n_s has penetrated through the master segment s_i, we add an interface force vector f_s:

$$f_s = -lk_i n_i \quad \text{if } l < 0 \tag{3.21}$$

To the degree of freedom corresponding to n_s and

$$f_m^i = \phi_i\left(\xi_c, \eta_c\right) f_s \quad \text{if } l < 0 \tag{3.22}$$

to the four nodes (i=1,2,3,4) that comprise master segment s_i. the stiffness factor k_i for master segment s_i is given in terms of the bulk modulus K_i, the volume V_i, and the face area A_i of the element that contains s_i as:

$$k_i = \frac{f_{si} K_i A_i^2}{V_i} \tag{3.23}$$

For the brick element and

$$k_i = \frac{f_{si} K_i A_i^2}{\max\left(shell\ diagonal\right)} \tag{3.24}$$

For shell elements where f_{si} is a scale factor for the interface stiffness and is normally defaulted to 0.10. Larger values may cause instabilities unless the time step size is scaled back in the time step calculation.

The number of coupling points assigned to the surface of each Lagrangian shell is 16 in the case study considered and the coupling direction is normal in compression only. A search algorithm finds or each slave node its nearest point on the master surface.

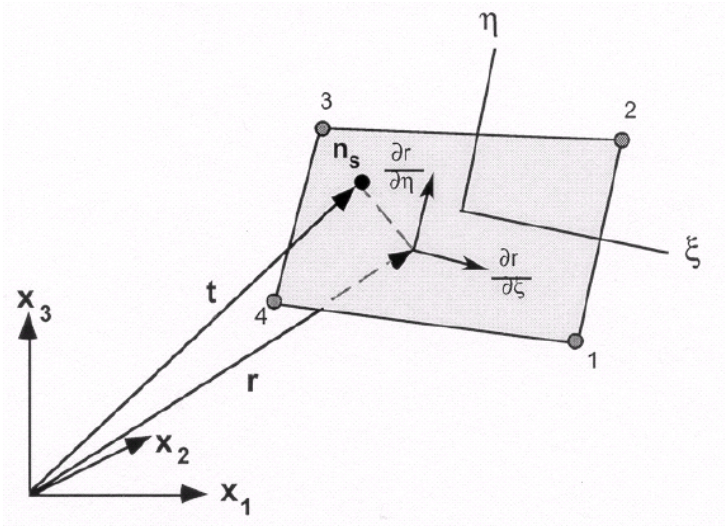

Figure 3.3 Location of a contact point when ns lies above master segment

3.6 Summary and Conclusions

This chapter describes the basic governing equations of LS-DYNA flow solver and provides a desription of the explicit time integration method that is used to solve the equations. A description of the contact algorithm that is based on the penalty method is also provided.

Chapter 4

4 Development of finite element model in LS-DYNA and ANSYS

4.1 Abstract

The main objective of this chapter is to develop a three dimensional computer model capable of performing simulation of the complex dynamic behavior of a liquid tank subjected to a strong seismic base excitation. The model takes in consideration both large amplitude liquid sloshing and non-linear liquid structure interaction using the finite element method.

The program also has the following features:

The program uses an updated Eulerian-Lagrangian description of the liquid-solid interface in order to enforce compatibility between solid and liquid elements. The resulting nonlinear Euler-Lagrange equations are solved using an efficient time integration technique that has been specially developed to solve the liquid-structure interaction problems.

4.2 Introduction

In recent years numerical simulations have gathered on their importance and the recent trends are shifting from solving the individual problems to solving multi-physical problems by taking into account all the interacting systems. Detailed modelling of coupled problems is of crucial importance to assure the reliability of dynamic simulations. This part describes methods for simulating fluid-structure interaction with the LS-DYNA software system. Different formulations (Lagrange, Euler, ALE and SPH) for fluid simulation in LS-DYNA are presented and applied to a real fluid sloshing problem.

4.3 Different formulation of system physical state description

Lagrangian formulation is usually used for describing a solid mechanics problem. The problem is described with a high number of mass particles, where the motion of every single particle is being observed in space and time (Figure 4.1). The problem is exactly defined when the motion of all the particles is known. The lagrangian formulation is very simple and easy to use for one or only a few mass particles. However, the method becomes very complicated and complex for description of high number of mass particles. In the Eulerian formulation the problem is being observed at one point in space which does not follow the motion of the single particle. In one time step Δt several mass particles may pass the observed point. Their motion is exactly determined in the moment of passing through that point. In the observed point the field variables are time dependent.

The basic difference between the Lagrangian and Eulerian formulation is that at the Lagrangian formulation the magnitudes, x, y and z are variables coordinates of a moving particle. At the Eulerian formulation those coordinates represent steady coordinates of the defined field point.

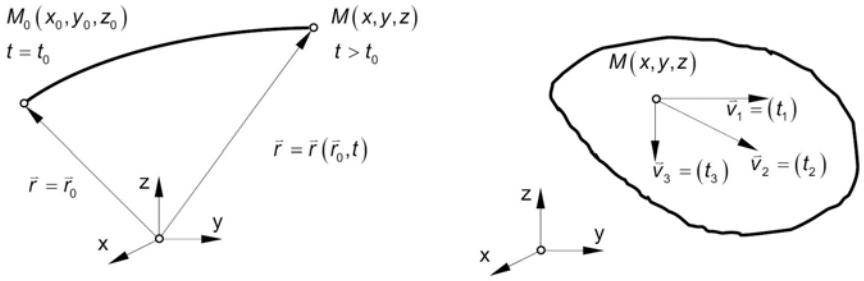

Figure 4.1 Lagrangian and Eulerian Formulation

4.4 Computational fluid-dynamics methods in LS-DYNA

LS-DYNA is based on the finite element method and it was originally designed for solving structural dynamic problems. Its ability to model structural responses in general is well defined. However, the modelling of coupled problem of fluid-structure interaction is still quite challenging.

4.4.1 Lagrangian Formulation

In the Lagrangian formulation one finite element represents the same part of the material throughout the course of the analysis. The fluid domain can be described with a material model which skips the calculation of deviatoric stresses. By defining a low bulk modulus for fluid such as water, the elastic shear forces become negligible, and by using a low yield stress, fast transition to plasticity can be achieved (e.g. by only considering the gravitation). Under high dynamic loading, the shear forces and any unreal introduced forces become negligible in comparison to the inertial forces of the fluid. Figure 4.2 illustrates the solution process of a simple fluid problem using the Lagrangian formulation. It is presumed that the loading influences only the central node. The result of the loading is the shift of that node in a computational time step. If the influence of the loading does not stop or change, the node takes a new

position in the next time step and the mesh deforms even more, since the mesh follows the material flow.

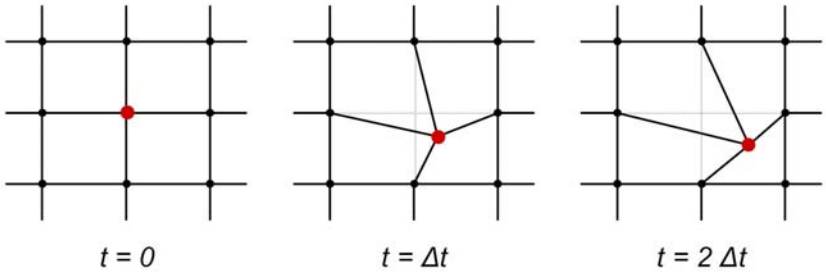

Figure 4.2 Solving a problem according to the Lagrangian formulation

4.4.2 Eulerian Formulation

In LS-DYNA it is also possible to apply the Eulerian formulation for the fluid flow analyses, where the fluid flow through the fixed mesh in a space is observed. The material point moves from one finite element to another and the finite element mesh does not move or deform. Although the Eulerian mesh in LS-DYNA appears not to move or deform during the analysis, it does actually change its position and form only within the single time step. The reason for this is the use of Lagrangian formulation in single time steps, which is much more advanced in LS-DYNA. The Eulerian mesh in LS-DYNA is treated in a special way (Figure 4.3). To illustrate the use of the Eulerian mesh the same example is used as in the previous chapter. Because of the central node loading, the observed node changes its position during one computational time step (mesh deforms). After the time step the analysis stops and the following two approximations are performed:

Mesh smoothing: all the nodes of the Eulerian mesh, that have been displaced due to loading, are moved to their original position;

Advection: the internal variables (stresses, flow field, velocity field) for all the nodes that have been moved are computed (interpolated) so that they have

the same spatial distribution as before the mesh smoothing. In this way the mesh smoothing does not affect the internal variable distribution.

The described procedure is being repeated for each time step of the analysis and provides the analyst with a non-movable and undeformable Eulerian mesh.

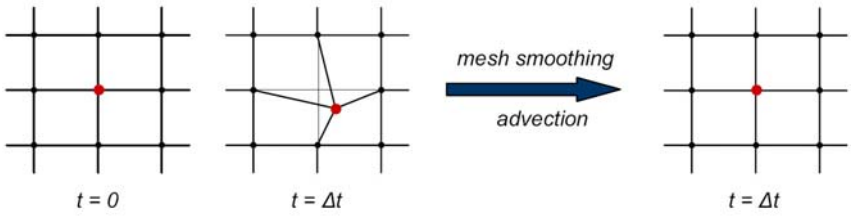

Figure 4.3 solving a problem according to the Eulerian formulation

4.4.3 Arbitrary lagrangian Eulerian formulation (ALE)

The Arbitrary Lagrangian Eulerian (ALE) method has been developed based on the idea of separating material and mesh displacements to eliminate mesh distortion in the lagrangian method. The ALE method uses an operator split technique during which the analysis is performed in two steps: a Lagrangian step followed by an Eulerian step. In the lagrangian step the governing equations are solved to fulfill equilibrium and obtain material displacements. In the Eulerian step, a new mesh is generated for the deformed domain to obtain the mesh displacements.

In this formulation the mesh partly moves and deforms because it follows the material (Lagrangian formulation), while at the same time the material can also through the mesh (Eulerian formulation). The ALE solving procedure is similar to Eulerian procedure. The only different is the mesh smoothing. In the Eulerian formulation the nodes are moved back to their original positions, while in the ALE formulation the positions of the moved nodes are calculated according to the average distance to the neighboring nodes.

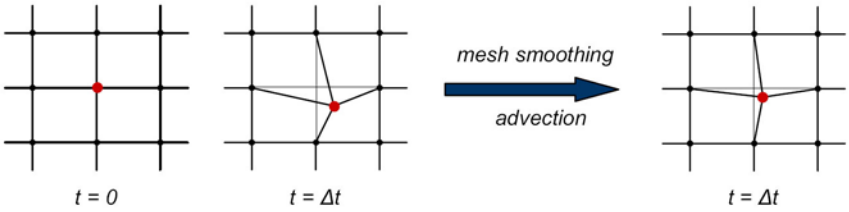

Figure 4.4 solving a problem according to the Arbitrary Lagrange Eulerian formulation

In LS-DYNA there are two types of ALE elements: single material and multimaterial. Single material element type can contain only one phase (fluid) at one moment, while the multi material element type is able to contain several materials. The advantage of the ALE formulation is evident when a stress front needs to be followed and the mesh is automatically refined. Another example is the analysis of sloshing in tanks filled with fluid, because in this case the boundary surface is continuously changing due to interaction between fluid and tank surface.

4.4.4 Smoothed particle hydrodynamics (SPH)

The SPH method is an integration scheme which was developed by Lucy, Gingold and Monaghan (1977). It is based on the lagrangian formulation with the purpose to avoid the mesh restrictions when large deformations appear within the finite element method. The main difference between the standard methods and the SPH is the absence of the mesh, since the SPH formulation is essentially a mesh less method.

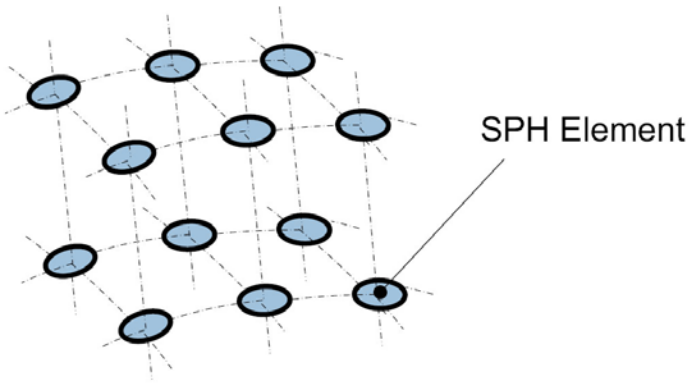

Figure 4.5 SPH method

4.5 Tank characteristics and problem set up

A nonlinear dynamic analysis was performed for the transversal section of the semi-module T300. The tank is 3.9×3.6×19.6 meters as shown in Figure 4.6. The maximum fluid height is 3.80 meters, so the provided freeboard is 0.1 meters. The base of the tank is assumed to be fixed.

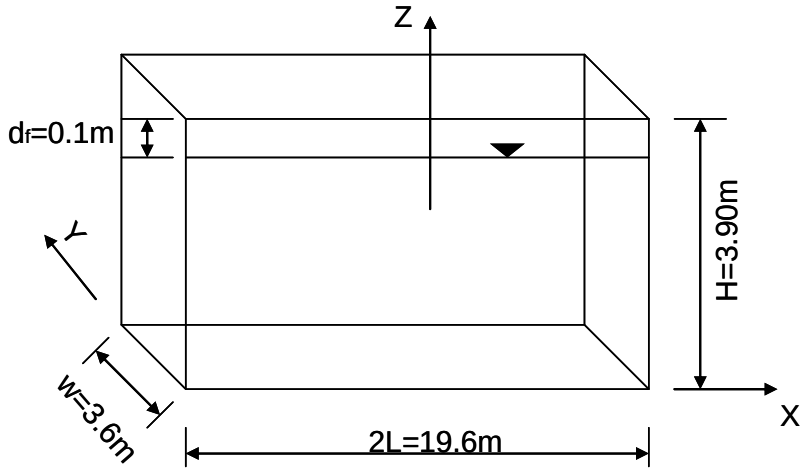

Figure 4.6 Dimensions of the tank: Semi-module T300

The model is subjected to a synthetic earthquake record in the North-South direction (Y-direction) scaled to a peak ground acceleration of 0.63g, with a duration of 20 seconds. Since the tank is base isolated the SAP model described in chapter 2 is used to evaluate the time history analysis at the base of the tank that is shown in Figure 4.8.

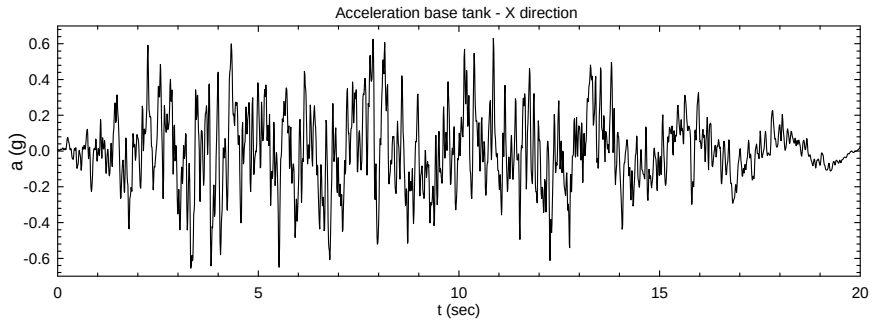

Figure 4.7 Acceleration time history at the base of the tank in the X direction

The response spectrum of this ground motion is shown in Figure 4.8 for 0.5 % critical damping that is typically used for liquid sloshing.

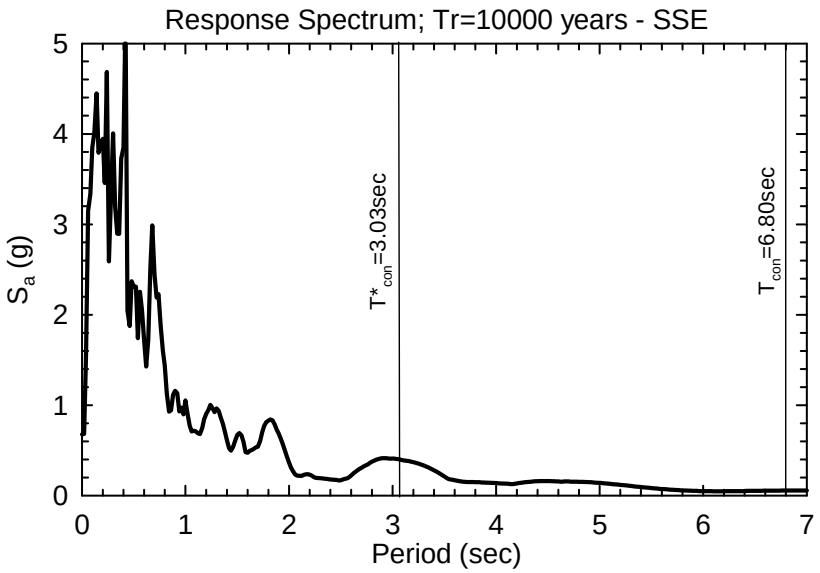

Figure 4.8 Response spectrum for a return period of 10000 yrs with 0.5% damping

The period of oscillation of the first sloshing mode for rectanglar tank is given by the following approximated formula (Eurocode 8, part 4):

$$T_1 = 2\pi \left(\frac{L/g}{\frac{\pi}{2}\tanh\left(\frac{\pi}{2}\frac{H}{L}\right)} \right)^{1/2} \tag{4.1}$$

where the meaning of the terms are shown in Figure 4.8, while g is the gravitational acceleration. Using equation (4.1) the sloshing period of the tank without a roof is $T_{con}=6.80sec$. Comparison with a similar formula taken from Indian code gives a sloshing period of 6.77sec, in agreement with the result of Eurocode. Given that the freeboard is less than the maximum wave height for the given spectral acceleration at the sloshing period, an updated convective mass, which is reduced with respect to the initial one due to the confinement's effect according to equation (7.16), can be used to determine the new sloshing period due to the presence of the roof ($T^{*}_{con}=3.03sec$).

4.6 Finite elements models

A three-dimensional finite element model of the above tank has been developed with the general purpose computer codes ANSYS (2004) and LS-DYNA (LSTC, 2003).

For the ANSYS model (Figure 4.9a), the fluid domain is modeled with three dimensional, eight-noded, 24 DOF fluid elements (FLUID80). These elements have 3 DOF at each node (displacement in three directions) and are used to model contained fluids that have no net flow rate and do not exhibit very large nodal displacements. The fluid-structure interaction is accounted by coupling the common interfaces of the fluid and the tank walls only in the normal direction. This means that the water is free to move relative to the tanks' shell wall in the vertical and tangent directions. The fluid is also free to move relative to the roof in the horizontal direction. The contact between the bottom of the roof and the fluid is modeled using a non-linear contact-friction element that acts only in compression (ANSYS element Type CONTACT52).

On the contrary the tank in LS-DYNA is modeled using four-noded Belytschko-Tsay shell elements with three integration points through the thickness. The tank is made of steel and modelled with an elastic material model ($\rho=7500kg/m^3$, $E=2.1\cdot10^{10}kg/m^2$, $\nu=0.3$). The nodes at the bottom surface of the tank were constrained in all DOFs.

Argon in liquid and gas state are modeled with solid elements. The material model Null (Type 9) is used for liquid Argon (ρ=1395 kg/m^3 at 87 K) and gas Argon (ρ=1.395 kg/m^3 at 293 K). The linear polynomial (liquid and gas) and Ideal Gas (only for gas) equations of state have been used. The model is also loaded with the constant gravitational acceleration (g=9.81 m/sec^2). The contact between fluid and structure is defined with the "CONSTRAINED_LAGRANGE_IN_SOLID" command, using an Eulerian-Lagrangian penalty coupling algorithm. The Eulerian mesh of the fluid consists of 150880 solid elements with a unit length of 0.05 m and the Lagrangian mesh consists of 2340 shell elements with a unit length of 0.1 m. (Figure 4.9b). Explicit dynamic analysis was carried out by using LS-DYNA version 970.6763.169. The computational time frame was set to 20 sec and the time step of the simulation was defined according to the lowest resonant frequency of the structure ($2.51 \cdot 10^{-5}$ sec in this case).

During the dynamic analysis the authors found difficulties of convergence of the ANSYS model, so they decided to adopt LS-DYNA model. This latter computer code uses a different approach to solve fluid-structure interaction problems, which is described in the following section, and it has shown to be very economical and suitable for analysis of large and more complex models (Vesenjak *et al.*, 2004).

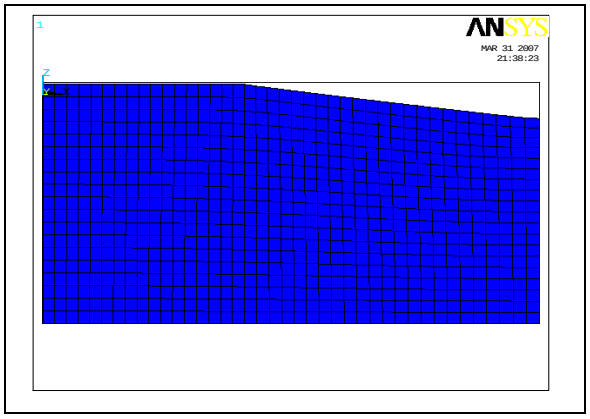

(a)

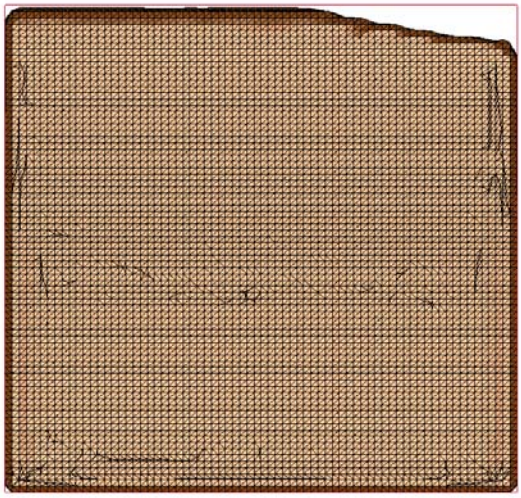

(b)

Figure 4.9 Finite element model of the LAr tank in ANSYS (a) and LS-DYNA (b)

4.7 Computational results of dynamic analysis

For the updated sloshing period shown in Figure 4.8 ($T^*_{con}=3.03sec$) a spectral acceleration of 0.40g is obtained and substituted in equations (7.12), (7.13) and (7.14) to obtain a maximum roof pressure of 64.56 kPa and a total roof force of 531.64 kN per meter width in the transverse direction.

In the LS-DYNA model, the pressure exerted on the roof of the tank was measured at the center of the shell elements using the "FSI_SENSOR" command. Sensors were located in the bottom of the tank, on the top and along all the lateral walls. During the entire time history 8 impacts of the sloshing wave against the roof were counted. They occur respectively at 2.5-2.8, 3.3-3.4, 4.7, 5.1-5.2, 6.0, 6.8-6.9, 7.1 and 7.5-7.6 seconds. These high peak force values

are generated by the sloshing waves that impact the corner between the roof and the lateral walls of the tank.

Figure 4.10 to Figure 4.24 show the contour pressure of the liquid Argon inside the tank, from a lateral and top view, during the major events when the sloshing waves impact the top of the roof.

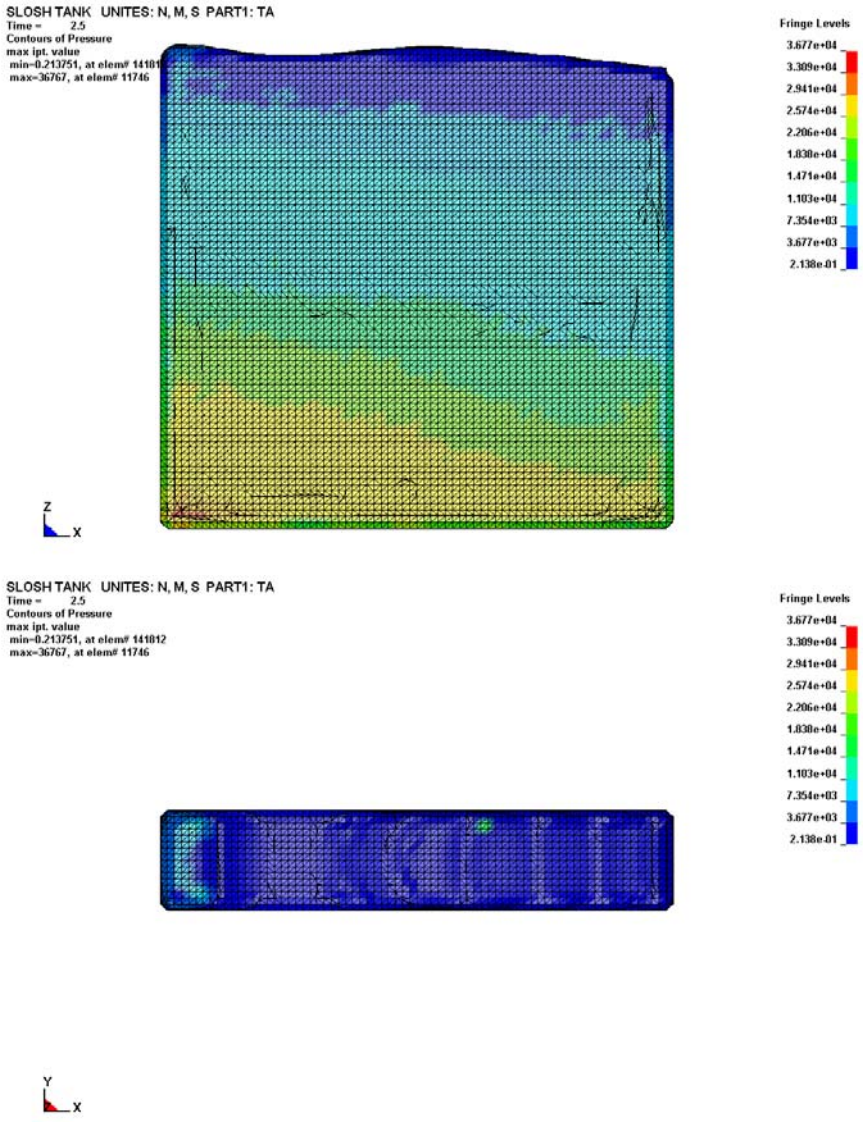

Figure 4.10 Contours of pressure distributions (Pa) at the 1st impact (t=2.5sec)

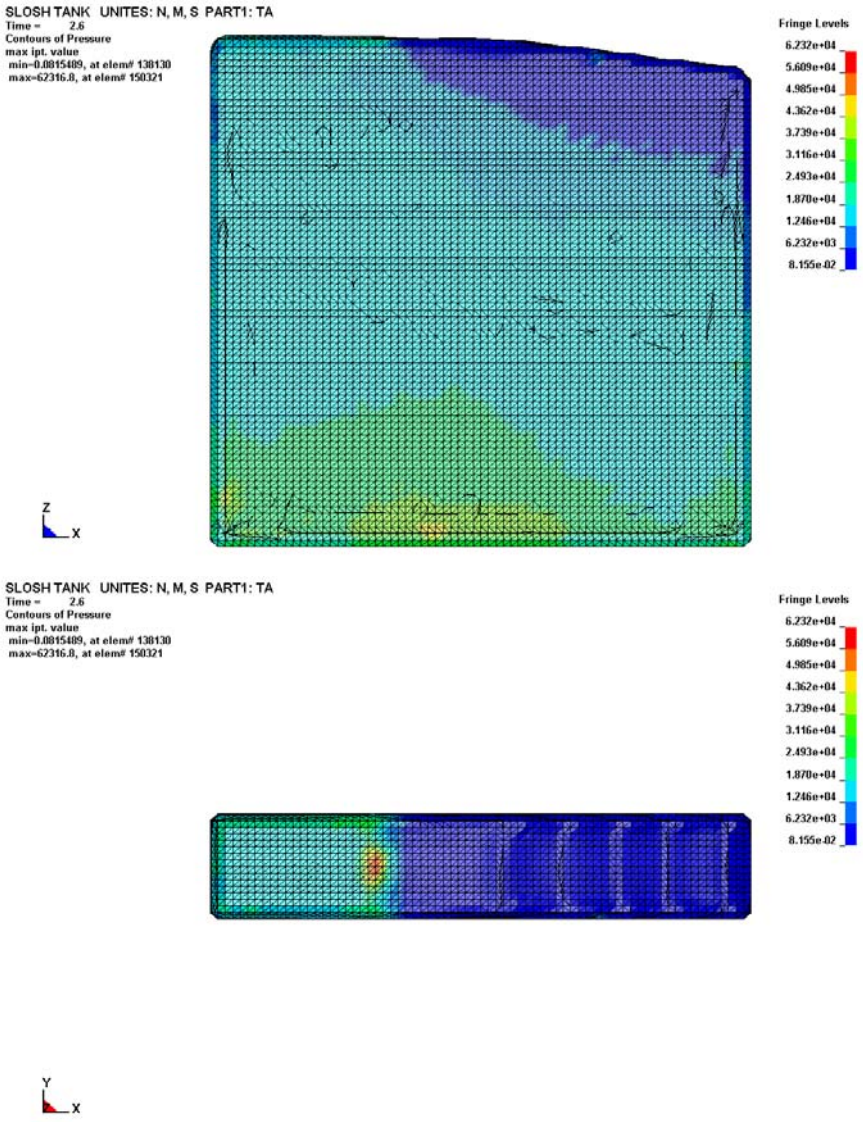

Figure 4.11 Contours of pressure distributions (Pa) at the 1st impact (t=2.6sec)

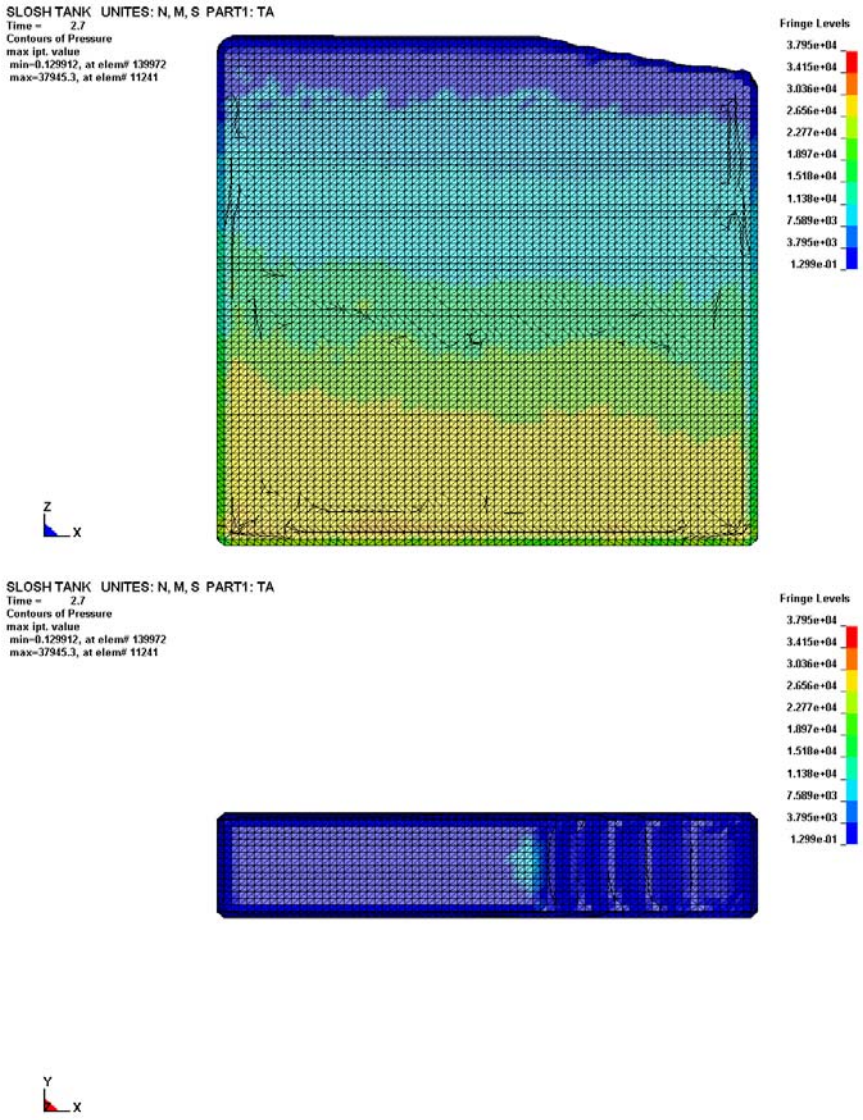

Figure 4.12 Contours of pressure distributions (Pa) at the 1st impact (t=2.7sec)

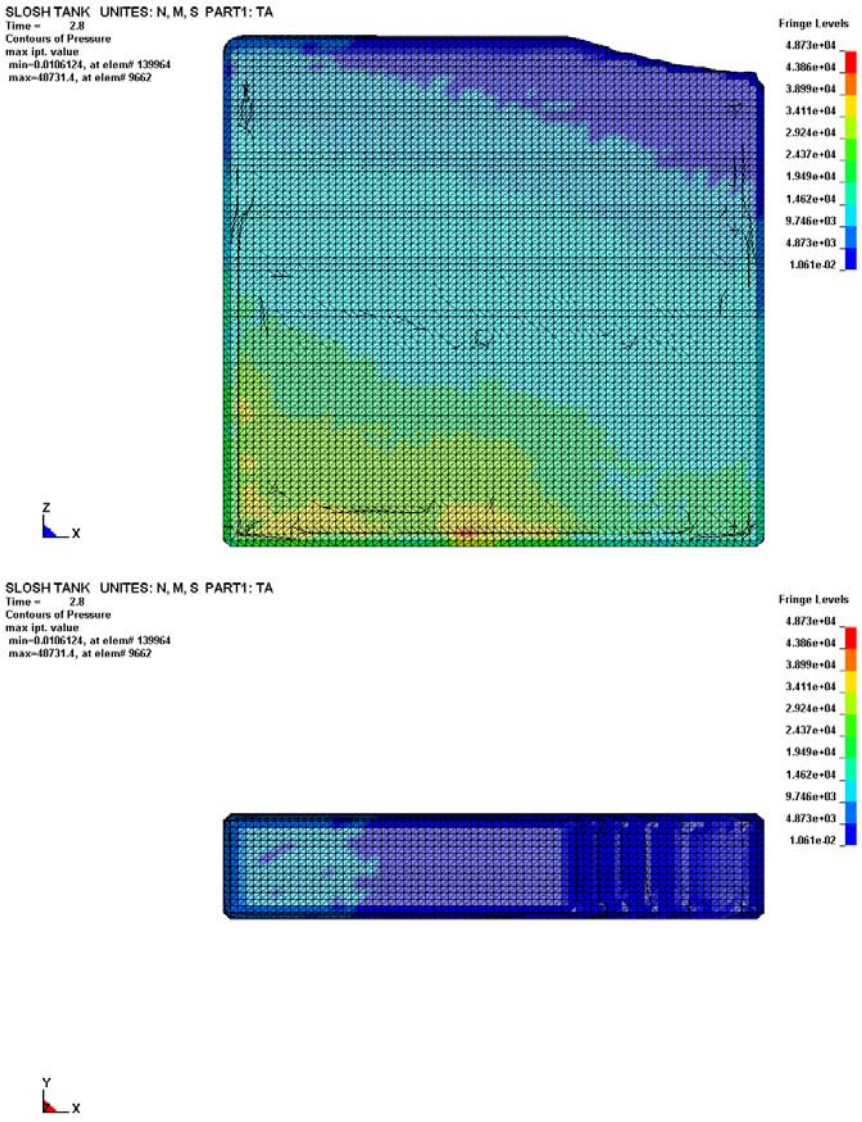

Figure 4.13 Contours of pressure distributions (Pa) at the 1st impact (t=2.8sec)

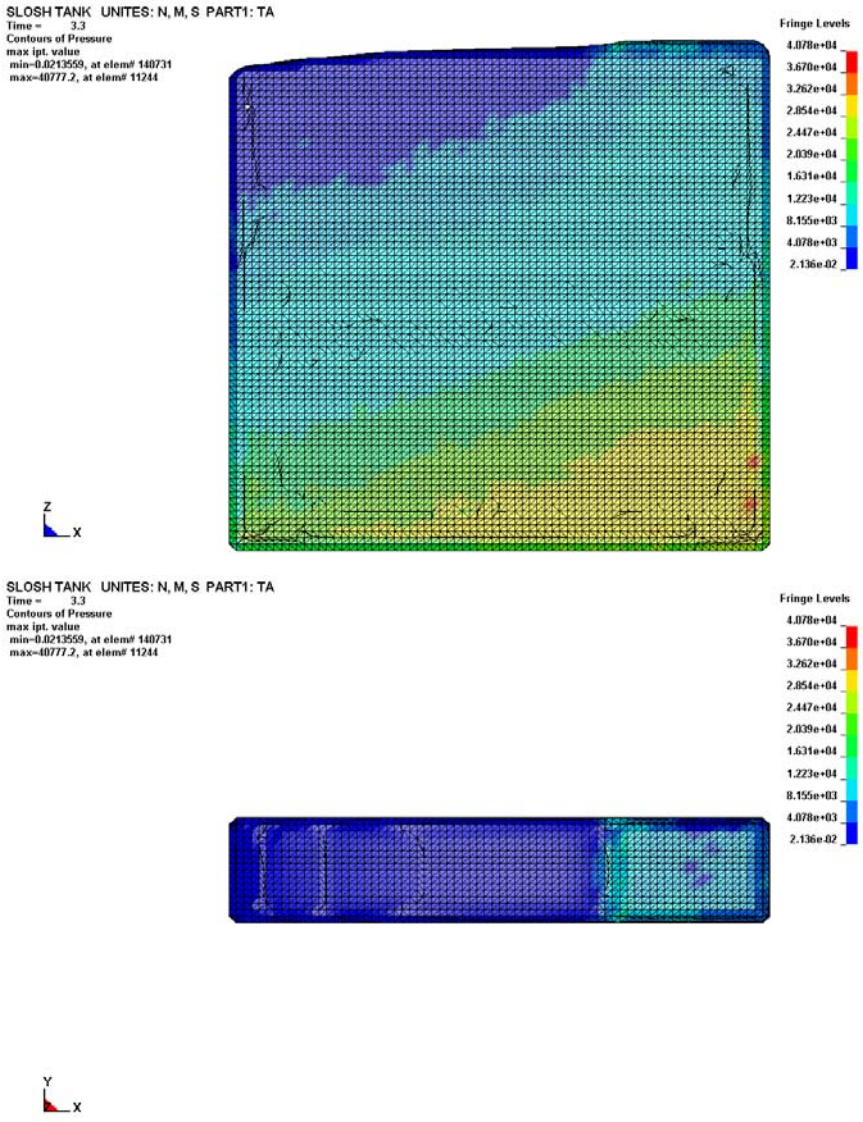

Figure 4.14 Contours of pressure distributions (Pa) at the 2 nd impact (t=3.3sec)

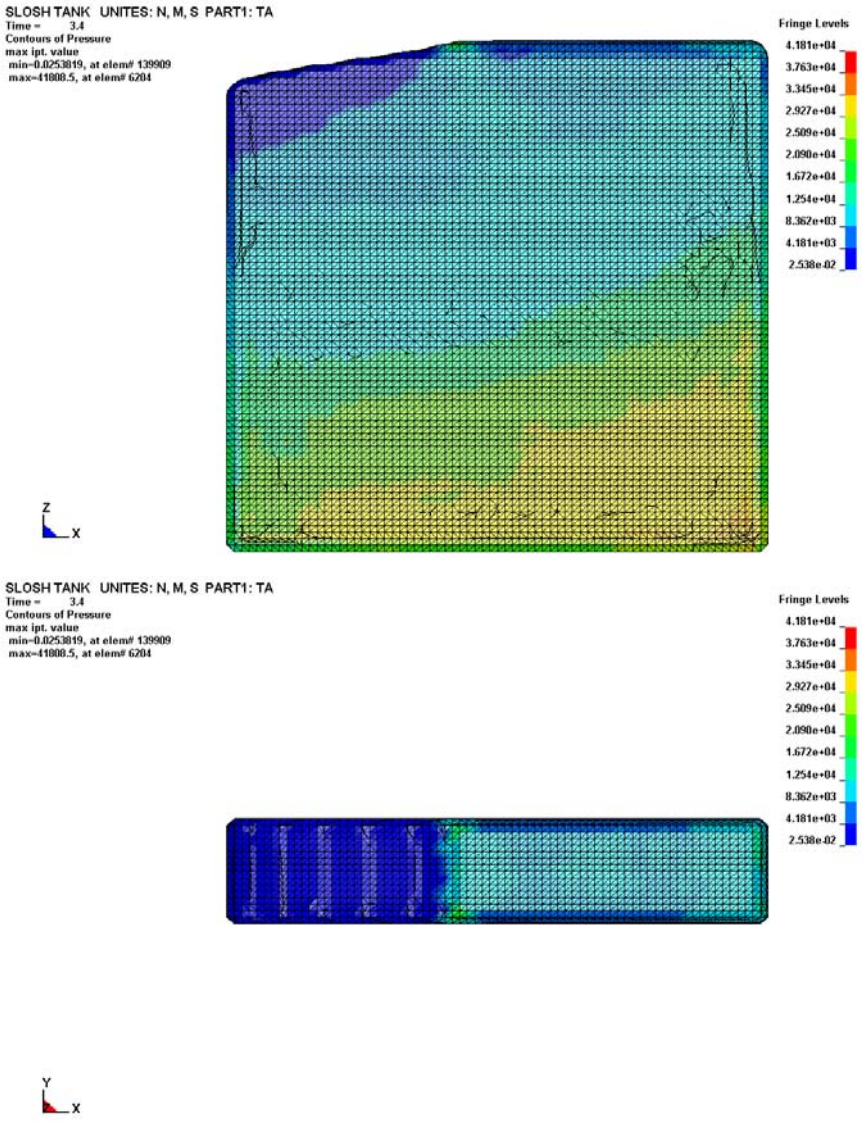

Figure 4.15 Contours of pressure distributions (Pa) at the 2 nd impact (t=3.4sec)

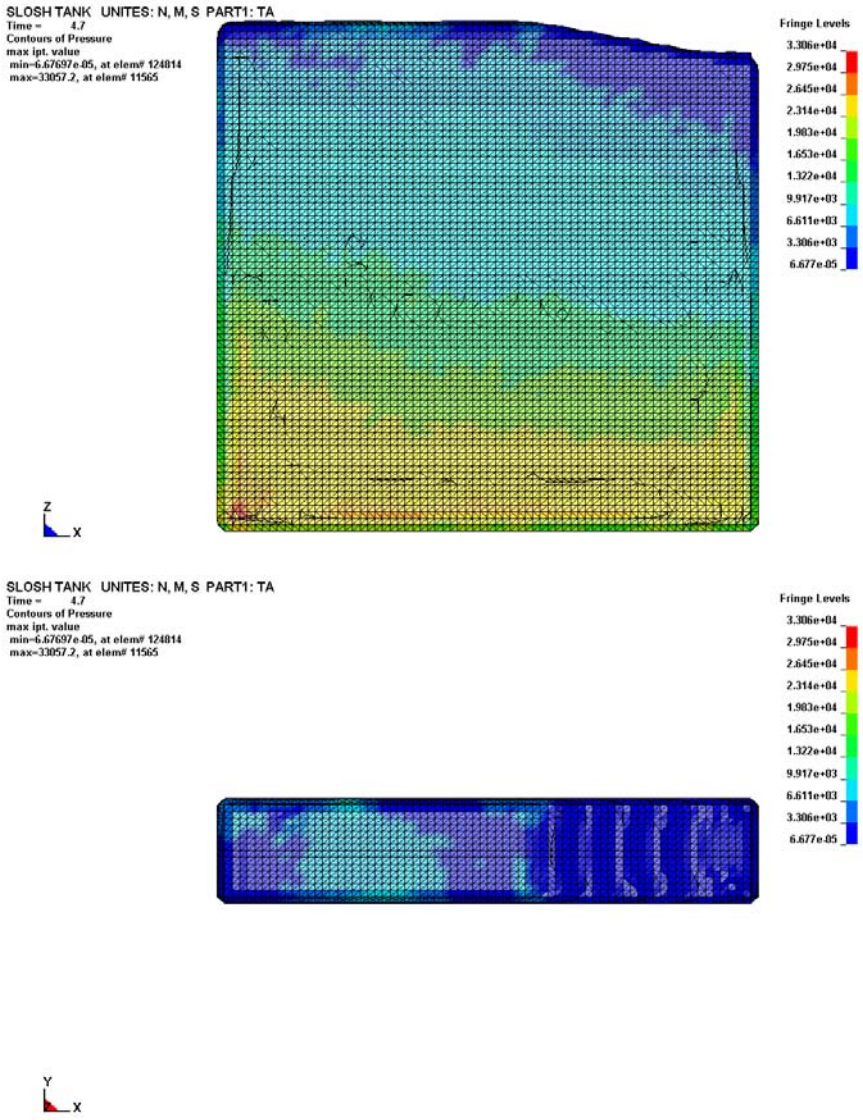

Figure 4.16 Contours of pressure distributions (Pa) at the 3rd impact (t=4.7sec)

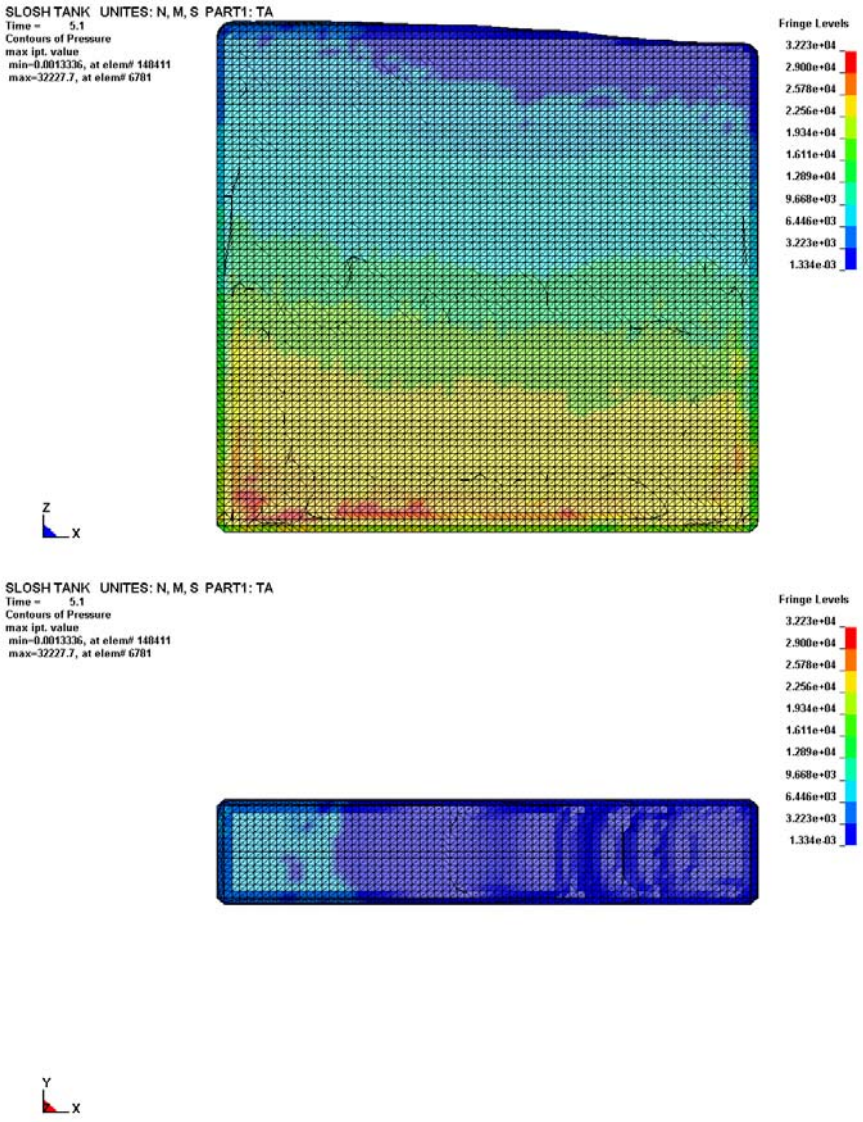

Figure 4.17 Contours of pressure distributions (Pa) at the 4 th impact (t=5.1sec)

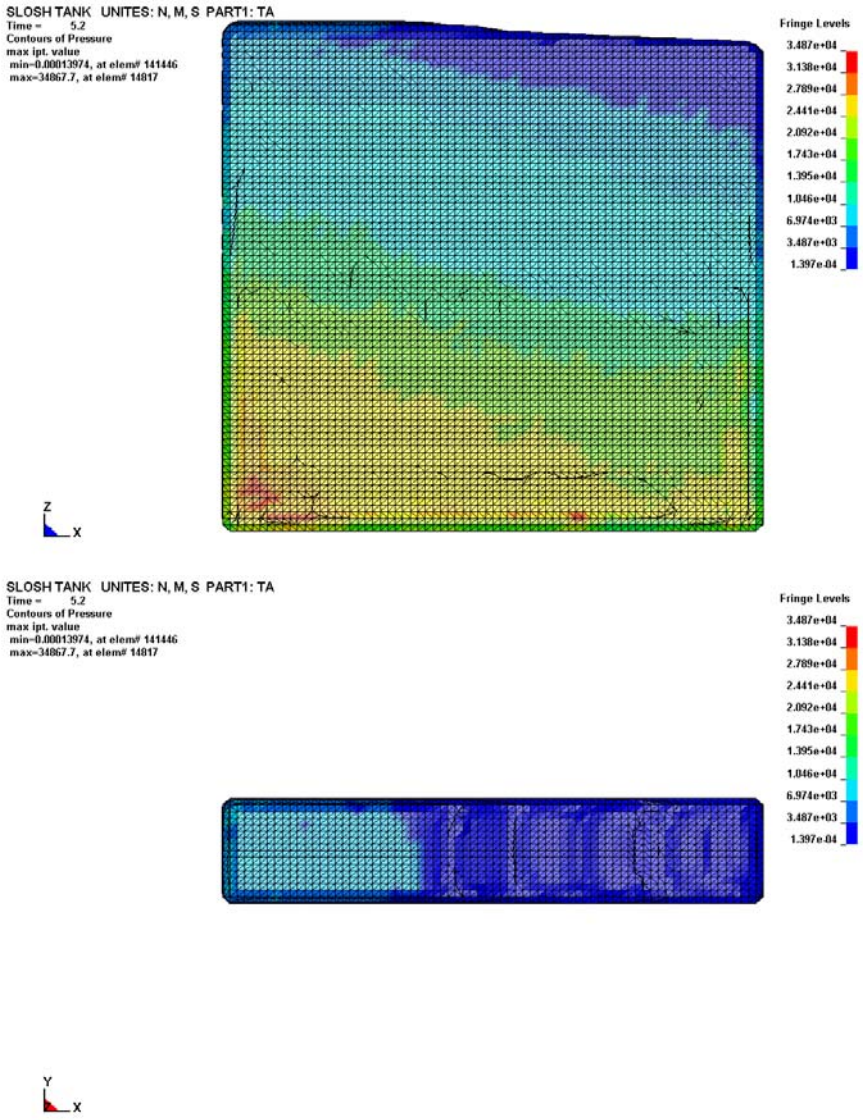

Figure 4.18 Contours of pressure distributions (Pa) at the 4th impact (t=5.2sec)

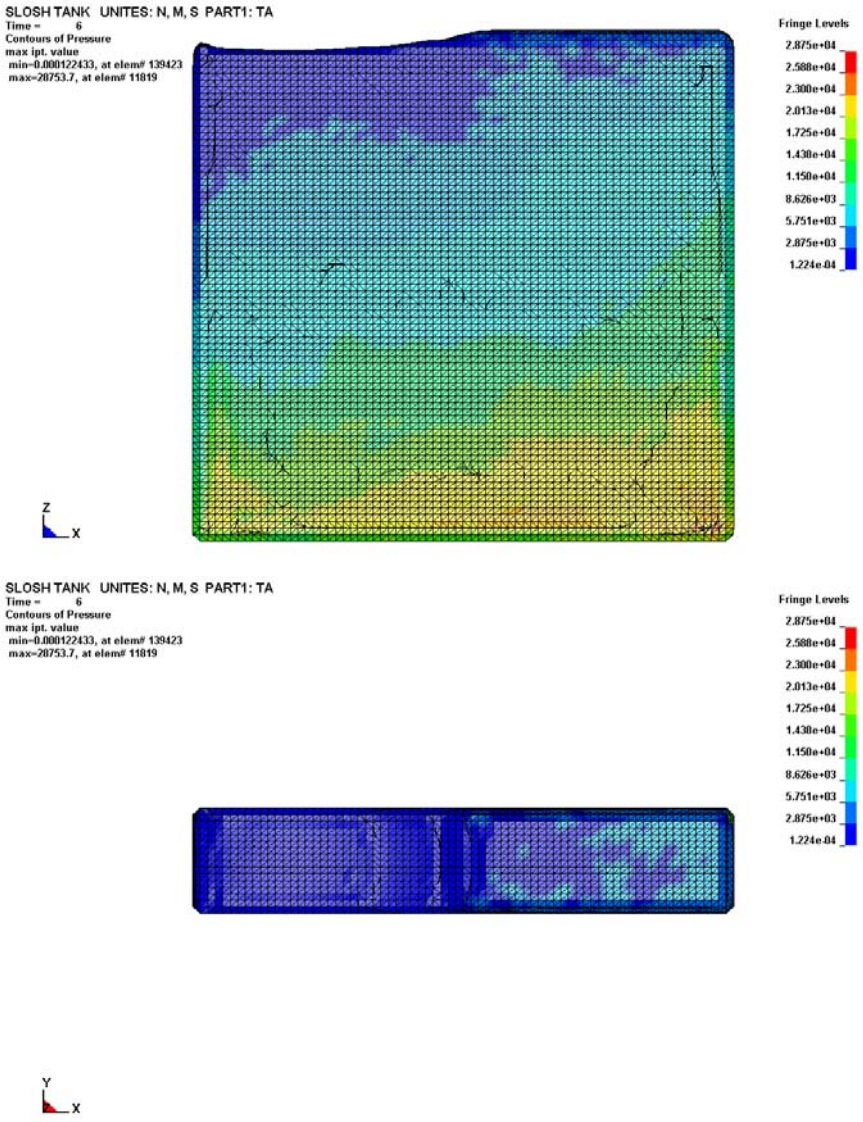

Figure 4.19 Contours of pressure distributions (Pa) at the 5th impact (t=6.0 sec)

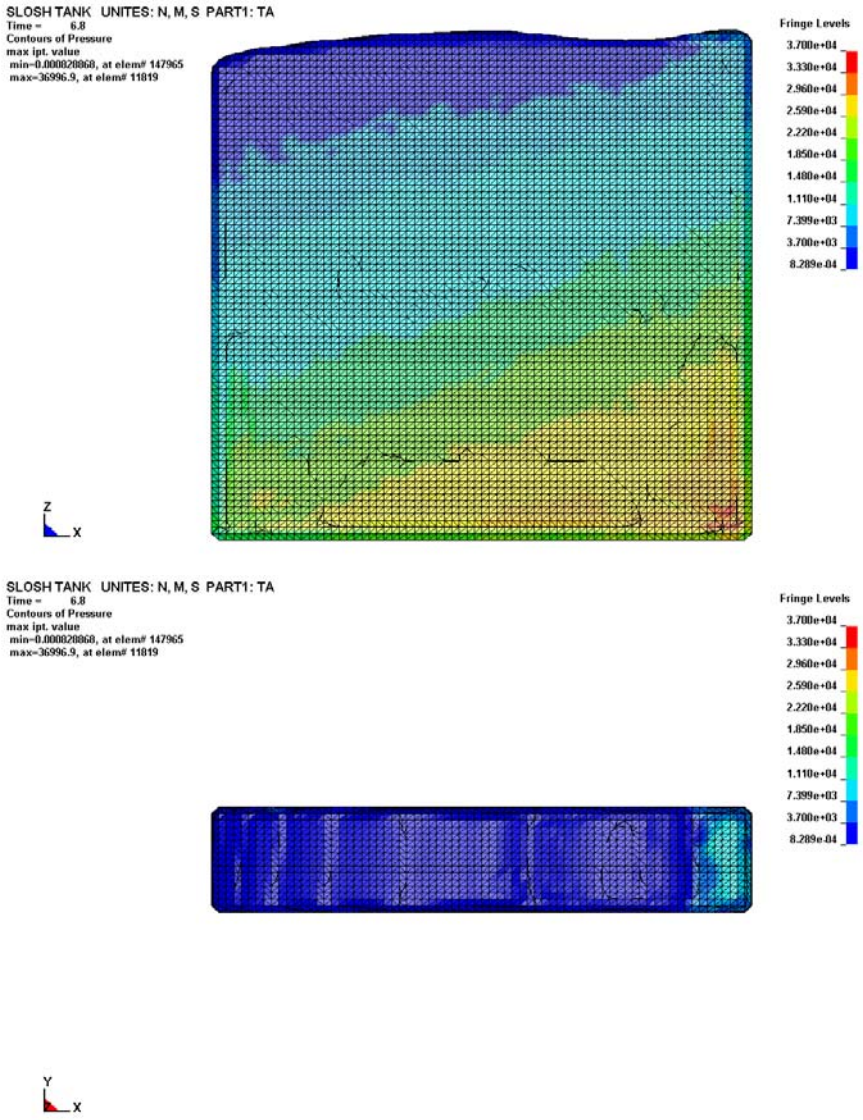

Figure 4.20 Contours of pressure distributions (Pa) at the 6th impact (t=6.8 sec)

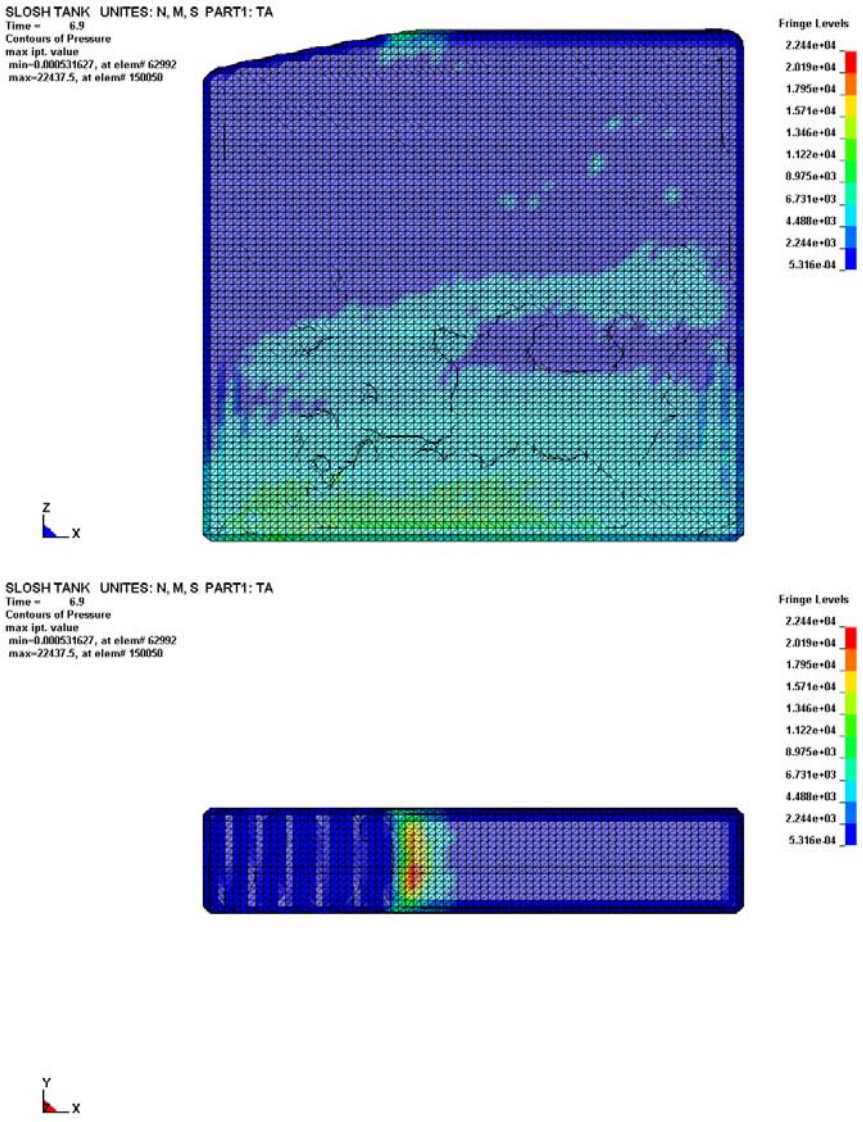

Figure 4.21 Contours of pressure distributions (Pa) at the 6th impact (t=6.9 sec)

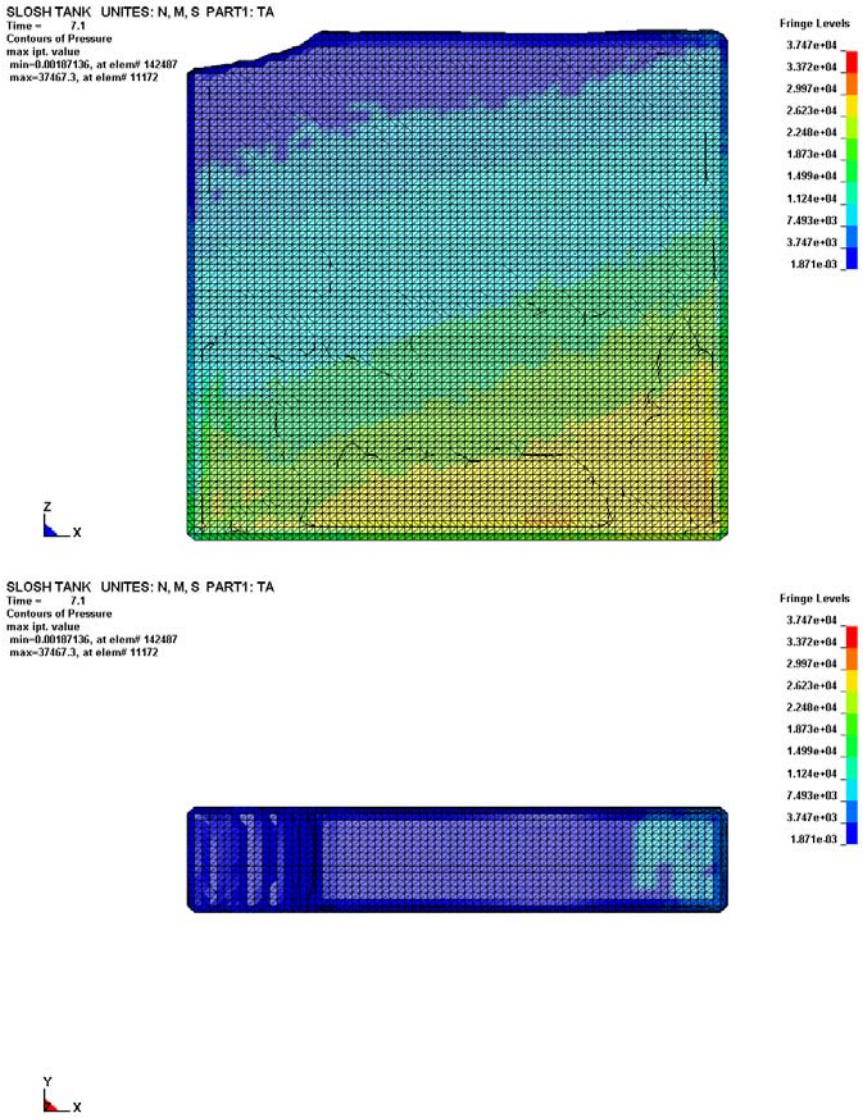

Figure 4.22 Contours of pressure distributions (Pa) at the 7th impact (t=7.1 sec)

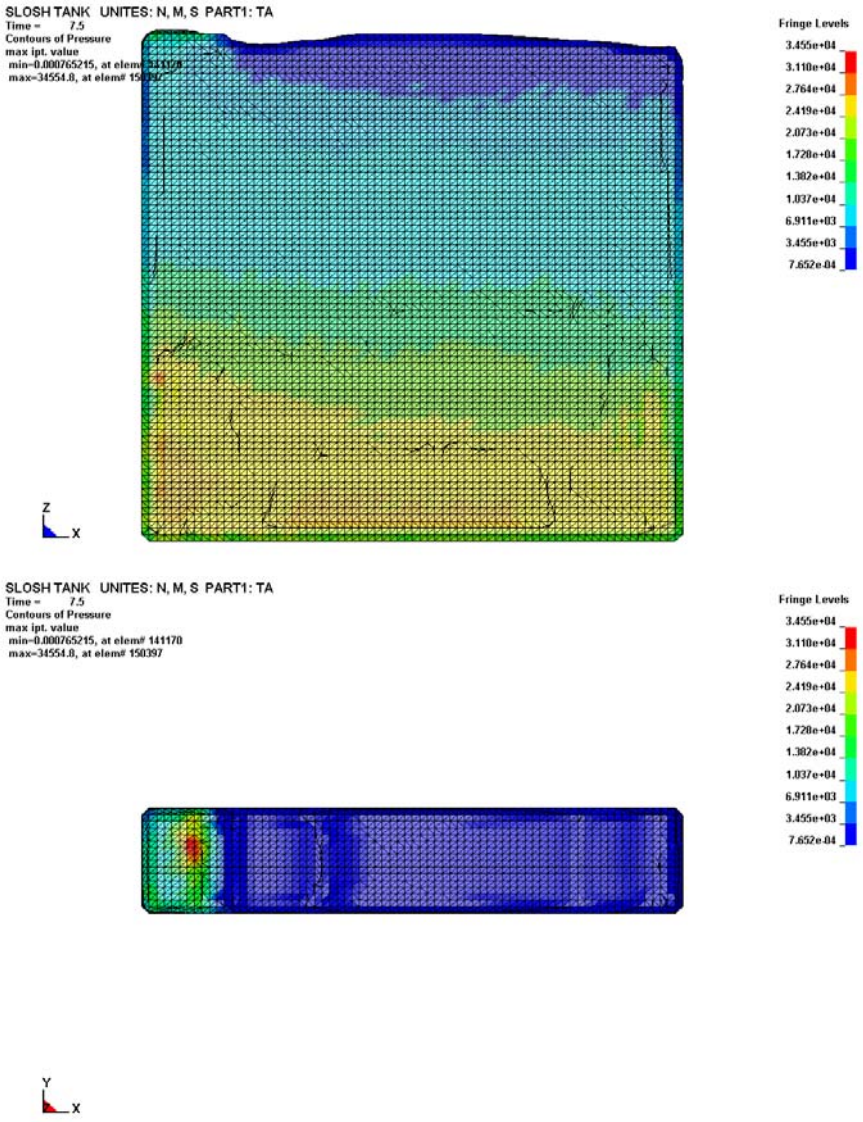

Figure 4.23 Contours of pressure distributions (Pa) at the 8th impact (t=7.5 sec)

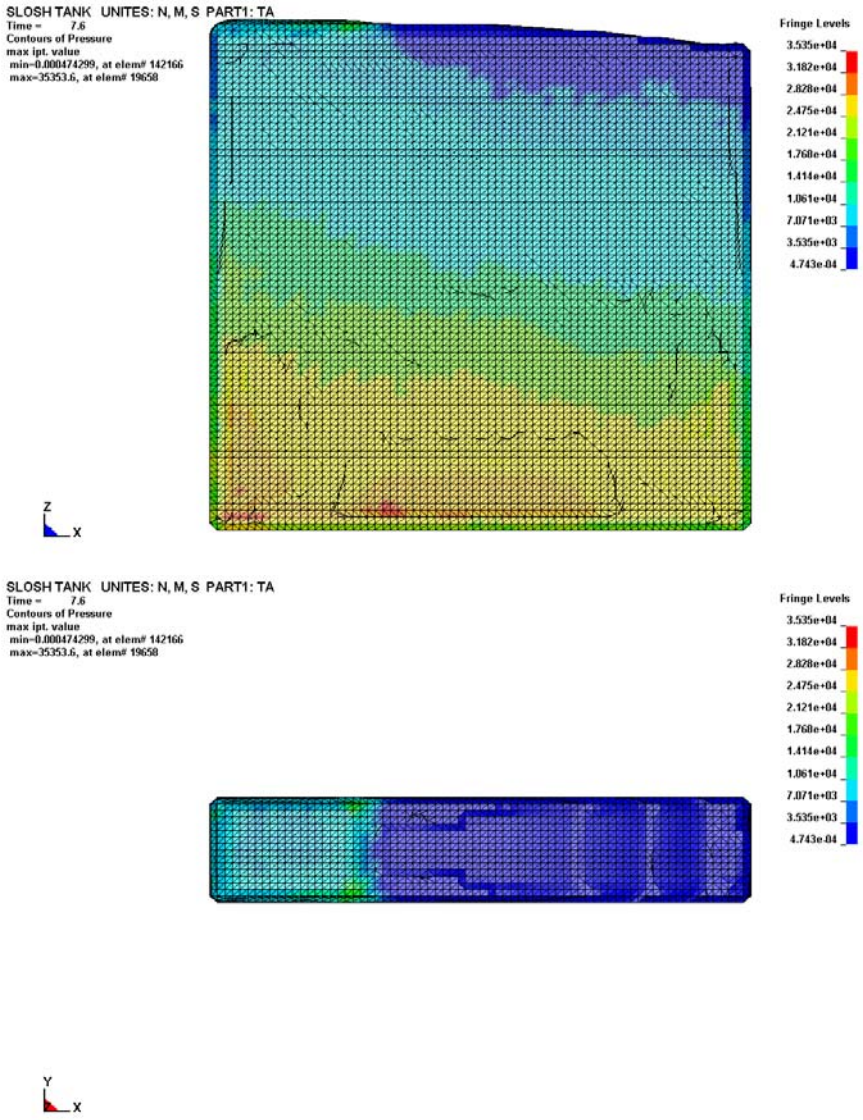

Figure 4.24 Contours of pressure distributions (Pa) at the 9th impact (t=7.6 sec)

4.8 Summary and conclusions

In this chapter is developed a three dimensional finite element model capable of performing simulation of the complex dynamic behavior of a liquid tank subjected to a strong seismic base excitation. The model uses an updated Eulerian-Lagrangian description of the liquid-solid interface in order to enforce compatibility between solid and liquid elements.

The sloshing waves developed by the seismic ground motion generate additional hydrodynamic pressures due to confinement's effects that are not taken into account by approximated formulae available in literature and described in section 7.6. A finite element model in LS-DYNA has been developed that takes into account these nonlinear effects.

For the analyzed tank the peak total force developed by the impact of the sloshing waves on the roof is one order of magnitude bigger than the force determined with the simplified formula (Cimellaro *et al*., 2007a). These discrepancies are attributed to the high spectral values in the low frequency range of the selected ground motion that generate high amplitude waves. In this case, the confinement of the tank amplifies the hydrodynamic forces and the linearized approach can not capture the governing nonlinear phenomena.

This comparison, even if derived from a single case, shows that the hydrodynamic pressures applied on the tank roof, during a seismic event, may be well above the expected level. This indicates that further research studies should be conducted on this topic, focusing on the parameters that affect the magnitude of the applied pressures, such as the tank geometry ratios, the vertical component of ground motions and the flexibility of the tank walls. This can lead to the development of a more realistic and accurate approach to estimate hydrodynamic roof pressures due to sloshing in tanks with insufficient freeboard.

Chapter 5

5 Characterization of input ground motion

5.1 Introduction to the methods available to simulate earthquake ground motions

The seismic input is one of the most uncertain quantities involved in the evaluation of the structural response under seismic excitation, being the magnitude of the ground motion as well as its frequency content and its duration very difficult to predict. Such parameters are usually assumed statistically, and they are characterized by a relevant dispersion.

When acceleration time histories are required as the input to the engineering design or analysis, three basic options are available:

1. Select **real accelerograms** from strong motion database:
2. Simulate **synthetic ground motions** from theoretical seismological models of seismic fault rupture;
    a. *Dynamic models*;
    b. *Kinematics models* (point source, finite fault);
3. Simulate **artificial accelerograms**, from stochastic or random variable theory methods, to match target response spectra.

Among all methods available, the last one is the most popular and it is generally used by engineers.

5.1.1 Selection of real accelerograms

The flow chart in Figure 5.1 describes an overview of the options available for *selecting real accelerograms* to be used in engineering analysis and design. After a deterministic seismic hazard analysis (DSHA) or probabilistic seismic hazard analysis (PSHA) the selection of real earthquakes can be done in term of *seismological parameters* or selection in term of *spectral matching*. When this last option is considered and spectrum compatible ground motions are considered they require satisfying the following conditions:

1. *They need to be realistic;*
2. *Reasonable in amplitude;*
3. *Reasonable in frequency content;*
4. *Reasonable in duration;*
5. *Reasonable correlation between components;*

If we want to summarize these conditions with a unique sentence, they need to have the *characteristics of real earthquakes*. Therefore, we have two options. The first one is to find actual recorded ground motions with *all* the characteristic you need:

1. *Matches desired "target" spectrum;*
2. *Matches desired duration;*
3. *Consistent source mechanism (source effects);*
4. *Consistent with regional and local geology (path effects);*
5. *Consistent with local soil conditions (site effects);*

Of course, find a record with all the characteristics you want is very unlikely, so we have the other option: finding actual recorded ground motion with *some* of the characteristic you want:

1. *Similar magnitude and distance (source effects);*
2. *Similar regional and local geology (path effects);*
3. *Similar local soil conditions (site effects);*

In order to select these real recorded ground motions numerous web sites are available (e.g. PEERS database - http://peer.berkeley.edu/smcat/search.html , European strong motion database http://www.isesd.hi.is/, http://www.isesd.cv.ic.ac.uk/ESD/frameset.htm, http://www.cosmos-eq.org etc.) where thousand of records are available. The selection can be provided by several search utilities that are based on:

1. *Range of magnitude;*
2. *Range of distance;*
3. *Style of faulting;*
4. *Range of maximum acceleration;*

However, several *methods* are also available in literature *for selection of real earthquakes* and here are reported four methods that can be considered as the most popular ones:

- **METHOD 1**: select according to the parameters (magnitude, site classification, source-to-site-distance, etc.) that define the design earthquake scenario;

- **METHOD 2**: select directly records that match the shape and/or amplitude of the target spectrum (Naeim *et al*. 2004);

- **METHOD 3**: First select records from broadly similar scenarios, but with a reasonable good match in terms of magnitude. Then, search within these records for those records with the smallest deviations from

the shape of the design spectrum. (This method can be considered as a combination of the first and the second method)

- **METHOD 4**: Select records that have characteristics (duration, root-mean-square acceleration, peak velocity etc.) that have been previously found to produce stable median estimates of inelastic behaviors (Hancock *et al*., 2004);

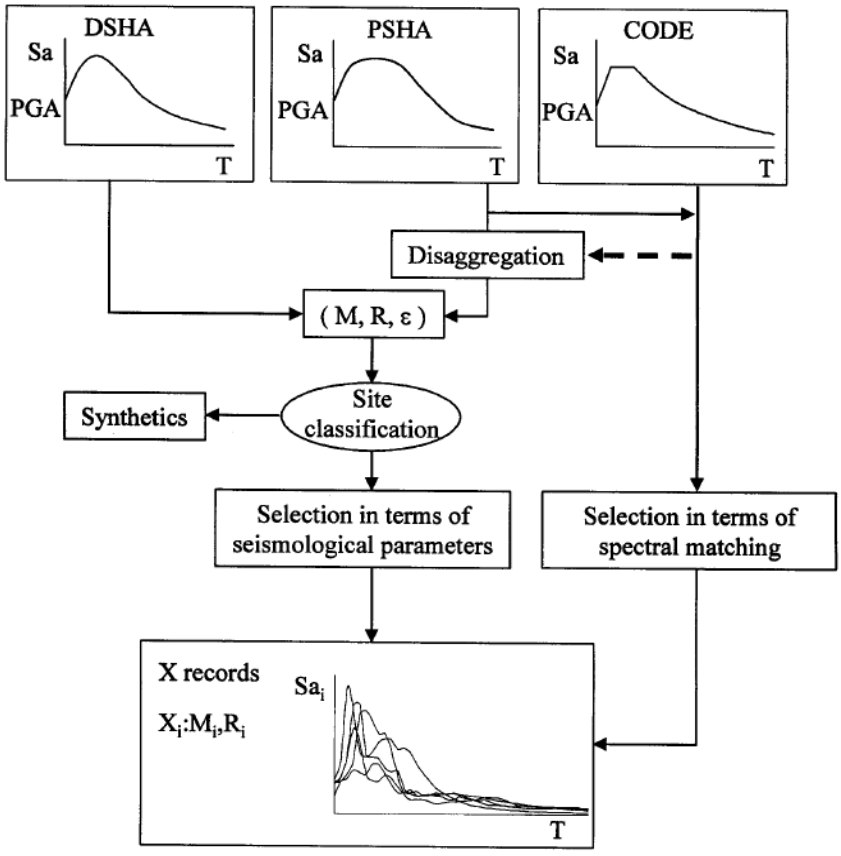

Figure 5.1 Flow chart for selecting real accelerograms (Bommer & Acevedo, 2004)

5.1.1.1 Scaling of accelerograms

After selecting the ground motions, the second option engineers have to face is scaling the records. The flow chart in Figure 5.2 shows the options available for scaling:

- Scaling in amplitude;
- Scaling in time and amplitude;
- Adjust by wavelets;
- Adjust by FFT;
- Generate synthetic earthquakes;

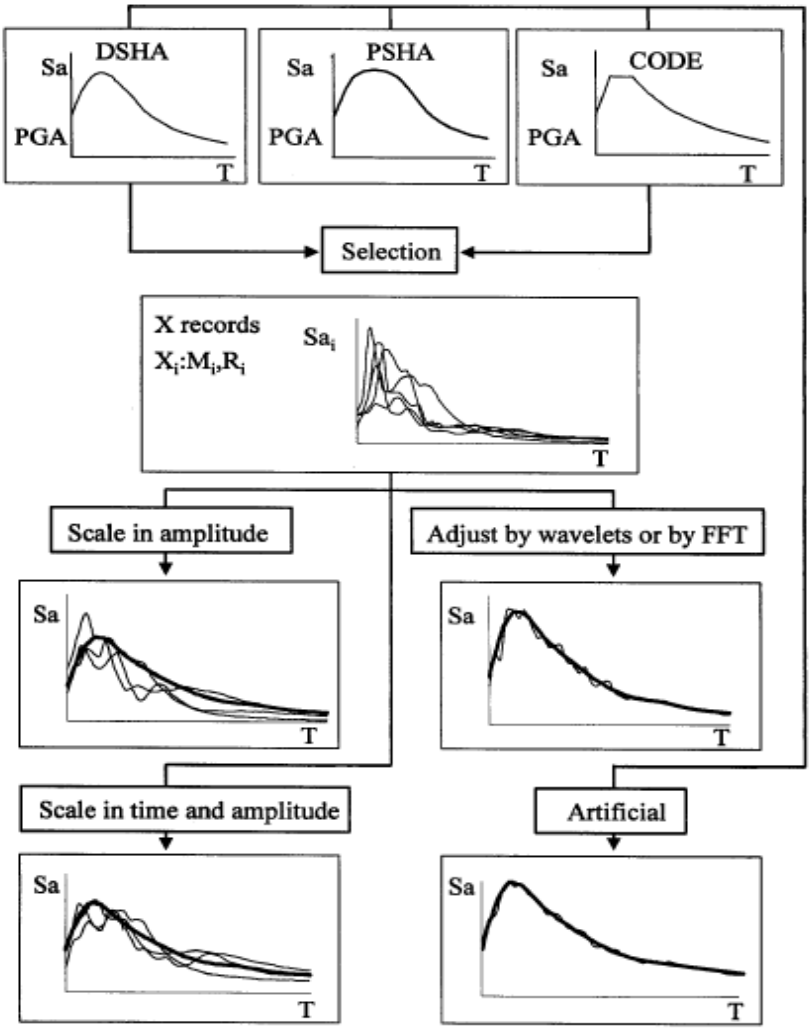

Figure 5.2 Flow chart for scaling accelerograms (Bommer & Acevedo, 2004)

In the following figures (Figure 5.3-Figure 5.6) are shown some of the scaling procedures:

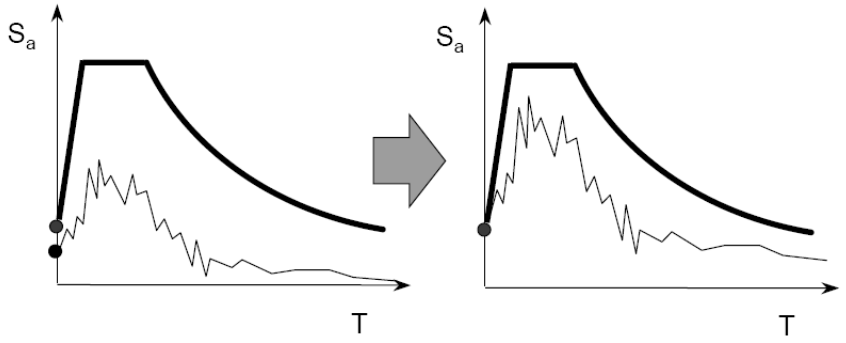

Figure 5.3 Matches to peak ground acceleration (PGA)

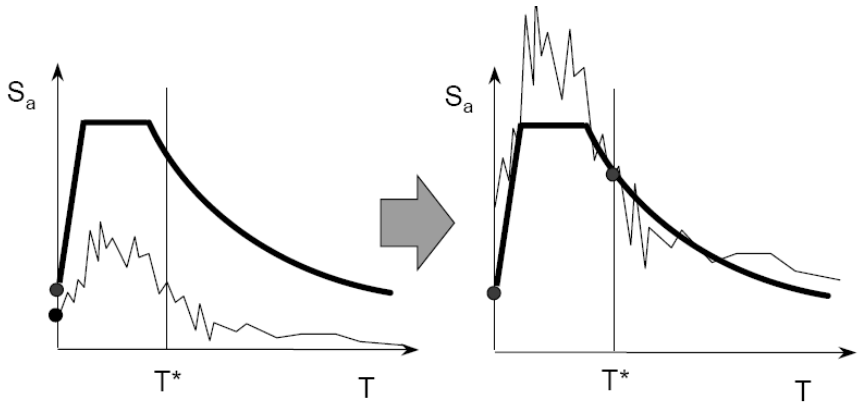

Figure 5.4 Matches spectral acceleration to some period ($S_a(T^*)$)

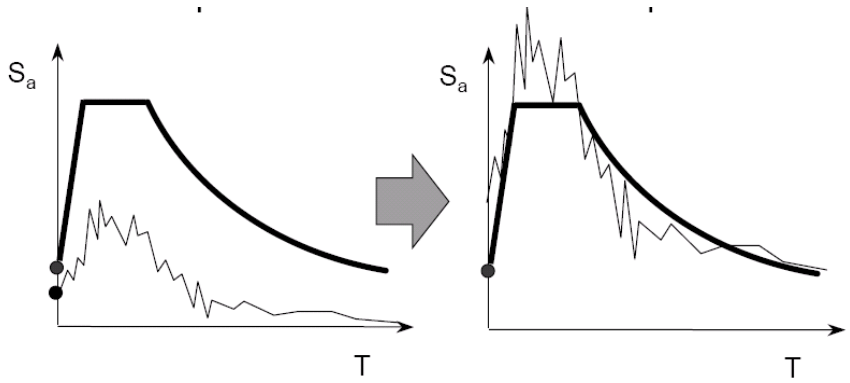

Figure 5.5 matches spectral acceleration in least square sense

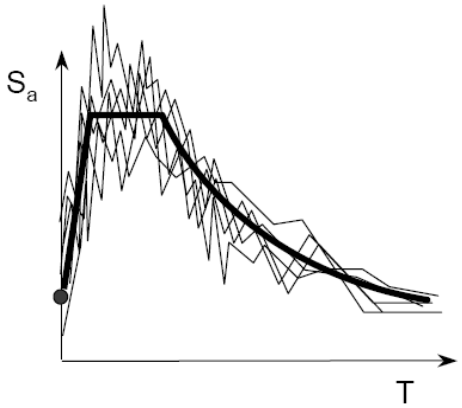

Figure 5.6 for multiple motion matches the median in least square sense (the scaling factor should be the smaller between 2/3 and 3/2)

Figure 5.6 shows multiple motions matching method where the median is scaled to the target response spectrum that is valid when the scaling factor is between 2/3 and 3/2.

5.1.1.2 Pitfalls and fallacies of the methods

The scaling method presented in Figure 5.6 where the median response spectrum of multiple motions is scaled to the target response spectrum has some weakeness. If the target response spectrum is defined by probabilistic seismic hazard analysis (PSHA) then the variability in the ground motion is already accounted for and should not be double counted by being also included in the suite of selected and scaled records. In this case in fact records should be individually rather than collectively scaled to the design elastic response spectrum.

The uniform hazard spectrum (UHS) at the site is influenced by multiple sources, so different part of UHS may be controlled by different sources (e.g. short fault located nearly influence high frequency content and long fault located farther away influence low frequency content). Consequentially no individual source may be capable of producing a motion consistent with the UHS, because UHS may contain more energy than any single earthquake could produce. So, using UHS compatible motions may lead to over-softening and over-damping during the analysis.

5.1.2 Synthetic accelerograms (Stochastic models)

These methods grew out of the consideration that **large part of the strong shaking**, usually associated with the arrival of S waves, appears incoherent and essentially **random in nature**. Random motion that has no predominant frequency and has a flat amplitude spectrum is called white noise. This lead to the assumption that strong ground motion can be approximated by finite duration (arrival of S waves) **band limited Gaussian** (normally distributed) **white noise**. Under this assumption, by fixing an array of spectral amplitudes and then generating different arrays of phases (random numbers uniformly distributed between 0 and 2π) is possible to generate **synthetic accelerograms that are similar in general appearance** (e.g. frequency content) but **different** in the "**details**". In the following paragraph are shown the equations for one of the methods available in literature that generates synthetic accelerograms.

5.1.2.1 Generating samples of univariate and multivariate random parameters

The ground motion is modeled as a random function $\ddot{y}_g(t)$, which is characterized by a Power Spectral density (*PSD*) function and an equivalent duration of strong shaking t_d. The Kanai-Tajimi spectral density function has been adopted for the generation of ground acceleration $\ddot{y}_g(t)$. The Kanai-Tajimi spectral density function has the form of:

$$S_g(\omega) = \frac{1 + 4\zeta_g^2 \left(\frac{\omega}{\omega_g} \right)^2}{\left[1 - \left(\frac{\omega}{\omega_g} \right)^2 \right]^2 + 4\zeta_g^2 \left(\frac{\omega}{\omega_g} \right)^2} S_0 \tag{5.1}$$

Where ω_g, ζ_g and S_0 may be regarded as the characteristics and the intensity of an earthquake in a particular geological location. In this study the *modified Kanai-Tajimi spectral density function* (Clough and Penzien, 1993) is also used to see the effects of the excitation spectral density function in the low frequency range on the spectral response. The modified Kanai-Tajimi spectral density function has the form of (Figure 5.7):

$$S_g(\omega) = \frac{\left[1 + 4\zeta_g^2 \left(\frac{\omega}{\omega_g} \right)^2 \right] \cdot S_0}{\left[1 - \left(\frac{\omega}{\omega_g} \right)^2 \right]^2 + 4\zeta_g^2 \left(\frac{\omega}{\omega_g} \right)^2} \times \frac{\left(\frac{\omega}{\omega_k} \right)^4}{\left[1 - \left(\frac{\omega}{\omega_k} \right)^2 \right]^2 + 4\zeta_k^2 \left(\frac{\omega}{\omega_k} \right)^2} \tag{5.2}$$

Where the parameters ω_k, and ζ_k are introduced to produce the desired filtering of the very low frequencies. The parameters of the ground acceleration

spectral density functions expressed by equations (5.1) and (5.2) are selected in this case as:

$$\omega_g = 15.0\,rad/s\,; \quad \zeta_g = 0.6\,; \quad \omega_k = 1.5\,rad/s \quad \zeta_k = 0.6\,.$$

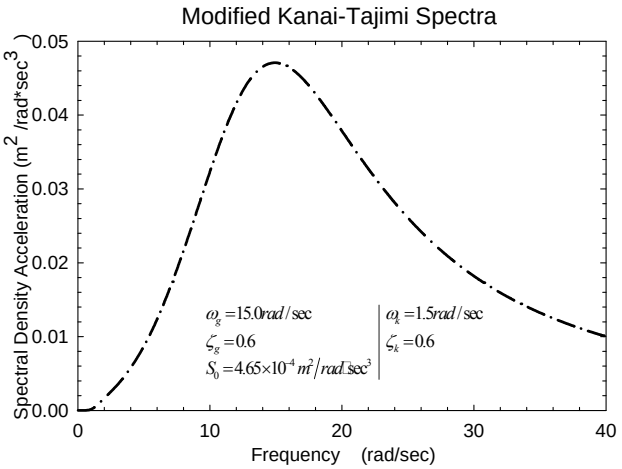

Figure 5.7 Power spectral density function of ground acceleration (firm soil condition)

These parameters have been used to reflect firm-soil conditions in some literature (Heredia-Zavoni *et al*., 1994). S_0 is taken as $4.65\times10^{-4}\ m^2/rad\ s^3$, which is compatible with that of the Housner average response spectra (Housner *et al*., 1970).

There are numerous techniques for generating samples of univariate and multivariate random parameters. Most of these techniques use random number generators producing independent realizations that are uniformly distributed over (0, 1). If we consider a zero-mean, real valued, stationary Gaussian process $Y(t)$ with covariance function $R(\tau)=E\{Y(t)Y(t+\tau)\}$ and one-side power spectral density $G(\omega)$ the process has a spectral representation:

$$Y(t) = \int_0^{\infty} \left[\cos \omega t dU(\omega) + \sin \omega t dV(\omega) \right] \tag{5.3}$$

In which $U(\omega)$ and $V(\omega)$ are real-valued, zero-mean, independent Gaussian processes with orthogonal increments and increment variances $E\{dU^2(\omega)\} = E\{dV^2(\omega)\} = G(\omega)d\omega$.

It is no possible to generate samples of $Y(t)$ from Equation (5.3), because it involves an uncountable set of random variables in the processes $U(\omega)$ and $V(\omega)$. Simulation is usually based on approximations of $Y(t)$ that involves a finite number of random variables on any bounded time interval. The simulation technique used is based on an approximate spectral representation of $Y(t)$. First we consider a frequency $\tilde{\omega}$ so chosen that:

$$\int_0^{\tilde{\omega}} G(\omega) d\omega = \int_0^{\infty} G(\omega) d\omega \,. \tag{5.4}$$

Let $\tilde{Y}(t)$ be a zero-mean Gaussian process with one side-power spectral density:

$$\begin{aligned} \tilde{G}(\omega) &= G(\omega), \quad 0 \le \omega \le \tilde{\omega} \\ &= 0, \qquad\quad \omega \ge \tilde{\omega} \end{aligned} \tag{5.5}$$

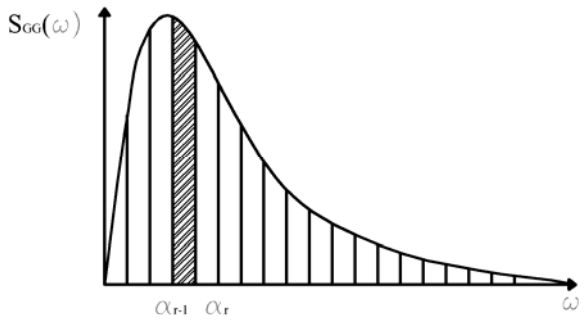

Figure 5.8 Discrete description of the PSD

Figure 5.8 shows this spectrum and a partition of the frequency range $(0,\tilde{\omega})$ in m no overlapping intervals I_k of width $\Delta\omega_k$ and midpoints ω_k, $k=1,\ldots,m$. We approximate $\tilde{G}(\omega)$ by the discrete spectrum:

$$G_m(\omega) = \sum_{k=1}^{m} \sigma_k^2 \delta(\omega - \omega_k) \tag{5.6}$$

In which:

$$\sigma_k^2 = \int_{I_k} G(\omega)\, d\omega \approx G(\omega_k)\Delta\omega_k \tag{5.7}$$

constitutes the contribution of the power in interval I_k to the total variance of process $\tilde{Y}(t)$ and δ is the delta function equal to 1 for $\omega=\omega_k$ and 0 for $\omega \neq \omega_k$. Let $Y_m(t)$ be the process associated with one-sided power spectral density $G_m(\omega)$. It is seen from previous equations that $Y_m(t)$ has the spectral representation

$$Y_m(t) = \sum_{k=1}^{m} \sigma_k \left(V_k \cos\omega_k t + W_k \sin\omega_k t\right) \tag{5.8}$$

In which V_k and W_k are independent Gaussian random variables with zero means and unit variances.

5.1.2.2 Envelope functions

The realization is subsequently windowed using the envelope function of Saragoni and Hart (1974, see in Boore, 1983):

$$w(t) = a \cdot t^b \cdot e^{-ct} H(t) \tag{5.9}$$

Where *H(t)* is the Heaviside function and the other parameters are given as $\varepsilon=0.2$, $\eta=0.05$ (Boore, 1983) and:

$$b = \frac{-\varepsilon \ln \eta}{1+\varepsilon\left(\ln \varepsilon - 1\right)} \tag{5.10}$$

$$c = \frac{b}{\varepsilon T_W} \tag{5.11}$$

$$a = \left(\frac{e^1}{\varepsilon T_W}\right)^b \tag{5.12}$$

Equation 4 results an envelope function whose maximum value is one (Figure 5.9).

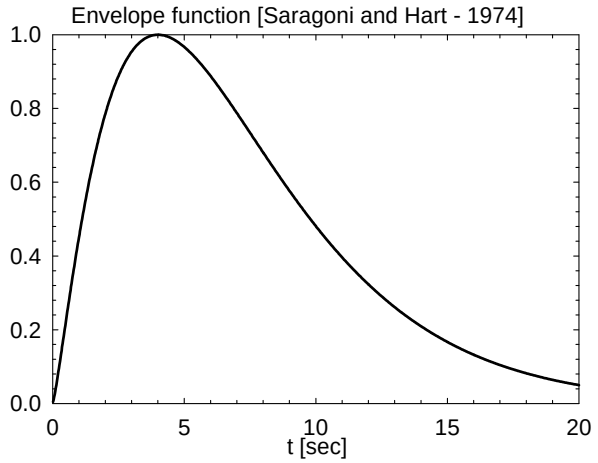

Figure 5.9 Saragoni function (1974)

So the ground acceleration is modeled by a non stationary Gaussian Shot noise with $X''_0(t)=W(t)\cdot Y(t)$, in which $Y(t)$ is a zero mean Gaussian white noise and $W(t)$ is a deterministic modulating function, the *Saragoni function*. One sample of the synthetic generated ground motion is showed in Figure 5.10.

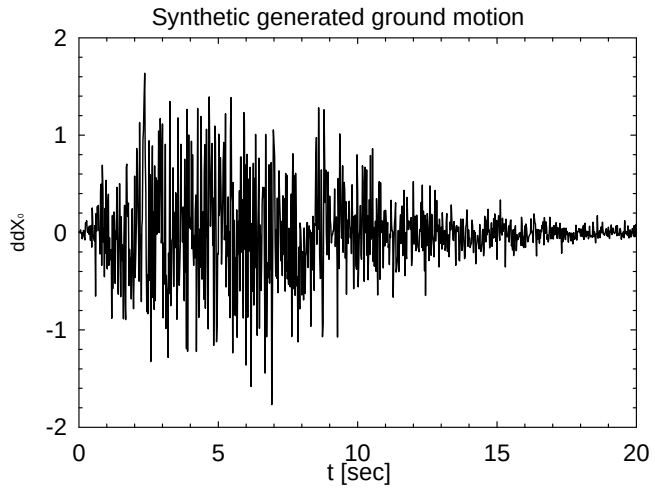

Figure 5.10 Synthetic Generated Ground Motion sample

When samples have been generated they need to be scaled to obtain different samples with different peak ground accelerations. Two techniques can be used for example:

1 Each sample $\tilde{X}''_0(t)$ can be normalized to the respective peak ground acceleration;
2 Each sample $\tilde{X}''_0(t)$ can be normalized to the median of the *PGA* of all the samples;

In the first case the peak ground acceleration related to each sample is computed:

$$PGA_i = MAX\left(\left|\ddot{X}_{0i}(t)\right|\right) \quad i = 1,\ldots,n \tag{5.13}$$

where n is the number of realizations and then each sample is scaled to the respective PGA_i so:

$$\ddot{X}_{0i}(t) = \frac{\tilde{\ddot{X}}_{0i}(t)}{PGA_i} \quad i = 1,\ldots,n \tag{5.14}$$

In the second case one time the peak ground acceleration of each sample is computed, the median of the peak ground acceleration is estimated:

$$\overline{PGA} = E\left(PGA_i\right) \quad i = 1,\ldots,n \tag{5.15}$$

And then each sample is normalized with the median of the peak ground acceleration of all samples:

$$\ddot{X}_{0i}(t) = \frac{\tilde{\ddot{X}}_{0i}(t)}{\overline{PGA}} \quad i = 1,\ldots,400 \tag{5.16}$$

5.2 Case study: Earthquake source characterization

The case study considered is the Gran Sasso laboratory is located in latitude 42.4583 North and longitude 13.5833 East which corresponds to a value of a_{max}=0.259157g for a return period of 475 yrs in *category 2* according to the seismic zoning of 20 of March 2003.

In Figure 5.11 it is represented the seismic hazard map in the Gran Sasso region that has been updated the 20 of March 2003. The contour plot represents different values of absolute accelerations with probability of exceed of 10% in

50 years (return period of 475 years). These data are related to hard soil with wave speed bigger than 800m/sec. The region of Assergi corresponds to a range between 0.1598 - 0.2397g.

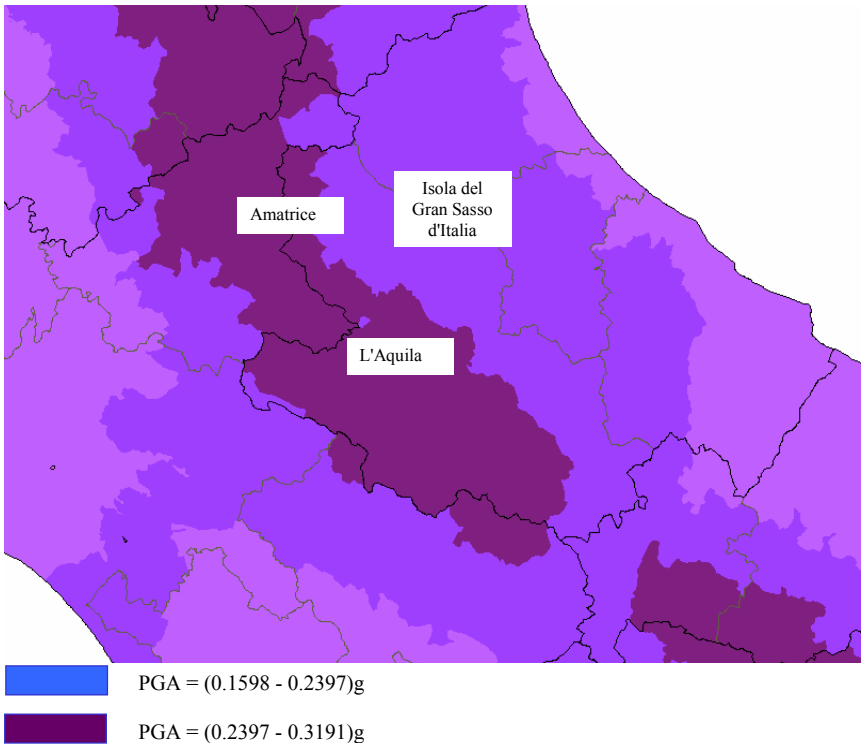

Figure 5.11 Seismic Hazard map (PE=10% in 50 yrs or Tr=475 yrs)

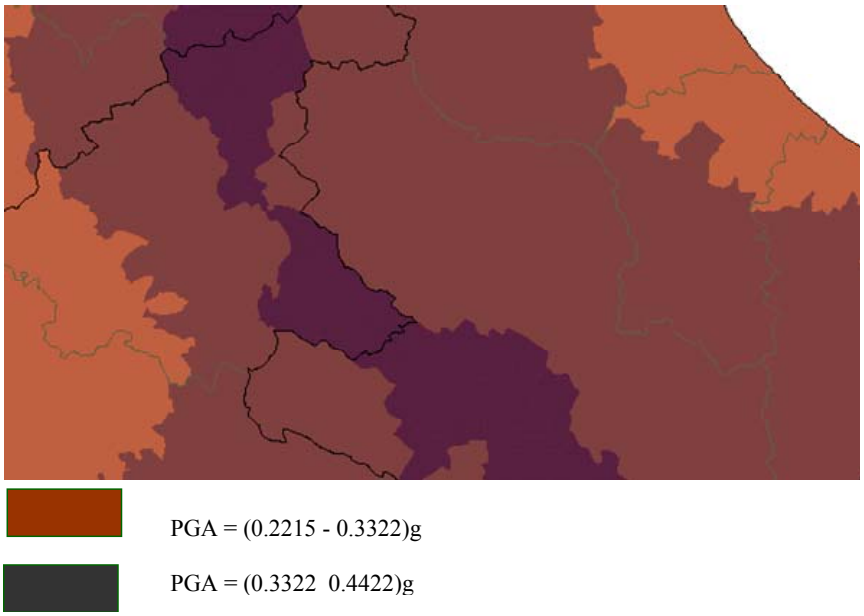

Figure 5.12 Seismic Hazard map (PE=5% in 50 years or Tr=975yrs)

The values of peak ground acceleration corresponding to different PE are also available. For example Figure 5.12 provides the peak ground accelerations (PGA) corresponding to a return period of 975 yrs that is between 0.2215 - 0.3322g. Other maps relate to different return periods are also available. For example for PE=50% in 50 years the PGA ranges between (0.0635 ÷ 0.0953) g, while for an earthquake with 100% PE in 50 years (this means that the return period of the earthquake is 50 years) the PGA ranges between (0.0476 ÷ 0.0714) g.

Finally in Figure 5.13 are plotted the response spectra according to Eurocode 8 using the peak ground accelerations provided by seismic zoning at the site for different hazard values, expressed in form of return periods and for the condition of rock soil (A category).

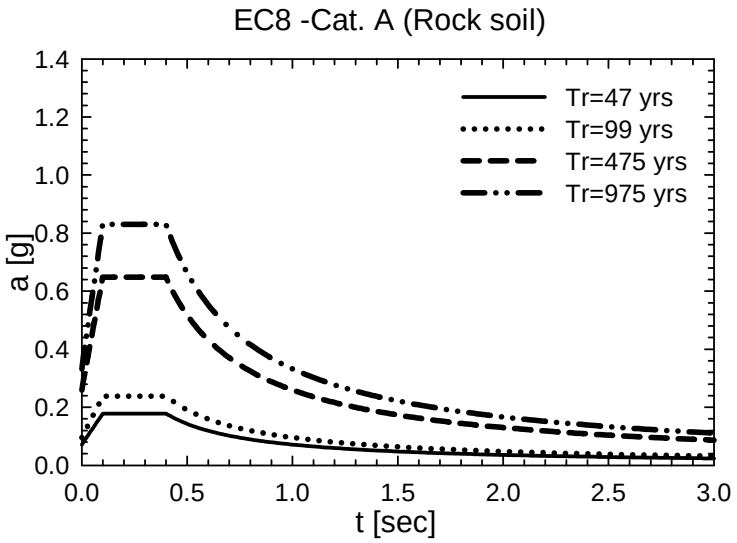

Figure 5.13 Elastic spectra for different return periods

Previous studies have been done for the determination of the design spectrum of the Gran Sasso laboratories (LNGS). For example, Sabetta and Faccioli (Faccioli, 1997) determined a specific response spectrum, through a specific risk analysis at the site. A complete and detailed report has been done also by ISMES (ISMES, 1998), where two different levels of seismic risks have been distinguished:

1. OBE (*Operating Base Earthquake*)
2. MCE (*Maximum Credible earthquake*)

OBE corresponds to the maximum historical earthquake at the site, while *MCE* corresponds to the maximum potential earthquake. *OBE* and *MCE* have been evaluated in free field condition with 5% damping. For the *MCE* a response spectrum has been estimated inside the tunnel of LNGS, though a numerical analysis based on a finite element model of the geological site. A

transfer function has been adopted to scale the spectral ordinate from free field conditions to the internal tunnel. In details, *OBE* spectrum has been evaluated through a statistical analysis of the earthquake catalogues and through the application of National attenuation relationships. For safety reasons, the maximum response spectrum has been considered, instead of considering a response spectrum associated to a given hazard level (return period). MCE spectrum has been estimated through the elaboration of real earthquake records available in databases, describing the maximum expected earthquakes in the Gran Sasso region.

Finally "*INFN spectrum*" (see Appendix A) is the consequences of discussions and comparison of spectra among Faccioli, Scarpa, De Luca and ISMES. In particular, The INFN spectrum coincides with the spectrum proposed by Faccioli that is more conservative respect to the others. Faccioli also proposes to use the same spectra both in the horizontal and vertical component. In Figure 5.14 it is shown the comparison between the elastic response spectrum generated with EUROCODE 8 corresponding to areturn period of 475 yrs and the INFN spectrum. The EC8 spectrum is an envelope of the INFN spectrum at the higher frequencies, while at the lower frequencies the INFN spectrum provides higher spectral accelerations.

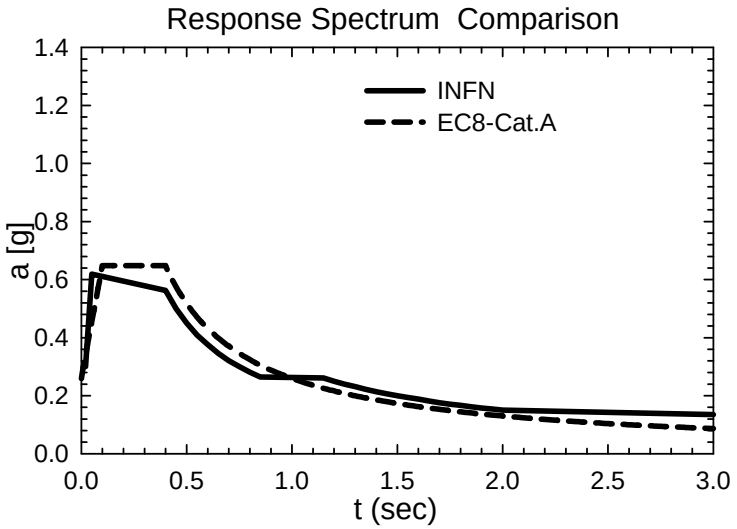

Figure 5.14 Comparison between EC8 spectrum and INFN spectrum (Sabetta and Faccioli)

According to the seismic report written by Castellani (2005), the LNGS is subjected also to the British Standard BS EN 1473, 1997. In this provision are considered 2 events: one is ***SSE*** (Safe Shutdown Earthquake) that corresponds to a return period of 10000 years and the other one is ***OBE*** corresponding to a return period of 475 years. In the first event case permanent damage are accepted, but the structure should not collapse and tank of toxic liquid should not loose the function of containment. In the case of ***SSE*** event, the system stops and it should be inspected before starting again. If ***OBE*** event happens, no damage should appear in the structure and the system should not stop. For liquid storage tank under ***OBE*** event, they should be verified under the following load combination.

$$1.05\times G + 1.05 \times E \qquad (5.17)$$

where G is he gravitational load and E is the earthquake load. The load combinations adopted are the following proposed by the EUROCODE8. The PGA corresponding to ***SSE*** of 10000 years is determined following the procedure describe in EC8 (*Performance requirements and compliance criteria*[1]*, 2.1 Fundamental requirements*). The important factor γi is:

$$\gamma_i = \left(\frac{T_{LR}}{T_L}\right)^{-\frac{1}{k}} = \left(\frac{475}{T_L}\right)^{-\frac{1}{3}} = \left(\frac{10000}{475}\right)^{\frac{1}{3}} = 2.76 \tag{5.18}$$

Therefore, the peak ground acceleration for a return period of 10000 yrs is given by:

$$a_{10000} = \gamma_i a_{475} = 2.76 \cdot 0.25g = 0.69g; \tag{5.19}$$

This peak ground acceleration will be used for critical and high-risk systems like ICARUS project.

So, in conclusion the earthquake motion on the surface of the laboratory is represented by the elastic ground acceleration response spectrum, having the same significance of the "elastic response spectrum" of Eurocode 8.

[1] At most sites the annual rate of exceedance, $H(a_{gR})$, of the reference peak ground acceleration a_{gR} may be taken to vary with a_{gR} as: $H(a_{gR}) \sim k_o \ a_{gR}^{-k}$, with the value of the exponent k depending on seismicity, but being generally of the order of 3. Then, if the seismic action is defined in terms of the reference peak ground acceleration a_{gR}, the value of the importance factor γ_I multiplying the reference seismic action to achieve the same probability of exceedance in T_L years as in the T_{LR} years for which the reference seismic action is defined, may be computed as $\gamma_I \sim (T_{LR}/T_L)^{-1/k}$.

5.2.1 Identification of earthquake sources: Geologic description

To evaluate the seismic hazard of the laboratory, all possible sources of seismic activity must be identified and their potential for generating future strong ground motion evaluated.

The geologic-structural analysis and the geomorfologic study of GNDT in the 1998 have characterized the systems of normal faults of *Assergi*, of the *Tre Selle-Corno Grande*, of *M. Camicia*, close to Campo Imperatore, that are located in the area of Grans Sasso d`Italia (central Appennino).

For the system of normal faults of Assergi it has been noticed:

a) Geologic disruption of approximately 1200m;
b) a minimal geomorfologic disruption ranging between 600 m in the western field to 1000 meters in the east field. They have been determined based on the breakup of the surface of the upper plane, generated during the Quaternary activity;
c) a slip-rate of about 1mm/yrs for the late Quaternary activity (beginning from the Superior Pleistocene).

For the faults of the *Tre Selle-Corno Grande*, and of *M. Camicia*, has been recognized:

a) The belongings to a unique distensive sinsedimentaric meso-cenozoic system;
b) A dip angle very low for the faults of the system of *M. Camicia*, associated to the spin on horizontal axis realized as a result of the structure of the chain; The orginal slope is maintained in the *Tre Selle-Corno Grande* that has been reactivated during the distensive quaternary tectonic with a maximum geomorfologic disruption of 300-400 m and a slip rate related to the late quaternary activity between 0.7 and 1.0 mm/yrs.

The border system of *Campo Imperatore* realized:

a) A geologic disruption of 500-600m in the western section comparable with the geomorphologic ones (Quaternaryt activity);
b) A displacement of 10 m of the conoid of Medium and Superior Pleistocene, while olocenic sediments are displaced of few meters;

In the zone of M.ti della Laga and Campo Imperatore there are some silent sources that are related to normal fault. Paleosismic studies on the surface of the source suggest a repetitive activation during Oleocene with a magnitude between 6.5 and 7 that has been estimated according to the length of rupture (Galadini and Galli, 2000).

In Figure 5.15 and Figure 5.17 are shown in details the galleries of the laboratory and the position of the three principal faults. The fault closer to the lab is a normal fault that is under observation from University of L`Aquila.

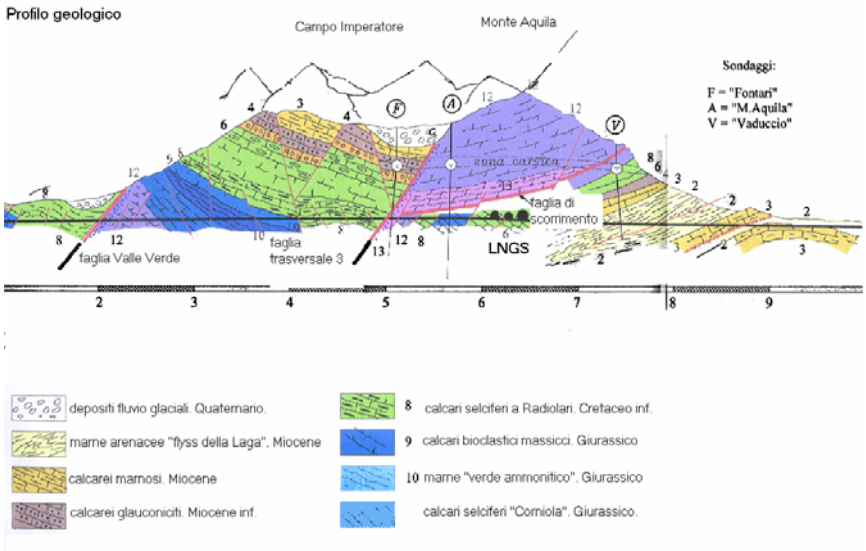

Figure 5.15 Geological section of mountain Gran Sasso in the center of Italy

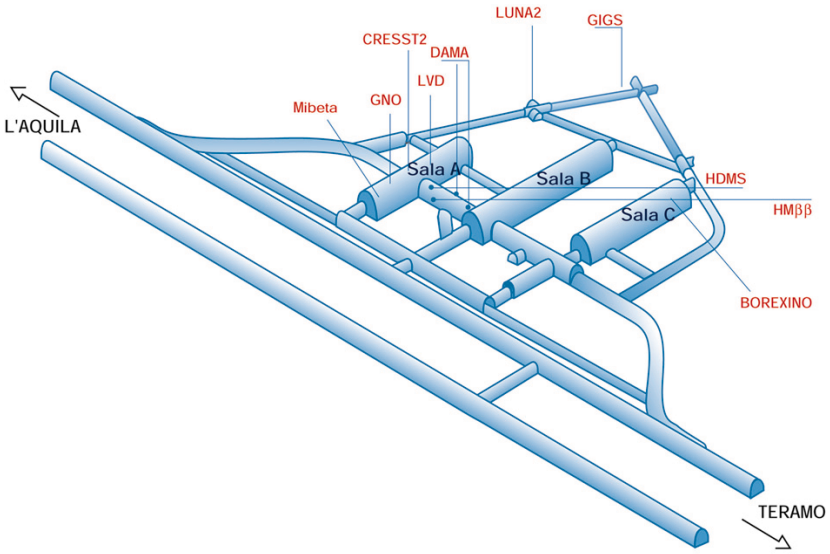

Figure 5.16 Tri-dimensional view of the laboratory LNGS

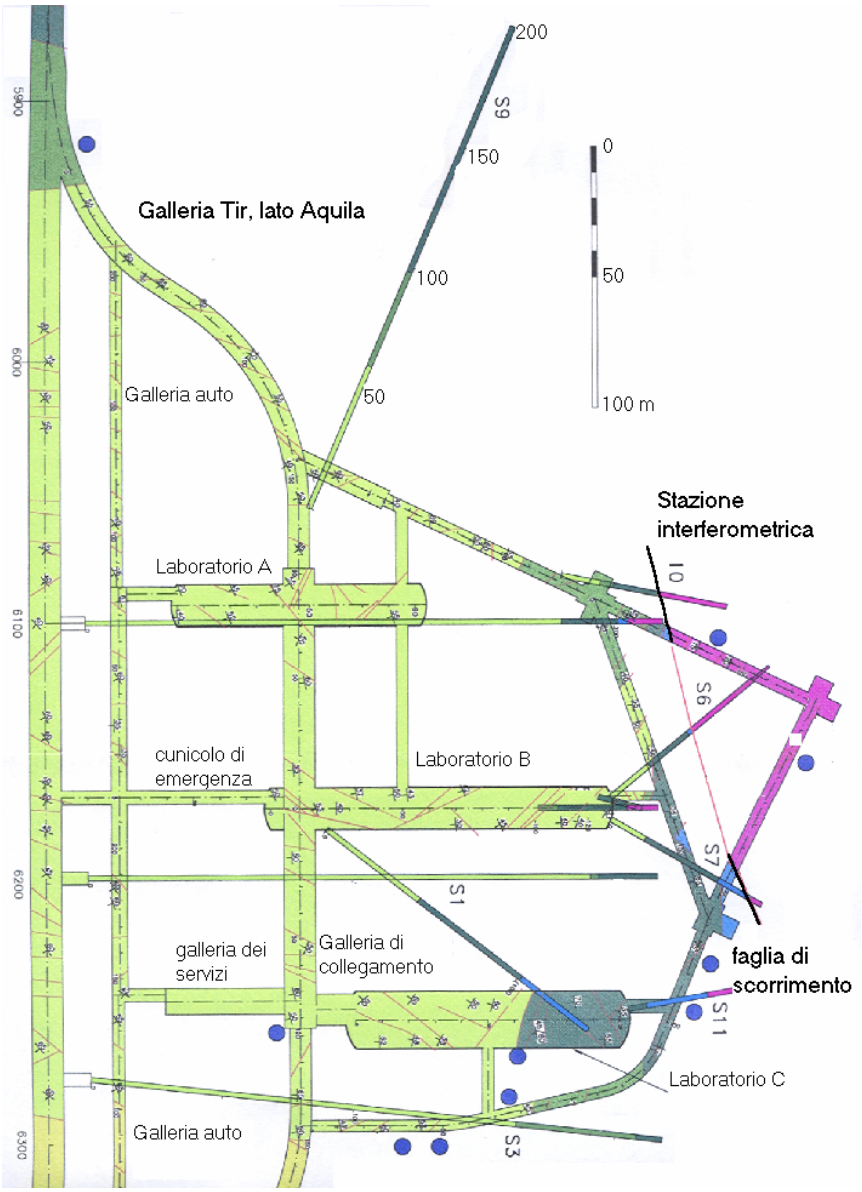

Figure 5.17 Plan view of the laboratory and of the fault

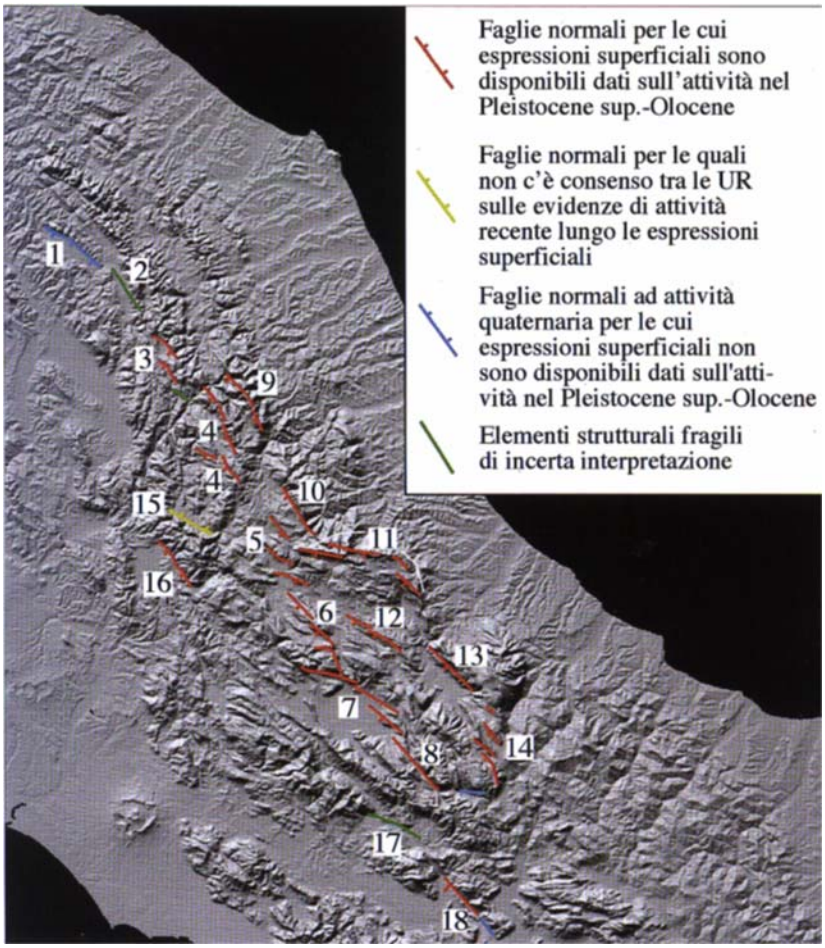

Figure 5.18 Position of different fault type in the center of Italy

5.2.2 Estimation of fault movement using DSHA

In this paragraph the relative displacement inside the fault is estimated and the consequences on wall covers are analyzed using deterministic seismic hazard analysis (DSHA). The DSHA is shown schematically in Figure 5.19.

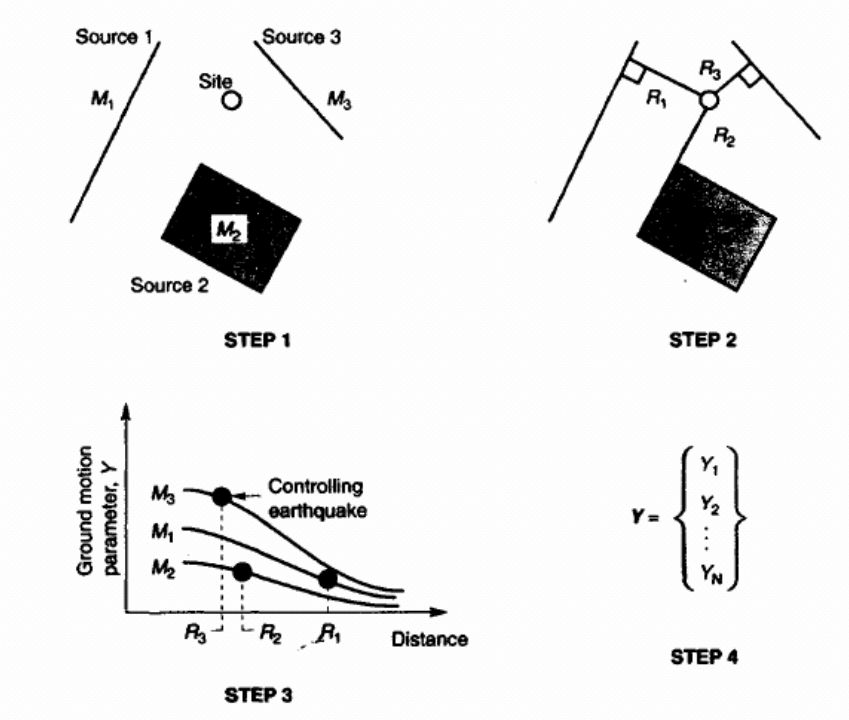

Figure 5.19 Four steps of deterministic seismic hazard analysis (Kramer, 1996)

A DSHA involves the development of a particular seismic scenario upon which a ground motion hazard evaluation is based. The scenario consists of the postulated occurrence of an earthquake of a specified size occurring at a specified location. In this case it is possible to assume two possible scenarios with reference to the fault shown in Figure 5.15 and Figure 5.17:

Scenario 1: The epicenter of the earthquake is located in a very deep position inside the fault (*Source zone 1*);

Scenario 2: The epicenter of the earthquake is located at a given distance from the fault (*Source zone 2*) that is not the source of energy release of the earthquake;

The first scenario (catastrophic scenario) is more demanding than the second one, but with less probability of occurrence. In the second scenario, the relative movement inside the fault is a secondary effect due to another earthquake source. The probability of occurrence of the second scenario is assumed 1% in 50 yrs. Data available in literature are associated to the first scenario, while no information has been found related to the second scenario.

The reference peak ground acceleration corresponding to a return period of 475 yrs is 0.25g at the Gran Sasso site. The magnitude associated to a return period of 475 yrs can be determined from empirical correlation from Sabetta and Pugliese (1999):

$$\log\left(a_{\max}\right) = -1.562 + 0.306M - \log\left(r^2 + 5.8^2\right) \qquad (5.20)$$

Where *log* is the natural logarithm, *M* is the moment magnitude, *r* is the distance from epicenter (between 0 and 30 km). So with amax=0.25g a moment magnitude between 5.5 and 6 is obtained. The expected relative displacements inside the fault are evaluated from Figure 5.20 and are around 4-5 cm.

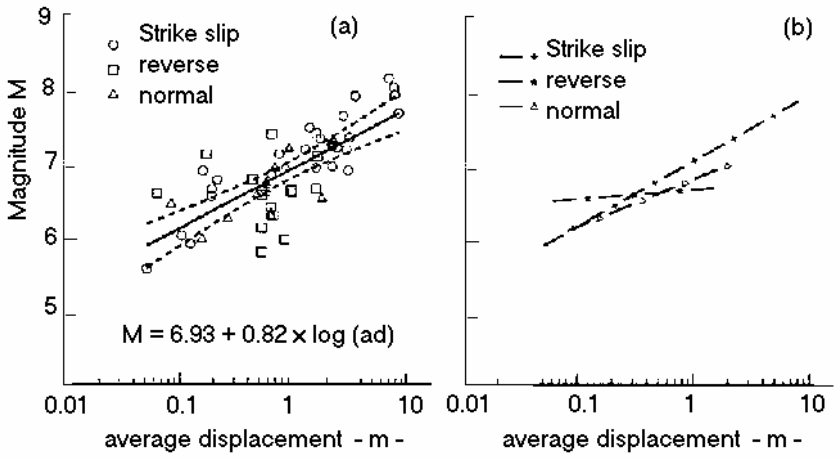

Figure 5.20 Correlation between magnitude and relative displacement fault

This relative displacement can generate damage to some instruments and ventilation pipelines.

5.3 Probabilistic seismic hazard analysis

Deterministic seismic hazard analysis (DSHA) provides a straightforward framework for evaluation of worst case ground motions, but id does not provides information on the likelihood of occurrence of the controlling earthquake, the likelihood of occurring where it is assumed to occur, or the effects of uncertainties in the various steps required to compute the various ground motion characteristics.

On the other hand, Probabilistic Seismic Hazard Analysis (PSHA) provides a framework in which these uncertainties can be identified, quantified and combined in a rational way to provide a more complete picture of the seismic hazard. The PSHA can be described by a procedure of four steps (Kramer, 1996) as illustrated in Figure 5.21:

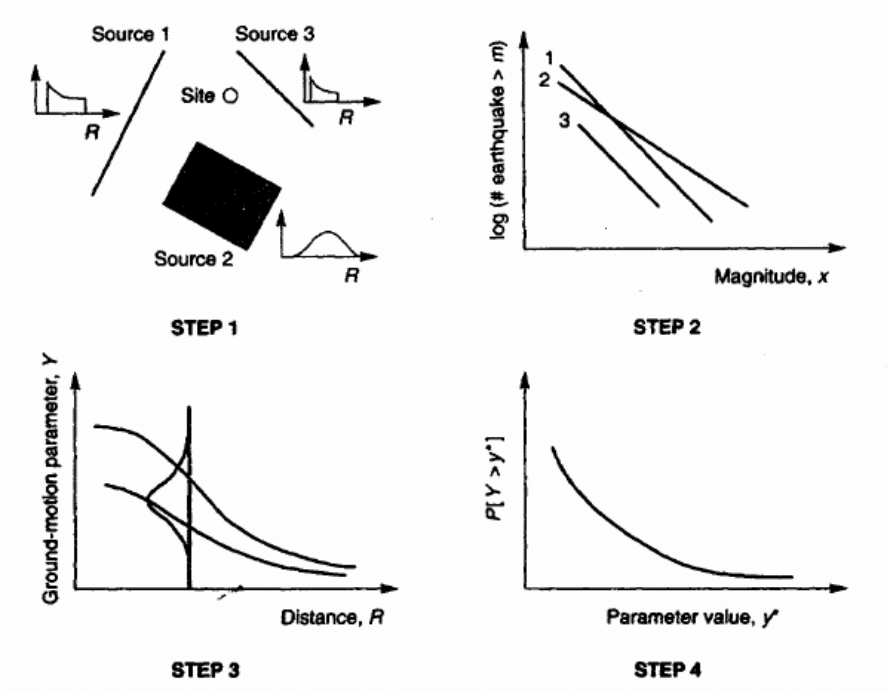

Figure 5.21 Four steps of Probabilistic Seismic hazard analysis (Kramer, 1996)

The first step of the procedure consists in identifying and characterize the earthquake source. This step also requires a seismic deagreggation map that is not available at the site. Therefore, the lack of informations at the site didn`t allow to use this more sophisticated method for the determination of the Seismic Hazard at the site.

5.3.1 Recurrence law

In the second step of PSHA shown in Figure 5.21 the seismicity or temporal distribution of earthquake recurrence is characterized. A recurrence relationship

specifies the average rate at which an earthquake of some size will be exceeded. It can be used to characterize the seismicity of each source zone. For example Figure 5.22 and Figure 5.25 are used to characterize the source zone related to the first scenario of DSHA in section 5.2.2 and are obtained using data available about maximum historical earthquake at the site in section 5.3.2.

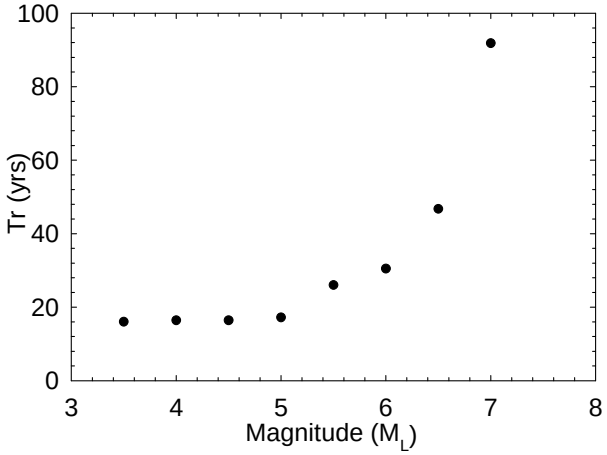

Figure 5.22 Return Period vs. magnitude for scenario 1

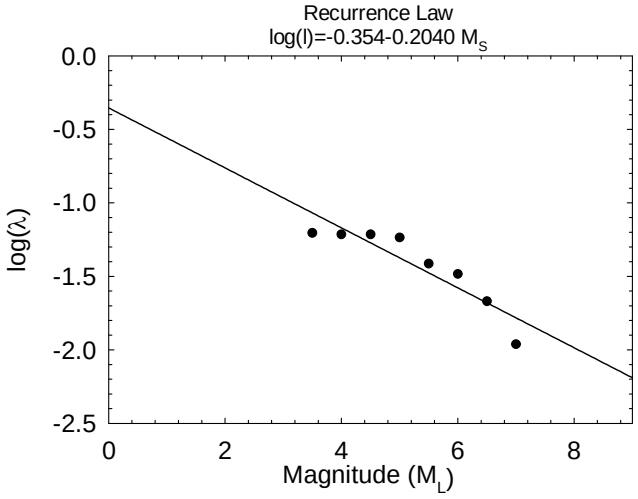

Figure 5.23 Mean annual rate of exceedance λ_m vs. magnitude M_L for scenario 1

5.3.2 Statistical evaluation of the maximum historical earthquake

In Table 5-1 are reported the names of the Catalogues that has been used as base for the following analysis, while in Table 0-1 are reported the seismic events starting from 1000 D.C. up to a distance of 15 km from the site.

On the basis of the values of magnitude reported in Table 0-1 in

Appendix B the histogram in Figure 5.24 has been generated, that cover a period range of about 705 yrs and shows that the maximum earthquakes have a magnitude of 7. Scarpa & De Luca (1997) in a technical report make reference to a consistent seismic activity in the post-glacial time of a local fault for which they estimated a total disruption of 15 m in 18000 yrs. The entity of this deformation and the period indicate the presence of at least 4 big earthquakes

with a return period of 1000 yrs and a magnitude of 7-7.5 that is in agreement with the results shown in Figure 5.24.

Table 5-1 Magnitude and std for CPTI (Catalogo parametrico dei terrmeoti italiani) and NT (NT4.1.1.)

denominazione e enti promotori	Periodo coperto	Soglia intensità	Soglia magnitudo	Numero totale *record*	anno
Catalogo dei Forti Terremoti in Italia 1 ING-SGA	461 a.C.-1980	VIII-IX*	-	346**	1995
Catalogo dei Forti Terremoti in Italia 2 ING-SGA	461 a.C.-1990	VIII-IX*	-	559**	1997
Catalogo NT4.1.1/DOM4.1 GNDT-CNR	1000-1980	V-VI	4.0	2421	1997
Catalogo NT4.1.1/'81-'92 GNDT-CNR	1981-1992	V-VI	4.0	67	1998

* si intende che questo catalogo riporta tutti gli eventi noti al catalogo del Progetto Finalizzato Geodinamica con intensità pari o superiore a tale valore; tuttavia, per alcune aree, esso include anche alcuni eventi con intensità minore;

** nel numero indicato sono inclusi anche alcune decine di terremoti considerati "falsi" dai compilatori e quindi mai avvenuti realmente.

Table 5-2 Correlation between different Intensity parameters

Io	Mm (CPTI)	Mm (NT)	Sd (CPTI)	Sd (NT)
XI	7.1	(7.3)	0.32	(.25)
X/XI	6.8	(-)	0.31	(-)
X	6.6	(6.7)	0.30	(-)
IX/X	6.3	(6.4)	0.29	(.41)
IX	6.0	(6.2)	0.26	(.39)
VIII/IX	5.8	(5.9)	0.21	(.37)
VIII	5.4	(5.5)	0.28	(.47)
VII/VIII	5.1	(5.2)	0.45	(.43)
VII	4.8	(5.0)	0.45	(.40)
VI/VII	4.6	(4.7)	0.49	(.45)
VI	4.3	(4.4)	0.39	(.35)
V/VI	4.0	(4.3)	0.20	(.31)

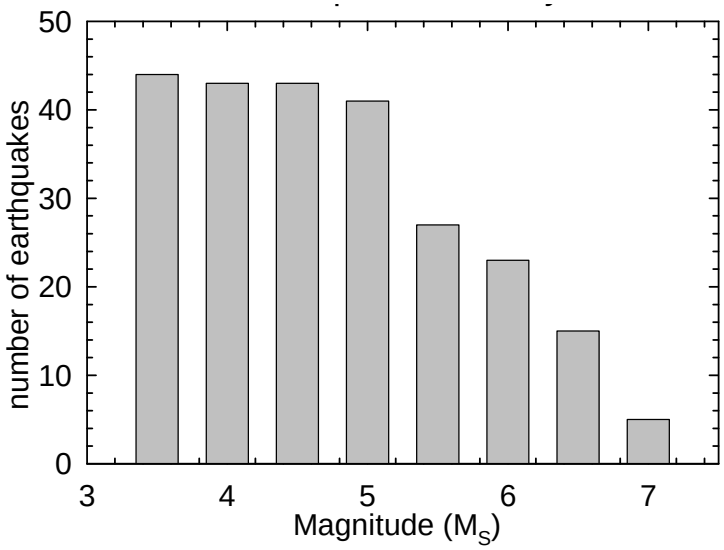

Figure 5.24 Histogram of historical Earthquakes bigger than magnitude 3.5 over a period of 705 yrs

For the cases where in the catalogue the magnitude of the event was not available, but only the epicentral intensity, then the magnitude *M* in Table 0-1 in Appendix B is evalutated using the following equation:

$$M_s = 0.56 \cdot I_0 + 0.94 \tag{5.21}$$

where I_0 is the epicentral intensity. The total seismic energy released during an earthquake is often estimated from the relationship (Gutenberg and Ritcher, 1956):

$$\log E = 11.8 + 1.5 M_s \tag{5.22}$$

where *E* is expressed in ergs. The results of energy are reported in Table 0-1 in Appendix B.

5.3.3 Attenuation relationship

The third step of PSHA described in Figure 5.21 consists in using attenuation relationships for determining the ground motion produced at the site by earthquakes of any possible size occurring at any possible point.

Attenuation relationships are empirical relationship that correlates parameters of seismic motion with magnitude (M) of the earthquake, the distance from the earthquake source (R), the local condition at the site, and sometime the mechanism type and the directivity effects.

These relationships are nearly always obtained empirically by regression analysis of a large set of recorded ground motion accelerograms.

5.3.3.1 *Sabetta & Pugliese* attenuation relationship

This attenuation relationship has been obtained for the Italian territory using 180 historical earthquakes recorded between 1978 and 1984 using the database of ENEL and ENEA. All data are recorded in *free-field* conditions for a range of magnitude between 4.5-6.8 and a range of distance between 1-180 km. This attenuation relationship correlates the peak ground acceleration with with the magnitude of the earthquake, the distance from the fault and the site condition. The magnitude M is defined as magnitude of surface waves M_s , if $M \geq 5.5$ and as M_L (local magnitude) if $M \leq 5.5$. The distance R from the fault is defined as the minimum distance of the site from the projection of the fault plane on the free surface. Finally the site classifications are rigid, thin alluviums and deep alluviums.

They consider the pseudospectral velocity PGV and the peak ground acceleration PGA in both horizontal and vertical direction using 5% damping. In order to represent the spectral form with a reduce number of points, 14 frequencies were selected uniformly distributed between 0.25 and 25 Hz.

The (mean+σ) PGA in the horizontal direction is given by:

$$\log(PGA) = -1.845 + 0.363 \cdot M - \log\sqrt{R^2 + 5^2} + 0.195 \cdot S + 0.190 \qquad (5.23)$$

In the vertical direction:

$$\log(PGA) = -2.365 + 0.387 \cdot M - \log\sqrt{R^2 + 4.9^2} + 0.182 \cdot S + 0.181 \qquad (5.24)$$

Where R is the epicentral distance and S=0 for rigid soil and deep alluviums and S=1 for thin alluviums.

The PSV (cm/sec) are given by:

$$\log(PGV) = a + b \cdot M - \log\sqrt{R^2 + h^2} + e_1 \cdot S_1 + e_2 \cdot S_2 + \varepsilon \qquad (5.25)$$

where the variables S_1 and S_2 are equal to 1 for deep alluviums and thin alluviums, while they are equal to 0 for rigid soils. The parameters a, b, e_1, e_2, are dependent on the frequency while ε is the standard deviation and it is also dependent on the frequency.

The spectral shape of the spectrum described in equation (5.25) is practically independent from the distance R (as the distance increases the amplitude reduces, but the shape remains the same), while it depends on the magnitude.

Using equation (5.23) under the assumption of rigid soil and with value of magnitude equal to 7 and distance equal to 5 km the mean PGA is 0.496, while the PGA+σ is equal to 0.739. However it must be noticed that the equation is used out of the range of values for which it was build, so these value can be considered as extrapolations.

5.4 Selection of real accelerograms from database

From the tectonic characterization of the area around the Gran Sasso laboratory and from the analysis of the catalogues is shown that the maximum credible earthquake corresponds to a magnitude of 7 and a distance of about 5km from the site. The laboratory is located inside rock, so the soil can be classified as rigid. So according to these geological conditions a suite of historical records earthquakes have been selected from PEER database (http://peer.berkeley.edu/smcat/search.html) first, and from European Strong Motion Database (http://www.isesd.hi.is/).

The lack of data for fault normal using the PEER database imposes to select earthquake with different type of mechanisms. However, this choice will not underestimate the earthquake that is obtained with fault normal mechanisms (McGarr, 1984). In Figure 5.25 and Table 5-3 are shown the response spectrum of the selected real earthquakes with 5% damping and compared with the Eurocode spectrum corresponding to a return perio of 475 yrs. Figure 5.26 show the comparison of the *Eurocode spectrum* with the *median response spectrum* and the *median*±σ. This shows that the selected records are characterized by a large dispersion that is probably due to the fact that the earthquakes were recorded very close to the seismic source (R=5km), so directivity effects due to the rupture propagation and local emission of energy close to the fault can influence the seismic motion.

Table 5-3 Selected real accelerograms from PEER database

	Earthquake	**Date**	**Station**	**M**	**R (km)**	**Soil type**	**PGA (g)**
1	Kocaeli, Turkey	1999/08/17	Izmit	7.4	4.8	Rock	0.2037
2	Northridge, California	1994/01/17 12:31	Pacoima Dam (upper left)	6.7	8	Rock	1.585
3	Whittier Narrows	1987/10/01 14:42	90019 San Gabriel - E Grand Av	6	9	rock	0.304
4	Coalinga	1983/07/22 02:39	1703 Sulphur Baths	5.8	9.7	rock	0.141
5	Parkfield	1966/06/28 04:26	1438 Temblor pre-1969	6.1	9.9	rock	0.357
6	Oroville	1975/08/01 20:20	1051 Oroville Seismograph Station	6	9.5	rock	0.092
7	Helena, Montana	1935/10/31 18:38	2022 Carroll College	6.2	8	Rock	0.173
8	Nahanni, Canada	1985/12/23	6098 Site 2	6.8	8	Rock	0.489

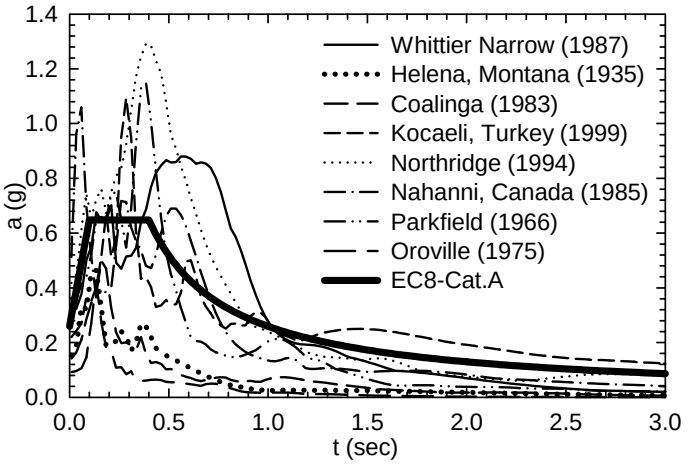

Figure 5.25 Real Historical Earthquake with same geological conditions and magnitude range

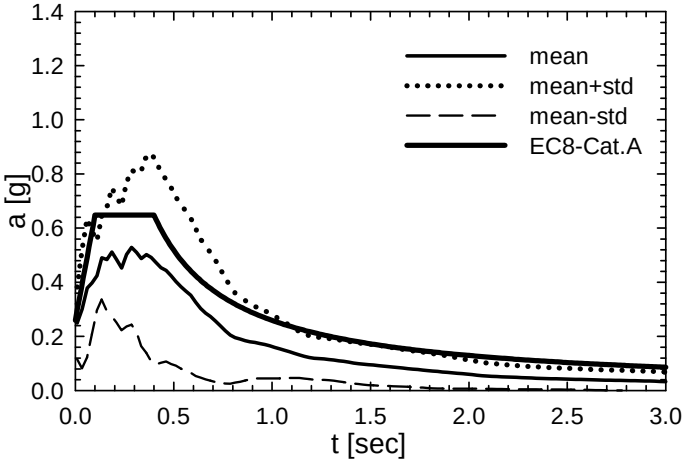

Figure 5.26 Comparison of the mean of historical earthquakes chosen vs. EC8

The average peak ground acceleration of the earthquake selected is similar to the values obtained by the attenuation relationship of Sabetta and Pugliesi (1996) described in the paragraph 5.3.3.1. So this will allow saying that the seleted records are representative of the seismogenetic conditions of the Laboratory of Gran Sasso.

The second bin of ground motion has been selected from the European Strong Motion Database (Table 5-4). All selected earthquakes happen in Italy except one which happen in Greece. They are all characterized by the same type of fault normal mechanism and the soil type is rock. Magnitude and distance were used as parameter for the selection as in the PEER database.

Table 5-4 Selected real accelerograms from ESMD database

Earthquake	Date	Station ID	M	R (km)	Fault mechanism	Soil type
Irpinia, Campano Lucano	November 23, 1980	98	6.9	10	Normal	Rock
Irpinia, Campano Lucano	November 23, 1980	93	6.9	6	Normal	Rock
Irpinia, Campano Lucano	November 23, 1980	96	6.9	14	Normal	Rock
Kozani, Greece	May 13, 1995	1320	6.5	14	Normal	Rock
Umbria Marche	September 26,1997	238	6	14	Normal	Rock

In Figure 5.27 are shown the response spectrum of the selected real earthquakes with 5% damping.

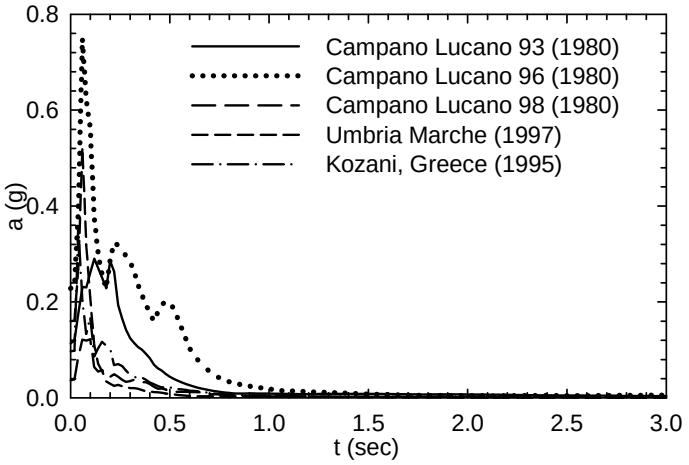

Figure 5.27 Response spectrum of real earthquakes selected from ESMD

5.5 Generation of Synthetic accelerograms

In this paragraph are shown the results of the method used to generate synthetic accelerograms described in details in section 5.1.2.1 The program SIMQKE (Gasparini, 1976) was used to generate a synthetic input motion.

Figure 5.28a-c shows the time history response in term of acceleration, velocity and displacement. The earthquake duration is 20 sec and the sampling frequency is 100Hz. In Figure 5.29 is shown the energy flux response of a single realization for a return period of 475 yrs. A total of six spectrum compatible earthquakes were generated and in Figure 5.30 is shown the comparison with the EC8 elastic response spectrum. Anologous procedures and figures were generated for earthquakes with return periods of 10000 yrs (SSE) and results similar to the ones shown for return period of 475 yrs are shown in Figure 5.31, Figure 5.32 and Figure 5.33.

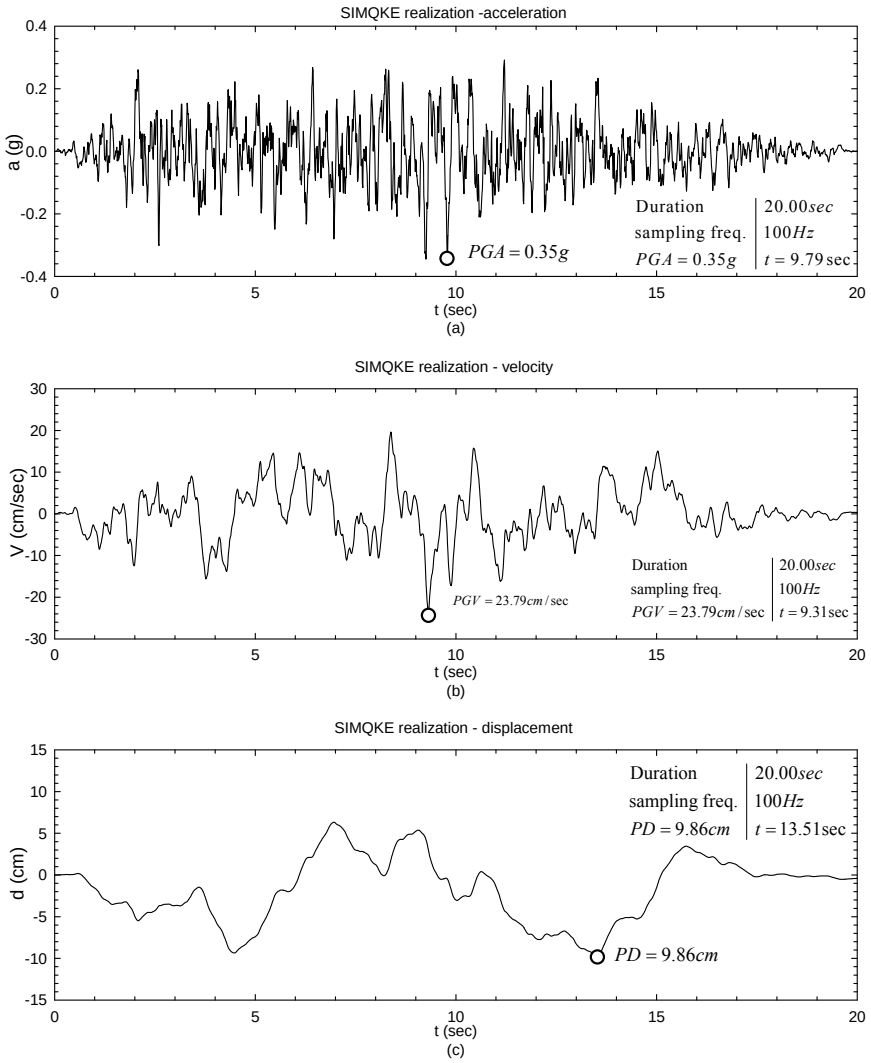

Figure 5.28 Acceleration, velocity and displacement of a single realization (Tr=475 yrs)

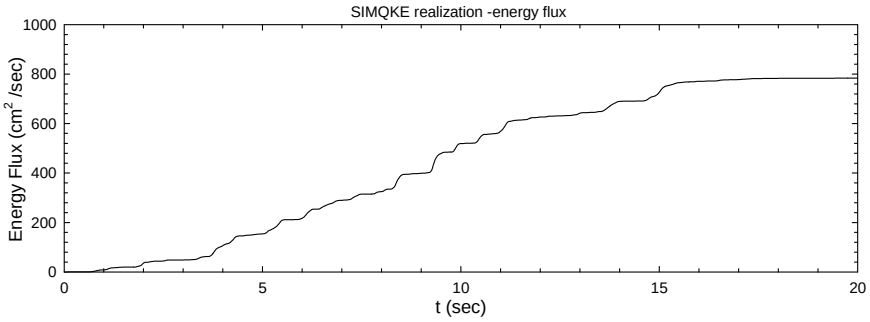

Figure 5.29 Energy flux time history of a single realization (Tr=475 yrs)

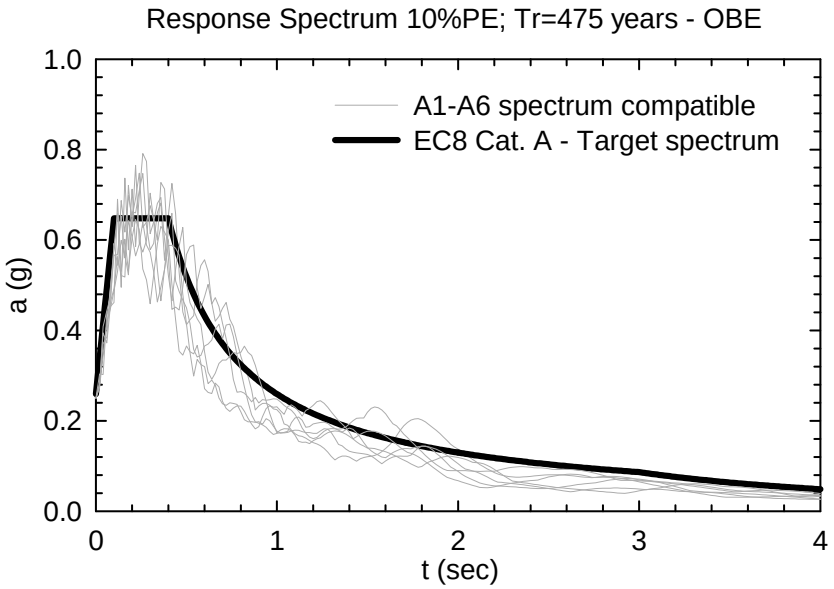

Figure 5.30 Comparison of synthetic spectrum compatible earthquakes vs. EC8 (Tr=475 yrs)

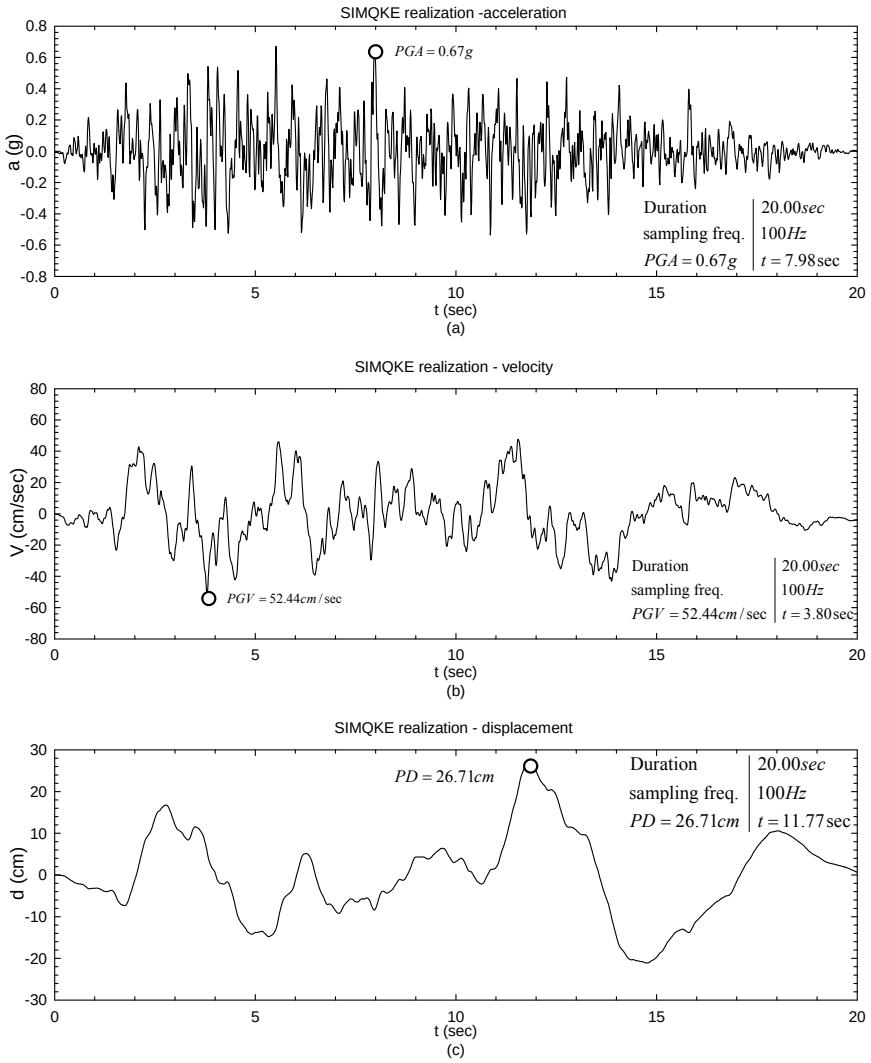

Figure 5.31 Acceleration, velocity and displacement of a single realization (Tr=10000 yrs)

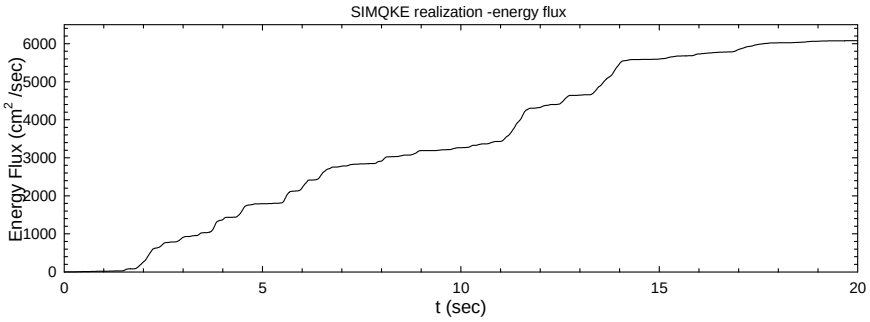

Figure 5.32 Energy flux time history of a single realization (Tr=10000 yrs)

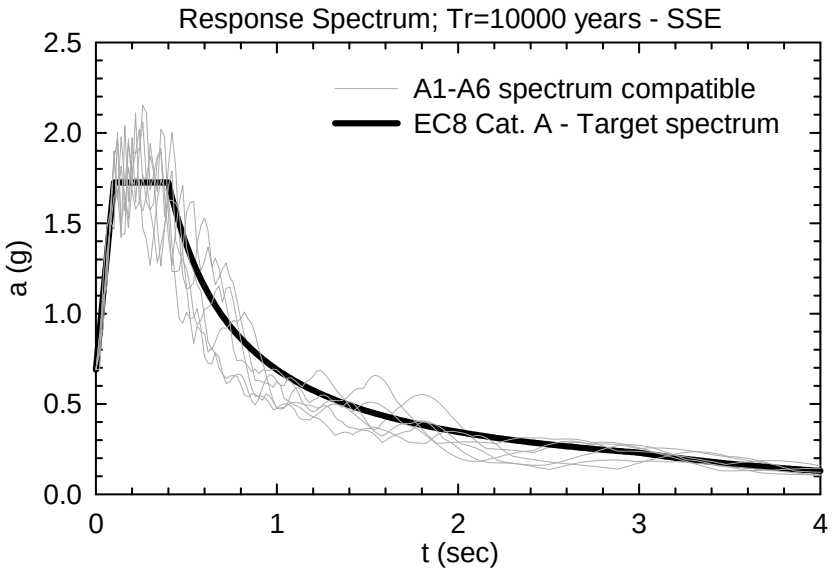

Figure 5.33 Comparison of synthetic spectrum compatible earthquakes vs. EC8 (Tr=10000 yrs)

5.6 Summary and conclusions

In conclusion the earthquake motion on the surface of the laboratory is represented by the elastic ground acceleration response spectrum of Eurocode 8.

The peak ground acceleration will be used for critical and high-risk systems like ICARUS project corresponds to an earthquake with return period of 10000 yrs (SSE) that corresponds to a pga of 0.69g (6.77m/sec^2).

The shape of the elastic response spectrum is the same for the two levels of seismic action: OBE and SSE that correspond respectively to damage limitation requirements and ultimate limit state requirements.

The horizontal seismic action is described by two orthogonal components assumed as being independent and represented by the same response spectrum.

According to Eurocode 8, the vertical component of the seismic excitation shall be accounted for in a limited number of cases, but since the T600 does not coincide with one of these cases, in general the vertical component is not taken into account.

Two sets of loading combinations are associated with this earthquake: 1) the *Ultimate limit state*, or no-collapse requirement. The loading combination is:

$$G + L + \gamma_I E$$

where G are the gravity loads, L an amount of live load, E is the earthquake, and γ_I is the importance factor. Since the plant importance has been taken into consideration by increasing a_g, it is $\gamma_I = 1$.

2) The *Serviceability limit state*, or damage limitation requirement. The acceleration at the ground is:

$$a_g = 0.15 \times 0.4 = 0.06$$

in ‘g units. According to Eurocode 8, the “damage limitation requirement” is considered to have been satisfied, if, under this seismic action the interstorey drifts are limited. Additional verifications might be required in the case of buildings important for civil protection or containing sensitive equipment.

Chapter 6

6 Earthquake loads due to sloshing in the horizontal cylindrical tanks

6.1 Abstract

This chapter is related to the evaluation of seismic forces due to sloshing and impulsive motion of the two horizontal cylindrical tanks filled with liquid Nitrogen and liquid Argon of T600 module of ICARUS project. Overturning moments and lateral forces have been evaluated in the transversal and longitudinal direction for four different liquid heights.

The approach described in the paper of Karamanos et al. (2006) has been adopted, because of the lack of information in the provisions (ENV 1998-4).

6.2 Introduction

Behavior of large tanks during seismic events has implications far beyond the mere economic value of the tanks and their contents. If, for instance, a water tank collapses, as occurred during the 1933 Long Beach and the 1971 San Fernando earthquakes, loss of public water supply can have serious consequences. Similarly, failure of tanks storing combustible materials, as occurred during the 1964 Niigata, Japan and the 1964 Alaska earthquakes, can

lead to extensive uncontrolled fires. The case study considered of the Cryostat T600 in case of failure may also have dramatic conseguences due fo example to the leaking of piping system that can diffuse Nitrogen and Argon gas inside the underground Hall B suffocating the persons inside.

Many researchers have investigated the dynamic behavior of liquid storage tanks both theoretically and experimentally. Investigations have been conducted to seek possible improvements in the design of such tanks to resist earthquakes. Intensive research on the subject started in the late 1940s in fields of aerospace technology. The emphasis of those studies was on the influence of the vibrational characteristics of liquid containers on the flight control system of space vehicles.

This chapter evaluates the earthquake design loads due to sloshing for the two horizontal cylindrical tanks filled with liquid Nitrogen and liquid Argon. Because the density of Argon ($\delta = 1.395 kg/lt$) is bigger than density of Nitrogen ($\delta = 0.808 kg/lt$), the worst case considered is for the tank filled with liquid Argon.

6.3 Literature review

The first pioneering work related to sloshing in tanks is presented from Housner (Housner, 1957) where no deformable vertical cylinder and rectangular tanks are considered. The effects of liquid-structure interaction and sloshing of the contained liquid were uncoupled by dividing the hydrodynamic pressure acting on the shell into two components: (1) the *impulsive pressure* caused by the portion of the liquid which is rigidly attached to the shell wall and accelerates with the tank, and (2) the *convective pressure* caused by the portion of the liquid sloshing in the tank. This approach is adopted by most of the design codes such as the API 650 standard provisions (American_Petroleum_Institute, 1995) and the EUROCODE (Eurocode, 1998). Since then, there has been a considerable amount of work on liquid sloshing and most of these studies are reported in the book of Ibrahim *et al.* (2005).

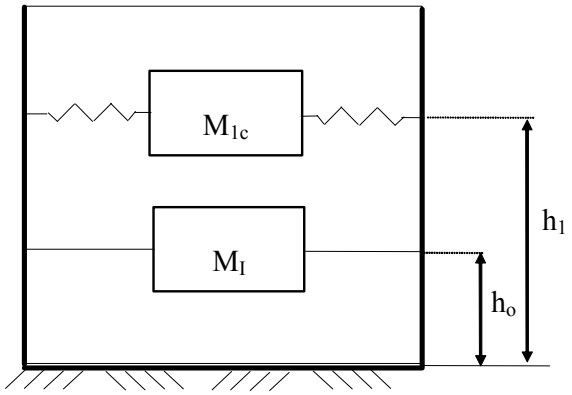

Figure 6.1 spring mass analogy for rigid tank (Housner, 1957)

Not many works can be found in literature about the seismic behavior of horizontal tanks and little attention is given to horizontal cylinder in tanks in API provisions.

So the following design procedure is taken from the paper of professor Karamanos (Karamanos *et al*. 2006), where an efficient and unified methodology for earthquake –induced sloshing analysis in horizontal cylinders under horizontal ground motion is considered. The method is based on modal analysis that provides sloshing frequencies and the corresponding sloshing masses, so that the liquid response and the total seismic force are readily calculated.

The excitation both in transversal and longitudinal direction is considered.

For the particular case of a horizontal cylinder tank under longitudinal excitation, the equivalence with an "appropriate rectangular tank" is applied, because results have been shown to be quite accurate both numerically and experimentally (Platyrrachos *et al.*, 2005, Kobayashi *et al.*, 1989).

6.4 Geometric properties of the horizontal cylindrical tanks

The horizontal cylinder tank considered (Figure 6.2) has a radius of R=1325mm and the longitudinal length is L=8500mm.

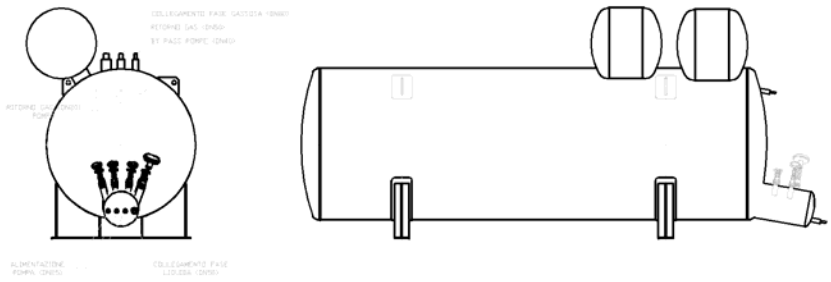

Figure 6.2 Geometry of the liquid tank

The ratio $L/R \approx 6.4 \le 10$, so it is reasonable to assume that the vessel wall is no deformable (rigid).

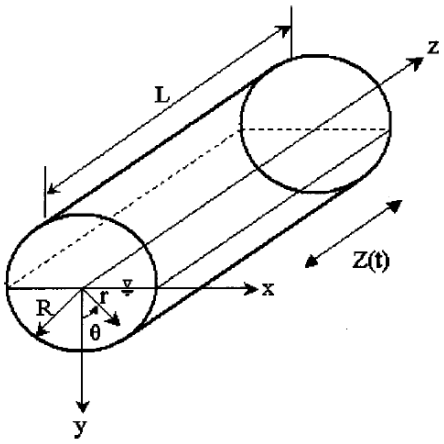

Figure 6.3 Configuration of horizontal cylinder liquid container

The total liquid mass of the container M_L can be considered as the sum of:

- The "impulsive mass" M_I which represents the mass that follows the container motion $X(t)$,
- The "convective" or "sloshing masses" M_{nc} (n=1,2,3…) which correspond to liquid motion due to free-surface elevation (convective motion).

The sum of all convective masses is referred to as "convective mass;

$$M_c = \sum_{n=1,2,3...}^{\infty} M_{nc} \tag{7.1}$$

During the seismic design procedure, the impulsive force M_I should comprise the inertia force of the container's shell mass M_{SH}, so that:

$$M_I = \left(M_L + M_{SH}\right) - \sum_{n=1,2,3...}^{\infty} M_{nc} = M_L + M_{SH} - M_C \qquad (7.2)$$

And the sum of M_{SH} and M_L is the total moving mass M_T of the container-liquid system.

6.5 Horizontal cylinder tank under transversal excitation

The sloshing frequency related to the first mode is computed according to Table 1 of the paper of Karamanos *et al.* (2006) and results are reported in Table 6-1 for 4 different liquid levels. The liquid mass and the container's shell mass are $M_L=31.85\times10^3$ kg, and $M_{SH}=10\times10^3$ kg, using a density of steel of 7800 kg/m^3.

Table 6-1 First mode sloshing frequency with respect to the liquid heights (Transversal direction)

H/R	$\omega_1^2 R/g$	ω_1 (rad/sec)	f_1 (Hz)	T_1 (sec)	S_a (g)
(1)	(2)	(3)	(4)	(5)	(6)
0.05	1.0000	2.7247	0.4339	2.3048	0.254
0.5	1.2985	3.1049	0.4944	2.0226	0.289
1.0	1.3557	3.1725	0.5052	1.9795	0.295
1.5	1.9215	3.7770	0.6014	1.6627	0.352
1.95	6.1519	6.7582	1.0761	0.9292	0.628

The sloshing mass ratio related to the first mode is reported in Table 6-2.

Table 6-2 Impulsive and convective mass for different liquid heights (transversal direction)

H/R	M_{1c}/M_L	M_I/M_L	M_L (10^3 Kg)	M_{1c} (10^3 Kg)	$M_I=M_{SH}+M_L-M_C$ (10^3 Kg)
(1)	(2)	(3)	(4)	(5)	(6)
0.05	1.00000	0.0000	0.416	0.416	10.000
0.5	0.87731	0.1182	12.673	11.118	11.497
1.0	0.56916	0.4054	32.437	18.462	23.151
1.5	0.20074	0.7587	52.201	10.479	49.604
1.95	0.03793	0.9406	64.458	2.445	70.629

Values in Table 6-2 show that when the cylinder is nearly full (H=1.95R), the entire mass responds impulsively and it follows the motion of the container and the sloshing effects are negligible. On the other hand, when the container is nearly empty (H=0.05R), the impulsive mass is only equal to the mass of the container`s shell and sloshing dominates liquid response. In all other cases mass is divided in an "impulsive" mass and a "convective" or "sloshing" mass. The sloshing mass ratio related to the higher modes are considerably smaller than the first sloshing mass ratio therefore for practical engineering purposes the estimates of the total sloshing force employ only the first sloshing mode. Typically the contribution of higher modes is less than 5% of the total.

Regarding direction of forces F_c and F_I, since all pressures on the container's wall are in the radial direction, the resultant forces always pass through the center of the container. The calculation of the maximum convective force $F_{C,MAX}$ is done using only the first mode:

$$F_{C,MAX} = M_{1C}\ddot{u}_{1,MAX} \tag{7.3}$$

Where $\ddot{u}_{1,MAX}$ corresponds to the spectral acceleration at the base of the tank. The maximum impulsive force is given by:

$$F_{I,MAX} = M_I a_{\max} \tag{7.4}$$

where a_{max} is the peak acceleration at the base of the tank. The Eurocode 8 elastic spectra under rock soil condition with a return period of 10000 yrs is considered for design (Figure 6.4). The peak ground acceleration considered is pga= 0.69g=6.77m/sec^2. The first natural period in the transversal direction of the steel frame with the horizontal cylindrical tank is T_0=1.18sec. Consequently the peak acceleration at the base of the tank is a_{max}=0.584g. The spectral accelerations at the base of the tank are evaluated, considering the response spectrum at the base of the tank that is assumed to have the same shape of the Eurocode 8 spectrum, but a peak acceleration of 0.584g (Figure 6.5). The spectral accelerations evaluated for the first sloshing frequency, but for different liquid levels are given in column 6 of Table 6-1.

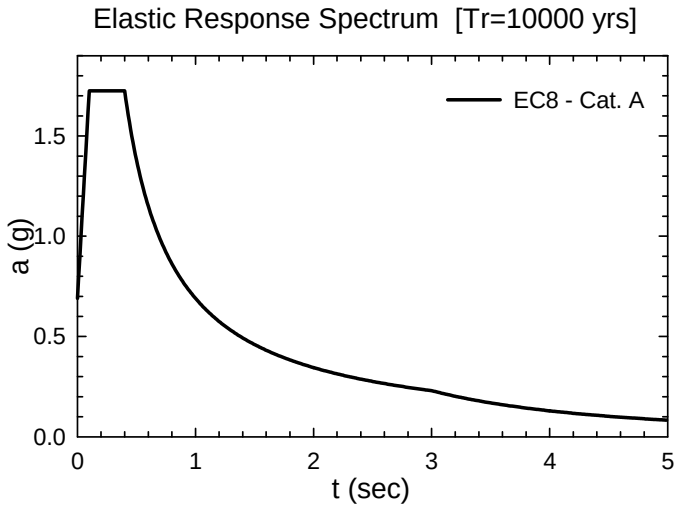

Figure 6.4 EC8 elastic response spectrum at the ground level

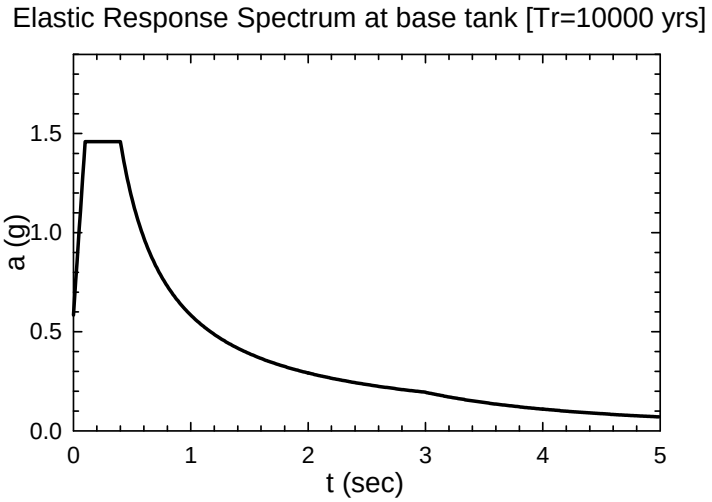

Figure 6.5 Response spectrum at the base of the cylindrical tank

For simplicity the seismic design force can be calculated through the SRSS combination as suggested by Eurocode 8:

$$F_D = \sqrt{\left(F_{I,MAX}\right)^2 + \left(F_{C,MAX}\right)^2} \tag{7.5}$$

Alternatively, the sum of the impulsive and convective maximum values, as suggested in API 650 can be employed.

$$F_D = F_{I,MAX} + F_{C,MAX} \tag{7.6}$$

Results of the design forces in the transversal direction are reported in Table 6-3.

Table 6-3 Impulsive, convective, total force and overturning moment in transversal direction for different positions of the liquid surface

H/R	$F_{I,MAX}$ (kN)	$F_{C,MAX}$ (kN)	F_D (kN) [EC8]	F_D (kN) [API 650]	M_D (kN*m) [EC8]	M_D (kN*m) [API]
(1)	(2)	(3)	(4)	(5)	(6)	(7)
0.05	57.23	1.03	57.24	58.27	75.56	76.91
0.5	65.80	31.50	72.95	97.30	96.30	128.44
1.0	132.50	53.36	142.84	185.86	188.55	245.34
1.5	283.89	36.13	286.18	320.02	377.76	422.42
1.95	404.23	15.05	404.51	419.27	533.95	553.44

The worst condition in the transversal direction is with full tank, because of the high values of the impulsive force.

6.6 Horizontal Cylinder tank under Longitudinal Excitation

There exist no analytical or numerical results for externally induced sloshing in the horizontal cylinder tank under excitation in the longitudinal direction. However it has been shown numerically and experimentally that the sloshing response is similar to the sloshing response of an *equivalent rectangular container*, which has the same free-surface dimensions with the cylindrical vessel, and contains the same liquid volume (Figure 6.6).

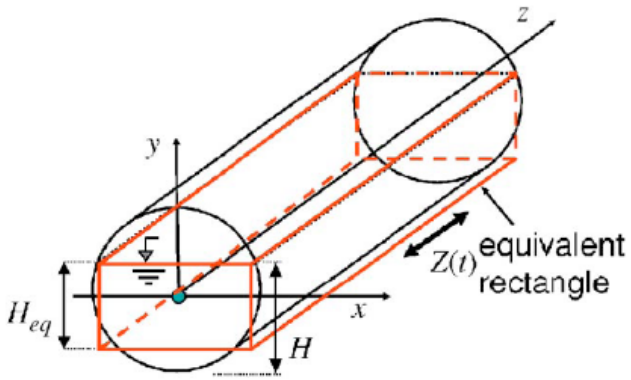

Figure 6.6 Equivalent rectangular container concepts to approximate the sloshing response of horizontal cylinders under longitudinal excitation

The liquid height H_{eq} of the equivalent rectangle can be easily computed using simple geometric considerations:

$$\frac{H_{eq}}{R} = \frac{1}{2}\left[\left(H/R - 1\right) + \frac{\sin^{-1}\left(H/R - 1\right) + \pi/2}{\sqrt{\left(H/R\right)\left(2 - H/R\right)}} \right] \tag{7.7}$$

According to sloshing solutions in rectangular container (Platyrrachos and Karamanos, 2005), the following closed form expressions can be used to calculate the sloshing frequencies and the corresponding convective masses:

$$\frac{\tilde{\omega}_p^2 R}{g} = \frac{(2p-1)\pi R}{L} \tanh\left[\frac{(2p-1)\pi H_{eq}}{L}\right]; \quad p = 1,2,3,\ldots \tag{7.8}$$

$$\frac{\tilde{M}_{pc}}{M_L} = \frac{8\tanh\left[(2p-1)\pi H_{eq}/L\right]}{\left(H_{eq}/L\right)\pi^2(2p-1)^3}; \quad p = 1,2,3,\ldots \tag{7.9}$$

The equivalent height and the sloshing frequency related to the first mode is computed according to equation (7.7) and (7.8) and values are reported in Table 6-4 for 4 different liquid levels. For containers with small values of $H_{eq}/L<0.1$ the following expressions for the sloshing frequencies and masses can be used:

$$\frac{\tilde{\omega}_p^2 R}{g} = \frac{(2p-1)^2 \pi^2 H_{eq}}{L}; \quad p = 1,2,3,\ldots \tag{7.10}$$

$$\frac{\tilde{M}_{pc}}{M_L} = \frac{8}{\pi^2(2p-1)}; \quad p = 1,2,3,\ldots \tag{7.11}$$

Table 6-4 First mode sloshing frequency with respect to the liquid height (Longitudinal direction)

H/R	H_{eq} (mm)	w_{eq} (mm)	$\omega_1 R/g$	ω_1 (rad/sec)	f_1 (Hz)	T_1 (sec)	S_a (g)
(1)	(2)	(3)	(4)	(5)	(6)	(7)	(8)
0.05	42.54	824.34	0.00766	0.24	0.04	26.33	0.099
0.5	467.46	2286.31	0.08338	0.79	0.13	7.98	0.099
1.0	1036.20	2640.00	0.17804	1.15	0.18	5.46	0.099
1.5	1925.54	2286.31	0.29818	1.49	0.24	4.22	0.099
1.95	6594.45	824.34	0.48021	1.89	0.30	3.33	0.159

The sloshing mass ratios related to the first mode calculated according to equation (7.9) are reported in Table 6-5.

Table 6-5 Impulsive and convective mass for different liquid heights (Longitudinal direction)

H/R	M_{1c}/M_L	M_L (10^3 Kg)	M_{1c} (10^3 Kg)	$M_T=M_{SH}+M_L$ (10^3 Kg)
(1)	(2)	(3)	(4)	(5)
0.05	2.54756	0.416	0.337	10.416
0.5	2.52274	12.673	10.283	22.673
1.0	2.43022	32.437	26.319	42.437
1.5	2.19026	52.201	42.356	62.201
1.95	1.02996	64.458	66.389	74.458

Recorded spectra are considered unreliable at periods in excess of about 4 sec. The considered tank have sloshing mode periods of vibration of up to 4 sec in the longitudinal direction and so the lack of reliability in the long period end of the spectra is of particular concern. Above 4 seconds, because of safety issues, a constant spectral acceleration has been considered equal to the spectral value at 4.22 seconds. Results of the design forces in the transversal direction are reported in Table 6-6.

Table 6-6 Impulsive, convective, total force and overturning moment in transversal direction for different positions of the liquid surface

	$F_{I,MAX}$ (kN)	$F_{C,MAX}$ (kN)	F_D (kN) [EC8]	F_D (kN) [API 650]	M_D (kN*m) [EC8]	M_D (kN*m) [API]
H=0.0R	59.61	0.01	59.61	59.62	78.69	78.70
H=0.5R	129.76	2.79	129.79	132.55	171.32	174.97
H=1.0R	242.88	15.22	243.35	258.09	321.22	340.68
H=1.5R	355.99	41.03	358.35	397.02	473.02	524.07
H=1.95R	426.14	103.41	438.51	**529.55**	578.83	**699.01**

The worst condition in the longitudinal direction is with full tank as in the transversal direction.

6.7 Horizontal Cylinder tank under Vertical Excitation

Under vertical excitation the sloshing is not expected to be the major problem, so it is possible to consider only the impulsive part of the seismic force.

6.8 Summary and conclusions

This chapter evaluates the earthquake forces (convective and impulsive) expressed in form of lateral forces and overturning moments that should be used to design the connections between the cylindrical tank and the steel service structure. Forces has been evaluated for the worst case when the cylindrical tank is filled with liquid Argon and different liquid heights has been considered.

The higher forces both in longitudinal and transversal directions are obtained when the tank is filled completely.

Chapter 7

7 Earthquake loads in the rectangular tank of Cryostat T600

7.1 Abstract

The seismic forces due to sloshing and impulsive motion have been evaluated also in the semi-module of T600 that from engineering point of view can be considered as a rectangular tank. The design procedure for rectangular tank is taken from the New Zealand report (1986) that is the base for ENV 1998-4. Overturning moments, lateral forces and pressures distributions on the walls have been evaluated both in the longitudinal and transversal direction. Hydrodynamic pressures generated on the roof of the tank due to sloshing have been evaluated following the procedure described in the paper of Malhotra (2005) that has been opportunely modified to be adapted to rectangular tank.

7.2 Introduction

In this section are determined the earthquake loads due to sloshing in rectangular tank using the procedure described in the New Zealand report (Priesley *et al*., 1986), that is the base for ENV 1998-4.

7.3 Pressure distributions along the walls

For tanks whose walls can be assumed as rigid, a solution of the Laplace equation for horizontal excitation can be obtained. The total pressure on the walls, perpendicular to the direction of motion, is given by the sum of an impulsive p_i and a convective p_c contribution:

$$p(z,t) = p_i(z,t) + p_c(z,t) \tag{7.1}$$

The impulsive components on the walls are given by:

$$p_i(z,t) = q_0(z)\rho L S_a(t) \tag{7.2}$$

where L is the half-width of the tank (Figure 7.1) in the direction of the seismic action, and the function $q_0(z)$ which is plotted in Figure 7.2 and Figure 7.3 as function of the geometric ratio H/L.

The maximum convective pressure on the walls in the first sloshing mode of vibration is:

$$p_{c1}(z) = q_1(z)\rho L S_a(T_1) \tag{7.3}$$

The dimensionless convective pressure functions for the first two sloshing modes are shown in Figure 7.4.

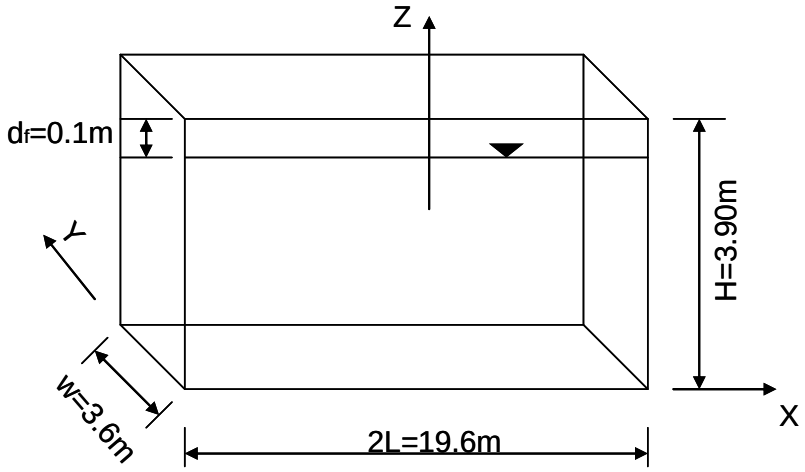

Figure 7.1 Nomenclature for rectangular tank

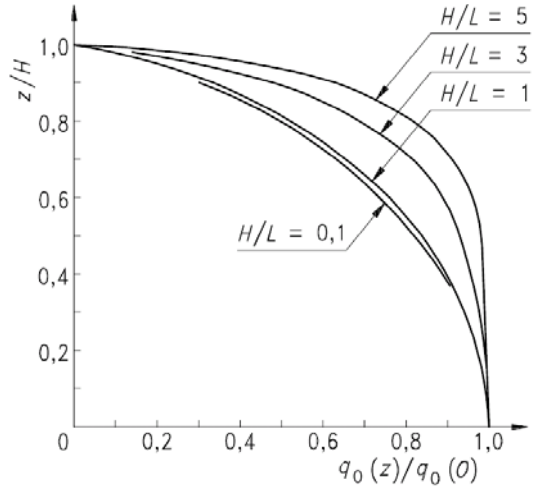

Figure 7.2 Dimensionless impulsive pressures on rectangular tank wall perpendicular to direction of earthquake (Priesley *et al.* , 1986)

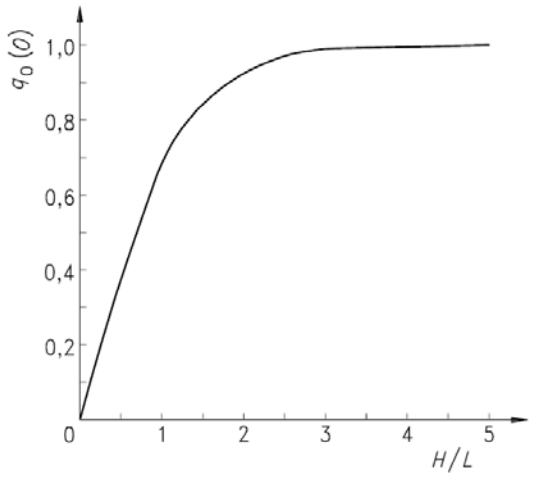

Figure 7.3 Peak values of dimensionless impulsive pressures on rectangular wall perpendicular to direction of earthquake (Priesley *et al.* , 1986)

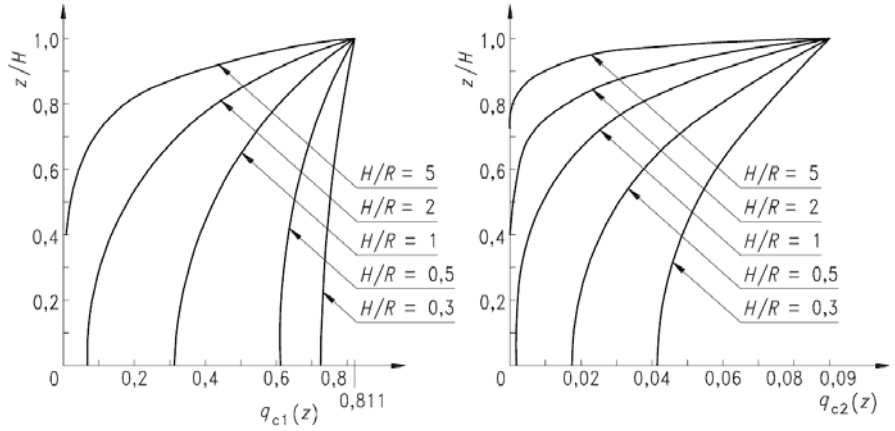

Figure 7.4 Dimensionless convective pressures on rectangular tank wall perpendicular to direction of earthquake (Priesley *et al.* , 1986)

The impulsive and convective pressures in the longitudinal direction are reported in Table 7-1 where $q_0(0)$=0.25 is obtained from Figure 7.3 when the ratio *H/L*=0.39:

Table 7-1 Impulsive and convective pressure distributions vs. high of the tank (earthquake in Longitudinal X Direction)

Z/H	Z (m)	$q_o(z)/q(0)$	$q_o(z)$	$p_o(z)$ (N/m^2)	$q_1(z)$	$p_1(z)$ (N/m^2)	$p(z)=p_o(z)+p_1(z)$ (N/m^2)
(1)	(2)	(3)	(4)	(5)	(6)	(7)	(8)
0	0.00	1.00	0.2500	351686.5	0.65	19158.5	196676.5
0.1	0.38	0.99	0.2475	348169.6	0.66	19453.3	195196.0
0.2	0.76	0.97	0.2425	341135.9	0.68	20042.8	192235.2
0.3	1.14	0.93	0.2325	327068.4	0.69	20337.5	185429.2
0.4	1.52	0.89	0.2225	313001.0	0.70	20632.3	178623.2
0.5	1.90	0.81	0.2025	284866.0	0.71	20927.0	164716.5
0.6	2.28	0.73	0.1825	256731.1	0.72	21221.8	150809.9
0.7	2.66	0.64	0.1600	225079.3	0.73	21516.5	135128.0
0.8	3.04	0.5	0.1250	175843.2	0.75	22106.0	110865.0
0.9	3.42	0.31	0.0775	109022.8	0.78	22990.2	78020.8
1.0	3.80	0.00	0.0000	0.0	0.80	23579.7	23579.7

The impulsive and convective pressures in the transversal direction are reported in Table 7-2 where $q_0(0)$=0.93 obtained from Figure 7.3 when the ratio is *H/L*=2.16:

Table 7-2 Impulsive and convective pressure distributions vs. high of the tank (earthquake in Transversal Y Direction)

Z/H	Z (m)	$q_o(z)/q(0)$	$q_o(z)$	$p_o(z)$ (N/m^2)	$q_1(z)$	$p_1(z)$ (N/m^2)	$p(z)=p_o(z)+p_1(z)$ (N/m^2)
(1)	(2)	(3)	(4)	(5)	(6)	(7)	(8)
0.0	0.00	1.00	0.93	240295.2	0.07	1274.7	122566.5
0.1	0.38	0.99	0.9207	237892.2	0.08	1456.8	121535.7
0.2	0.76	0.98	0.9114	235489.3	0.09	1638.9	120504.9

0.3	1.14	0.95	0.8835	228280.4	0.1	1821.0	117048.2
0.4	1.52	0.92	0.8556	221071.6	0.13	2367.3	113955.8
0.5	1.90	0.88	0.8184	211459.7	0.16	2913.6	109650.4
0.6	2.28	0.83	0.7719	199445.0	0.24	4370.3	105042.6
0.7	2.66	0.73	0.6789	175415.5	0.31	5645.0	94188.1
0.8	3.04	0.59	0.5487	141774.1	0.43	7830.2	79392.4
0.9	3.42	0.40	0.372	96118.1	0.59	10743.8	59260.5
1.0	3.80	0.00	0.00	0.0	0.80	14567.8	14567.8

In Figure 7.5 are compared the heightwise pressure distribution along the wall of the rectangular tank for the case when the earthquake shakes in the longitudinal and transversal direction.

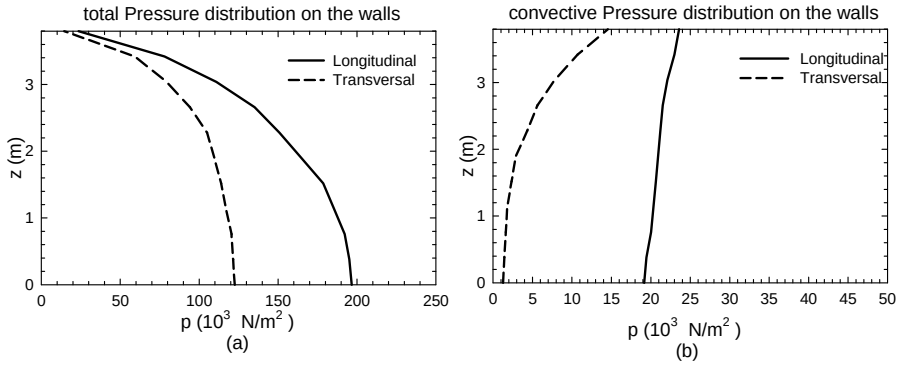

Figure 7.5 (a)Total and convenctive (b) maximum pressure distributions on the walls of the rectangular tank of the T600 module for earthquake in X and Y direction

7.4 Rectangular tank under longitudinal excitation

The values of the sloshing frequencies, the masses and equivalent heights are calculated according to the ENV 1998-4. The sloshing frequency associated to the first mode is given by the following equation (ENV 1998-4 A.45):

$$T_1 = 2\pi \left(\frac{L/g}{\frac{\pi}{2}\tanh\left(\frac{\pi}{2}\cdot\frac{H}{L}\right)} \right)^{\frac{1}{2}}; \tag{7.4}$$

The values of the first sloshing frequency and the respective spectral accelerations for the two different hazard levels considered are shown in Table 7-3, assuming that there is no confinement effect due to the roof. Due to the presence of the roof the sloshing frequencies increase and consequentialy also spectral acceleration increase. The new sloshing frequencies and spectral acceleration are evaluated according to the procedure described in section 7.6, while results are shown in Table 7-3.

Table 7-3 First mode sloshing frequency with respect to the liquid heights (Longitudinal directions)

H/L	f_{1C} (Hz)	T_{1C} (sec)	S_a (g) Tr=475 yrs	S_a (g) Tr=10000 yrs	$T_{1C,MOD}$ (sec)	$S_{a,MOD}$ (g) Tr=475 yrs	$S_{a,MOD}$ (g) Tr=10000 yrs
0.4	0.147	6.799	0.01	0.03	3.07	0.08	0.22

The first natural period of the semi-module T300 is approximately calculated knowing the mass of the container (M=7.35E+6 kg), the impulsive liquid and the horizontal stiffness of the bearings and it is T_0= 2.41sec. The lateral stiffness of the rubber bearings have a coefficient of uncertainties of 10%, so the upper and lower bound of the natural period are T_0=2.29sec. and T_0=2.54 sec. Inside this range of the natural period spectral accelerations range between 0.27 and

0.30g for an earthquake with return period of 10000 yrs. The impulsive masses, convective masses, and equivalent heights are given by the graph associated with vertical cylinder tanks, given in ENV 1998-4. The sloshing mass ratio related to the impulsive part and to the convective part (first mode) is reported in Table 7-4.

Table 7-4 Impulsive and convective mass (longitudinal direction X)

H/L	M_{1c}/M_L	M_0/M_L	M_L (Kg)	M_0 (Kg)	M_{1c} (Kg)	$M_{0,\,mod}$ (Kg)	$M_{1c,\,mod}$ (Kg)
0.4	0.70	0.220	360000	8081.6	25714.3	24396.9	9399.0

Because the actual freeboard d in the longitudinal direction is smaller than the required freeboard d_f, the constraint on the sloshing motion increases the mass participation in the impulsive mode and reduces the mass participation in the convective mode. For this reasons, values of impulsive and convective masses have been modified as shown in Table 7-4, according to Equation (7.15) and Equation (7.16) to consider the effect of containment of the roof of the tank as described in next section 7.6. The calculation of the maximum impulsive Base shear $Q_{0,MAX}$ and the maximum convective Base shear $Q_{C,MAX}$ is done using only the first mode.

$$Q_{0,MAX} = M_0 S_a\left(T_0\right) g \tag{7.5}$$

$$Q_{1c,MAX} = M_{1c} S_a\left(T_1\right) g \tag{7.6}$$

The calculation of the maximum impulsive Moment above the base $M_{0,MAX}$ and the maximum convective Moment above the base $M_{C,MAX}$ is done using only the first mode.

$$M_{0,MAX} = M_0 S_a\left(T_0\right) g \cdot h_0 \tag{7.7}$$

$$M_{1c,MAX} = M_{1c} S_a\left(T_1\right) g \cdot h_1 \tag{7.8}$$

Analogously, the calculation of the maximum impulsive Moment below the base $M'_{0,MAX}$ and the maximum convective Moment above the base $M'_{C,MAX}$ is done using only the first mode.

$$M'_{0,MAX} = M_0 S_a(T_0)\, g \cdot h'_0 \tag{7.9}$$

$$M'_{1c,MAX} = M_{1c} S_a(T_1)\, g \cdot h'_1 \tag{7.10}$$

The equivalent heights to evaluate moments are given

Table 7-5 Equivalent height (Longitudinal Direction)

H/L	h_0/H	h_1/H	h_o (m)	h_1 (m)	h'_0/H	h'_1/H	h'_o (m)	h'_1 (m)
0.4	0.4	0.55	1.52	2.09	1.85	1.85	7.03	7.03

The maximum base shear and moments are shown in Table 7-6.

Table 7-6 Impulsive, Convective Base shears and Moments (Longitudinal Direction)

H/L	$Q_{0,MAX}$ (kN)	$Q_{1c,MAX}$ (kN)	Q_{MAX} (kN) [EC8]	Q_{MAX} (kN) [API]	$M_{0,MAX}$ (kN*m)	$M_{1,MAX}$ (kN*m)	M_{MAX} (kN*m) [EC8]	M_{MAX} (kN*m) [API]
0.4	693.4	202.6	722.4	896.0	1053.9	423.5	1135.8	1477.4

7.5 Rectangular tank under transversal excitation

The procedure is analogous at the longitudinal direction. The values of the first sloshing frequency and the respective spectral accelerations for the two different hazard levels considered are shown in Table 7-7.

Table 7-7 First mode sloshing frequency (Transversal Direction)

H/L	f_{1C} (Hz)	T_{1C} (sec)	S_a (g) Tr=475 yrs	S_a (g) Tr=10000 yrs	$T_{1C,MOD}$ (sec)	$S_{a,MOD}$ (g) Tr=475 yrs	$S_{a,MOD}$ (g) Tr=10000 yrs
2.1	0.465	2.1508	0.11	0.30	0.93	0.28	0.74

The natural period of the base isolated tank ranges between T_0=2.29sec. and T_0=2.54 sec. Inside this range of the natural period the spectral accelerations range between S_a=0.27 and 0.30g for an earthquake with return period of 10000 yrs, while for an earthquake with return period of 475 yrs the return period ranges between S_a=0.10 and 0.11g.

The impulsive masses, convective masses, and equivalent heights are given by the graph associated with vertical cylinder tanks, given in ENV 1998-4. The sloshing mass ratio related to the impulsive part and to the convective part (first mode) is reported in Table 7-8, together with the modified value of masses, because also in the transversal direction the actual *d* is smaller than the required freeboard d_f:

Table 7-8 Impulsive and convective mass (Transversal direction)

H/L	M_{1c}/M_L	M_0/M_L	M_L (Kg)	M_0 (Kg)	M_{1c} (Kg)	$M_{0,\,mod}$ (Kg)	$M_{1c,\,mod}$ (Kg)
2.1	0.23	0.76	360000	27918.4	8449.0	34020.4	2346.9

The equivalent heights to evaluate moments are given in Table 7-9:

Table 7-9 Equivalent height (Transversal direction)

H/L	h_0/H	h_1/H	h_o (m)	h_1 (m)	h'_0/H	h'_1/H	h'_o (m)	h'_1 (m)
2.1	0.43	0.75	1.63	2.85	0.5	0.75	1.9	2.85

The maximum base shear and moments are shown in Table 7-10.

Table 7-10 Impulsive, Convective base shear and Moments (Transversal Direction)

H/L	$Q_{0,MAX}$ (kN)	$Q_{1c,MAX}$ (kN)	Q_{MAX} (kN) [EC8]	Q_{MAX} (kN) [API]	$M_{0,MAX}$ (kN*m)	$M_{1,MAX}$ (kN*m)	M_{MAX} (kN*m) [EC8]	M_{MAX} (kN*m) [API]
2.1	793.4	612.7	1002.5	1406.2	1296.5	1746.3	2174.9	3042.7

7.6 Simplified approach to evaluate roof pressures due to sloshing

During an earthquake, sloshing waves are generated inside a tank. When the actual freeboard d_f is less than the maximum height d of the convective (sloshing) waves, hydrodynamic pressures will be exerted on the roof.

The estimation of these pressures requires the solution of a complex non-linear wave problem that involves geometric parameters such as the slope of the roof and the height of the roof above the liquid surface. A simplified approach to evaluate the maximum vertical displacement of the convective sloshing wave from the at-rest level of the liquid for rectangular tanks is given by:

$$d = L \cdot \frac{S_a(T_1)}{g} \tag{7.11}$$

where L is half the length of the tank in the direction of the earthquake and S_a is the spectral acceleration at the first sloshing frequency for a given response or design spectrums. In Eurocode 8 equation (7.11) is modified with a reduction coefficient of 0.84, which is the participation factor of the first sloshing mode (Eurocode 8, 1998). For a horizontal acceleration of $S_a(T_1)$, the free-surface of the liquid is still at an angle θ from the horizontal. However, a portion of the tank roof is wetted, as seen in Figure 7.6. The wetted width x_f of the tank roof (Figure 7.6) can be determined by simple geometric considerations by equating

the volume of the empty space in the tank to the volume of the empty space at rest (Malhotra, 2005). This gives the following:

$$\frac{x_f}{L} = 2\left(1 - \sqrt{\frac{d_f}{d}}\right) \tag{7.12}$$

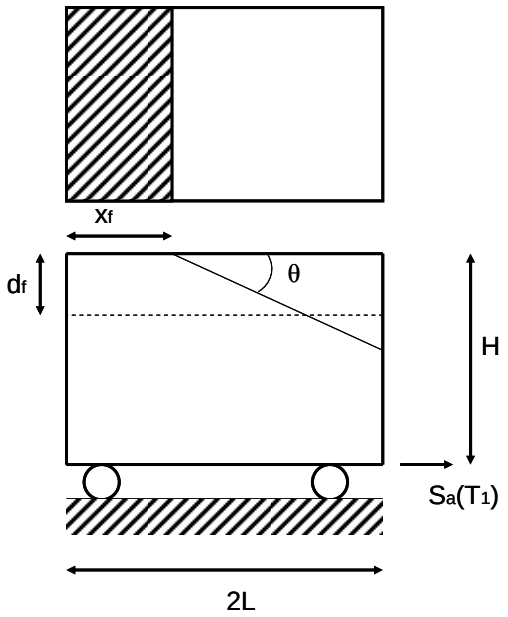

Figure 7.6 Liquid filled tank translating with an acceleration $S_a(T_1)$ and with insufficient free board

Figure 7.7 shows the normalized wetted width x_f/L vs. the normalized freeboard d_f/d. It is important to mention that in this formulation the amplification of roof pressure due to the dynamic response of the tank roof has not been considered. The maximum upward pressure on the tank roof due to sloshing wave is:

$$P_{MAX} = \rho g x_f \tan(\theta) \tag{7.13}$$

The upward force on the roof is resisted by the vertical tensile force in the shell. The connection between the shell and the roof should be designed to transfer this force.

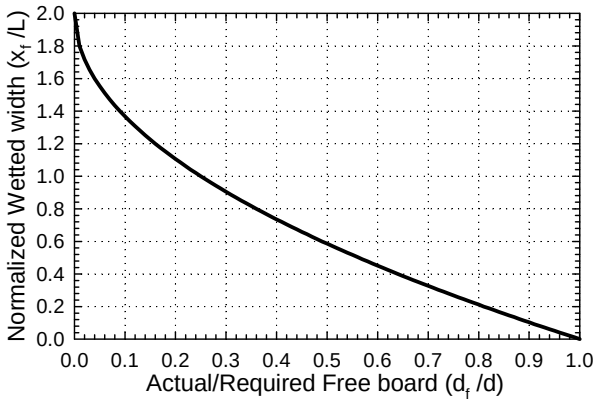

Figure 7.7 Normalized wetted width for rectangular tank roof, x_f/L as a function of actual /required free-board, (d_f/d)

If x_f is small compared to L, the total force per unit length of rectangular tank may be approximated as follows:

$$F_{MAX} = \frac{1}{2} P_{MAX} x_f = \frac{1}{2} \rho g x_f^2 \tan(\theta) = \frac{1}{2} \rho x_f^2 S_a(T_1) \tag{7.14}$$

where F_{MAX} is the force for unit length of rectangular tank. Equation (7.14) assumes that the upward force is resisted by the wet side of the tank shell only. This is not a good assumption when x_f /L is greater than 0.5. In this case F_{MAX} should then be estimated from more accurate static force-equilibrium analysis

of the tank roof. The constraint on the sloshing motion increases the mass participation in the impulsive mode. In the limiting case, if the freeboard is reduced to zero, the entire liquid in the tank becomes impulsive. Therefore, the smaller the actual/required freeboard d_f/d, the smaller the convective mass and the larger the impulsive mass. Assuming that the convective mass reduces linearly from m_c to *0* as d_f/d reduces from 1 to 0, the adjusted values of the impulsive and convective masses are:

$$\bar{m}_i = \begin{cases} m_i + m_c \times \left(1 - \dfrac{d_f}{d}\right) & \text{for } d_f < d \\ m_i & \text{for } d_f \geq d \end{cases} \tag{7.15}$$

$$\bar{m}_c = \begin{cases} m_c \times \dfrac{d_f}{d} & \text{for } d_f < d \\ m_c & \text{for } d_f \geq d \end{cases} \tag{7.16}$$

For tanks with insufficient freeboard, masses $\bar{m}_i$ and $\bar{m}_c$ should be used instead of m_i and m_c to compute the impulsive and convective periods, respectively. Based on the new convective period, equations (7.11) to (7.14) should be recalculated to obtain the maximum force applied on the roof due to sloshing.

Applying equation (7.11) the maximum wave height is 27 cm in the longitudinal direction and 36 cm in the transversal direction, so in both cases the roof is touched by the sloshing wave, so uplift pressures are generated. From equation (7.12) a wetted width of 15.38m are determined in the longitudinal direction and 2.61m in the transversal direction after confinement effects are considered. These results are in agreement with the result obtained in the finite element model in section 4, e.g. observing Figure 4.19, Figure 4.24.

Due to cointainement effects the first sloshing frequency changes and the period shift to the left from 6.80 sec to 3.07 sec in the longitudinal direction while for transversal direction the period shift from 2.15 sec to 0.93 sec. it is

important to mention that this approximated results are obtained with the approximated equation (7.4). The maximum upward pressures and the maximum upward forces for both directions are shown in the following table:

Table 7-11 Maximum upward pressure and total force in the roof evaluated with simplified approach

DIR	P_{MAX} (kPa)	F_{MAX} (kN)	X_f (m)
X long.	33.15	254.95	15.38
Y transv	18.95	24.77	2.61

7.7 Summary and conclusions

In this section are determined the earthquake loads due to sloshing in rectangular tank using the procedure described in the New Zealand report (Prisley *et al*., 1986), that is the base for ENV 1998-4, while the upward pressure on th roof are determined using a simplified approach proposed by Malhotra.

Chapter 8

8 Seismic performance of T600 piping system

8.1 Abstract

The goal of this chapter is to identify location and type of bracing connection for the piping system of T600 module. The type of seismic qualification requirements and the type of seismic braces (cable and solid) are described.

Different types of seismic interactions are also described, and a final pipe support arrangement is proposed.

8.2 Introduction

The behavior of piping systems during earthquakes has been not enough investigated. The improper bracing of systems, the use of non ductile components and the lack of understanding of the behavior of these systems have all contributed to the poor performance of piping systems during past earthquakes.

The damage of pipeline system in ICARUS T600 module has as consequences economic losses due to repair and replacement with consequent downtime of the experiment, but also casualties losses because the leaking of

piping system can diffuse Nitrogen and Argon in gas state inside the underground Hall B and they can suffocate the persons inside. So in order to ensure the correct behavior pipelines should be properly anchored.

8.3 Literature review

Very little research has been done on entire piping systems. One of the few studies that did deal with an entire system was performed at the University of California Berkeley. There, researchers completed a study of two alternative seismic restraints to snubbers, which are commonly used in nuclear power plants (Nims 1991). The research objectives were to find an alternative seismic restraint device that did not have the maintenance problems and associated costs of the snubbers, and study the effects of the new devices on pipe forces, stresses and behavior.

Researchers found that the high frequencies did influence the piping and devices where they attached to the frames. The seismic restraints were also found to introduce high frequencies into the piping system.

In 1999, Tauby et al. published a practical guide to seismic restraint. The authors of this guide give design and analysis examples of all types of seismic restraint (Tauby et al. 1999).

8.4 Seismic Qualification requirements

The seismic qualification requirements differ depending on the seismic function of the piping system that are defined as: *operability*, *leak tightness*, or *position retention*.

1. *Operability* is defined as the ability of a piping system to deliver and control flow during or after an earthquake.

2. *Leak tightness* is the ability of a piping system to not leak during and after an earthquake.

3. *Position retention* is the ability of a piping system not to fall or collapse in the case of earthquake.

In the following sections are described the three functionality levels of the piping system.

8.4.1 Operability

The seismic qualification of piping systems that must remain operable during or following the design basis earthquake must be established by static or dynamic analysis or by testing. At each point along the piping system model, the output from the seismic analysis consists of loads (forces and moments), total longitudinal stress (Equation (8.1)), displacements and rotations, and loads on support, restraints and equipment nozzles. Some software can also provide acceleration at every point.

The seismic qualification of piping systems for operability must demonstrate the seismic adequacy of the piping itself, the pipe supports and their attachment to the building structure, and the equipment and components within the scope of seismic qualification. In summary the extend of seismic qualification depends function, as illustrated in Table 8-1.

Table 8-1 Seismic qualification requirements

Criterion	Operability	Leak Tight NPS>5cm PSA>0.3g	Leak Tight NPS<5cm PSA≤0.3g	Position retention
Pipe stress	Y	Y	N	Sway bracing[2]
Mech. Joint	Y	Y	Y	N
Eq`t. Anchored	Y	Y	Y	Y
Eq`t. operable	Y		N	N
Restraints	Y	Y	Y	Y
Interactions	Y	Y	Y	Y

Pipe Stress - The elastically calculated longitudinal stresses due to the *design basis earthquake*, calculated by static or dynamic analysis, and the concurrent sustained operating loads should comply with the following equation

$$\frac{PD}{4t} + 0.75i\frac{\left(M_w + M_s\right)}{Z} \le 1.5S_Y \tag{8.1}$$

where:

P= normal operating pressure

D= pipe outer diameter

t=nominal pipe wall thickness

i=stress intensity factor

M_w=resultant moment due to weight

M_S=resultant seismic moment amplitude (inertia and anchor motion)

[2] Sway bracing: the selection and placement of lateral and longitudinal restraints (braces) to brace the pipe against excessive lateral and longitudinal movement during a design basis earthquake.

Z=pipe section modulus
S_Y= minimum specified material yield stress at operating temperature

When the elastic longitudinal stress limit of 1.5 S_Y can not be met, the piping system may be qualified by more detailed analysis techniques (WRC379, 1993).

Active Equipment - The operability of active equipment[3] during or following the design basis earthquake may be established by testing, analysis where applicable, or by similarity of earthquake experience as defined in seismic qualification standards.

Static Equipment - The adequacy of static equipment[4] should be established in accordance with the applicable design and construction code, such as the ASME Boiler and Pressure Vessel Code for pressure vessels, API 650 for oil storage tanks, and AWWA D100 for water storage tanks.

Pipe and Equipment Restraints - Seismic qualification must establish the seismic adequacy of pipe supports and restraints and their attachment to the building structure. The seismic load on each pipe support and restraint should be calculated by seismic static or dynamic analysis, and their seismic adequacy must be determined in accordance with a structural design and construction code.

[3] *Active equipment* is defined as mechanical or electrical equipment or components that must perform an active function (involving moving parts or signals) during or following the design basis earthquake. Examples of active mechanical equipment include valve operators, pumps, compressors, etc. that must change state (open, close, start-up, shutdown, throttle, etc.) during or following the earthquake.

[4] *Static equipment* is defined as mechanical equipment or component that does not perform an active function (involving moving parts) during or following the design basis earthquake. Examples of static equipment include storage tanks, pressure vessels, heat exchangers, and manual valves.

8.4.2 Leak tightness

The requirements for seismic qualification of piping systems that must remain leak tight during or following the design basis earthquake vary with pipe size and the magnitude of seismic input (Table 8-1). For pipe larger than 5cm nominal pipe size (NPS) and for a design basis earthquake with a peak spectral acceleration (PSA) larger than 0.3g, it is recommended that the seismic design and retrofit requirements for leak tightness be identical to the operability requirements of section 8.4.1, except for the operability requirements of active equipment, which are not applicable. For piping 5cm NFS and smaller, or where the PSA is below 0.3g, the position retention rules of 8.4.3 may apply for leak tightness, with the additional requirement that the loads imposed on non-welded and non-flanged pipe joints (for example swage fittings, groove couplings, etc.) be within vendor limits.

8.4.3 Position retention

Pipe Stress - The seismic qualification of piping systems that must retain their position, but need not be leak tight or perform a function, may be established by sway bracing following standard support and restraint spacing criteria.

One possible spacing criterion consists in spacing weight supports in accordance with the support spacing reproduced in Table 8-2, and placing a lateral seismic support approximately every 12.2m and a longitudinal support approximately every 24.4 m. A lateral support within 61cm of an elbow or bend may provide longitudinal seismic restraint to the pipe run passed the elbow or bend.

Table 8-2 Spacing of weight supports

NPS (cm)	Water (m)	Gas (m)
2.5	2.1	2.7
5.1	3.0	4.0
7.6	3.7	4.6
10.2	4.3	5.2
15.2	5.2	6.4
20.3	5.8	7.3
30.5	7.0	9.1
40.6	8.2	10.7
50.8	9.1	11.9
61.0	9.8	12.8

The seismic load on each pipe support should be calculated by seismic static or dynamic analysis, and the seismic adequacy of supports and anchorage for position retention should be demonstrated with a safety factor of 2 or more against failure modes that could cause loss of position. Permanent deformation of supports is acceptable in this case, provided it does not cause the pipe to disengage and fall off.

8.4.4 Material conditions

The seismic retrofit of existing piping systems should take into account the material condition of the system. Where corrosion or environmental cracking are suspected, the piping should be inspected by non-destructive volumetric techniques. The quality of construction and the maintenance condition of the system should be inspected in the field, and the maintenance record of equipment and components should be investigated with the facility engineer to assess their adequacy, operability and structural integrity.

8.5 Seismic bracing

In order for piping systems to withstand the code derived forces, seismic restraints must be designed to absorb the required force demands. The following sections briefly describe the types of restraints used on piping systems. The two primary types of seismic restraints (also referred to as bracing) for piping systems are *cable* and *solid braces*. Both types have a vertical hanger rod (also referred to as support rod) and both limit the lateral deflection of the pipe.

8.5.1 Cable Restraints

Cable bracing restrains the deflection of the pipe by utilizing cables that take tension only. Since the cables take only tension, two cables are necessary to brace the pipe. The cable is generally some kind of prestretched high strength cable (Figure 8.1).

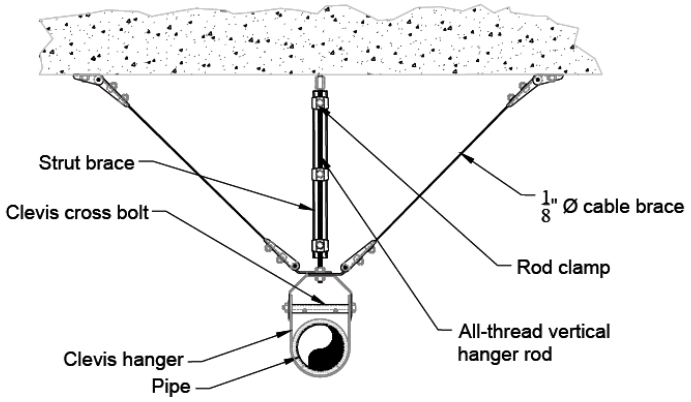

Figure 8.1 Typical Transverse cable brace

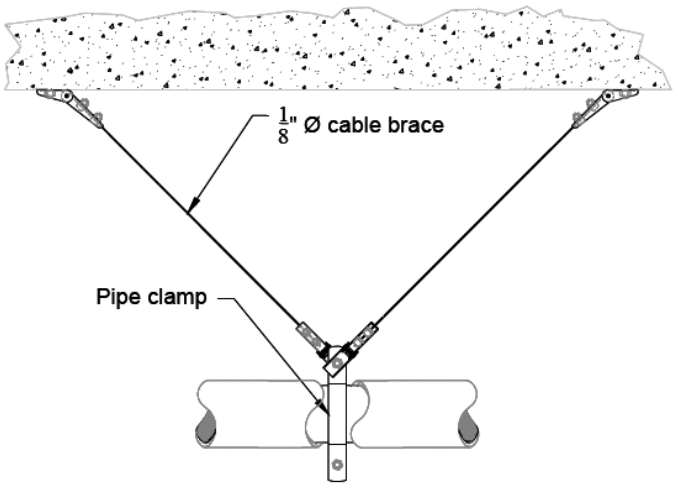

Figure 8.2 Typical longitudinal cable brace

In a seismic event, cable bracing causes the vertical support rod to be in compression, regardless of the direction of the seismic force (Lama, 1998). This may cause the vertical support rod to buckle. Bracing manufacturers require an angle or strut to be clamped to the vertical hanger rod to prevent buckling. The clamps combined with the angle or strut reduces the unbraced length of the vertical hanger rod thereby increasing the compression capacity of the rod. Since the cables do not take compression, a hook may be used to connect the brace to the clevis. Hooking devices cannot be used on solid seismic bracing due to the fact that the solid cable brace, when in compression could break the hook free. Another distinct advantage of cable bracing is that the cables can be cut to the approximate length and adjusted easily during installation.

A typical longitudinal brace is shown in Figure 8.2. It requires a pipe clamp and a disruption in the insulation, bu does not require a vertical hanger rod. A longitudinal brace should be located within 4 in (102mm) of a hanger rod to prevent uplift due to horizontal seismic loads (Lama, 1998). An advantage of transversal brace respect to longitudinal brace is that it does not require

disruption in the insulation (Figure 8.1), but it requires a clevis (Figure 8.3) and a vertical hanger rod.

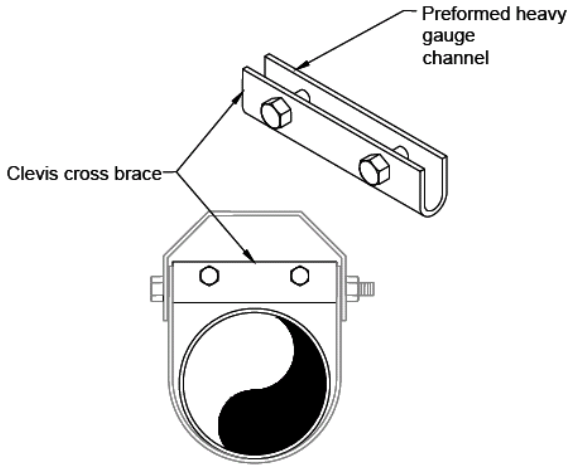

Figure 8.3 Clevis cross brace

8.5.2 Solid Restraints

Solid bracing consists of a single steel member, generally an angle or 12 gauge channel strut, installed at the hanger rod connection to the system up to the structure at an angle between 30 and 60 degrees from horizontal. One advantage of this system is that it needs access to the structure on only one side (Figure 8.4).

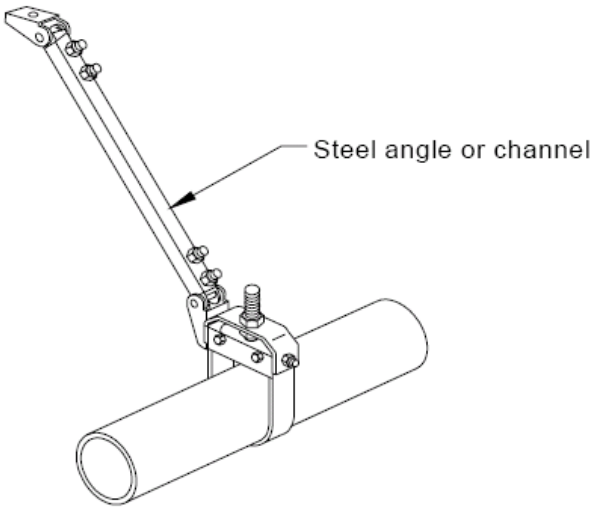

Figure 8.4 Typical Transverse solid brace

There are two disadvantages to using solid bracing. First, the length of the brace must be limited in order to effectively resist compression loads without buckling. Also, when the solid brace is in compression, the support rod is forced into tension. This tension may cause pullout failure at the connection point, and is most crucial when support rods are anchored to concrete slabs (Lama, 1998).

8.5.3 Wall and Floor Penetrations as Brace Locations

Wall and floor penetrations might be appropriate brace locations for ductwork, but piping generates much higher loads in a more concentrated area which may damage most walls. Light framed walls required for area separation, smoke barriers or other fire or life safety related functions should not be used to

brace piping. In all other cases, the structural engineer of record should determine if a wall may act as a sway brace for piping (Tauby et al. 1999).

8.6 Piping system description

The system consists of three pumps located in the ground (Figure 8.5) and two cylindrical tanks of mass respectively 41.85×10^3 kg and 28.45×10^3 kg that are positioned on the service structure and they are connected through piping system to the pumps.

A layout of the geometry of the piping system is shown in Figure 8.6 and Figure 8.7 that show the elevation views in the longitudinal and transversal direction of the system.

Piping and cylindrical tanks rest on distinct structural systems, therefore relative displacements due to different seismic movements between the service structure and the floor of the gallery shall be accounted.

According to ENV 1998-4 paragraph 3.4.1.2, in order to guarantee serviceability limit states, if accurate analysis are not made, a minimum value of imposed relative displacement between the first anchoring point and the tank will be assumed:

$$\Delta = \gamma_1 \frac{x d_g}{500} \tag{8.2}$$

where x is the distance between the anchoring point and the point of connection with the tank, and d_g is the maximum floor displacement (in m units).

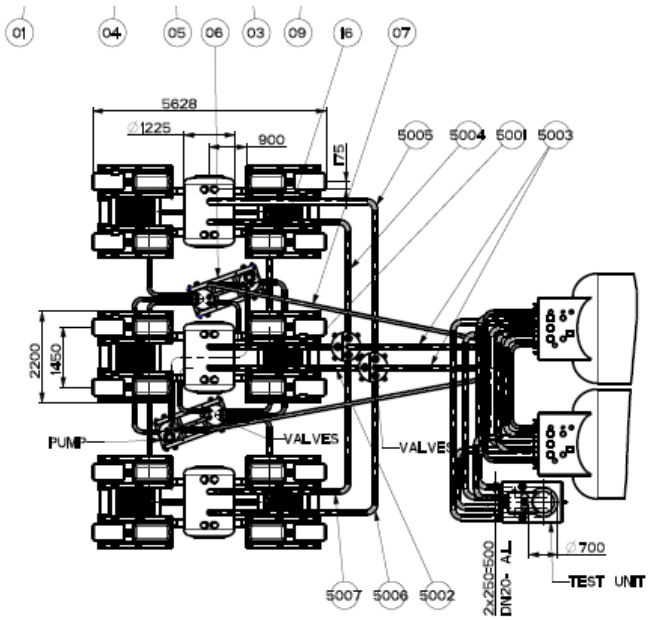

Figure 8.5 Plan view of the pipeline system connecting pumps with cylindrical tanks

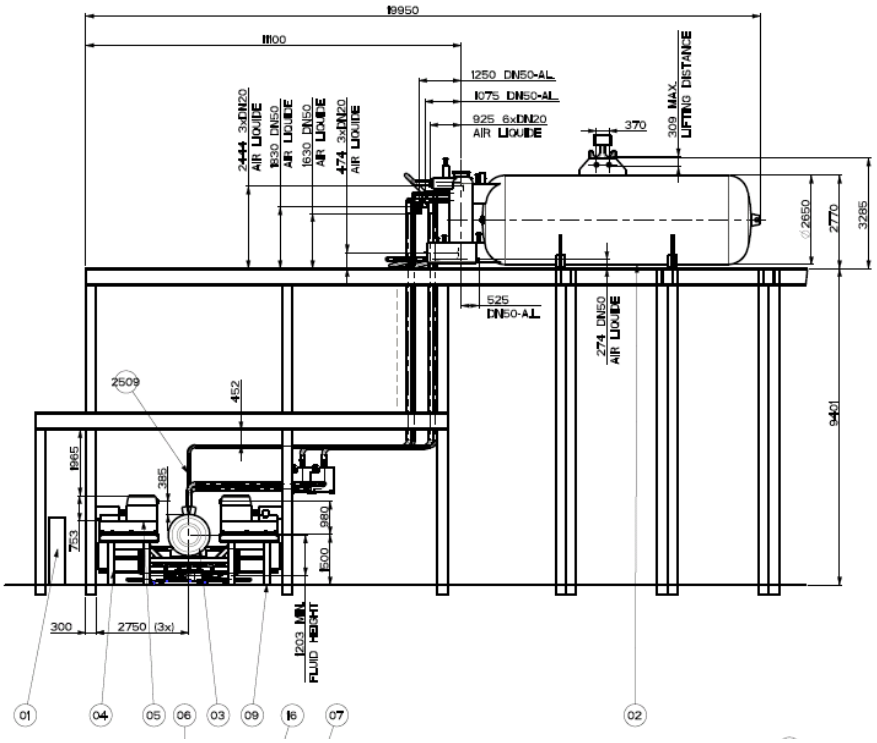

Figure 8.6 Elevation view of of the pipeline system set up connecting pumps with cylindrical tanks

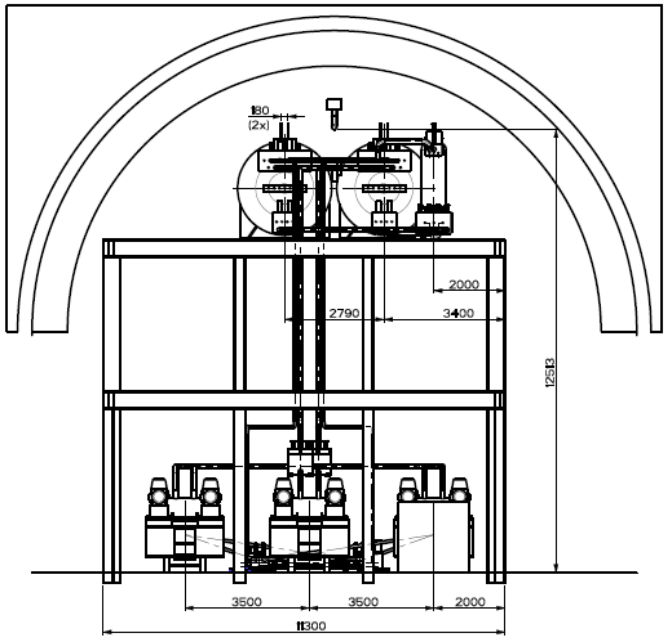

Figure 8.7 Transversal elevation view of of the pipeline system set up connecting pumps with cylindrical tanks

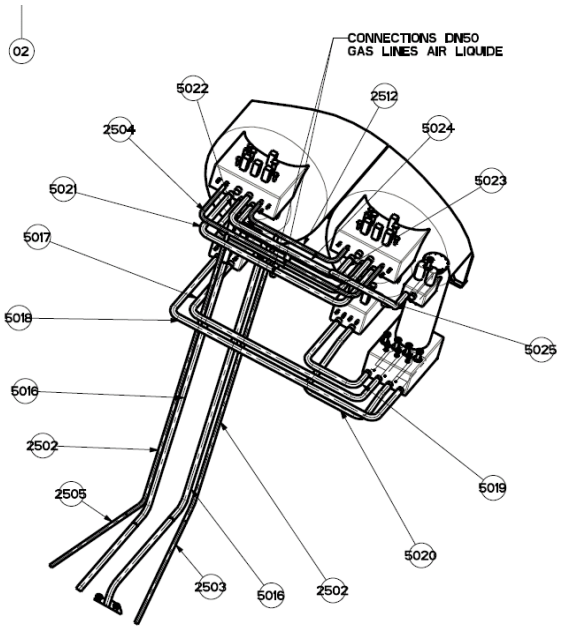

Figure 8.8 Details of the connections of gas line AIR LIQUIDE

8.6.1 Seismic input

The seismic input excitation defined in chapter 5 is applied to the numerical model in SAP2000 both in horizontal and vertical direction. Both horizontal direction in X and Y were considered. Nonlinear time history analysis were performed. Displacement response of the time history analysis are shown in section 2.4.

8.6.2 Seismic restraint adopted

The braces used for the seismic retrofit of the pipeline system of T600 are cable style braces shown in Figure 8.9. These braces connect the piping assembly to the steel frame of the services and provide vertical support both in the longitudinal and transverse directions. The location of the brace points and the hanger points should be determined when the preliminary design of the piping system is complete.

The cable consists of 3.175 mm diameter prestreched galvanized 7×19 aircraft grade steel.

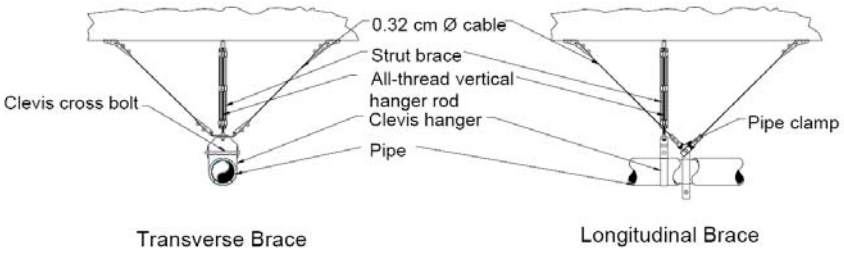

Figure 8.9 Typical brace details

Figure 8.10 shows the lateral view of the piping system with mark in red the postion of the restraints.

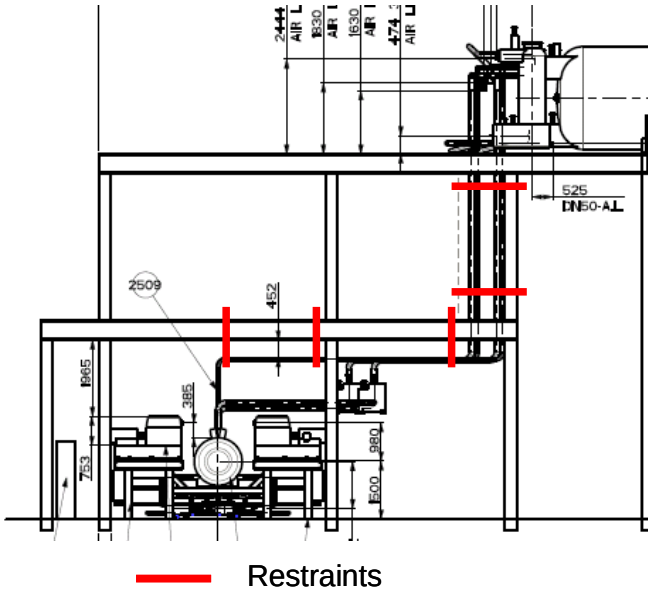

Figure 8.10 Seismic restraint location

8.6.3 Anchorages

Anchorages should be designed to remain elastic under the pertinent seismic load combination and they should be provided with an adequate amount of ductility, in order to avoid brittle failure. An example of a possible connection is shown in Figure 8.11.

Figure 8.11 piping system connection in seismic zone utilized in Hospital project in Wellington, New Zealand, (Three center field mission - August 2006)

However, it should be considered the fact that the liquid Argon will be at the temperature of -189 C, so accurate analysis of the rubber behavior at that temperature should be taken in account. In fact, it is well known that rubber at cold temperature tends to have a brittle behavior.

8.7 Final pipe support arrangment

In order to make the right design or retrofit decisions, and before proceeding with seismic analysis and testing, the designer should be familiar with lessons learned from seismic tests and real earthquakes to recognize and avoid features and conditions that caused failure.

All the equipment to which the pipes are attached should be anchored in order to avoid pipe failure due to sliding or rocking. Most of the pipes connect two different structures called service and the T600 module that have different movements during the earthquake. It is recommended to use flexible assemblies to decouple the seismic displacement of one side of the piping system from the other side, for example when crossing building joints.

Stiff branch lines - When a large pipe header is suspended on rods, it will tend to sway sideways during an earthquake. This would cause branch lines attached to the header to snap if they are rigidly tied to the building.

Inertia - The seismic load will force the pipe to sway sideways and, for large earthquakes, to uplift off its supports. It is therefore necessary to brace the pipe against sideway swaying and, for large earthquakes, to provide vertical seismic restraints.

A preliminary bracing scheme, prior to proceeding with computer analysis for final design, would consist in placing lateral horizontal and vertical bracing every third or fourth weight support, leading to seismic spans (distance between lateral braces) three to four times those in Table 8-2.

It is advisable to brace the pipe close to equipment nozzles to limit the load applied by the pipe on the equipment. Next to load sensitive equipment it may be necessary to design an anchor (a support that resists loads in all degrees of freedom).

Here below are reported some guidelines to brace the piping system during the installation.

"Each straight run of the piping system should be braced with a minimum of two transverse braces installed perpendicular to the piping and one longitudinal brace installed parallel to the piping. Transverse braces should be located at the final support of each run of pipe with two supports. If the distance between the braces exceeds the maximum transverse brace spacing, additional transverse braces should be located to limit the brace spacing to the maximum transverse brace spacing. A longitudinal brace should be located on each straight run of the pipe. If the length of the pipe run exceeds the maximum longitudinal brace spacing, additional longitudinal braces should be located on the pipe run while limiting the brace spacing to the maximum longitudinal

brace spacing. A transverse brace located within the maximum offset length of the pipe can provide limited longitudinal bracing for the straight run of pipe around a 90° turn, or elbow. The maximum offset length is based on the maximum stress of the pipe and a maximum ¼ in (6 mm) deflection of the offset of the pipe with welded, brazed, or groove-fitted joints. Vertical drops from horizontal runs of piping to the equipment require a transverse brace at the final support location before the pipe drop. Avoid bracing a pipe to separate portions of the structure that may act differently in response to an earthquake.

For example, do not connect a transverse brace to a wall and a longitudinal brace to a floor or roof at the same brace location."

8.7.1 Bunding

All tanks that are designed to control or avoid leakage shall be bunded, i.e. must be surrounded by a ditch and/or an embankment. The bunding shall be designed to retain its full integrity (absence of leaks) under a seismic event at least as intense as the one considered for ultimate limit state of the enclosed system. This part has been already verified in the Seismic Report of AIR LIQUIDE.

8.7.2 Serviceability limit States of tanks and pipes

According to ENV 1998-4:

1. Tank system should maintain its tightness against leakage of the content. Adequate free board should be provided, in order to prevent damage to the roof due to the pressures of the sloshing liquid or, if the tank has no rigid roof, to prevent the liquid from overstepping;
2. the hydraulic systems which are part of, or are connected to the tank, are capable to accommodate stresses and distortions due to tank displacements relative to each other and to the soil, without impairment of their functions;

3. Local buckling, if it occurs, does not initiate collapse and it is reversible; for instance, local buckling of structures due to stress concentration is acceptable.

8.7.3 Ultimate limit States of tanks and pipes

According to ENV 1998-4 it shall be ensured that under the relevant design seismic action:

1. The overall stability of the tank is satisfied with respect to collapse. The overall stability refers to rigid body behavior and may be impaired by sliding or overturning;
2. The spread of inelastic behavior is restricted within limited portions of the tank, and the ultimate deformations of the materials are not exceeded;
3. The nature and the extend of buckling phenomena in the shell are adequately controlled;
4. The hydraulic systems which are part of, or connected to the tank are designed so as to prevent loss of the tank content following the failure of some of its components;
5. The foundation shall not attain a failure mechanism before failure of the tank;

8.8 Seismic interactions

Al seismically qualified piping systems should be evaluated for seismic interactions. Credible and significant interactions should be identified and resolved by analysis, testing or hardware modification.

8.8.1 Description

An interaction is the seismic induced failure of a structure, system or component, other than the piping systems being qualified, that affects the function of the piping system. An interaction source is the component or structure that could fail and interact with a target. An interaction target is a component that is being impacted, sprayed or accidentally activated. A *credible interaction* is one that can take place. A *significant interaction* is one that can result in damage to the target. There are four types of seismic interactions:

1. *Falling* - A falling interaction is an impact on a critical component due to the fall of overhead or adjacent equipment or structure.

2. *Swing* - A swing or sway interaction is an impact due to the swing or rocking of adjacent component or suspended system.

3. *Spray* - A spray interaction is spray or flooding due to the leakage or rupture of overhead or adjacent piping or vessels.

4. *System* - A system interaction is an accidental or erroneous signal resulting in unanticipated operating conditions, such as the unintended start-up of a pump or closure of a valve.

8.8.2 Interaction review

A photographic record of the interaction walk-down should be realized documenting credible and significan sources of interaction. It is not nececessary to list or evaluate every single overhead or adjacent component in the area around the target; only those that could interact (credible interaction) and whose interaction could damage the target (significant interaction).

8.8.3 Falling interactions

In most cases, judgment is sufficient to establish whether a falling object can reach a target and be a credible interaction. Where judgment is insufficient, onecan calculate the radius R of the zone in which a falling object can strike. This zone is called the *zone of influence*:

$$R = V_H \left\{ \left[\left(\frac{V_V}{g} \right)^2 + \frac{2H}{g} \right]^{0.5} - \frac{V_V}{g} \right\} \tag{8.3}$$

where R is the radius of the zone of influence; V_H is the horizontal spectral velocity; V_V is the vertical spectral velocity; g is the gravity and H is the height of fall.

When a falling body of weight W falls from a height h and impact a target of weight W_b and stiffness k, the impact force and deflection can be calculated based on energy conservation, where P is an overestimate of the impact force because it does not account for rebound, deformation of the source or friction and heat loss at impact:

$$\begin{aligned} P &= W + W_b + \sqrt{W_b^2 + 2W\left(W_b + kh\right)} \\ d &= d_t + \sqrt{d_{st}^2 + 2h\left(d_{st} - d_s\right) - d_s^2} \end{aligned} \tag{8.4}$$

where P is the impact force; W is the weight of the falling body, W_b is the weight of the elastic member; k is the stiffness of elastic member, referenced to point of impact; h is the height of free fall; d is the maximum displacement at impact; d_s is the static displacement of elastic member due to its own weight W_b and d_{st} is the static displacement of member due to W plus W_b.

8.8.4 Rocking or Swing impact

The potential for sliding, rocking or overturning of free standing, unanchored equipment can be predicted based on the slenderness ratio (the height of the equipment's center of gravity relative to the width of its base), the coefficient of friction between the equipment and floor, and the horizontal and vertical acceleration. The swing amplitude of a suspended system (suspended piping, HVAC, cable trays, etc.) can be estimated by

$$d = 1.3 S_a / \omega^2$$
$$f_a = (g/L)^{0.5} / (2\pi) \quad (8.5)$$

where d is the swing amplitude, S_a is the spectral acceleration at frequency f_a, ω is the natural circular frequency of swing motion, f_a is the swing frequency; L is the pendulum length and g is the acceleration of gravity.

8.8.5 Significant Impact

Credible impacts that are significant must be documented. They include impacts on active components such as a pump or valve, instruments and impact sensitive components, pipe impacts by a pipe larger than the target pipe, collapse of portion of a wall or structure, impact by a heavy component, an overhead architectural feature or ceiling, or grating.

8.9 Summary and conclusions

The main objective of this chapter is to identify location and type of bracing connection for the piping system by subjecting the numerical model in SAP 2000 to an earthquake ground motion with a return period of 10000 yrs.

The bracing adopted are effective in limiting displacement response of the piping system and they do not have a major effect on the acceleration response.

The tube adopted should be flexible in order to accommodate the large lateral displacements and should be braced in order not interact with other pipes.

Due to the displacement and acceleration spectra for the SIMQKE input motion, the accelerations for the braced and unbraced systems were similar while the displacements for the braced system were smaller than the unbraced system.

This justifies that a stiffer system (i.e. larger frequency) would have smaller displacements but approximately the same accelerations.

Chapter 9

9 Coupled Building control

9.1 Abstract

In this chapter, the seismic response of a set of pairs of adjacent linear building structures linked to one another at different floor levels by linear passive devices is comprehensively evaluated. Two types of connectors were considered: linear viscous dampers and linear springs. Various possible combinations of type and location of the connectors were analyzed for wide ranges of values of their characteristic constants. Two response quantities were considered: interstory drift and absolute floor acceleration. Possible influence of properties of the structures (e.g., ratio of number of stories and ratio of fundamental periods) and of properties of the excitation (frequency content) on the response of the coupled structures were also evaluated. It was found that reduction of both response quantities in both buildings is not possible if the structures are connected to one another solely by linear springs, but it is feasible if the structures are linked to one another by either: (a) viscous dampers; or (b) combinations of viscous dampers and springs. Results also indicate that response reductions corresponding to case (b) are in general smaller than those corresponding to case (a), which means that the springs are not necessary. Finally, it was found that the coupling control approach might be more effective in controlling the response than the "standard" passive control approach (i.e.,

addition of supplemental dampers to each of the adjacent structures without coupling them to one another).

9.2 Introduction and literature review

A creative, non-standard approach to control the seismic response of multistory buildings consists of linking adjacent structures to one another at floor levels with connective devices. In doing so, it is then in principle possible to control the response of both structures simultaneously, which is precisely the attractiveness of the idea. In the case where the connectors are of the passive type, the viability of the coupling control approach has been shown in several analytical studies (Kobori *et al.*, 1988; Luco and Barros, 1998; Zhu and Iemura, 2000; Xu *et. al*. 2003; Bhaskararao and Jangid, 2006 and many others), as well as in some experimental investigations (Xu *et al*. 1999; Yang *et al*. 2003). The idea of linking adjacent structures to one another with passive devices has also been considered as a strategy to prevent or mitigate pounding effects (Westermo, 1989; Filiatrault and Folz, 1992; Reinhorn and Valles, 1997) and, more recently, as a mean to implement the "mass-proportional" supplemental damping system (Trombetti and Silvestri, 2004).

The aforementioned investigations have also shown that the effectiveness of the coupling control approach depends heavily on the properties of the adjacent buildings (e.g., natural periods and number of stories) and on the properties of the connectors (e.g., force-displacement relationship and height-wise distribution). While the number of possible combinations of building and connector properties is virtually unlimited, only a relatively small number of cases were considered in previous studies. Consequently, there is still a need to characterize comprehensively the effectiveness of the coupling control approach as a function of the aforementioned properties, a need that has already begun to be addressed in recent publications (Christenson et al. 2006, 2007). The objective of this study is to contribute to the general characterization of the efficiency of the coupling control approach. The dependency of the seismic response of a series of pairs of adjacent building structures on properties of the structures themselves (e.g., ratio of natural periods and ratio of number of

stories), of the connective devices (e.g., values of their characteristic constants and height-wise distribution) and of the seismic excitation (e.g., frequency content) has been analyzed comprehensively. The connective devices considered in this study are linear elements of the passive type.

9.3 Description of the model and of the analysis procedure

A total of four structural systems representative of building structures were considered. The first two systems have 4 and 2 stories, respectively, and are actual steel models of multi-story buildings structures (Figure 9.1).

Figure 9.1 Structural models (scale 1:5) of steel buildings

The models were designed by setting the length scale factor, λ_L, the Young's modulus scale factor, λ_E, and the acceleration scale factor, λ_a, as the dimensionally independent scale factors. The values of λ_E and λ_a were set equal

to unity because both the prototype and the model are made up of the same material, and both are subjected to the same gravity acceleration. The value of the length scale factor λ_L, on the other hand, was set equal to 5, hence *complete similarity* (Harris and Sabnis 1999) was not achieved, as it is usual in models of structural systems (while complete similarity is certainly desirable, it is often not possible because of economical and technological constraints). According to standard similitude theory, scale factors for stresses, strains and damping ratio are then equal to unity, and the scale factors for time, λ_t, and circular frequency, λ_ω, are given by:

$$\lambda_t = \left(\lambda_L / \lambda_a\right)^{0.5} = 2.236, \quad \lambda_\omega = \left(1/\lambda_L\right)^{0.5} = 0.4472 \tag{9.1}$$

These steel models, linked to one another with different types of connectors (e.g., nonlinear passive devices and semi-active devices), are being subjected to shaking table tests at ENEA's Structural Dynamics and Vibration Control Laboratory in Casaccia, Italy (Cimellaro and Marazzi, 2004). These particular structures were selected because a direct comparison between the performance of the connectors considered in this study (i.e, linear connectors of passive nature) and the performance of those considered in the aforementioned experimental program (which are of different nature) will in principle be possible in future studies. These structures were modeled as 2D, lumped-mass (i.e., one DOF per floor level) linearly elastic systems. Their mass and stiffness properties are shown in Figure 9.2a. It can be observed that, in both structures, the stiffness of the first story is significantly less than that of the other stories; hence, the structures exhibit a "soft story" vertical irregularity. The damping matrices, obtained through structural identification techniques, are shown below (Cimellaro and Marazzi, 2004):

$$\mathbf{C}_{\text{4-story}} = \begin{bmatrix} 393.2463 & -84.6960 & 217.0729 & -194.4571 \\ -84.6960 & 659.1534 & -420.3321 & 149.0861 \\ 217.0729 & -420.3321 & 594.6167 & -79.8796 \\ -194.4571 & 149.0861 & -79.8796 & 365.6510 \end{bmatrix} \frac{\text{N sec}}{\text{m}} \tag{9.2}$$

$$\mathbf{C}_{\mathbf{2\text{-}story}} = \begin{bmatrix} 508.1378 & -158.0441 \\ -158.0441 & 400.0242 \end{bmatrix} \frac{\text{N sec}}{\text{m}} \tag{9.3}$$

The corresponding fundamental natural periods and damping ratios, calculated using complex eigenvalue analysis, are $T_{4\text{-story}} = 0.13$ sec, $\xi_{4\text{-story}} = 2.5\%$, $T_{2\text{-story}} = 0.06$ sec and $\xi_{2\text{-story}} = 1.2\%$, respectively.

The two remaining systems considered in this study have 3 and 1 stories, respectively, and were conceived in order to account for possible influence building properties such as ratio of natural periods and ratio of number of stories. The values of their properties were set based on the properties of the 4-story and 2-story models. Mass and stiffness properties are shown in Figure 9.2Figure 9.2 Mass and stiffness properties of the building modelsb, where it can be observed that the 3-story model also exhibits a "soft story" vertical irregularity at the first story. The damping matrix of the 3-story model was calculated assuming Rayleigh-type damping, for which the values of the first and second modal damping ratios were set equal to 1.82% and 1.02%, respectively. The value of the damping coefficient of the 1-story model was set equal to 204.98 N-sec^2/m, which makes the corresponding damping ratio equal to 0.52%. The natural periods of these models are $T_{3\text{-story}} = 0.09$ sec and $T_{1\text{-story}} = 0.04$ sec, respectively.

All the combinations of two models (out of the four models described above) having different number of stories were considered as pairs of adjacent buildings (total number of pairs = 6). The model having the greater number of stories is generically denoted as structure "A", and the remaining structure is then generically denoted as structure "B". Two types of connector devices were considered: linear viscous dampers, characterized by the damping coefficient c, and linear springs, characterized by the stiffness coefficient k.

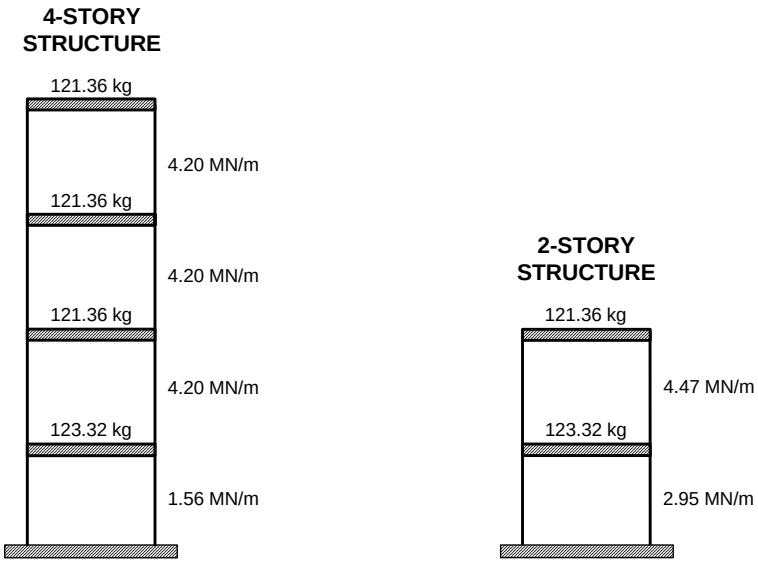

(a) actual steel models

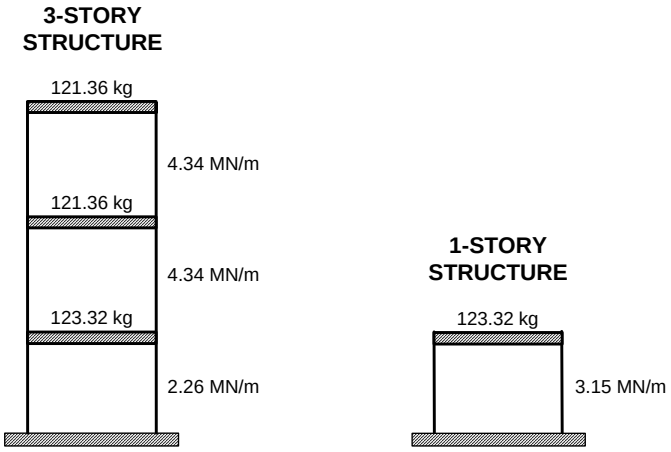

(b) additional models

Figure 9.2 Mass and stiffness properties of the building models

In any given pair of adjacent buildings, the number of possible locations of the connectors is equal to n_B, the number of stories of structure "B". In the general case where the structures are linked to one another at all floor levels with viscous dampers and springs acting in parallel (Figure 3Figure 9.2 Mass and stiffness properties of the building models), mass, damping and stiffness matrices of the coupled structural system are given by (Xu *et al.* 1999):

$$\mathbf{M} = \left[\begin{array}{c|c} \mathbf{M_A} & 0 \\ \hline 0 & \mathbf{M_B} \end{array}\right] \tag{9.4}$$

$$\mathbf{C} = \mathbf{C_0} + \mathbf{C_C} \tag{9.5}$$

$$\mathbf{K} = \mathbf{K_0} + \mathbf{K_C} \tag{9.6}$$

where:

$$\mathbf{C_0} = \left[\begin{array}{c|c} \mathbf{C_A} & 0 \\ \hline 0 & \mathbf{C_B} \end{array}\right] \tag{9.7}$$

$$\mathbf{C_C} = \left[\begin{array}{c|c|c} \mathbf{C_D} & 0 & -\mathbf{C_D} \\ \hline 0 & 0 & 0 \\ \hline -\mathbf{C_D} & 0 & \mathbf{C_D} \end{array}\right] \tag{9.8}$$

$$\mathbf{C_D} = \begin{bmatrix} c_1 & \dots & 0 \\ \dots & \dots & \dots \\ 0 & \dots & c_{n_B} \end{bmatrix} \tag{9.9}$$

$$\mathbf{K_0} = \left[\begin{array}{c|c} \mathbf{K_A} & 0 \\ \hline 0 & \mathbf{K_B} \end{array}\right] \tag{9.10}$$

$$\mathbf{K_C} = \left[\begin{array}{c|c|c} \mathbf{K_D} & 0 & -\mathbf{K_D} \\ \hline 0 & 0 & 0 \\ \hline -\mathbf{K_D} & 0 & \mathbf{K_D} \end{array}\right] \tag{9.11}$$

$$\mathbf{K_D} = \begin{bmatrix} k_1 & \dots & 0 \\ \dots & \dots & \dots \\ 0 & \dots & k_{n_B} \end{bmatrix} \tag{9.12}$$

and, in turn, c_i is the damping coefficient of the viscous dampers located at the i-th story level, k_i is the stiffness coefficients of the springs located at the i-th story level, $\mathbf{M_A}$, $\mathbf{C_A}$, $\mathbf{K_A}$ are the mass, damping and stiffness matrices of structure "A", and $\mathbf{M_B}$, $\mathbf{C_B}$, $\mathbf{K_B}$ are the mass, damping and stiffness matrices of structure "B".

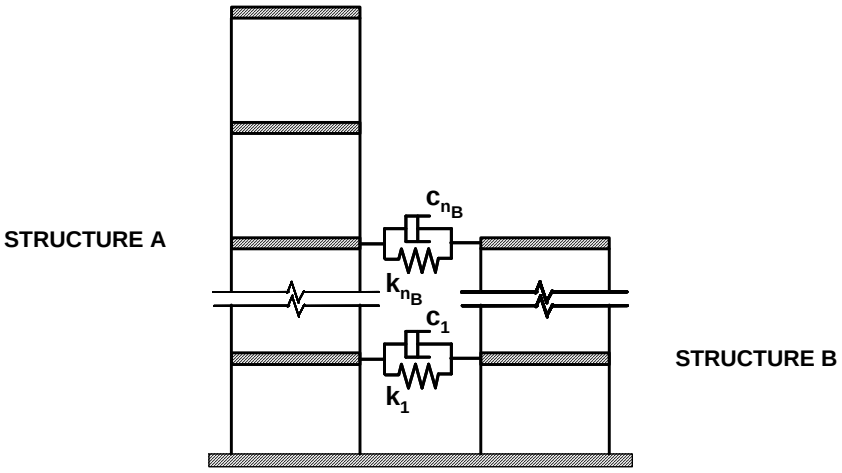

Figure 9.3 Structures linked at floor levels by viscous dampers and springs arranged in parallel

The response of the structures was evaluated in terms of stationary root-mean-square (RMS) response values. Two response quantities were considered: interstory drift and absolute floor acceleration. The corresponding vectors of power spectral density (PSD) functions are given by:

$$\mathbf{G_{ID}}(\omega) = |\mathbf{H_{ID}}(\omega)|^2 \; G_g(\omega) \tag{9.13}$$

$$\mathbf{G_{FA}}(\omega) = |\mathbf{H_{FA}}(\omega)|^2 \; G_g(\omega) \tag{9.14}$$

where $\mathbf{H_{ID}}(\omega)$ is the vector of transfer functions from ground acceleration to interstory drifts, and $\mathbf{H_{FA}}(\omega)$ is the vector of transfer functions from ground acceleration to floor absolute accelerations. The former is given by:

$$\mathbf{H_{ID}}(\omega) = \mathbf{T}\,\mathbf{H_D}(\omega) \tag{9.15}$$

where

$$\mathbf{T} = \begin{bmatrix} \mathbf{T_A} & 0 \\ 0 & \mathbf{T_B} \end{bmatrix}, \tag{9.16}$$

$$\mathbf{T_A} = \begin{bmatrix} 1 & 0 & \dots & 0 & 0 \\ -1 & 1 & \dots & 0 & 0 \\ \dots & \dots & \dots & \dots & \dots \\ 0 & 0 & \dots & 1 & 0 \\ 0 & 0 & \dots & -1 & 1 \end{bmatrix}_{n_A \; x \; n_A} \tag{9.17}$$

$$\mathbf{T_B} = \begin{bmatrix} 1 & 0 & \dots & 0 & 0 \\ -1 & 1 & \dots & 0 & 0 \\ \dots & \dots & \dots & \dots & \dots \\ 0 & 0 & \dots & 1 & 0 \\ 0 & 0 & \dots & -1 & 1 \end{bmatrix}_{n_B \; x \; n_B} \tag{9.18}$$

is a matrix relating floor displacements to interstory drifts, and $\mathbf{H_D}(\omega)$ is the vector of transfer functions from ground acceleration to floor displacements relative to the ground. This vector is given by:

$$\mathbf{H_D}(\omega) = -\left[-\omega^2\ \mathbf{M} + i\ \omega\ \mathbf{C} + \mathbf{K}\right]^{-1}\ \mathbf{M}\ \boldsymbol{\iota} \tag{9.19}$$

where, in turn, $i = \sqrt{-1}$ and $\boldsymbol{\iota} = \{1 \quad \ldots \quad 1\}^T_{n_A + n_B}$. The latter vector implicitly indicates that both structures are assumed to experience exactly the same excitation simultaneously, which is acceptable when the distance between the adjacent structures is relatively very small (Jeng and Kasai 1999). Vector $\mathbf{H_{FA}}(\omega)$ is given by:

$$\mathbf{H_{FA}}(\omega) = -\mathbf{M}^{-1}\left[i\ \omega\ \mathbf{C} + \mathbf{K}\right]\mathbf{H_D}(\omega) \tag{9.20}$$

The vectors of RMS response values are given by:

$$\sigma_{ID} = \left\{\sigma_{ID-A1} \quad \cdots \quad \sigma_{ID-An_A} \quad \sigma_{ID-B1} \quad \cdots \quad \sigma_{ID-Bn_B}\right\} = \sqrt{\int_0^\infty G_{ID}(\omega)\,d\omega}$$
$$\sigma_{FA} = \left\{\sigma_{FA-A1} \quad \cdots \quad \sigma_{FA-An_A} \quad \sigma_{FA-B1} \quad \cdots \quad \sigma_{FA-Bn_B}\right\} = \sqrt{\int_0^\infty G_{FA}(\omega)\,d\omega} \tag{9.21}$$

where the letter and the number in the second set of sub indexes in the quantities σ indicate the structure and the story level, respectively. For each response quantity, the response of each structure was assumed to be represented by the greatest of the corresponding RMS response values, i.e.:

$$\sigma_{\text{ID-A}} = \max\left(\sigma_{\text{ID-A1}}\ ,\ \sigma_{\text{ID-A2}}\ ,\ \ldots\ ,\ \sigma_{\text{ID-An}_\text{A}}\right) \tag{9.22}$$

$$\sigma_{\text{ID-B}} = \max\left(\sigma_{\text{ID-B1}}, \sigma_{\text{ID-B2}}, \cdots, \sigma_{\text{ID-Bn}_B}\right) \tag{9.23}$$

$$\sigma_{\text{FA-A}} = \max\left(\sigma_{\text{FA-A1}}, \sigma_{\text{FA-A2}}, \cdots, \sigma_{\text{FA-An}_A}\right) \tag{9.24}$$

$$\sigma_{\text{FA-B}} = \max\left(\sigma_{\text{FA-AB1}}, \sigma_{\text{FA-B2}}, \cdots, \sigma_{\text{FA-Bn}_B}\right) \tag{9.25}$$

Finally, these quantities where normalized by the same quantities corresponding to the case where no connectors are provided and the structures are not linked to one another (uncoupled configuration), i.e.:

$$\psi_{\text{ID-A}} = \frac{\sigma_{\text{ID-A}}}{\sigma'_{\text{ID-A}}} \tag{9.26}$$

$$\psi_{\text{ID-B}} = \frac{\sigma_{\text{ID-B}}}{\sigma'_{\text{ID-B}}} \tag{9.27}$$

$$\psi_{\text{FA-A}} = \frac{\sigma_{\text{FA-A}}}{\sigma'_{\text{FA-A}}} \tag{9.28}$$

$$\psi_{\text{FA-B}} = \frac{\sigma_{\text{FA-B}}}{\sigma'_{\text{FA-B}}} \tag{9.29}$$

where the apostrophe indicates response of the uncoupled configuration. The quantities ψ can be thought of as "response modification factors" in the sense that they indicate directly the effect of the connectors on the seismic response of the structures. Values of ψ that are less than unity indicate that the addition of the connectors reduces the corresponding response quantity, whereas the opposite is indicated by values of ψ that are greater than unity. Clearly, the lesser the value of ψ, the more beneficial the effect of the connectors.

9.4 Seismic input

The seismic excitation was modeled as a stationary random process whose one-sided PSD is defined in terms of the well-known modified Kanai-Tajimi function (Clough and Penzien 1993), i.e.:

$$G_g(\omega) = \left[\frac{\omega^4}{\left(\omega_f^2 - \omega^2\right)^2 + 4\,\xi_f^2\,\omega^2\,\omega_f^2} \right] \left[\frac{\omega_g^4 + 4\,\xi_g^2\,\omega^2\,\omega_g^2}{\left(\omega_g^2 - \omega^2\right)^2 + 4\,\xi_g^2\,\omega^2\,\omega_g^2} \right] G_0 \quad (9.30)$$

where ω denotes circular frequency, ω_g, ξ_g, ω_f and ξ_f are the parameters of the function, and the constant G_0 is an intensity factor. Values of ω_g, ξ_g, ω_f and ξ_f were set equal to 12.50 rad/sec, 0.60, 2.00 rad/sec and 0.70, respectively. As shown in other studies (Soong and Grigoriu 1993, Zanoni and Vanmarcke, 1994; Christenson *et al*. 2007), these values define a PSD function whose frequency content is, in the prototype scale, similar to that of actual, recorded seismic excitations. In order to evaluate the possible influence of the frequency content of the excitation on the response of coupled structures, however, several other values of ω_g (the parameter defining the main frequency of the excitation) were also considered. Since the response modification factors ψ were defined in such a way that their values are independent of the intensity factor G_0, the value of this quantity was set equal to unity. For illustration purposes, the PSD function corresponding to ω_g = 12.50 rad/sec, converted into model scale ($\omega_g^m = \sqrt{\lambda_L}\,\omega_g^p = 2.236\omega_g^p$) in accordance with standard similitude theory and subsequently normalized in such a way that $\int_0^\infty G_g(\omega)\,d\omega = 1$, is shown in Figure 9.4.

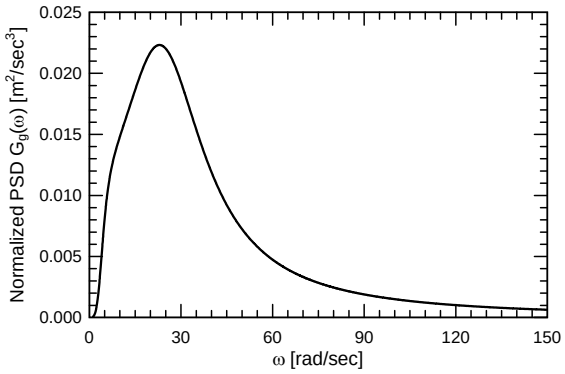

Figure 9.4 Normalized PSD function $G_g(\omega)$ (model scale)

9.5 Response of the structure linked by linear viscous dampers

The case where the structures are linked to one another by linear viscous dampers is examined in this section. Results are expressed in terms of the quantity $C = \sum_{i=1}^{n_B} c_i$, which may be conceptually thought of as the "total added damping" of the coupled system. Six possible structural configurations (i.e., pairs of coupled buildings) were considered and divided into three groups. Group I is made up of the three configurations where structure "B" is the 1-story structure, Group II is made up of the two configurations where structure "B" is the 2-story building, and Group III is made up of the case where structure "B" is the 3-story structure and structure "A" is the 4-story structure . For convenience, each structural configuration is denoted by (*i-j*), where *i* is the number of stories of structure "A" and *j* is the number of stories of structure "B". Therefore, Group I is made up of configurations (4-1), (3-1) and (2-1), Group II is made up of configurations (4-2) and (3-2), and Group III is made up

of configuration (4-3). In the configurations of Group I, there is only one possible location for the connectors; hence, the height-wise distribution of the linking devices is not an issue. In the configurations of Group II, there are two possible locations for the connectors, and all the possible height-wise distributions of the linking devices were examined in order to get insight into possible optimization of the location of the height-wise distribution of the connectors. In the configuration of Group III, there are three possible locations for the connectors. Because examination of all of the possible height-wise distributions of the linking devices would have been cumbersome in this case, only a relatively small number of significant, practical distributions were examined.

A comparison between response modification factors ψ for the three structural configurations of Group I, obtained considering the seismic excitation defined by ω_g = 12.50 rad/sec, is shown in Figure 9.5. The corresponding values of the period ratio T_B/T_A are also indicated. It can be observed that the value of ψ is in almost all cases less than unity (the only exception is $\psi_{ID\text{-}B}$ at very large values of C for the (4-1) configuration, the period ratio T_B/T_A is equal to 0.30 in this case). In other words, there are, for each configuration, wide ranges of values of C for which values of ψ are in all cases less than unity, which in turn means that it is then possible to reduce *both* response quantities in *both* structures simultaneously by linking them to one another using linear viscous dampers only.

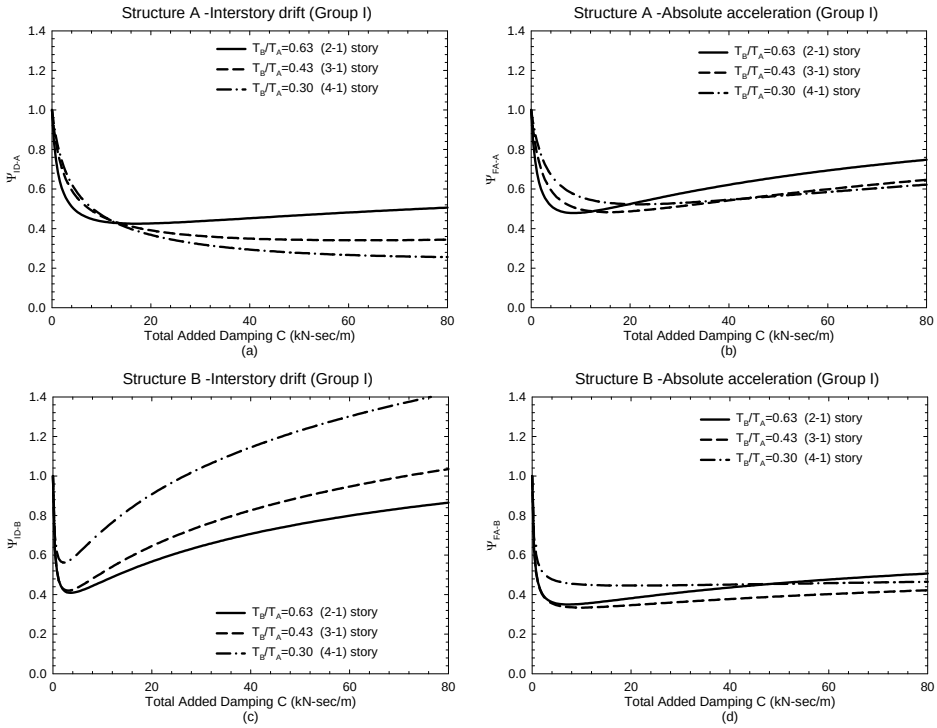

Figure 9.5 Response modification factors for configurations (4, 1), (3, 1) and (2, 1) of coupled structures linked by linear viscous dampers

Since the optimal value of *C* is, in each configuration, different for each response quantity in each structure, an optimal value of *C* for a given configuration is not uniquely defined. For each configuration, however, it is possible to define *a range* of values of *C* for which values of ψ are in all cases less than a given limit (a possible but not unique optimality criterion). It is interesting to note that the absolute acceleration response is essentially the same for the three structural configurations, whereas the interstory drift response does exhibit a significant dependency on the structural configuration, especially the response of structure "B". As the value of *C* increases, the interstory drift response of structure "A" increases with increasing values of the period ratio,

but the opposite trend applies for structure "B". Finally, the corresponding first-mode damping ratios, calculated by complex eigenvalue analysis, are shown in Figure 9.6. In all cases, there is clearly a value of C that maximizes the first-mode damping ratio. A joint examination of Figure 9.5 and 10.6, however, shows that the value of C that maximizes the first-mode damping ratio is not necessarily equal to the value of C that minimizes the response. Figure 9.6 also shows that the maximum first-mode damping ratio increases with decreasing values of the period ratio.

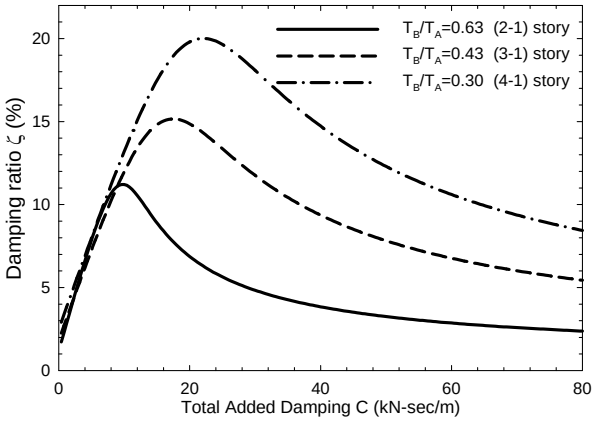

Figure 9.6 First-mode damping ratios of the Group I structural configurations (structures coupled by linear viscous dampers)

As mentioned before, there are two possible locations for the connective devices in the structural configurations of Group II (i.e., the (4-2) and (3-2) configurations). In these cases, 201 combinations of c_1 and c_2 ranging from $c_1 = C$, $c_2 = 0$ to $c_1 = 0$, $c_2 = C$ were considered for each value of C. Optimal height-wise distributions (i.e., the combinations of c_1 and c_2 that minimize the value of ψ) obtained considering the seismic excitation defined by $\omega_g = 12.50$ rad/sec are indicated graphically in Figure 9.7.

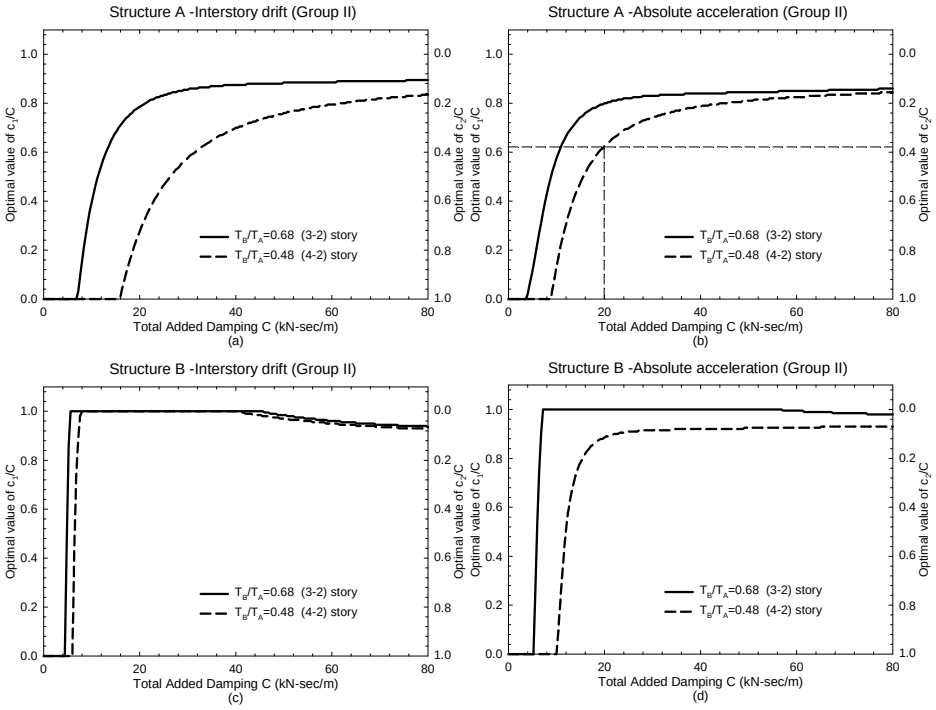

Figure 9.7 Optimal height-wise distributions of linear viscous dampers in the (4-2) and (3-2) configurations

For clarity, the meaning of the plots is illustrated in Figure 9.7b. In fact, when C = 20 kN-sec/m, the optimal height-wise distribution for the absolute acceleration response of structure "A" of the (4-2) configuration is given by c_1 = 0.625 C = 12.5 kN-sec/m and c_2 = 0.375 C = 7.5 kN-sec/m. Figure 9.7 shows also that the optimal height-wise distribution depends on the value of C, and that the relationship between the value of C and its optimal height-wise distribution is, in a qualitatively way, the same for each response quantity in each structure. When the value of C increases, the optimal height-wise distribution evolves from a distribution where c_1 = 0, c_2 = C to a distribution where c_1 has a relatively large value and c_2 has a relatively small value. Quantitatively, however, the optimal height-wise distribution is, strictly

speaking, different for each response quantity in each structure. In the case of the (4-2) configuration, a comparison between response modification factors ψ for optimal distributions and those for more practical (and hence more likely to be implemented in practice) distributions is shown in Figure 9.8 (the seismic excitation is again that defined by ω_g = 12.50 rad/sec).

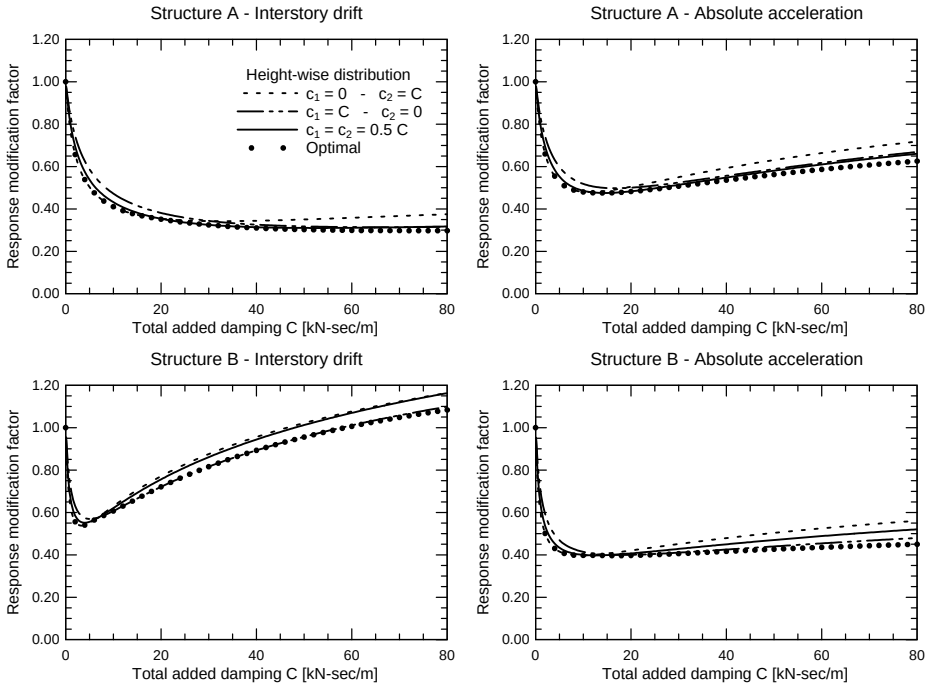

Figure 9.8 Response modification factors Ψ for configuration (4-2) of coupled structures linked by linear viscous dampers

It can be observed that, in all cases, the value of ψ depends on the *value* of *C* but is essentially independent of the *height-wise distribution* of *C*, which makes considerations about optimal height-wise distributions of no practical interest. It

can also be observed that, as in the case of the Group I configurations, the values of ψ are in almost all cases less than unity (the only exception is $\psi_{ID\text{-}B}$ at very large values of C). In other words, there is again a wide range of values of C for which values of ψ are in all cases less than unity, which in turn means that it is then possible to reduce *both* response quantities in *both* structures simultaneously by linking them to one another using linear viscous dampers only. Since the optimal value of C is different for each response quantity in each structure, an optimal value of C for the coupled system is not uniquely defined. It is again possible, however, to define *ranges* of values of C for which values of ψ are in all cases less than a given limit (a possible but not unique optimality criterion). For instance, for 1.6 kN-sec/m $\leq C \leq$ 18.0 kN-sec/m, all values of ψ (i.e., $\psi_{ID\text{-}A}$, $\psi_{ID\text{-}B}$, $\psi_{FA\text{-}A}$ and $\psi_{FA\text{-}B}$) are always less than 0.70, indicating that, with respect to the uncoupled configuration, both response quantities in both structures are reduced by at least 30%. Results corresponding to the (3-2) configuration are qualitatively identical to those shown in Figure 9.8, and are not shown for brevity.

In the case of the (4-3) configuration (Group III), only the height-wise distributions indicated in Table 1 were considered. Results obtained considering the seismic excitation defined by ω_g = 12.50 rad/sec turned out to be qualitatively similar to those corresponding to the Group II configurations in that: (a) for a given value of C, the response is essentially insensitive to the height-wise distribution of C; (b) optimal values of C are different for each response quantity in each structure; and (c) there is a range of values of C for which it is possible to reduce both response quantities in both structures simultaneously. For illustration purposes, values of the response modification factors corresponding to the absolute acceleration response of the 4-story structure are shown in Figure 9.9.

Table 9-1 Height-wise distributions of linear viscous dampers (4-3 configuration)

story	Distr. 1	Distr. 2	Distr. 3	Distr. 4	Distr. 5	Distr. 6	Distr. 7
c_3 =	0	0	C	0	C / 2	C / 2	C / 3
c_2 =	0	C	0	C / 2	0	C / 2	C / 3
c_1 =	C	0	0	C / 2	C / 2	0	C / 3

A comparison between response modification factors ψ for the Group II and Group III configurations, obtained considering the seismic excitation defined by ω_g = 12.50 rad/sec, can be seen in Figure 9.10.

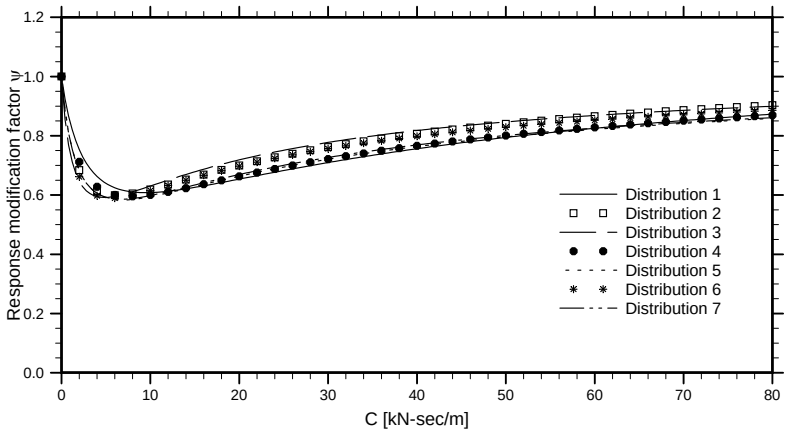

Figure 9.9 Response modification factors Ψ for configuration (4-3) of coupled structures linked by linear viscous dampers: absolute acceleration response of the 4-story model (structure "A")

In the case of the Group II configurations, the corresponding height-wise distributions are the optimal distributions indicated in Figure 9.7.

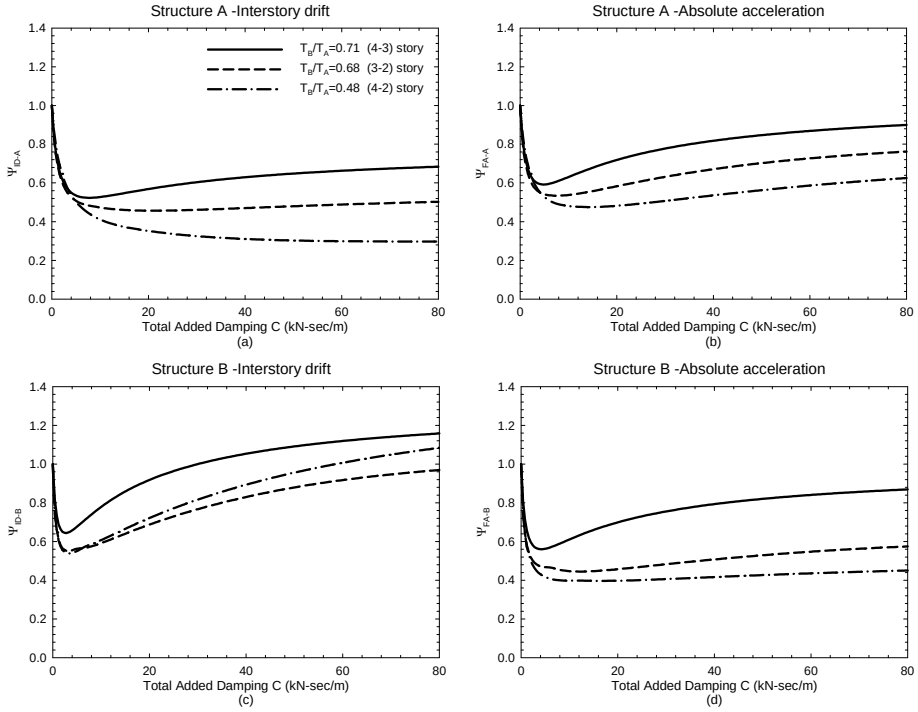

Figure 9.10 Response modification factors for optimal height-wise coupled system configurations when linked with linear viscous dampers

In the case of the Group III configuration, the corresponding height-wise distribution is in all cases that given by $c_1 = c_2 = 0$ and $c_3 = C$ (i.e., the distribution denoted as Distribution 3 in Table 9-1), which, out of the seven distributions considered, turned out to be one providing the maximum level of response reduction for most values of C. It can be observed that, with the exception of the interstory drift of structure "B", the level of response reduction corresponding to the (4-2) configuration is always greater than those corresponding to the other configurations. In more general terms, the degree of response reduction increases in general with increasing values of the period ratio. Figure 9.11 provides more insight into this last issue, where a performance index defined as the normalized sum of the four response

modification factors ψ (i.e., the sum of ψ_{ID-A}, ψ_{ID-B}, ψ_{FA-A} and ψ_{FA-B} considering the whole range of value of *C*) is plotted as a function of the period ratio of the six structural configurations (the seismic excitation is again that defined by ω_g = 12.50 rad/sec).

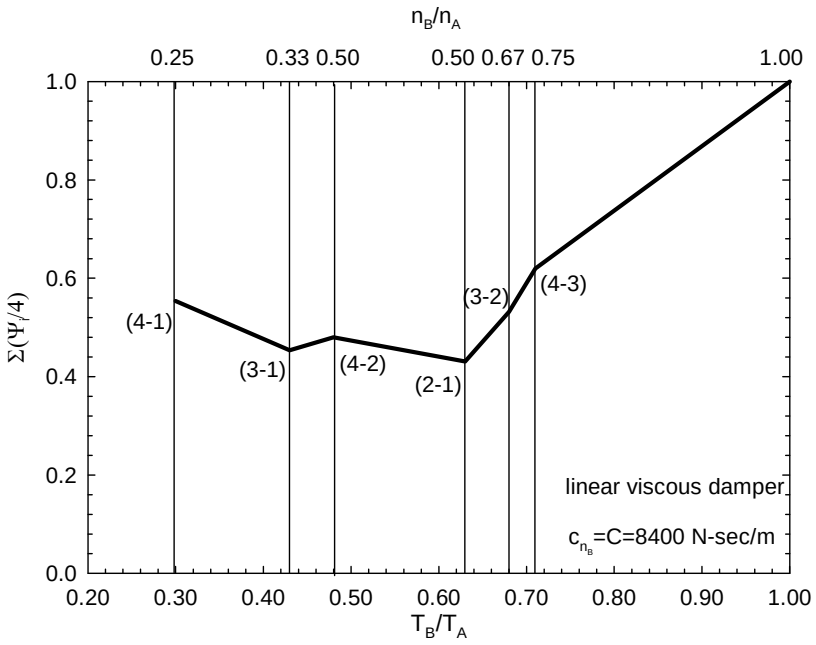

Figure 9.11 Normalized sums of response modification factors Y vs. period ratio TB/TA for the six configurations of coupled structures linked by a single linear viscous damper located at the roof level of structure "B"

The value of *C* is in all cases equal to 8400 N-sec/m, the value for which the average response of the four response quantities in the six configurations is minimized. The height-wise distribution of *C* is that defined by a single viscous damper located at the roof level of structure "B" (i.e., $c_1 = c_2 = 0$ and $c_3 = C$ in the Group III configuration, $c_1 = 0$ and $c_2 = C$ in the Group II configurations, and obviously $c_1 = C$, in the Group I configurations). Results shown in Figure

9.11 indicate that maximum (average) levels of response reductions are attained when the value of the period ratio is roughly equal to 0.5, (i.e., configurations (4-2) and (2-1)). This observation is consistent with the results obtained by Luco and Barros (1998). They proved that, when adjacent buildings are modeled as uniform, damped shear beams, the largest level of response reduction is achieved when the height of the taller structure is about twice the height of the shorter structure. Since the response of the configurations considered in this study was found to be essentially insensitive to the height-wise distribution of the connective dampers, results shown in Figure 9.11 are, qualitatively, valid for any height-wise distribution of the connectors.

Finally, some insight into the possible influence of the frequency content of the excitation on the seismic response of coupled structures was obtained by considering several values of ω_g, the parameter of the modified Kanai-Tajimi equation defining the main frequency of the excitation. Representative results are shown in Figure 9.12, which shows response modification factors ψ for the (4-2) configuration subjected to the seismic excitations defined by ω_g = 12.50 rad/sec (realistic in the prototype scale), ω_g = 21.69 rad/sec (fundamental frequency of Building A in the prototype scale), and ω_g = 45.03 rad/sec (fundamental frequency of Building B in the prototype scale). In all cases, the height-wise distribution of the connectors is that given by $c_1 = 0$ and $c_2 = C$. It can be observed that, again, there is in all cases a range of values of C for which it is possible to reduce both response quantities in both structures simultaneously, although, as expected, the level of response reduction is essentially always greater in the structure whose fundamental frequency is closer to the main frequency of the excitation. Results that are more representative are shown in Figure 9.13, which shows response modification factors ψ for the six different configurations considered in this study subjected to seismic excitations defined by values of ω_g ranging from 0 rad/sec to 200 rad/sec. In all cases, the value of C is equal to the value for which the sum of of $\psi_{ID\text{-}A}$, $\psi_{ID\text{-}B}$, $\psi_{FA\text{-}A}$ and $\psi_{FA\text{-}B}$ is minimized when ω_g = 12.50 rad/sec.

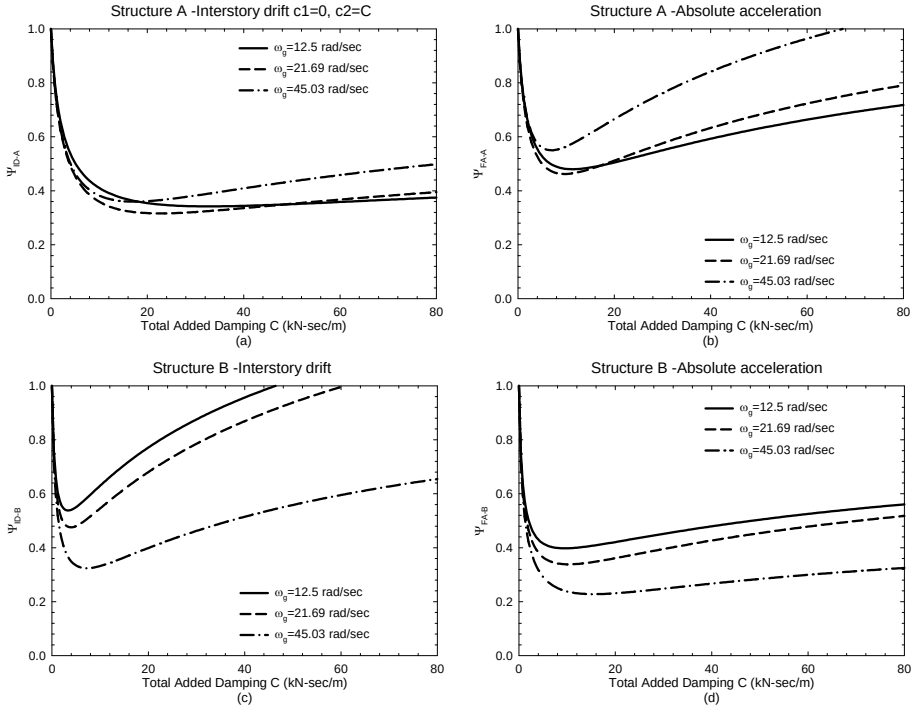

Figure 9.12 Response modification factors Y for configuration (4-2) of coupled structures linked by linear viscous dampers and subjected to seismic excitations having different values of the main frequency ω_g

In the Group II configurations, the height-wise distribution of the connectors is the optimal distribution shown in Figure 9.7 for the corresponding values of *C*. In the Group III configuration, the height-wise distribution of the connectors is that given by $c_1 = c_2 = 0$ and $c_3 = C$. It can be observed that, again, it is possible to reduce both response quantities in both structures simultaneously, regardless of the frequency content of the excitation (the only exception is the absolute acceleration response of the 4-story structure in the (4-1) configuration when the main frequency of the excitation is relatively very high). It can also be observed that, as the main frequency of the excitation increases, the response of structure "A" initially decreases, and then increases moderately in most cases

(the only exception is again the absolute acceleration response of the 4-story structure in the (4-1) configuration).

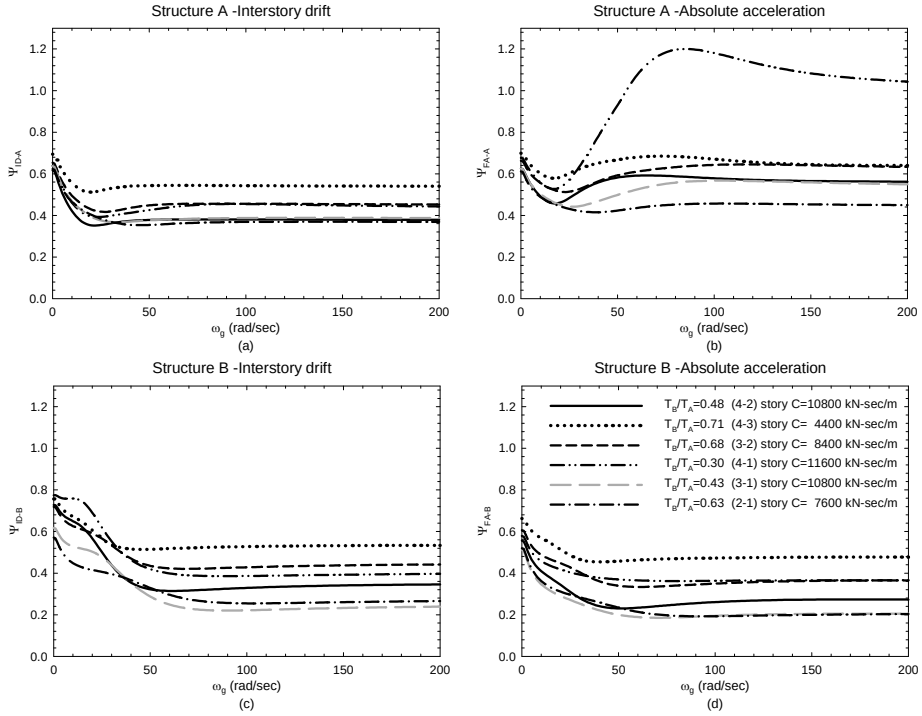

Figure 9.13 Response modification factors Y for different configurations of coupled structures linked by linear viscous dampers and subjected to seismic excitations having different values of the main frequency ω_g.

The response of structure "B", on the other hand, initially decreases and then remains essentially constant. Since the main frequency of structure "A" is always less than that of structure "B", these observations are consistent with those corresponding to the results shown in Figure 9.12. Results for other values of *C* are qualitatively identical to those shown in Figure 9.13 and are not shown for brevity.

9.6 Response of the structure linked by linear springs

The case where the structures are linked to one another solely by linear springs is examined in this section. Results are expressed in terms of the quantity $K = \sum_{i=1}^{n_B} k_i$, which may be conceptually thought of as the "total added stiffness" of the coupled system.

A comparison between response modification factors ψ for the three structural configurations of Group I, obtained considering the seismic excitation defined by ω_g = 12.50 rad/sec, is shown in Figure 9.14. It can be observed that, while values of $\psi_{ID\text{-}A}$ and $\psi_{FA\text{-}B}$ are always less than unity, values of $\psi_{ID\text{-}B}$ and $\psi_{FA\text{-}A}$ are actually *greater* than unity (in the case of factor $\psi_{ID\text{-}B}$, an exception occurs for a small range of relatively small values of *K*). In other words, it is then *not* possible to reduce both response quantities in both structures by linking them to one another using linear springs only. The latter observation is also valid for the case where the structures are connected to one another by rigid links that can be considered as springs having very large values of their stiffness coefficient. In fact, it can be deduced from the plots shown in Figure 9.14 that the upper limit of the range of values of *K* is large enough as to include values of *K* for which the springs behave essentially as rigid members. As mentioned before when describing the response of structures linked by viscous dampers, the absolute acceleration response is essentially the same for the three structural configurations, whereas the interstory drift response does exhibit a significant dependency on the structural configuration. Finally, the corresponding first-mode damping ratios, calculated by complex eigenvalue analysis, are shown in Figure 9.15. As expected, the first-mode damping ratio *decreases* in all cases with increasing values of *K*. A joint examination of Figure 9.14 and 15 shows again that the value of *K* that maximizes the first-mode damping ratio is not necessarily equal to the value of *K* that minimizes the response.

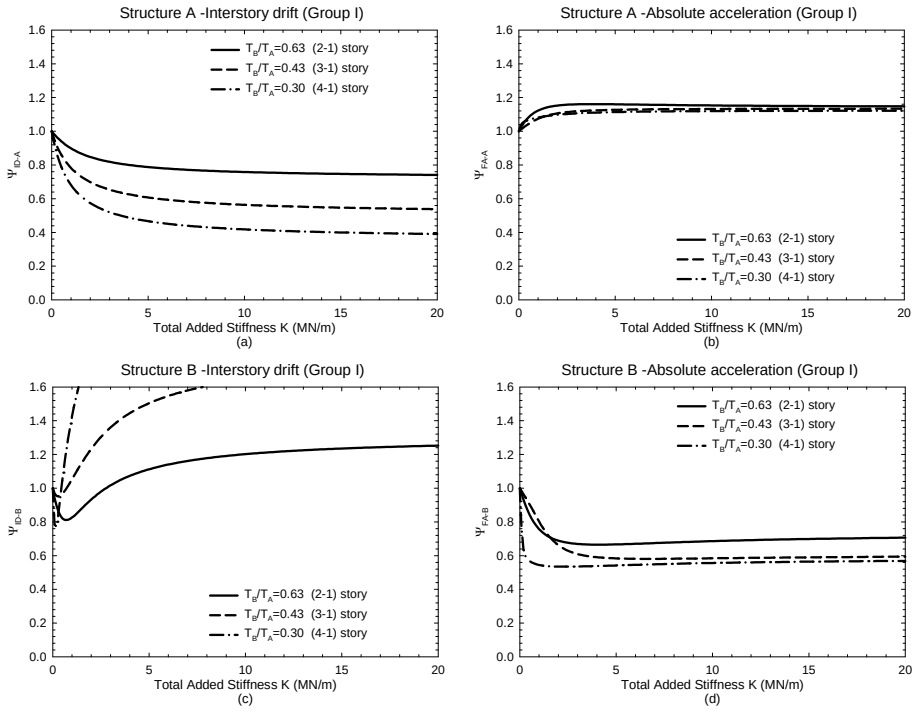

Figure 9.14 Response modification factors Ψ for configurations (4, 1), (3, 1) and (2, 1) of coupled structures linked by linear springs

In the case of the Group II configurations, 201 combinations of k_1 and k_2 ranging from $k_1 = K$, $k_2 = 0$ to $k_1 = 0$, $k_2 = K$ were considered for each value of K. Optimal height-wise distributions (i.e., the combinations of k_1 and k_2 that minimize the value of ψ) obtained considering the seismic excitation defined by ω_g = 12.50 rad/sec are indicated graphically in Figure 9.16, which is conceptually identical to Figure 9.7. In some cases, the line indicating the optimal height-wise distribution is nearly vertical, which means that the optimal height-wise distribution evolves from one extreme case to the opposite extreme case (i.e., from $k_1 = K$, $k_2 = 0$ to $k_1 = 0$, $k_2 = K$ or vice versa) in a relatively very short interval of values of K.

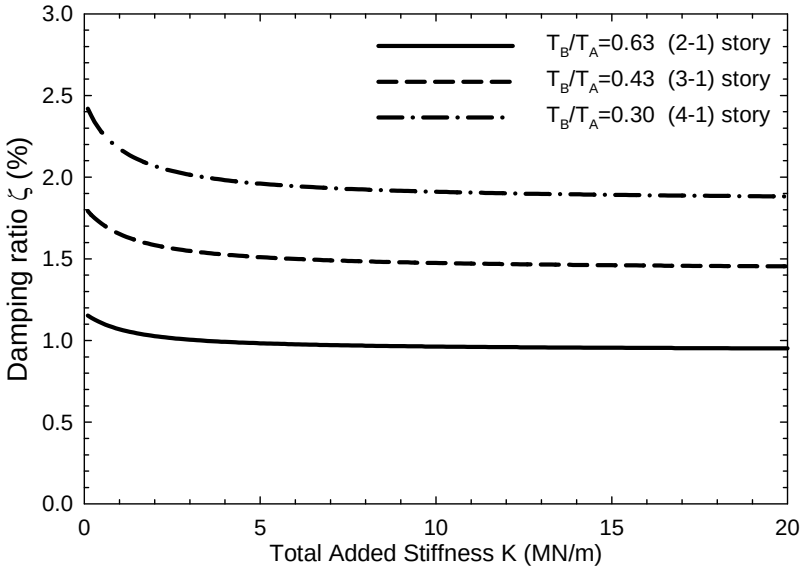

Figure 9.15 First-mode damping ratios of the Group I structural configurations (structures coupled by linear springs)

Unlike what was observed in the case where the connectors are linear viscous dampers, the relationship between the value of K and its optimal height-wise distribution is different for each response quantity in each structure both quantitatively and qualitatively. In the case of the (4-2) configuration, a comparison between response modification factors ψ for optimal distributions and those for more practical distributions is shown in Figure 9.17 (the seismic excitation is again that defined by ω_g = 12.50 rad/sec). It can be observed that, in all cases, the value of ψ depends on the value of K but is essentially independent of the height-wise distribution of K, which again makes considerations about optimal height-wise distributions of no practical interest. It can also be observed that, while values of $\psi_{ID\text{-}A}$ and $\psi_{FA\text{-}B}$ are always less than unity, values of $\psi_{ID\text{-}B}$ and $\psi_{FA\text{-}A}$ are actually *greater* than unity (in the case of factor $\psi_{ID\text{-}B}$, an exception occurs for a very small range of relatively small

values of *K*). In other words, it is again not possible to reduce both response quantities in both structures by linking them to one another using linear springs only, an observation that, as mentioned before, is also valid for the case where the structures are connected by rigid links.

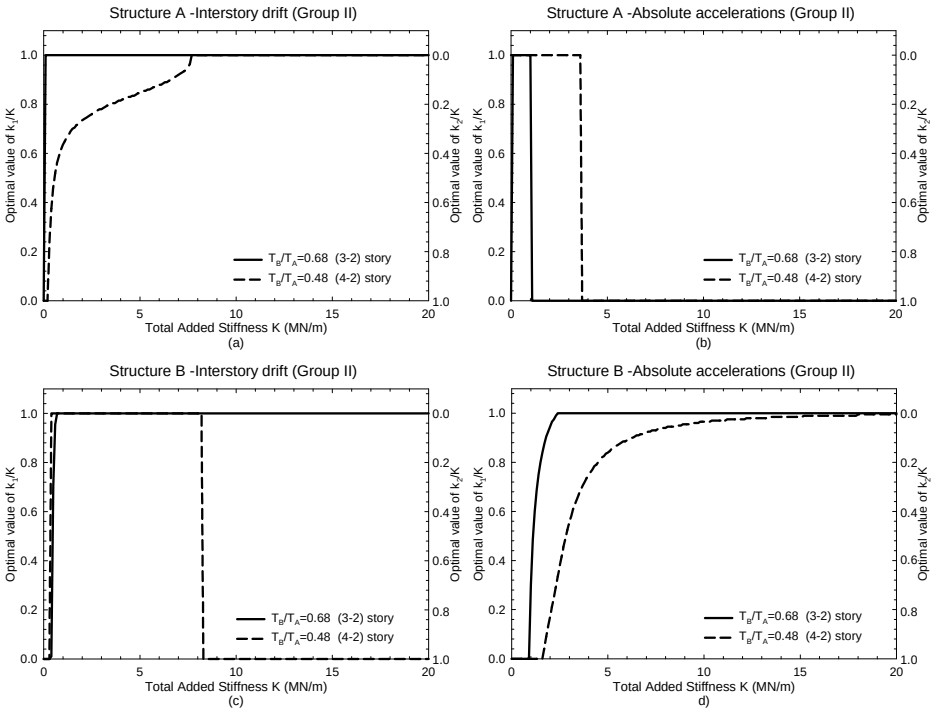

Figure 9.16 Optimal height-wise distributions of linear springs in the (4-2) and (3-2) configurations

It is interesting to note that, in the case of the response quantities for which the corresponding values of ψ are less than unity (i.e., interstory drift response of structure "A" and floor acceleration response of structure "B"), the relationship between *K* and its optimal height-wise distribution is qualitatively similar to that observed before for the case where the connectors are linear viscous dampers.

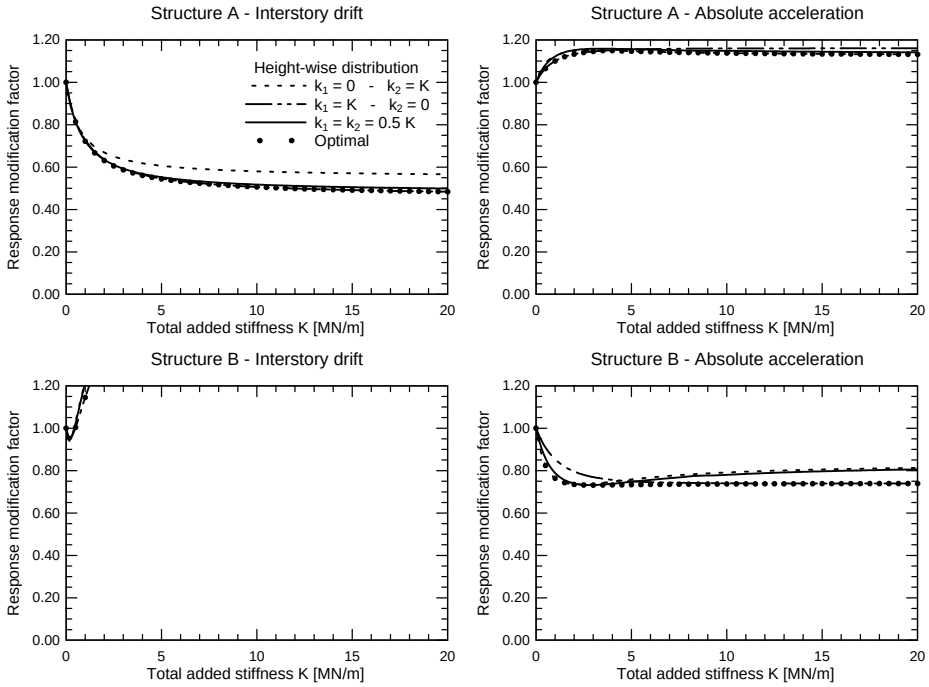

Figure 9.17 Response modification factors Ψ for configuration (4-2) of coupled structures linked by linear viscous dampers

Results corresponding to the (3-2) configuration are qualitatively identical to those shown in Figure 9.8, and are not shown for brevity. In the case of the (4-3) configuration (Group III), only the height-wise distributions indicated in Table 9-2 were considered. These distributions are conceptually analogous to those indicated in Table 9-1. Results obtained considering the seismic excitation defined by ω_g = 12.50 rad/sec turned out to be qualitatively similar to those corresponding to the Group II configurations in that: (a) for a given value of *K*, the response is essentially insensitive to the height-wise distribution of *K*; and (b) it is not possible to reduce both response quantities in both structures simultaneously. For illustration purposes, values of the response modification

factors corresponding to the absolute acceleration response of the 4-story structure are shown in Figure 9.18.

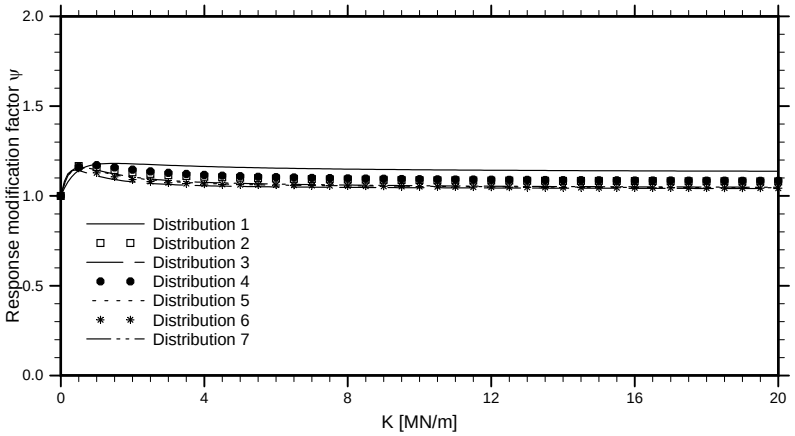

Figure 9.18 Response modification factors Ψ for configuration (4-3) of coupled structures linked by linear springs: absolute acceleration response of the 4-story model (structure "A")

Table 9-2 Height-wise distributions of linear springs (4-3 configuration)

story	Distr. 1	Distr. 2	Distr. 3	Distr. 4	Distr. 5	Distr. 6	Distr. 7
k_3 =	0	0	K	0	K / 2	K / 2	K / 3
k_2 =	0	K	0	K / 2	0	K / 2	K / 3
k_1 =	K	0	0	K / 2	K / 2	0	K / 3

Some insight into the relationship between the degree of response reduction and the period ratio is shown in Figure 19, where a performance index defined as the normalized sum of the four response modification factors ψ (i.e., the sum of $\psi_{ID\text{-}A}$, $\psi_{ID\text{-}B}$, $\psi_{FA\text{-}A}$ and $\psi_{FA\text{-}B}$ considering the whole range of values of *K*) is plotted as a function of the period ratio of the six structural configurations (the seismic excitation is again that defined by ω_g = 12.50 rad/sec). The value of *K* is in all cases equal to 700 kN/m, the value for which the average response of the four response quantities in the six configurations is minimized. The height-wise

distribution of K is that defined by a single spring located at the roof level of structure "B" (i.e., $k_1 = k_2 = 0$ and $k_3 = K$ in the Group III configuration, $k_1 = 0$ and $k_2 = K$ in the Group II configurations, and obviously $k_1 = K$, in the Group I configurations). Results shown in Figure 9.19 indicate that the average level of response reductions increases with decreasing values of the period, although the tendency is not strictly monotonic.

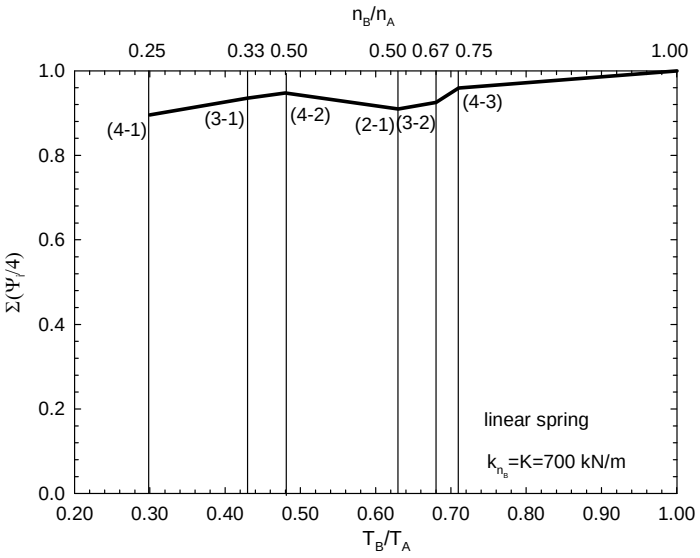

Figure 9.19 Normalized sum of response modification factors Y vs. period ratio TB/TA for the six configurations of coupled structures linked by a single linear spring located at the roof level of structure "B"

9.7 Response of the structures linked by linear combinations of linear viscous dampers and linear springs

The case where the structures are linked to one another by combinations of linear viscous dampers and linear springs is illustrated in this section. Two general types of combinations were considered. In the first type, viscous

dampers and springs are located at different story levels, whereas, in the second type, viscous dampers and springs are located at the same story levels (naturally, only the second type of combinations was considered in the Group I configurations). For illustration purposes, the combinations considered in the case of the (4-2) configuration are shown in Figure 9.20, where combinations "VDS" and "SVD" are of the first type, and combinations "KEL1", "KEL2" and "KELVIN" are of the second type. Results corresponding to the "KEL1" combination, obtained considering the seismic excitation defined by ω_g = 12.50 rad/sec, are shown in Figure 9.21. All combinations of values of C = 0, 400 N-sec/m, 800 N-sec/m, …,80,000 N-sec/m and K = 0, 100 kN/m, 200 kN/m, …,20,000 kN/m were considered. It can be observed that there are wide ranges of combinations of values of C and K for which all values of ψ are less than unity, which means that it is then possible to reduce both response quantities in both structures by linking them to one another with this particular combination of linear viscous dampers and linear springs. It is also observed, however, that, for any value of C, the value of ψ generally increases in an essentially monotonic fashion as the value of K increases (the only exceptions are the values of $\psi_{ID\text{-}A}$ when C is relatively small: they are slightly less for relatively large values of K than for K = 0).

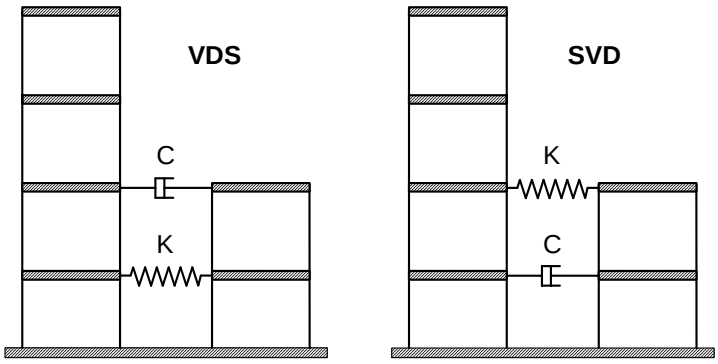

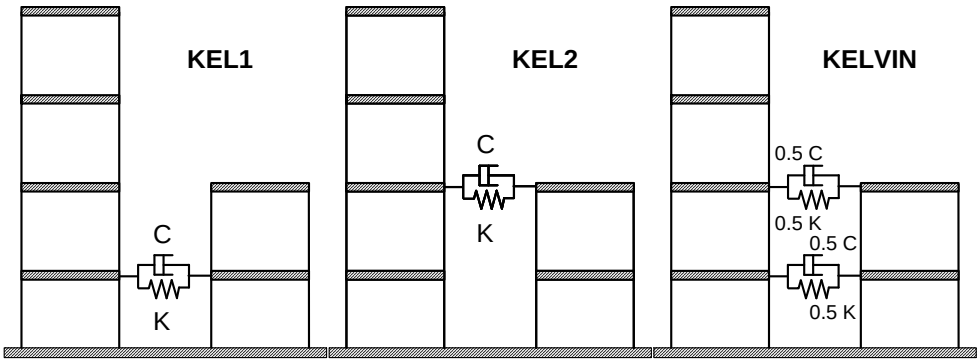

Figure 9.20 Structures of configuration (4-2) linked by combinations of linear viscous dampers and linear springs

Further support to this last observation is provided by the fact that the values of *K* corresponding to the optimal combinations of values of *C* and *K* are always very small. These observations indicate that the addition of a linear spring to an already existing viscous damper generally *increases* the response of the coupled system. There are a few cases where the addition of a linear spring actually results in an additional level of response reduction, but the magnitude of this additional reduction is small and of little practical interest. Results corresponding to the other combinations of dampers and springs shown in Figure 9.20 were found to be conceptually identical to those shown in Figure 9.21 and are not shown for brevity.

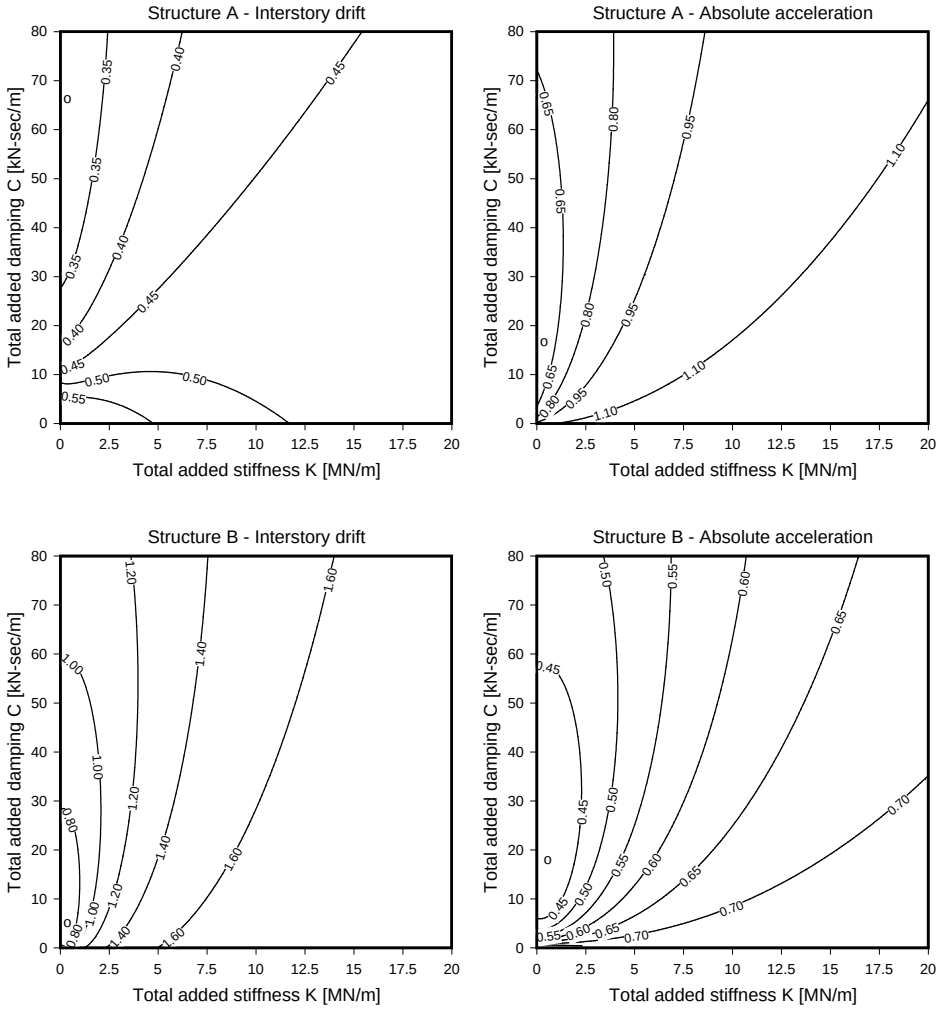

Figure 9.21 Contour lines of values of response modification factors Ψ for configuration (4-2) of coupled structures linked by combination KEL1 of viscous dampers and springs (symbol "o" indicates the optimal combination of C and K)

In part because these results indicated that it was not necessary, and in part because of the difficulties associated with the graphical representation of values of ψ as functions of four variables (c_1, c_2, k_1 and k_2), the case where the structures of the (4-2) configuration are linked with the more general combination of linear springs and linear viscous dampers (i.e., a coupled system were $c_1 \neq c_2$ and $k_1 \neq k_2$) was not investigated.

The combinations considered in the case of the (4-3) configuration are indicated in Table 9-3 and Table 9-4. In all cases, all combinations of values of C = 0, 400 N-sec/m, 800 N-sec/m, … 80,000 N-sec/m and K = 0, 100 kN/m, 200 kN/m, … 20,000 kN/m were considered, and the corresponding results turned out to be qualitatively identical to those shown in Figure 9.21.

Table 9-3 Combinations of dampers and springs located at different levels (Group III configuration)

story	Combo 1	Combo 2	Combo 3	Combo 4	Combo 5	Combo 6	Combo 7	Combo 8	Combo 9
3	0	K	0	K	C	C	K	C/2	C/2
2	K	0	C	C	0	K	C/2	K	C/2
1	C	C	K	0	K	0	C/2	C/2	K

Table 9-4 Combinations of dampers and springs located at the same level (Group III configuration)

story	combo 1	combo 2	combo 3	combo 4	combo 5	combo 6	combo 7
3	0	0	C-K	0	C/2-K/2	C/2-K/2	C/3-K/3
2	0	C-K	0	C/2-K/2	0	C/2-K/2	C/3-K/3
1	C-K	0	0	C/2-K/2	C/2-K/2	0	C/3-K/3

For illustration purposes, results corresponding to Combination 3 of Table 9-4 (i.e., the combination given by $c_1 = c_2 = 0$, $c_3 = C$ and $k_1 = k_2 = 0$, $k_3 = K$), obtained considering the seismic excitation defined by ω_g = 12.50 rad/sec, are shown in Figure 9.22.

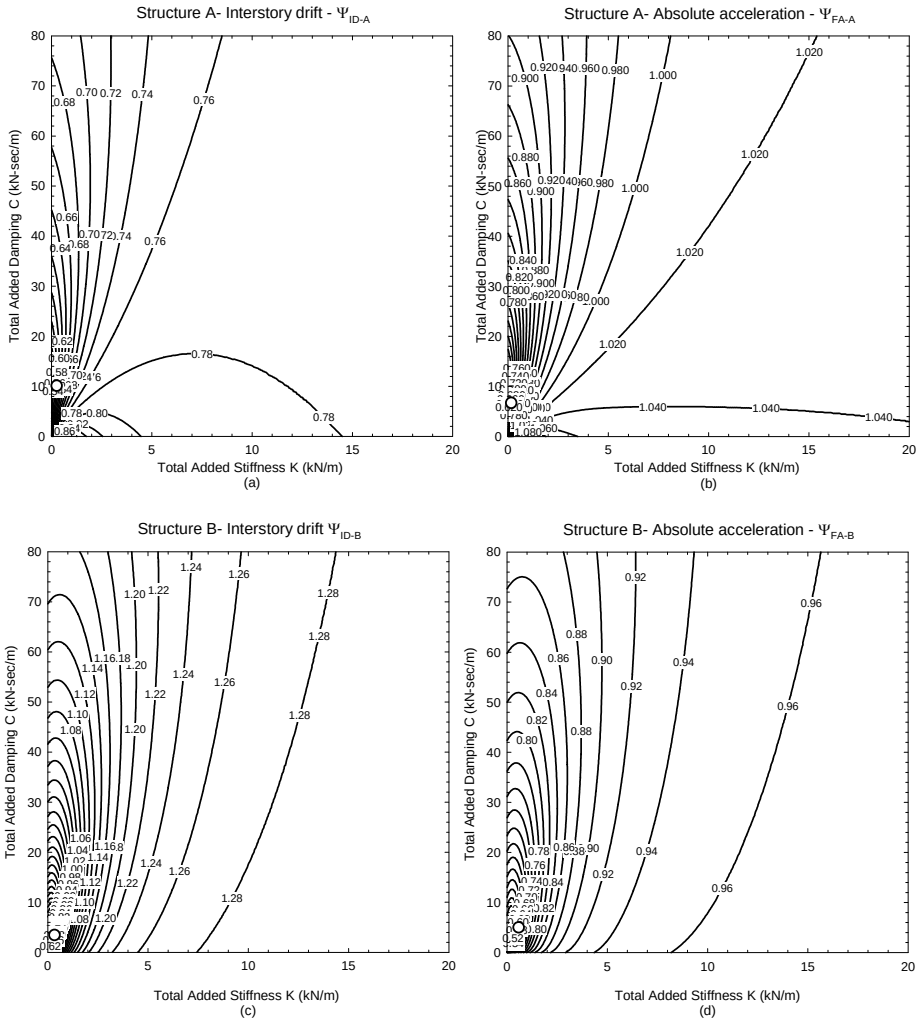

Figure 9.22 Contour lines of values of response modification factors Ψ for configuration (4-3) of coupled structures linked by a viscous dampers and a springs located at the 3rd story level (symbol "o" indicates the optimal combination of C and K)

Results corresponding to the Group I configurations were also found to be qualitatively identical to those shown in Figure 9.21 and are not shown for brevity.

9.8 Comparison with the response of the uncoupled structures equipped with supplemental linear viscous dampers

Adjacent structures linked by viscous dampers can be conceptually thought of as a structural system with supplemental damping where the supplemental dampers are placed in such a way that they connect two originally uncoupled structures to one another. Naturally, it is also possible to add the supplemental dampers to each of the structures without coupling them to each other (Figure 9.23), which is a more standard approach to incorporate supplemental damping into building structures. It is then of practical interest to investigate which approach is more effective in terms of response reduction.

A comparison between response modification factors ψ for the case where the structures of the (4-2) configuration are connected to one another with linear viscous dampers ("coupled configuration") and those for the case where the same structures are uncoupled and equipped with supplemental linear viscous dampers ("uncoupled configuration"), obtained considering the seismic excitation defined by ω_g = 12.50 rad/sec, can be seen in Figure 9.24. Initially, a uniform distribution of total added damping C among all the stories of both structures (Figure 9.23, left) was considered for the uncoupled configuration. Contrary to what was observed in the case of the coupled configuration, however, the response of the uncoupled configuration was found to be significantly sensitive to the height-wise distribution of the total supplemental damping C. An optimized distribution was first determined by applying the optimization algorithm proposed in (Christenson *et al*. 2007), which aims at minimizing the interstory drift response but does not takes into account the floor acceleration response in the optimization process. According to the algorithm,

equal parts of the total added damping C, which were set equal to $C/12$ based on what is recommended in (Lopez-Garcia and Soong, 2002), were incorporated into the structure sequentially.

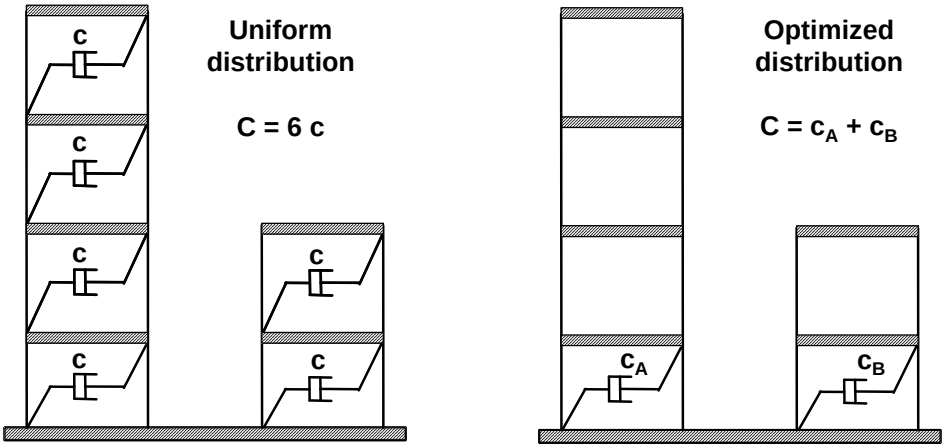

Figure 9.23 Uncoupled structures of the (4-2) configuration equipped with supplemental linear viscous dampers

The algorithm was implemented in such a way that the resulting values of $\psi_{ID\text{-}A}$ and $\psi_{ID\text{-}B}$ are essentially equal to each other. The optimized distribution turned out to consist of dampers located only at the first story of each structure (Figure 9.23, right). The corresponding values of c_A and c_B (the meaning of these symbols is indicated in Figure 9.23, right) as a function of C can be seen in Figure 9.25, which is conceptually identical to Figure 9.7 and Figure 9.16. In order to get more insight into the characteristics of optimized distributions, an alternative optimization algorithm (Cimellaro, 2007) was also considered. This algorithm aims at minimizing the *sum* of the interstory drift and absolute acceleration responses at all stories in the optimization process. The resulting distribution turned out to be qualitatively identical to the one described before (i.e., only one damper located at the first story of each structure). Because of this similarity, no effort was made to implement the second algorithm in a way

leading to equal values of $\psi_{ID\text{-}A}$ and $\psi_{ID\text{-}B}$. The values of factors ψ shown in Figure 9.24 for the optimized distribution are then the ones corresponding to the optimized distribution indicated by the "sequential" optimization algorithm.

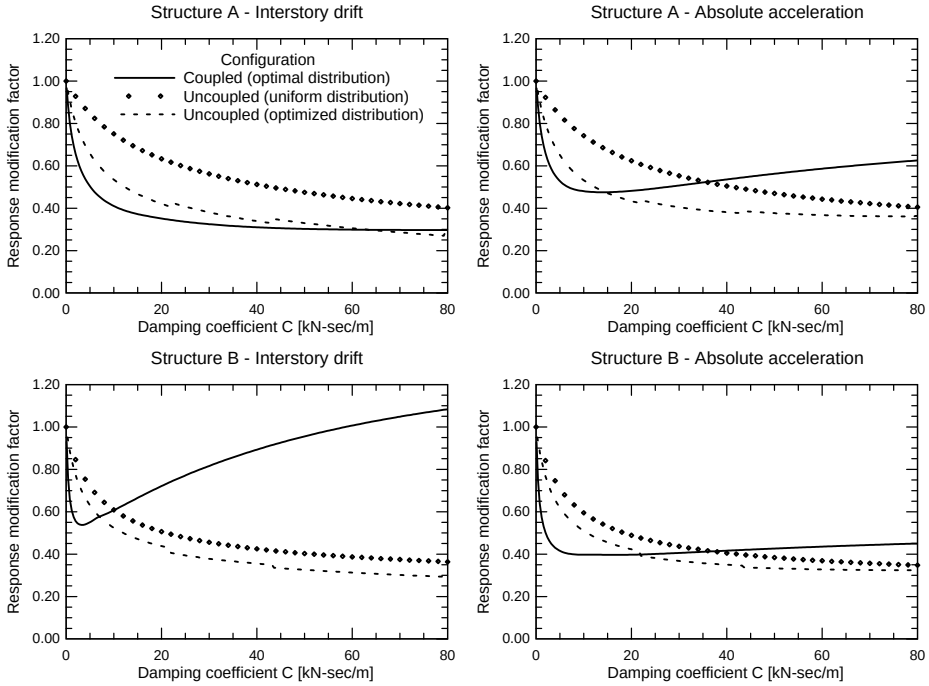

Figure 9.24 Response modification factors for the structures of the (4-2) configuration coupled with linear viscous dampers (coupled configuration) and uncoupled and equipped with supplemental linear viscous dampers (uncoupled configuration)

As it can be observed in Figure 9.24 , the optimized distribution leads to additional response reductions with respect to the response for the case where the distribution is uniform, especially in the case of Structure "A" at relatively small values of *C*. It must be noted that neither of the optimization algorithms considered assures that the resulting distribution is the optimal in a global sense,

which is the reason why the resulting distribution is referred to as "optimized" rather than as "optimal".

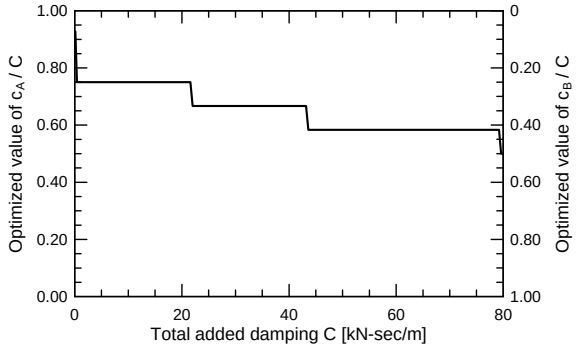

Figure 9.25 Uncoupled structures of the (4-2) configuration: optimized values of constants cA and cB indicated by the sequential optimization algorithm

Figure 9.24 indicates in all cases that greater response reductions are achieved with the coupled configuration at relatively small values of *C*, and that the opposite observation applies at relatively large values of *C*. Except in the case of the interstory drift response of Structure "B", the maximum response reduction is essentially the same for both configurations, although the value of *C* at which the maximum response reduction is attained is smaller in the case of the coupled configuration. Given that smaller values of *C* implies, up to a certain degree, smaller costs of the supplemental damping, the former observation suggest that the coupled configuration may then be more cost-effective than the uncoupled configuration, especially when the supplemental damping in the latter is uniformly distributed. Results corresponding to all of the other pairs of adjacent structures considered in this study were found to be qualitatively identical to those shown in Figure 9.24. For illustration purposes, results corresponding to the (3-2) configuration, obtained considering the seismic excitation defined by ω_g = 12.50 rad/sec, are shown in Figure 9.26.

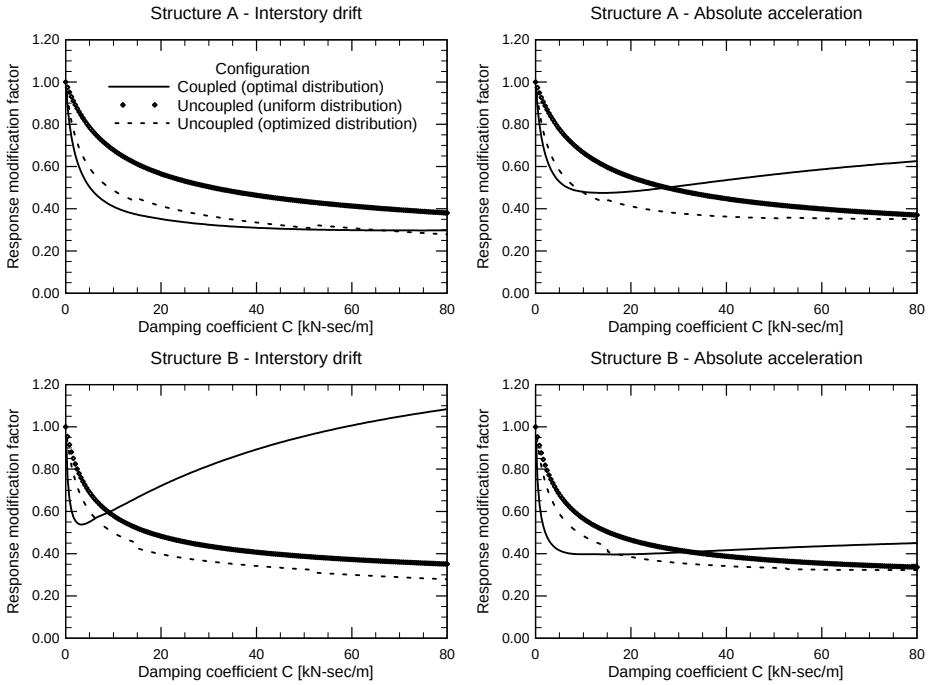

Figure 9.26 Response modification factors for the structures of the (3-2) configuration coupled with linear viscous dampers (coupled configuration) and uncoupled and equipped with supplemental linear viscous dampers (uncoupled configuration)

9.9 Seismic response of adjacent structures connected by nonlinear viscous dampers

9.9.1 Introduction

In preliminary design of damped systems viscous dampers are first modeled as linear (α=1), however in practical applications α is always smaller than 1, because they are easier to be manufactured.

Symans and Constantinou (1998); Pekcan et al. (1999), Rodrigez et al. (1994), Asher et al. (1996) have recently begun to focus on fluid viscous dampers exhibiting nonlinear force-velocity relationship because these devices can achieve essentially the same response reduction attained with linear dampers but the corresponding damper forces are much smaller.

The objective of this section is to characterize the efficiency of the coupling control approach by comprehensively analyzing the dependency of the seismic response of a specific pair of building structures on several properties (e.g., values of characteristic parameters and height-wise distribution) of nonlinear viscous dampers of the passive type.

9.9.2 Description of the model

The model considered in this section is a four story and a two story building, the same described in section 9.3. In the case where the structures are linked to one another with nonlinear viscous dampers (Figure 2) and are subjected to

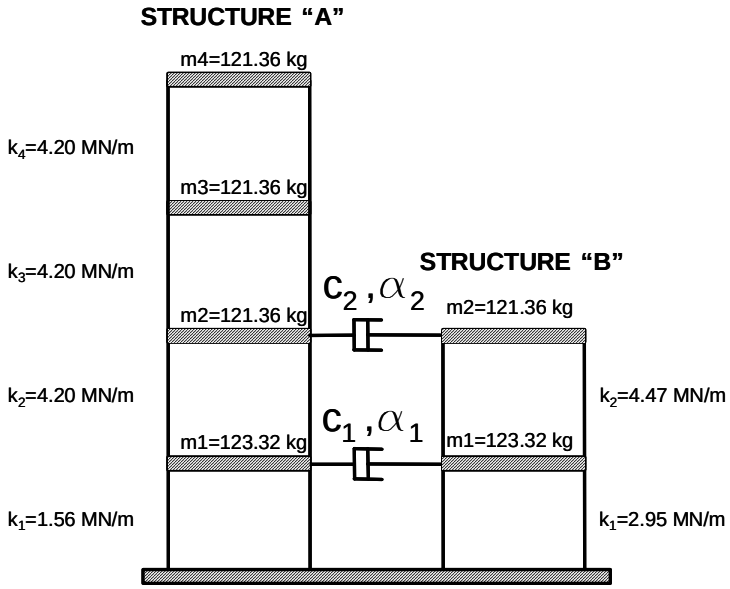

Figure 9.27 Mass and stiffness properties of the building model

one-dimensional earthquake ground acceleration $\ddot{y}_0(t)$, the vector equation of motion is given by:

$$\mathbf{M}\ddot{\mathbf{x}}(t) + \mathbf{C}_0\dot{\mathbf{x}}(t) + \mathbf{K}_0\mathbf{x}(t) = \mathbf{H}\mathbf{U}(t) + \boldsymbol{\eta}w(t) \tag{9.31}$$

where $\mathbf{x}(t)$ is an n-vector for story displacements; $\mathbf{M}$, $\mathbf{C}_0$ and $\mathbf{K}_0$ are (n×n) mass, damping and stiffness matrices of the system, respectively. $\mathbf{U}(t)$ is a (r×1)-vector containing forces from passive dampers, $\mathbf{H}$ is a (n×r) location matrix for passive damper; $\boldsymbol{\eta}$ is the excitation influence matrix (a (n×1) unit vector in the case of earthquake excitations) and $w(t)= \ddot{y}_0(t)$ is a scalar denoting the ground acceleration.

In the state space (9.31) becomes:

$$\dot{\mathbf{Z}}(t) = \mathbf{A}\mathbf{Z}(t) + \mathbf{B}\mathbf{U}(t) + \mathbf{E}(t) \tag{9.32}$$

Where:

$$\mathbf{Z}(t)=\begin{Bmatrix}\mathbf{X}(t)\\ \dot{\mathbf{X}}(t)\end{Bmatrix},;\ \mathbf{E}(t)=\begin{bmatrix}\mathbf{0}\\ \mathbf{M}^{-1}\boldsymbol{\eta}\ddot{y}_0(t)\end{bmatrix},$$
$$\mathbf{A}=\begin{bmatrix}\mathbf{0} & \mathbf{I}\\ -\mathbf{M}^{-1}\mathbf{K}_0 & -\mathbf{M}^{-1}\mathbf{C}_0\end{bmatrix},\ \mathbf{B}=\begin{bmatrix}\mathbf{0}\\ \mathbf{M}^{-1}\mathbf{H}\end{bmatrix}, \tag{9.33}$$

in which **Z**(t) is a (2n×1) state space vector; **A** is a (2n×2n) linear elastic system matrix; **B** is a (2n×r) passive damper location matrix; and **E**(t) is a 2n×1 excitation vector. The force f_i in the nonlinear viscous damper with velocity $\mathring{u}_d$ across the damper and brace deformation is:

$$f_i = c_\alpha \operatorname{sgn}\left(\dot{u}_d\right)\left|u_d\right|^\alpha \tag{9.34}$$

where the damping constant c_α have units of force per velocity, sgn( ) is the signum function; and α is a positive exponent characterizing the nonlinearity of the damper. Typical values of α range from 0.35 to 1 for seismic applications (Rodrigez *et al*., 1994; Asher *et al*., 1996). Greater values lead to poor performance and are expensive to implement.

The (n×1) vector **U**(t) containing forces from nonlinear viscous elastic dampers is given by:

$$\mathbf{U}(t)=-\mathbf{K}_\mathbf{c}\mathbf{x}(t)-\mathbf{U}_d(t) \tag{9.35}$$

where $\mathbf{U}_d$(t) for this particular problem is given by:

$$\mathbf{U}_d(t)=\begin{Bmatrix} \operatorname{sgn}(\dot{x}_1-\dot{x}_5)\,c_1\left|\dot{x}_1-\dot{x}_5\right|^{\alpha} \\ \operatorname{sgn}(\dot{x}_2-\dot{x}_6)\,c_2\left|\dot{x}_2-\dot{x}_6\right|^{\alpha} \\ 0 \\ 0 \\ -\operatorname{sgn}(\dot{x}_1-\dot{x}_5)\,c_1\left|\dot{x}_1-\dot{x}_5\right|^{\alpha} \\ -\operatorname{sgn}(\dot{x}_2-\dot{x}_6)\,c_2\left|\dot{x}_2-\dot{x}_6\right|^{\alpha} \end{Bmatrix}, \tag{9.36}$$

The vector is expressed as a function of the vector **Z**(t) as follow:

$$\begin{aligned} &\mathbf{U}\left(\mathbf{Z}(t)\right)=-\left[\mathbf{K_c}\quad \mathbf{0}\right]\mathbf{Z}(t)-\mathbf{diag(c)}\cdot \\ &\cdot\left(\left(\left|\left[\mathbf{I_0}\quad \mathbf{0}\right]\mathbf{Z}(t)\right|^{\alpha}\right)^{T}\operatorname{sgn}\left(\left[\mathbf{I_0}\quad \mathbf{0}\right]\mathbf{Z}(t)\right)\boldsymbol{\eta}^{T}\right)^{T} \end{aligned} \tag{9.37}$$

Where:

$$\mathbf{I_0}=\left[\begin{array}{c|c|c} \mathbf{I} & 0 & -\mathbf{I} \\ \hline 0 & 0 & 0 \\ \hline -\mathbf{I} & 0 & \mathbf{I} \end{array}\right];\ \mathbf{diag(c)}=\left[\begin{array}{c|c|c} \mathbf{C_D} & 0 & 0 \\ \hline 0 & 0 & 0 \\ \hline 0 & 0 & \mathbf{-C_D} \end{array}\right] \tag{9.38}$$

9.9.3 Comparison among different numerical methods

Due to the special type of damping function described in(9.34) the equation of motions became nonlinear and the most general solving strategy is represented by direct numerical integration of the ordinary differential equations represented by Equation(9.31).

Several competitive numerical integration techniques for nonlinear dynamic analysis of structures by the finite element method are examined and compared for the coupled building problem. Three numerical integration methods have been considered:

(1) Newmark-Beta implicit method (Argyris and Mlejnek, 1991);
(2) Fourth-order Runge-Kutta method with constant step;
(3) Adaptive fourth-order Runge-Kutta-Fehlberg method.

The Newmark-Beta implicit method shows to work very well for SDOF system, but for MDOF system and values of α close to the minimum allowed (0.30), the time step necessary to obtain convergence and to avoid numerical errors at the zero crossing velocity becomes very small, and the computational time increase. The fourth order Runge Kutta method shows better results respect to Newmark method, and finally the last method without sacrificing the accuracy of the solution is able to reduce the computational time of the analysis.

9.9.4 The effects of different values of α: The damping exponent

Structural dampers always use α value between 0.3 and 1.0, as any value above 1.0 produces very poor performance. Figure 9.28 shows a plot of force against velocity for several values of α, the damping exponent.

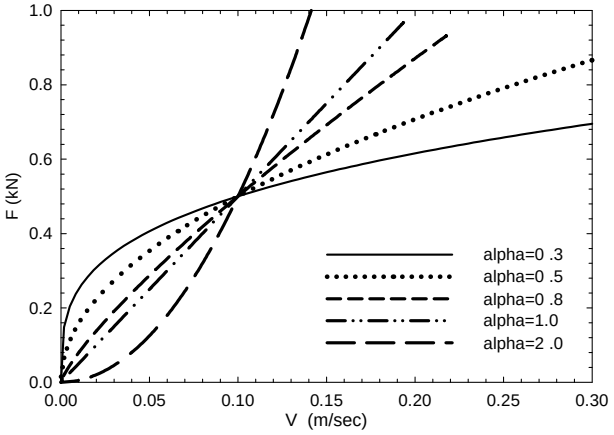

Figure 9.28 Force vs. velocity for several values of the damping exponent α

A value of α =1.0 is the curve for linear damping, which is a good place to start in the design of a damping system. The hysteresis loop for a linear damper is a pure ellipse, as shown in Figure 9.29. α = 0.3 is the lowest damping exponent normally possible and in this case the hysteresis loops assumes a rectangular shape. Figure 9.28 shows how the exponent α provides significantly more force at lower velocities than a linear damper, while lower forces are provided at higher velocities. Figure 9.29 compares the hysteresis loops for two values of α at high velocities and clearly shows that the advantage of using nonlinear viscous dampers is in the reduction of the damper forces at high velocities.

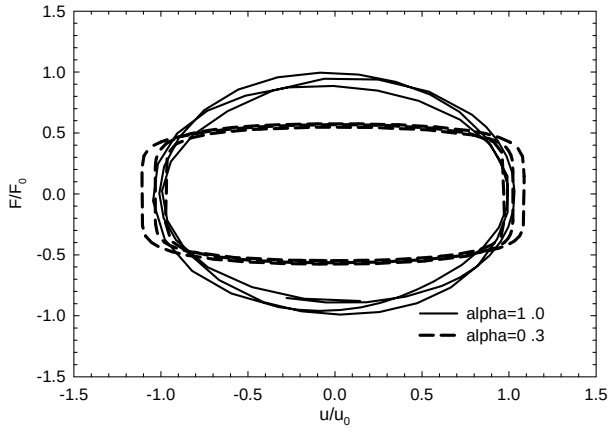

Figure 9.29 Hysteresis loops for linear and nonlinear damping for two values of the damping exponent α=0.3 and α=1.0

9.9.5 Ground motions

Ground excitations were synthetically generated as sample realizations of a nonstationary random process defined by a stationary power spectral density (PSD) function and an "envelope" (sometimes called "modulating" or

"window") function. The one-sided power spectral density G(ω) was defined in terms of the well-known modified Kanai-Tajimi function described in section 9.4. The envelope function was set equal to that originally proposed by Saragoni and Hart (1974), later calibrated by Boore (1983).

In the prototype scale, the duration of the excitations was set equal to 30 sec, and discrete values of the excitations were generated at a constant time step equal to 0.004 sec. The resulting acceleration histories were then converted into model scale in accordance with standard similitude theory described in section 9.3.

9.9.6 Response of the structure linked by nonlinear viscous dampers

The response of the structures was evaluated in terms of peak response values like in equation (9.21) and **Error! Reference source not found.**.

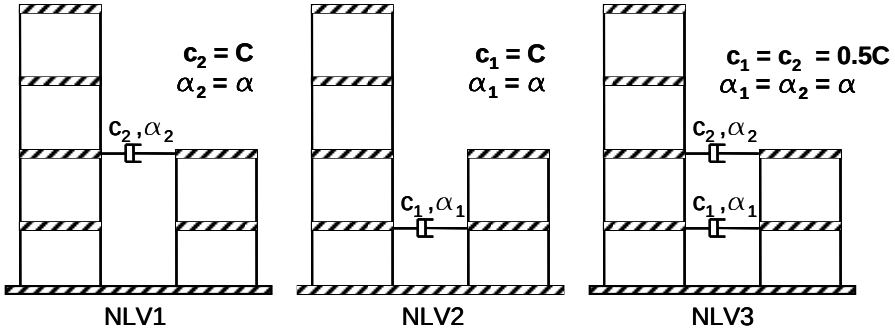

Figure 9.30 Structures linked by combinations of NL viscous dampers

The structural combinations considered in this study are illustrated in Figure 9.30. Results are expressed in terms of the quantity C = c1 + c2, which may be conceptually thought of as the "total added damping" of the coupled system. NLV1 corresponds to the structural configuration when the total added damping C is located at the connection of the second story level. NLV2 corresponds to

the structural configuration when the total added damping C is located at the connection of the first story level. NLV3 corresponds to the structural configuration when the total added damping C is located half at the first story level and half at the second story level. Figure 9.31 and Figure 9.32 shows respectively the influence of the number of records adopted on the mean value and standard deviation of the response modification factors for NLV1 configuration.

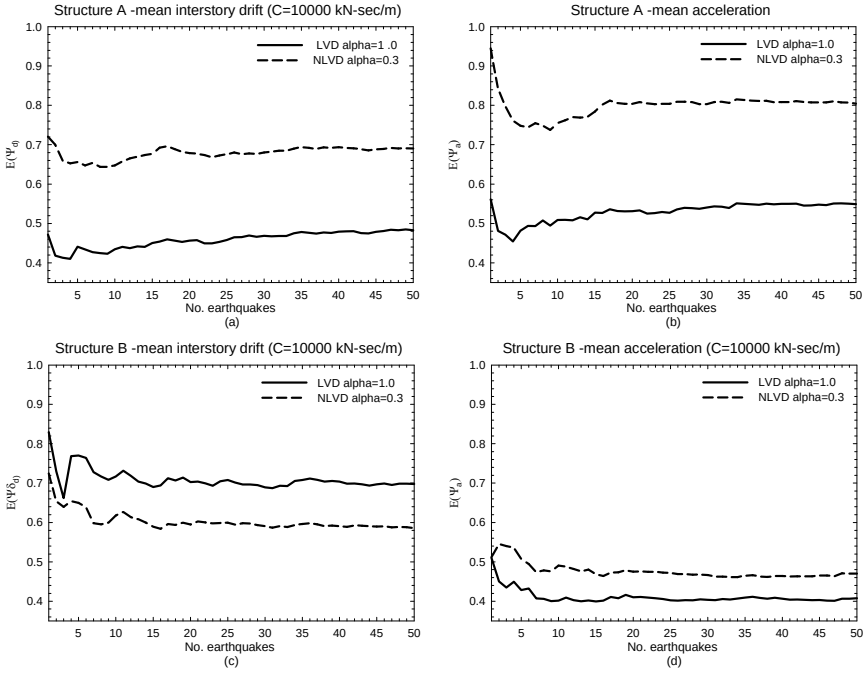

Figure 9.31 Mean response modification factor ψ vs. number of records for NLV1

It is shown that for a number of records equal to 10 the mean response modification factor tends to be stationary and similar trends have been observed for the other two structural configurations, NLV2 and NLV3. So all

combinations of values of C ranging from 0 to 80.000 N-sec/m, and of values of α ranging from 0.30 to 1.0 were considered. Nonlinear time history analyses were performed using 10 earthquakes records and mean response modifications factors Ψ. were evaluated for the three structural configurations considered. Results of the response modification factors Ψ for the three coupled systems NLV1, NLV2 and NLV3 are shown respectively in the form of contour plots inFigure 9.33, Figure 9.34 and Figure 9.35.

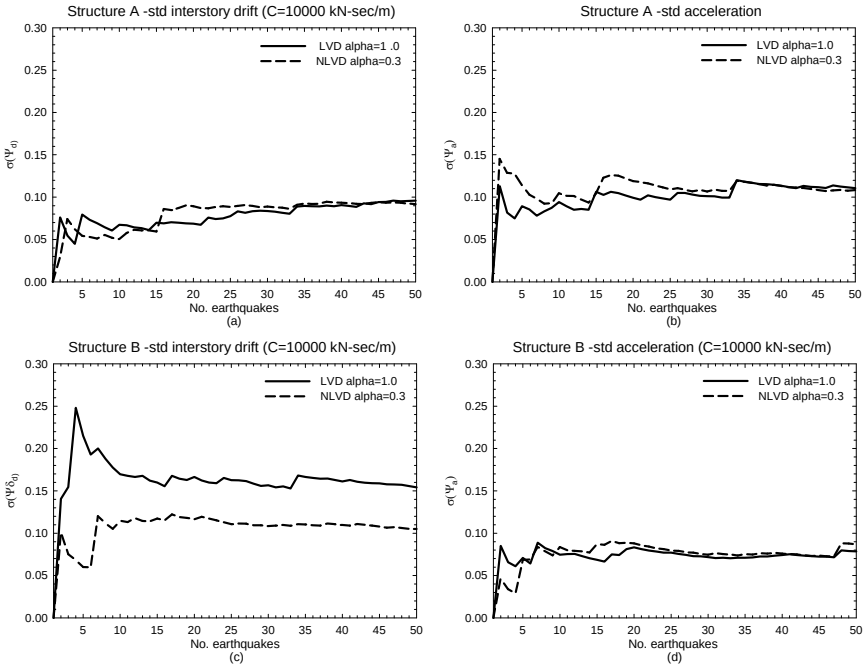

Figure 9.32 Standard deviation of the response modification factor ψ vs. number of records for NLV1

The darker area indicates the lower level of the response modification factor and consequentially the optimal values of C and α. It can be observed that there are wide ranges of combinations of values of C and α for which all values of Ψ are less than unity, which means that it is then possible to reduce both response

quantities in both structures by linking them to one another with nonlinear viscous dampers.

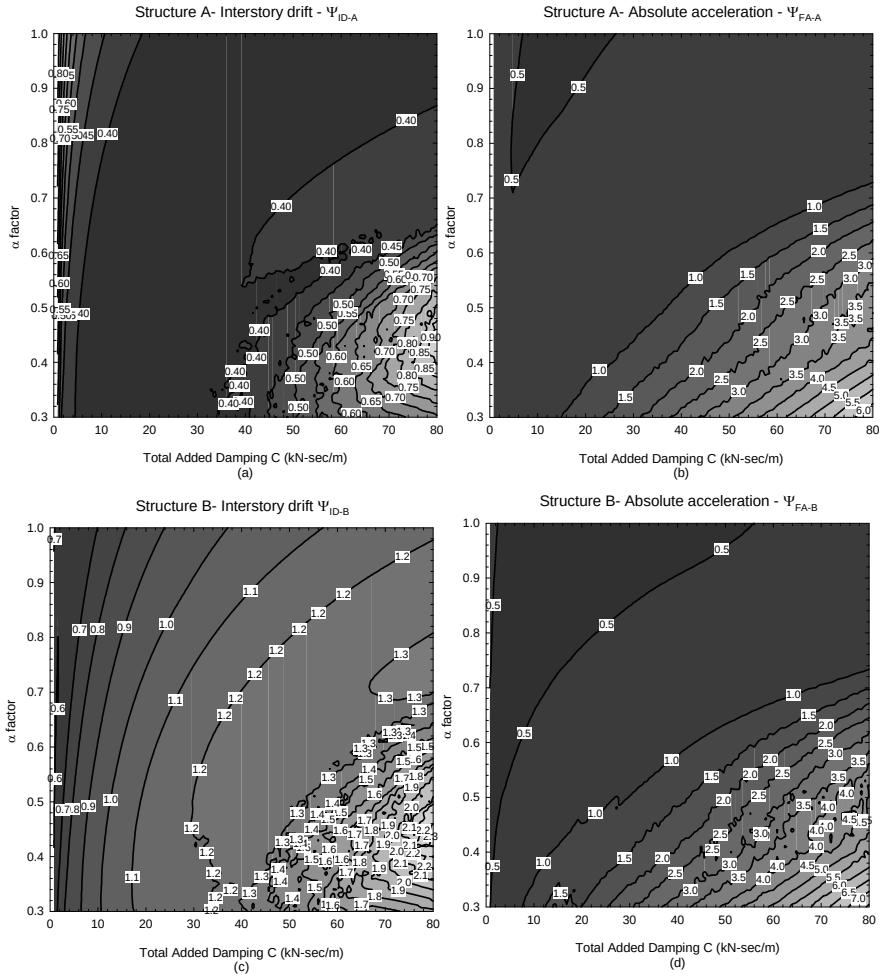

Figure 9.33 Contour lines of response modification factors ψ for the coupled system NLV1 (c1=0; c2=C, α)

By observations, the optimal values of C are between 10 and 20 kN×m/sec, while the optimal values of α ranges between 0.80 and 1.0.

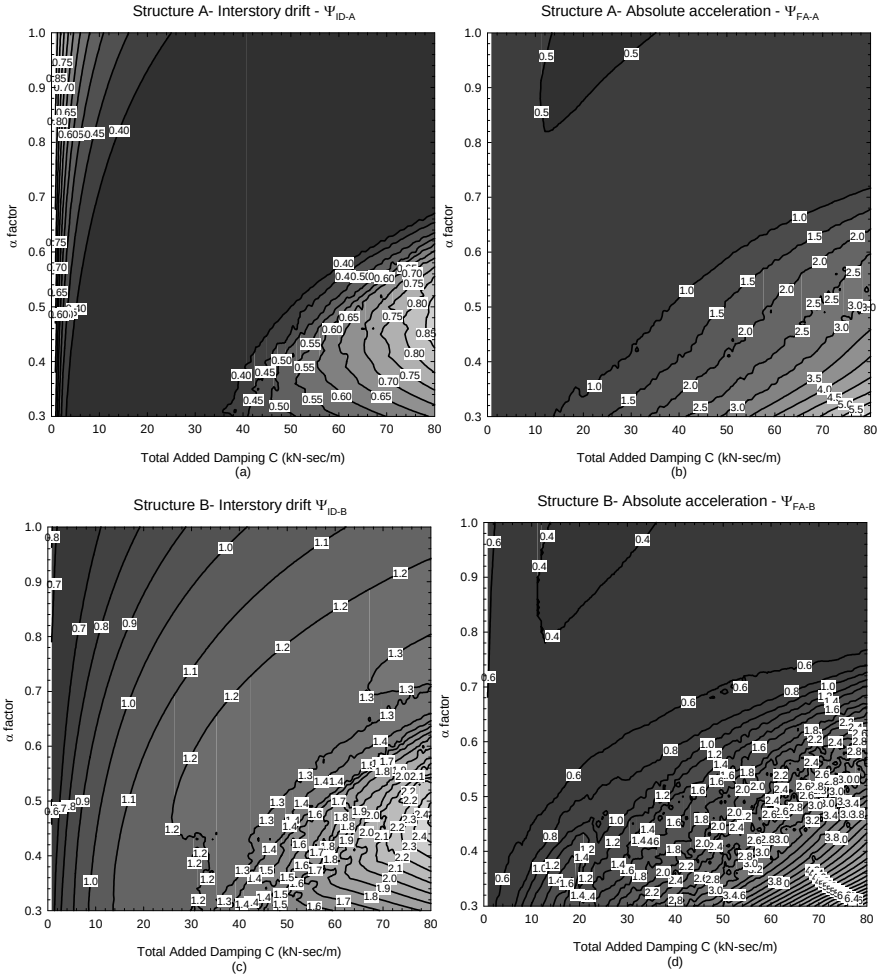

Figure 9.34 Contour lines of response modification factors ψ for the coupled system NLV2 (c1= C; c2=0, α)

In Figure 9.36 are compared the response factors of the two buildings connected at the top level (NLV1) both with linear (α=1.0) and nonlinear viscous dampers (α=0.80) for different values of the total added damping C.

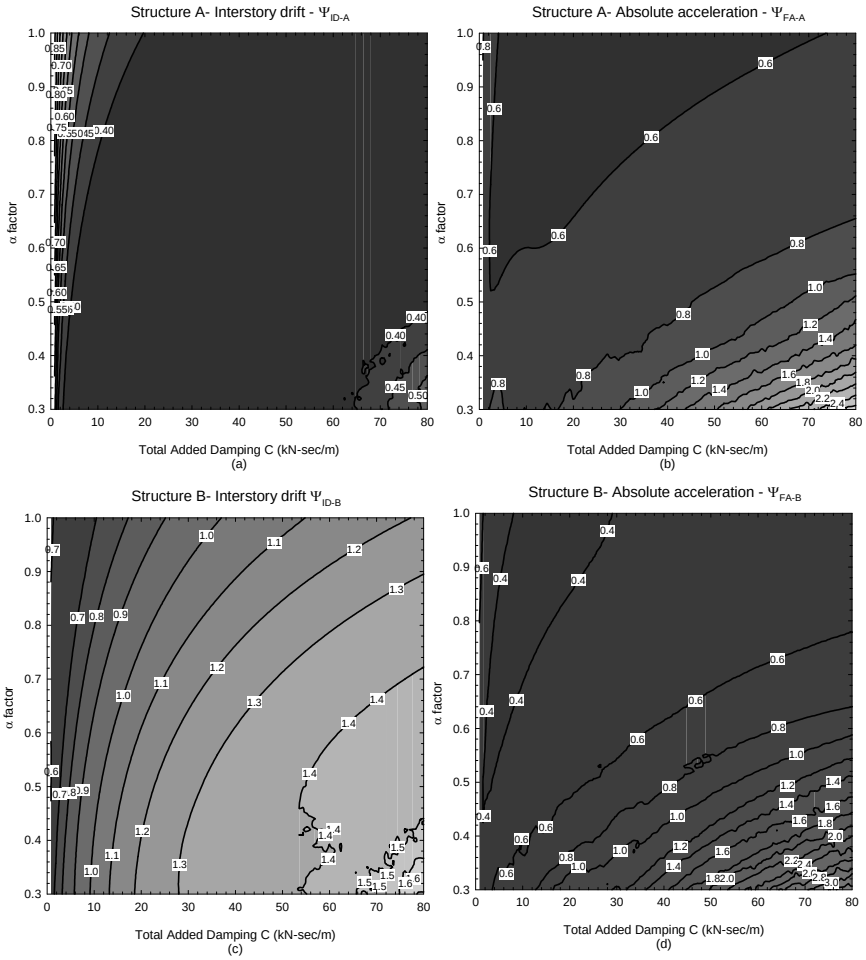

Figure 9.35 Contour lines of response modification factors ψ for the coupled system NLV3 (c1= 0.5C; c2=0.5C, α)

For the linear case (i.e., when α=1.0), it can also be observed that the values of Ψ are in all cases almost always less than unity with the only exception is $\Psi_{ID\text{-}B}$ at very large values of C (Figure 9.36c).

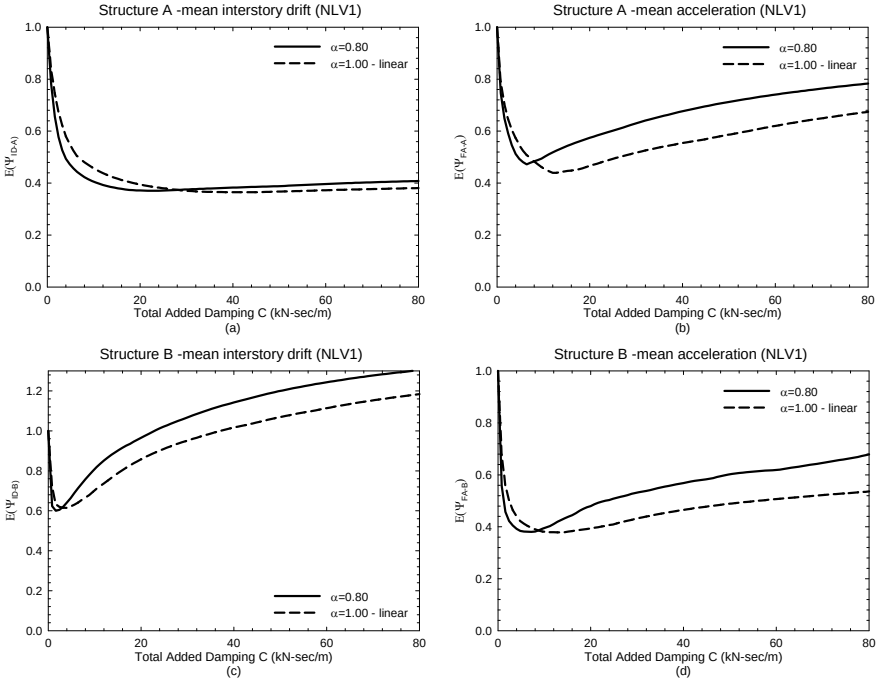

Figure 9.36 Response modification factors ψ vs. total added damping C for NLV1 configuration with linear and nonlinear viscous dampers

Furthermore, for low values of total added damping below C=10000kN×sec/m, the response of the system with nonlinear viscous dampers performs better, however for higher values of added damping the linear viscous damper performs always better. Reducing the value of α generally increases the response modifications factors of both buildings for all the three configurations considered. Figure 9.37 shows values of the response modification factors for the three structural configurations considered in this study for the case where the value of C is equal to the optimal value C_{opt}=10000 N sec/m.

The response modification factors Ψ tends to increase when α reduces, and this increment is more evident in the acceleration response. Only the interstory drifts of building "A" decreases with the decrement of α, but this reduction of 10% in drift will determine an increment of 40% in absolute acceleration when compared with respect to the case of the building connected with linear viscous dampers (α=1).

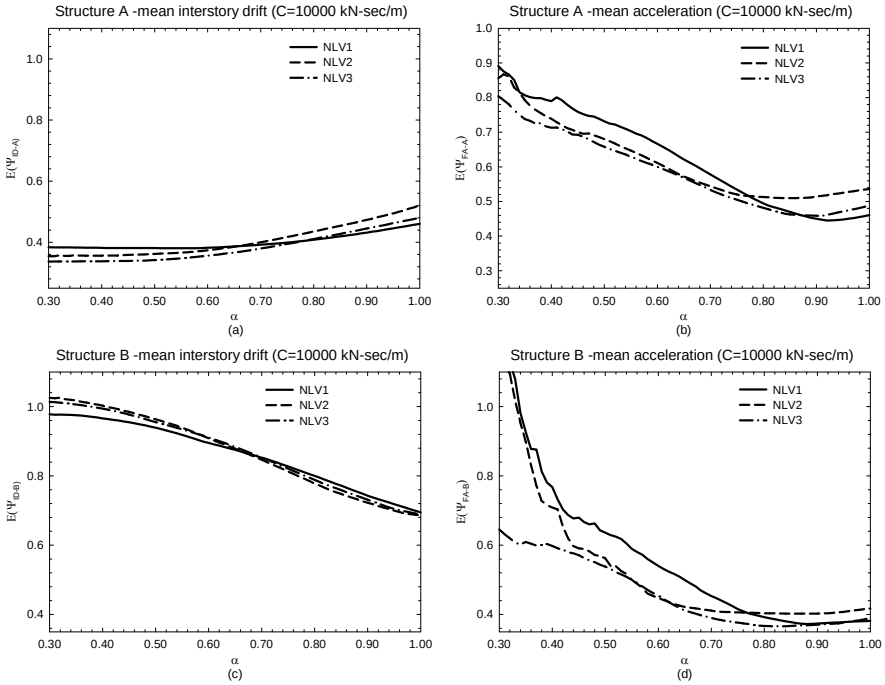

Figure 9.37 Response modification factor ψ vs. alpha for the three structural configurations considered

Furthermore, when α reduces only the accelerations response of building "B" is affected by the height wise distribution of the viscous dampers. In particular for α<0.5 the NLV3 distribution performs better in term of accelerations for building "B", while it does not affect the other response factors

of the system. The reasons of the better performance of linear damping is partly justified by the fact that linear damping in unlikely to excite higher modes in the structure.

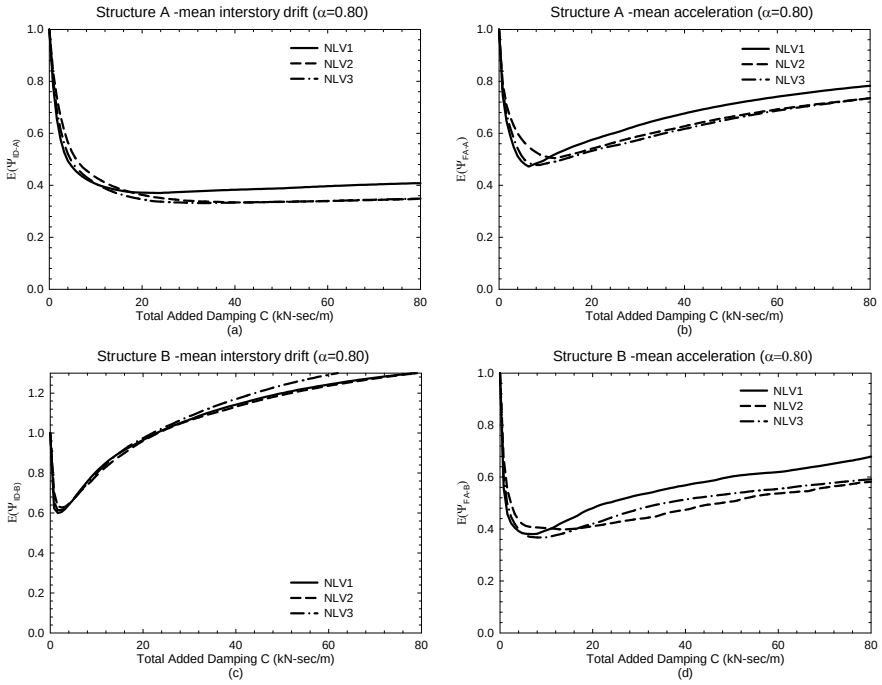

Figure 9.38 Response modification factor ψ vs. Total added damping C for the three structural configurations considered

Another advantage of linear damping is the little interaction between damping forces and structural forces in the building, because structural forces reach their maximum when damping forces are zero and viceversa. Nonlinear viscous dampers with a low exponent show much more a rectangular hysteresis curve and the damping forces tend more to superimpose on the structural forces.

By looking at the contour plots of Figure 9.33 , Figure 9.34 and Figure 9.35 an optimal range of the values of C and α are selected. In particular choosing α=0.80 in Figure 9.38 the response factor Ψ of the buildings do not change among the different configurations (NLV1; NLV2; NLV3) considered. Only acceleration of the building "B" is affected by the distributions for high values of total added damping.

9.10 Summary and conclusions

In this study, the seismic response of a set of pairs of adjacent, linearly elastic building models connected to each other with two types of linear passive devices (springs and viscous dampers) was evaluated analytically. A total of 4 buildings models having 1, 2, 3 and 4 stories were considered, and the multi-story models exhibit a soft-story vertical irregularity at the first story. All the combinations of two different structures out of the four models were considered as pairs of adjacent structures, and several combinations of type and location of the connecting devices having wide ranges of values of their characteristic constants were evaluated. Two response quantities were considered: interstory drift and floor acceleration. The response of the structures was normalized with respect to that of the originally uncoupled structures with no supplemental damping. Results indicate that:

- it is not possible to reduce both response quantities in both structures by connecting them to one another solely by linear springs or solely by rigid links.
- it is possible to reduce both response quantities in both structures by connecting them to one another using viscous dampers only. In this case, the level of response reduction is essentially insensitive to the height-wise distribution of the connecting dampers. Although the truly optimal value of total supplemental damping *C* is different for each response quantity in each structure, there exist wide ranges of

values of C for which similar levels of response reductions may be achieved for both response quantities in both structures.

- given an arbitrary height-wise distribution of connective viscous dampers, further addition of linear springs does not lead in general to additional response reductions. A few exceptions occur only when the value of the stiffness constant of the spring is optimized, and even in these cases, the additional level of response reduction attained is small.
- when the structures are linked to one another solely by linear viscous dampers, the coupling control approach is more effective in the structure whose fundamental natural frequency is closer to the main frequency of the excitation.
- the maximum level of response reduction that can be achieved by coupling the structures solely with linear viscous dampers (coupled configuration) is essentially equal to the maximum level of response reduction that can be achieved by adding supplemental viscous dampers to each structure without coupling them to one another (uncoupled configuration). The coupled configuration, however, is more effective at relatively low values of total supplemental damping C.

For the two adjacent, linearly elastic building models (4 story and 2 story) connected to each other with nonlinear viscous dampers of the passive type it was found that:

- The response of the system globally increases when the coefficient α of the viscous dampers reduces for all the three configurations considered. Only the interstory drift of building "A" tends to reduce with the reduction of α, but this reduction of 10% in drift will determine an increment of 40% in accelerations with respect to the building connected with linear viscous dampers;

- The response factors Ψ of the systems are not affected by the height-wise distribution of the connecting dampers when α=0.80. Only the accelerations of the building "B" are affected by the distributions for high values of total added damping C.
- For low values of total added damping C the response of the system with nonlinear viscous dampers (α=0.80) performs better, however for higher values of added damping the linear viscous damper (α=1.0) performs always better.

Chapter 10

10 Reccomandations and conclusions

In this Ph.D. dissertation two different systems were analyzed. The first is the T600 module of ICARUS project. Earthquake forces including the sloshing phenomena has been analyzed with both simplified approach and with a more accurate finite element model developed in LS-DYNA.

A finite element model in SAP 2000 of the entire system has been built and displacement and acceleration response of the main structural parts have been determined under different loading conditions. From analysis the worst loading condition for the piping system appears when one of the cylindrical tank is full with liquid Argon and the other is full with liquid Nitrogen. However, this condition is transient because it happens only during the loading condition and consequentially the probability to be combined with an earthquake event is very low.

Another three dimensional finite element model capable of describing the complex dynamic behavior of the liquid tank subjected to strong seismic base excitation is developed in LS-DYNA. The model uses an updated Eulerian-Lagrangian description of the liquid-solid interface in order to enforce compatibility between solid and liquid elements.

The characterization of the ground motion input at the site is provided. A clear descriptions of the method available to simulate earthquake ground motion is provided. A simplified approach taken from the paper of Karamanos et al. is used to describe the earthquake loads developed in the two horizontal cylindrical tanks, while the approach described in the New Zealand report of professor Priestley is used to determine the hydrodynamic pressure distributions on the lateral walls of of the semi-module T300 of the ICARUS project. Hydrodynamic pressures generated on the roof of the tank due to sloshing have been evaluated following the procedure described in the paper of Malhotra that has been opportunely modified to be adapted to rectangular tank.

Chapter 8 describes different seismic qualification requirements of the piping system and a final pipe support arrangement to retrofit the piping system of the entire project is provided.

The second of the complementary research efforts of this dissertation (in chapter 9) is the mitigation of earthquake response of a set of pairs of adjacent, linearly elastic building models connected to each other with two types of linear and nonlinear passive devices (springs and viscous dampers) was evaluated analytically. A total of 4 buildings models having 1, 2, 3 and 4 stories were considered, and the multi-story models exhibit a soft-story vertical irregularity at the first story. All the combinations of two different structures out of the four models were considered as pairs of adjacent structures, and several combinations of type and location of the connecting devices having wide ranges of values of their characteristic constants were evaluated.

Appendix A

Table 0-1 INFN design spectrum (Sabetta and Faccioli)

T (sec)	a (g)
0.02	0.3
0.05	0.619
0.4	0.563
0.45	0.5
0.5	0.45
0.55	0.409
0.6	0.376
0.65	0.346
0.7	0.321
0.75	0.3
0.8	0.281
0.85	0.265
1.15	0.261
1.2	0.25
1.25	0.24
1.3	0.231
1.35	0.222
1.4	0.214
1.45	0.207
1.5	0.2
1.55	0.194
1.6	0.188
1.65	0.182
1.7	0.176

1.75	0.171
1.8	0.167
1.85	0.162
1.9	0.158
1.95	0.154
2	0.15
10	0.03

Appendix B

Table 0-1 seismic events starting from 1000 D.C. up to a distance of 15 km from the site

EE Epicentral Zone			Castelli dell Aquilano		Appennino abruzzese	Italia centro-meridionale
Felt			13		15	218
Energy (ergs)	2.43E+09	1.59E+09	1.05E+09	2.43E+09	1.59E+09	5.62E+09
I	6	6	8	6.5	9	6
R(km)	90.549	57.61	15.4	63.4	36.2	35.889
M_s	6.5	6.3	6.0	6.5	6.3	7.1
Io	10	9.5	9	10	9.5	11
Lon			13.533		13.2	14.717
Lat			42.283		42.267	41.3
Date	1279	1298	1315	1328	1349	1456

Aquilano	Valnerina	Sannio	3 Appennino umbro-reatino	3 Appennino umbro-reatino	3 Aquilano
11	20	216	199	22	71
2.43E+09	1.05E+09	5.62E+09	5.62E+08	4.52E+09	2.43E+09
9	4.6	4.6	7	7	9
15.6	52.6	129.5	45.2	31.5	24.03
6.5	6.0	7.1	7.1	5.4	6.5
10	9	11	11	8	10
13.55	13.017	14.567	13.067	13.1	13.3
42.317	42.717	41.283	42.7	42.617	42.433
1461	1599	1688	1703	1703	1703

Maiella	Valnerino	Aquilan	Umbria meridionale	Aquilan	Molise	Basilicat a	Marche meridionali
99	115	6	33	7	223	337	196
3.69E+09	1.05E+09	1.05E+08	6.88E+08	2.97E+09	2.43E+09	5.62E+08	4.52E+09
6	6	7	4.6	7.5	6.5	4	3
58.6	46.47	17.6	67.92	21.8	110.2	261.5	59.8
6.8	6.0	6.0	5.7	5.1	6.5	7.1	5.4
10.5	9	9	8.5	7.5	10	11	8
14.083	13.117	13.583	12.783	13.367	14.467	15.85	13.25
42.083	42.75	42.3	42.533	42.317	41.5	40.35	43.083
1706	1730	1762	1785	1786	1805	1857	1873

Monti della Meta	Monti della Meta	Romagna sud-orientale	Valle del Clitunno	Valnerina	Abruzzo meridionale	Liguria occidentale	Monti della Meta
62	43	144	34	15	29	1517	76
2.97E+08	2.97E+08	4.52E+08	4.52E+08	4.52E+08	4.52E+09	1.05E+08	1.95E+08
4	3	2	4	4	5	0	3.5
67.6	71.5	161.6	83.0	52.1	62.1	486.9	64.2
5.1	5.1	5.4	5.4	5.4	5.4	6.0	4.9
7.5	7.5	8	8	8	8	9	7
13.783	13.833	12.55	12.683	13.05	14.283	8	13.75
41.683	41.65	44.067	42.85	42.767	42.233	43.883	41.717
1873	1874	1875	1878	1879	1881	1887	1901

Bibliographical reference	Marsica	Marsica	Marsica	Alto Adriatico	Molise occidentale	Irpinia	Maiella	Marche meridionali-Abruzzo
	56	22	860	132	50	511	326	131
	6.88E+08	3.64E+07	5.62E+09	4.52E+08	1.95E+08	2.43E+09	1.05E+09	6.88E+08
	4	4.6	8	5	0	4	4	5
	37.7	49.1	53.5	155.0	80.6	192.0	61.3	39.2
	5.7	3.7	7.1	5.4	4.9	6.5	6.0	5.7
	8.5	5	11	8	7	10	9	8.5
	13.317	13.25	13.65	12.617	14.183	15.367	14.183	13.65
	42.1	41.983	41.983	44.017	41.717	41.05	42.05	42.917
	1904	1904	1915	1916	1925	1930	1933	1943

	Aquilano	Valle del Velino	Valnerina	Irpinia-Basilicata	Appennino abruzzese
	152	71	694	1395	913
8	4.52E+08	2.97E+08	6.88E+08	2.43E+09	4.52E+08
8	7	4	5	4	5
4.834	13.6	45.3	47.6	197.7	77.6
5.4	5.1	5.1	5.7	6.5	5.4
8	7.5	7.5	8.5	10	8
	13.483	13.05	13.083	15.283	14.05
	42.333	42.4	42.717	40.85	41.667
1950	1958	1961	1979	1980	1984

Bibliographical references

1. ALGA.SPA (2001) “Impianto Rilevatore di Neutrini ICARUS – Caratteristiche Tecniche degli isolatori antisismici in Gomma and alta dissipazione di Energia ALGASISM HDRB”, *Technical Report*.

2. i. "Seismic Design of Strage Tanks-Appendix E." *Welded Steel Tanks for Oil Storage*, API Standard 650, Washington D.C.

3. ANSYS (2004), “ANSYS Structural Analysis Guide”, ANSYS, Inc., Houston, 2004.

4. Asadour H. Hadjian.,” A general framework for risk-consistent seismic design”, Earthquake Engineering and Structural Dynamics, Earthquake Engng Struct. Dyn. 2002; 31:601–626.

5. Asher, J., Young, R. P., and Ewing, R. D. (1996). "Seismic isolation design of the San Bernardino conty mediacl center replacement project." *Journal of Structural Design of Tall Buildings*, 5, 265-279.

6. ATC/SEAOC. (1999). "Seismic Response of Nonstructural Components, Part A: Overview of Component Types and Behavior." ATC/SEAOC Joint Venture Training Curriculum, Redwood City, California.

7. Albarello, D., Bosi, V., Bramerini, F., Lucantoni, A., Naso, G., Peruzza, L., Rebez, A., Sabetta, F. and Slejko, D. (2000) Carte di pericolosità sismica del territorio nazionale. *Quaderni di Geo.sica*, Vol. 12.

8. Bhaskararao, A. V., and Jangid, R. S. (2006). "Seismic analysis of structures connected with friction dampers." *Engineering Structures*, 28(5), 690-703.

9. Bommer, J. J., and Acevedo, A. B. (2004). "The use of real earthquake accelerograms as input to dynamic analysis." *Journal of Earthquake Engineering*, 8(1), 43-91.

10. Boore, D. (1983). "Stocastic simulation of high frequency ground motions based on seismological models of the radiated spectra." *Bull.Seism. Soc. Am.*, 73, 1865-1894.

11. Boschi E., Guidoboni E., Ferrari G., Mariotti D., Valensise G., Gasperini P., "Catalogue of strong Italian earthquakes from 461 b.c. to 1997", Annali di geofisica, ISSN vol. 43, N° 4, August 2000, pages 1590-1815.

12. Christenson, R. E., Spencer, J. B. F., Johnson, E. A., and Seto, K. (2006). "Coupled building control considering the effects of building/connector configuration." *Journal of Structural Engineering, ASCE*, 132(6), 853–863.

13. Christenson, R. E., Spencer, B. F., and Johnson, E. A. (2007). "Semiactive Connected Control Method for Adjacent Multidegree-of-Freedom Buildings." *Journal of Engineering Mechanics, ASCE*, 133(3), 290-298.

14. Cimellaro, G. P. (2003). "Coupled Buildings control." *Proceedings of 16th ASCE Engineering Mechanics Conference, paper n.233*, University of Washington, Seattle.

15. Cimellaro, G. P., and Lopez-Garcia, D. (2004). "Random Seismic Response of adjacent buildings structures linked by linear connective

devices." *Proceedings of the 3rd European Conference on Structural Control*, July 12-15, Vien, Austria, 88-91.

16. Cimellaro, G. P., and Marazzi, F. (2004). "Adjacent coupled building control using MR dampers." *Proceedings of Third European Conference on Structural Control*, Vienna, Austria, July 12-15.

17. Cimellaro, G. P., Reinhorn, A. M., and Bruneau, M. (2005). "Seismic resilience of a health care facility." *Proceedings of Annual Meeting of The Asian Pacific Network of Centers for Earthquake Engineering Research (ANCER)*, paper N3-Session III, 10-13 November, 2005, Seogwipo KAL Hotel Jeju, Korea.

18. Cimellaro, G. P., and Retamales, R. (2006). "Optimal Softening and damping design for buildings." *Journal of Structural Control and Health Monitoring*, published on web Oct 6 2006 (DOI: 10.1002/stc.181).

19. Cimellaro, G. P., Christovasilis, I. P., and Malhotra, P. K. (2007a). "Roof pressures due to sloshing loads in rectangular tanks with insufficient freeboard." *Proceeding of COMPDYN 2007- Computational Methods in Structural Dynamics and Earthquake Engineering*, 13-16 June 2007, Rethymno, Crete, Greece.

20. Cimellaro, G. P. (2007b). "Simultaneous stiffness-damping optimization of structures with respect to Acceleration, Displacement and Base Shear." *Engineering Structures*, published on line March 27, 2007 (DOI:10.1016/j.engstruct.2007.01.001).

21. Cimellaro, G. P., and Reinhorn, A. M. (2007c). "Selection of seismic records for fragility analysis of nonlinear systems with nonstructural components." *Proceeding of COMPDYN 2007- Computational Methods in Structural Dynamics and Earthquake Engineering*, 13-16 June, Rethymno, Crete, Greece.

22. Cimellaro, G. P., and Lopez-Garcia, D. (2007d). "Seismic response of adjacent Buildings connected by nonlinear viscous dampers." *Proceedings of Structures Congress 2007 (SEI 2007)*, May 16-20, Long Beach, California.

23. Cimellaro, G. P., and Lopez-Garcia, D. (2007e). "A study on the seismic response of adjacent building structures connected by linear viscous dampers." *Earthquake Engineering & Structural Dynamics*, accepted for publication.

24. Clough, R. W., and Penzien, J. (1993). *Dynamics of Structures, 2nd edition*, Mc Graw Hill, New York.

25. Comite`_Europeen_de_Normalization. (1998). "Part4: Silos, Tanks and pipelines." *Eurocode 8, part 4, Annex A*, CEN ENV-1998-4, Brussels.

26. Di Pasquale G., Orsini G., and Romeo R.W.,."New Developments in Seismic Risk Assessment" in Bulletin of Earthquake Engineering (2005) 3:101–128 © Springer 2005.

27. Elisabeth Pate´-Cornell, "Risk and Uncertainty Analysis in Government Safety Decisions", Risk Analysis, Vol. 22, No. 3, 2002.

28. ESD. (2007). "European Strong Motion Database." http://www.isesd.hi.is/.

29. Faccioli, E. (1997). "Studio del rischio sismico nel laboratorio sotterraneo del Gran Sasso (Esperimento Borexino) - Prima parte: Determinazione dei parametri di base dei terremoti di progetto per le analisi dinamiche strutturali." Rapporto tecnico per INFN, Milano.

30. Filiatrault, A., and Folz, B. (1992). "Nonlinear earthquake response of structurally interconnected buildings." *Canadian Journal of Civil Engineering*, 19(4), 560-572.

31. Galadini, F., and Galli, P. (2000). "Active Tectonics in the Central Apennines (Italy) – Input Data for Seismic Hazard Assessment." *Natural Hazard*, 22(3), 225-268.

32. Gasparini, D. A., and Vanmarcke, E. H. (1976). "Simulated Earthquake Motions Compatible with Prescribed Response Spectra." Massachusetts Institute of Technology, Cambridge, Massachusetts.

33. Gresho, P. M., Chan, S. T., Lee, R. L., and Upson, C. D. (1984). "A modified finite element method for solving the time-dependent, incompressible navier-stokes equations. part I Theory." *International Journal of Numerical Methods in Fluids*, 4, 557-598.

34. Gresho, P. M., Chan, S. T., Lee, R. L., and Upson, C. D. (1984). "A modified finite element method for solving the time-dependent, incompressible navier-stokes equations. part II Applications." *International Journal of Numerical Methods in Fluids*, 4, 619-640.

35. Gurley, K., Kareem, A., Bergman, L. A., Johnson, E. A., and Klein, R. E. (1994). "Coupling tall buildings for control of response to wind." Structural safety & reliability, G. I. Schueller, M. Shinozuka, and J. T. P. Yao, eds., Balkema, Rotterdam, The Netherlands, 1553–1560.

36. Gutenberg, B., and Richter, C. F. (1944). "Earthquake magnitude: intensity, energy and acceleration." *Bulletin of the Seismological Society of America*, 46, 104-145.

37. Hancock, J., Watson-Lampre, J., Abrahamson, N. A., Bommer, J. J., Markatis, A., McCoy, E., and Mendis, R. (2006). "An Improved method of matching response spectra of recorded earthquake ground motion using wavelets." *Journal of Earthquake Engineering*, Special issue, 10(1), 67-89.

38. Harris, H. G., and Sabnis, G. M. (1999). *Structural Modeling and Experimental Techniques, Second Edition*, CRC Press LLC.

39. Heredia-Zavoni, E., and Vanmarcke, E. H. (1994). "Seismic Random-Vibration Analysis of Multisupport-Structural Systems." *Journal of Engineering Mechanics, ASCE*, 120(5), 1107-1128.

40. Housner, G. W. (1957). "Dynamic pressures on Accelerated Fluid Containers." *Bull. Seism. Soc. Am.*, 47, 15-35.

41. Housner, G. W. (1970). "Design Spectrum." *Chapter 5 in Earthquake Engineering*, New Jersey: R.L Wiegel, Prentice-Hall., 93-106.

42. Ibrahim, R. A. (2005). *Liquid Sloshing Dynamics: theory and Applications*, Cambridge University Press.

43. The ICARUS Collaboration, “ICARUS II”, a second-generation proton decay experiment and neutrino observatory at the Gran Sasso Laboratory”, LNGS-94/99 Vol I & II, Proposal.

44. ICARUS Collaboration, "A first 600-ton ICARUS detector installed at the Gran Sasso Laboratory", Addendum to Proposal, LNGS-95/10 (1995).

45. ICARUS Collaboration, NIM A346 (1994), p. 550.

46. ISMES. (1998). "Revisione dello spettro di progetto per i laboratori sotterranei del Gran Sasso, Prog. STA-2144; Doc.n. RAT-STA-1846/97." ISMES spa, Seriate (BG), Italy.

47. Kamagata, K., Miyajima, K., and Seto, K. (1996). "Optimal design of damping devices for vibration control of parallel structures." Proc., 3rd Int. Conf. on Motion and Vibration Control (MOVIC), Vol. 2, Chiba, Japan, 334–339.

48. Karamanos, S. A., Patkas, L. A., and Platyrrachos, M. A. (2006). "Sloshing Effects on the Seismic Design of Horizontal-Cylindrical and Spherical Industrial Vessels." *Transaction of the ASME*, 128(August 2006), 328-340.

49. Kim, J., Ryu, J., and Chung, L. (2006). "Seismic performance of structures connected by viscoelastic dampers." *Engineering Structures*, 28(2), 183-195.

50. Klein, R. E., and Healy, M. D. (1987). "Semi-active control of wind induced oscillations in structures." Proc., 2nd Int. Conf. on Structural Control, Univ. of Waterloo, Ontario, Canada, Martinus Nijhoff Publishers, Dordrecht, The Netherlands, 354–369.

51. Kobayashi, N., Mieda, T., Shibata, H., and Shinozaki, Y. (1989). "A study of the liquid Slosh Response in Horizontal Cylindrical Tanks." *ASME, Journal Pressure Vessel Technology*, 111(1), 32-38.

52. Kobori, T., Yamada, T., Takenaka, Y., Maeda, Y., and Nishimura, I. (1988). "Effect of dynamic tuned connector on reduction of seismic response - application to adjacent office buildings." *Proceedings of the 9th World Conference on Earthquake Engineering*, Tokyo-Kyoto, Japan, 773-778.

53. Kramer, S. L. (1996). *Geotechnical Earthquake engineering*, Prentice-Hall International Series in Civil Engineering and Engineering Mechanics, Upper Saddle River, New Jersey 07458.

54. Lama, P. (1998). "Seismic Codes, HVAC Pipe Systems, and Practical Solutions." *ASHRAE Trans. 1998, American Society of Heating, Refrigerating and Air-Conditioning Engineers*, 104, Part 1.

55. Lopez Garcia D. , and G.P. Cimellaro G.P. (2005) , "N° A13-14 Respuesta sismica de estructuras adyacentes conectadas mediante

elementos leneales pasivos", *Proceedings of congreso Chileno de Sismologia e Ingenieria antisismica IX Jornadas,* 16-19 de Novembre de 2005. Concepcion - Chile.

56. Lopez-Garcia, D., and Cimellaro, G. P. (2006). "Seismic Response of Adjacent Structures connected by linear, passive devices." *Proceedings of the 4th World Conference on structural Control and Monitoring*, 11-13 July 2006, San Diego, California.

57. Lopez-Garcia, D., and Soong, T. T. (2002). "Efficiency of a simple approach to damper allocation in MDOF structures." *Journal of Structural Control*, 9(1), 19-30.

58. LSTC. (2003), "LS-DYNA Theoretical Manual", Livermore Software Technology Corporation, Livermore, 2003.

59. Luco, J. E., and Wong, H. L. (1994). "Control of the seismic response of adjacent structures." Proc., 1st World Conf. on Structural Control, Pasadena, Calif., TA2-21-30.

60. Luco, J. E., and Barros, F. C. P. (1998). "Optimal damping between two adjacent elastic structures." *Earthquake Engineering & Structural Dynamics*, 27(7), 649-659.

61. Malhotra, P. K. (2005). "Sloshing Loads in Liquid Storage-Tanks with Insufficient Freeboard." *Earthquake Spectra*, 21(4), 1185-1192.

62. McGarr, A. (1984). "Scaling of ground motion parameters, state of stress, and focal depth." *J. Geoph. Res.*, 89, 6969-6979.

63. Naeim, F., and Lew, M. (1995). "On the use of design spectrum compatible time histories." *Earthquake Spectra*, 11(1), 111-127.

64. Naeim, F., Alimorandi, A., and Pezeshk, S. (2004). "Selection and scaling of ground motion time histories for structural design using genetic algorithms." *Earthquake Spectra*, 20(2), 413-426.

65. Nims, D. K. (1991). "Large Scale Experimental Studies of Two Alternate Support Systems for the Seismic Restraint of Piping," Ph.D. Dissertation, University of California at Berkeley, Berkeley.

66. Ni, Y. Q., Ko, J. M., and Ying, Z. G. (2001). "Random seismic response analysis of adjacent buildings coupled with non-linear hysteretic dampers." *Journal of Sound and Vibration*, 246(3), 403-417.

67. PEER. (2007). "Strong motion database." *Pacific Earthquake Engineering Research Center*, http://peer.berkeley.edu/smcat/index.html.

68. Pekcan, G., Mander, J. B., and Chen, S. S. (1999). "Fundamental considerations for the design of non-linear viscous dampers." Earthquake Engineering & Structural Dynamics, 28, 1405-1425.

69. Platyrrachos, M. A., and Karamanos, S. A. (2005). "Finite elements analysis of Sloshing in Horizontal-Cylindrical Industrial Vessels under Earthquake Loading." *Presssure Vessel and Piping Conference*, ASME, PVP2005-71499, Denver, CO.

70. Priesley, M. J. N., Davidson, B. J., Honey, G. D., Hopkins, D. C., Martin, R. J., Ramsey, G., Vessey, J. V., and Wood, J. H. (1986). "Seismic design of Storage Tanks." *Reccomandation of a Study Group of the New Zealand National Society for Earthquake Engineering*.

71. Reinhorn, A. M. (1997). "Inelastic analysis techniques in seismic evaluations." *Proceedings of the International Workshop on Seismic Design Methodologies for the next Generation of Codes*, 24-27 June, Bled, Slovenia.

72. Robert P. Kennedy, ”Risk based seismic design criteria”, Nuclear Engineering and Design 192 (1999) 117–135.

73. Robin K. McGuire, “Deterministic vs. probabilistic earthquake hazards and risks”, Soil Dynamics and Earthquake Engineering 21 (2001) 377-384.

74. Rodriguez, S., Seim, C., and Ingham, T. (1994). "Earthquake protective systems for the seismic upgrade of the Golden Gate bridge." Proceeding 3rd US-Japan Workshop on Protective Systems for Bridges, Berkeley, California.

75. Romeo, R.W. and Pugliese, A. (2000) Seismicity, seismotectonics and seismic hazard of Italy. *Engineering Geology* **55**(4), 241–266.

76. Romeo, R.W., Paciello, A. and Rinaldis, D. (2000) Seismic hazard maps of Italy including site effects. *Soil Dynamics and Earthquake Engineering* **20**(1–4), 85–92.

77. Computers and Structures, I. (2005). "SAP2000." Berkeley, California, USA.

78. Saragoni, R., and Hart, G. (1974). "Simulation of artificial earthquakes." *Earthquake Engineering & Structural Dynamics*, 2, 249-267.

79. Slejko, D., Peruzza, L. and Rebez, A. (1998) The seismic hazard maps of Italy. *Annals of Geophysics* **41**(2), 183–214.

80. Scarpa, R., and Luca, G. D. (1997). "Terremoto di progetto per i laboratori Sotterranei del Gran Sasso." Rapporto tecnico preliminare per conto INFN.

81. Seto, K. (1994). "Vibration control method for flexible structures arranged in parallel." Proc., 1st World Conf. on Structural Control, Vol. 2, Pasadena, Calif., 62–71.

82. Soong, T. T., and Grigoriu, M. (1993). *Random Vibration of Mechanical and Structural Systems*, Prentice-Hall International, Inc., Englewood Cliffs, New Jersey 07632.

83. Symans, M. D., and Constantiou, M. C. (1998). "Passive fluid viscous damping systems for seismic energy dissipation." ISET J. Earthquake Technology, Paper No. 382, 35(4), 185-206.

84. Tauby, J. R., Lloyd, R., Noce, T., and Tunnissen, J. (1999). "A Practical Guide to Seismic Restraint." *American Society of Heating, Refrigerating and Air-Conditioning Engineers*, Atlanta, Georgia.

85. Trombetti, T., and Silvestri, S. (2004). "Added viscous dampers in shear-type structures: the effectiveness of mass proportional damping." *Journal of Earthquake Engineering*, 8(2), 275-313.

86. Valles RE, Reinhorn AM (1997): Evaluation, prevention and mitigation of pounding effects in buildings structures. Technical Report Nº NCEER-97-0001, National Center for Earthquake Engineering Research, Buffalo, USA.

87. Westermo, B. D. (1989). "The dynamics of interstructural connection to prevent pounding." *Earthquake Engineering & Structural Dynamics*, 18(5), 687-699.

88. Working Group, GNDT-ING-SSN (1999) Proposta di riclassificazione sismica del territorio nazionale. *Ingegneria Sismica* **XVI** (1), 15–23.

89. WRC 379 (1993). "Alternative methods for Seismic Analysis of Piping Systems." Welding Research Council Bulletin 379, New York.

90. Xu, Y. L., He, Q., and Ko, J. M. (1999). "Dynamic response of damper-connected adjacent buildings under earthquake excitation." *Engineering Structures*, 21, 135-148.

91. Xu, Y. L., Zhan, S., Ko, J. M., and Zhang, W. S. (1999). "Experimental investigation of adjacent buildings connected by fluid damper." *Earthquake Engineering & Structural Dynamics*, 28(6), 609-631.

92. Xu, Y. L., Yang, Z., and Lu, X. L. (2003). "Inelastic seismic response of adjacent buildings linked by fluid dampers." *Structural Engineering and Mechanics, An International Journal*, 15(5), 513-534.

93. Yang, Z., Xu, Y. L., and Lu, X. L. (2003). "Experimental seismic study of adjacent buildings with fluid dampers." *Journal of Structural Engineering*, 129(2), 197-205.

94. Zhang, R. H., and Soong, T. T. (1992). "Seismic design of viscoelastic dampers for structural applications." *Journal of Structural Engineering, ASCE*, 118(5), 1375-1392.

95. Zhang, W. S., and Xu, Y. L. (1999). "Dynamic characteristics and seismic response of adjacent buildings linked by discrete dampers." *Earthquake Engineering & Structural Dynamics*, 28(10), 1163-1185.

96. Zhang, W. S., and Xu, Y. L. (2000). "Vibration analysis of two buildings linked by Maxwell model-defined fluid dampers." *Journal of Sound and Vibration*, 233(5), 775-796.

97. Zhu, H. P., and Iemura, H. (2000). "A study of response control on the passive coupling element between two parallel structures." *Structural Engineering and Mechanics, An International Journal*, 9(4), 383-396.

98. Zhu, H. P., Wen, Y. P., and Iemura, H. (2001). "A study on interaction control for seismic response of parallel structures." *Computers & Structures*, 79(2), 231-242.